

Three-Dimensional Electrodes for Efficient  
Electrochemical Water Splitting

# Dissertation

zur Erlangung des Doktorgrades der  
Ingenieurwissenschaften (*Dr.-Ing.*)

der

Naturwissenschaftlichen Fakultät II  
Chemie, Physik und Mathematik

der Martin-Luther-Universität  
Halle-Wittenberg

vorgelegt von

Herr M. Sc. Haojie ZHANG

geboren am 13.12.1990 in Henan, China



Thesis referee:

Prof. Dr. Ralf B. Wehrspohn (Supervisor), Prof. Dr. A. Wouter Maijenburg, Prof. Dr.-Ing. Kai Sundmacher (MPI Magdeburg)

Defense committee:

Prof. Dr. Kathrin Dörr (Chairman), Prof. Dr. Ralf B. Wehrspohn, Prof. Dr. A. Wouter. Maijenburg, Prof. Dr.-Ing. Kai Sundmacher, Prof. Dr. Jamal Berakdar, Prof. Dr. Horst Beige, Prof. Dr. Jan Laufer, Prof. Dr. Georg Schmidt, Prof. Dr. Michael Bron

Thesis submission date: 08.04.2020

Defense date: 07.12.2020

# Abstract

In this thesis, we aimed to develop novel catalysts and prepare three-dimensional (3D) electrodes to improve the performance of electrochemical water splitting. Firstly, the background and basic reaction mechanisms of water splitting were introduced. Subsequently, the latest progress of the preparation of bifunctional heterostructured transitional metal phosphides (TMP)-based heterostructures and the corresponding mechanisms for enhanced catalytic activities for water splitting were reviewed and discussed in detail. Afterwards, two strategies were used to prepare 3D electrodes, which include developing highly active catalysts and preparing 3D electrodes based on abundant and robust substrates. In the case of highly active catalysts, the heterostructured 3D electrode consisting of NiFe layered double hydroxides nanosheets assembled NiCoP nanorods on nickel foam (NiFe LDH@NiCoP/NF) was prepared and demonstrated improved catalytic activities for hydrogen evolution reaction/oxygen evolution reaction (HER/OER) and overall water splitting in alkaline electrolyte. The enhanced performance can be attributed to the increased amount of active sites and accelerated charge transfer at the heterointerface. Moreover, a novel atomic layer deposition (ALD) recipe for the deposition of high quality, smooth and well-crystallized cobalt phosphide (Co-P) was developed and reported for the first time. The optimized ALD recipe followed the self-limited layer-by-layer deposition behavior and the deposited Co-P films demonstrated a better HER activity than the similar films prepared by the traditional post-thermal phosphorization method. In the case of the abundant substrate, the state-of-the-art catalysts (Pt and RuO<sub>2</sub>) were coupled with commercial stainless steel (SS) mesh by using carbon nanotubes as an interfacial material for the first time. The prepared 3D SS-based electrodes demonstrated excellent HER/OER activities and long-time stability. Our work gives examples for the design and preparation of 3D electrodes and highlights the advantage of 3D electrodes for efficient water splitting which also exhibits a huge potential to be employed in other electrochemical areas (e.g. fuel cells, batteries).



This is a blank page.

# Contents

<b>1</b>	<b>Introduction</b> .....	<b>1</b>
1.1	Background .....	2
1.1.1	Strategies to Improve the Performance of TMP-based Electrocatalysts.....	3
1.1.2	3D Electrodes Preparation.....	8
1.2	Thesis Scope and Outline .....	9
1.3	References .....	13
<b>2</b>	<b>Bifunctional Heterostructured Transition Metal Phosphides for Efficient Electrochemical Water Splitting</b> .....	<b>16</b>
2.1	Abstract .....	17
2.2	Author Biographies .....	18
2.3	Introduction .....	19
2.4	Mechanism of the Water Splitting Reactions.....	23
2.4.1	General Mechanisms of the HER and the OER in Alkaline Electrolytes .....	23
2.4.2	Insight into the Synergistic Effects of Heterostructures on the Improved HER/OER and Overall Water Splitting Activities in Alkaline Electrolytes.....	26
2.4.3	<i>In-situ</i> /operando Measurements for Mechanistic Studies of the Water Splitting Process.....	35
2.5	Synthetic Methods for the Preparation of TMP-Based Heterostructures.....	41
2.5.1	Growth-Phosphorization (GPM) Method.....	43
2.5.2	Growth-Phosphorization-Modification (GPM) Method .....	45
2.5.3	Metal-Organic Framework (MOF)-Derived Method.....	46
2.5.4	Other Methods.....	47
2.6	Bifunctional TMP-Based Heterostructures for Efficient Water Splitting.....	49
2.6.1	C/TMP Heterostructures .....	49
2.6.2	TM/TMP Heterostructures .....	54
2.6.3	TMO/TMP Heterostructures .....	57
2.6.4	TMH/TMP Heterostructures .....	60

2.6.5	TMP/TMP Heterostructures .....	64
2.6.6	TMS/TMP Heterostructures .....	67
2.6.7	Other Heterostructured TMP-Based Catalysts .....	70
2.7	Conclusions and Perspectives .....	73
2.8	Acknowledgment .....	76
2.9	References .....	76
<b>3</b>	<b>Bifunctional Heterostructure Assembly of NiFe LDH Nanosheets on NiCoP</b>	
	<b>Nanowires for Highly Efficient and Stable Overall Water Splitting.....</b>	<b>87</b>
3.1	Abstract .....	88
3.2	Introduction .....	89
3.3	Experimental Section .....	91
3.4	Results and Discussion.....	94
3.5	Conclusions .....	105
3.6	Acknowledgment .....	105
3.7	References .....	106
3.8	Supporting Information .....	108
<b>4</b>	<b>Optimization of Chemical Vapor Deposition Process for Carbon Nanotubes Growth</b>	
	<b>on Stainless Steel: Towards Efficient Hydrogen Evolution Reaction.....</b>	<b>118</b>
4.1	Abstract .....	119
4.2	Introduction .....	120
4.3	Experimental Section .....	120
4.4	Results and Discussion.....	121
4.5	Conclusions .....	125
4.6	Acknowledgment .....	125
4.7	References .....	125
<b>5</b>	<b>Novel Stable Three-dimensional Stainless Steel-based Electrodes for Efficient</b>	
	<b>Water Splitting .....</b>	<b>126</b>
5.1	Abstract .....	127

5.2	Introduction .....	128
5.3	Experimental Section .....	130
5.4	Results and Discussion.....	133
5.5	Conclusions .....	143
5.6	Acknowledgment .....	143
5.7	References .....	144
5.8	Supporting Information.....	147
<b>6</b>	<b>Atomic Layer Deposition of Cobalt Phosphide for Highly Efficient Hydrogen Evolution Reaction.....</b>	<b>160</b>
6.1	Abstract .....	161
6.2	Introduction .....	162
6.3	Experiment Sections.....	164
6.4	Results and Discussion.....	167
6.5	Conclusions .....	173
6.6	Acknowledgment .....	173
6.7	References .....	174
6.8	Supporting Information.....	176
<b>7</b>	<b>Conclusions and Outlook.....</b>	<b>182</b>
<b>8</b>	<b>Acknowledgements.....</b>	<b>184</b>
	<b>Acronyms .....</b>	<b>186</b>
	<b>Publications.....</b>	<b>187</b>
	<b>Curriculum Vitae .....</b>	<b>190</b>
	<b>Declaration.....</b>	<b>191</b>

This is a blank page.

# **1 Introduction**

## 1.1 Background

Fossil fuel combustion created a significant threat to the sustainable development of the world by causing serious environmental pollution, global warming and an energy crisis.<sup>[1]</sup> A report from the International Energy Agency reveals that the global energy demand expands by over 25% between 2017 and 2040, and that the energy-related CO<sub>2</sub> emission will rise gradually to 35.8 Gt/year in 2040.<sup>[2]</sup> Therefore, enormous efforts are focused on developing techniques for the utilization of clean and renewable energies to meet the energy demand and sustainable development of future societies, such as solar energy, wind energy, geothermal energy and hydropower.<sup>[3-6]</sup> Among the renewable energies, H<sub>2</sub> has been considered as a promising alternative to traditional fuels owing to its comparably high energy density (142 MJ/kg) and low carbon emission properties.<sup>[7]</sup> However, almost all the hydrogen consumed in 2019 by the chemical industry was produced by steam reforming of methane, which simultaneously exhausts a large amount of carbon dioxide as a by-product.<sup>[8]</sup> Therefore, producing hydrogen by electrolysis from water is important for the low-carbon economy, especially when it can be combined with renewable energies.<sup>[9]</sup> In a commercial electrolyzer, the reactions happen on the cathode and anode are named as hydrogen evolution reaction (HER) and oxygen evolution reaction (OER), respectively. Furthermore, the high cost and scarcity of state-of-the-art electrodes used in commercial electrolyzers (Pt for cathode and Ru/Ir-based electrocatalysts for anode) severely limit their large-scale utilization for the hydrogen economy in the terawatt scale.<sup>[10]</sup> Although enormous efforts have been devoted to improving the performance of electrolysis, the cost of electrolytic hydrogen is still dramatically high (3-7.5 USD/kg).<sup>[7]</sup> So, it is vital to develop highly efficient and abundant electrocatalysts for efficient electrochemical water splitting.

In the past decades, several different types of highly active and cheap electrocatalysts have been prepared and investigated with promising catalytic performance, including transition metal oxides (TMO),<sup>[11]</sup> transition metal nitrides (TMN),<sup>[12,13]</sup> transition metal phosphides (TMP),<sup>[14,15]</sup> transition metal carbides (TMC)<sup>[16,17]</sup> and transition metal sulfides (TMS).<sup>[18,19]</sup> Among them, TMP-based electrocatalysts stand out from the crowd and exhibit excellent water

splitting activities, which can be attributed to their superior electrical conductivity, faster charge transfer and better reaction kinetics.<sup>[20,21]</sup>

### **1.1.1 Strategies to Improve the Performance of TMP-based Electrocatalysts**

The water splitting activities of TMP-based electrocatalysts are determined by various factors, including composition, crystalline phase, morphology, substrate mass loading, etc. However, the electrocatalytic performance of TMP-based electrocatalysts can be enhanced by reasonable design and preparation strategies, which will be highlighted in the following.

#### **1.1.1.1 Tuning the P/M Ratio in TMP**

The P content demonstrates a significant influence on the intrinsic properties of TMP. In general, a higher P content leads to tuning of the electronic structure to expose more active sites for the HER, but leads to a reduction of the conductivity resulting in a weakened OER performance. Therefore, the balance between the active sites and conductivity derived from different P concentrations in TMP should be taken into account when designing and preparing bifunctional TMP-based electrocatalysts for overall water splitting. For instance, Menezes et al. synthesized different phases of Ni phosphides exhibiting various HER and OER activities associated with the P/Ni ratio.<sup>[22]</sup> According to their findings, Ni<sub>12</sub>P<sub>5</sub> ( $\eta_{10} = 240$  mV, where  $\eta_{10}$  represents the overpotential at a current density of 10 mA cm<sup>-1</sup>) deposited on fluorine-doped tin oxide (FTO) glass demonstrated a better OER activity than Ni<sub>2</sub>P ( $\eta_{10} = 260$  mV) due to the higher concentration of Ni, benefiting from the formation of a NiOOH/Ni(OH)<sub>2</sub> shell on the phosphide core. On the other hand, Ni<sub>2</sub>P ( $\eta_{10} = 85$  mV) exhibited a much higher HER performance than Ni<sub>12</sub>P<sub>5</sub> ( $\eta_{10} = 170$  mV) owing to the higher P content favorably forming moderate bonding states with the intermediates and products. When nickel foam (NF) was used as the substrate, the prepared Ni<sub>2</sub>P (1.58 V @ 10 mA cm<sup>-2</sup>) demonstrated a superior overall water splitting performance as compared to Ni<sub>12</sub>P<sub>5</sub> (1.64 V @ 10 mA cm<sup>-2</sup>) in a 1 M KOH electrolyte. Therefore, the optimal overall water splitting activity can be achieved by tuning the P/M ratio in order to reach/obtain a balance of intrinsic active sites and conductivity.



### 1.1.1.2 Alloying

The alloying effect can significantly influence the electronic structures of TMP and optimize the adsorption energy of intermediates resulting in improved HER/OER activity. The Volvano plot of TMP was obtained by Jaramillo et al. employing DFT calculations.<sup>[23]</sup> They revealed that the alloying effect can optimize the hydrogen adsorption free energy  $\Delta G_{H^*}$ , thus improving the intrinsic performance of TMP for the HER. Li and coauthors prepared  $Ni_{2-x}Co_xP$  with different Ni/Co ratios.<sup>[24]</sup> They found that NiCoP with an optimized Ni/Co ratio of 1 demonstrates the best HER performance due to the enhanced  $H_2$  desorption ability after the addition of Co. Subsequently, Yu et al. found that the OER activity can also be improved simultaneously.<sup>[25]</sup> They found that optimized  $Ni_{0.51}Co_{0.49}P$  exhibits outstanding overall water splitting with a low cell voltage of 1.57 V to deliver  $10 \text{ mA cm}^{-2}$  and durable stability for more than 100 h. Very recently, Wu et al. prepared Janus particles consisting of  $Ni_{0.1}Co_{0.9}P$  on conductive carbon fiber paper (CFP) by electrodeposition and subsequent annealing.<sup>[26]</sup> The prepared  $Ni_{0.1}Co_{0.9}P/CFP$  exhibits improved bifunctional catalytic performance for both the OER and the HER in neutral media when compared with CoP. The XPS and XANES measurements demonstrate that the electron transfer is facilitated by Ni addition (**Figure 1-1(a, b)**). The shorter bond length of Co-P in  $Ni_{0.1}Co_{0.9}P$  compared with CoP suggests that the introduction of Ni leads to the modified local coordination environment of CoP (**Figure 1-1(c)**).<sup>[27]</sup>

The accelerated electron transfer for  $Ni_{0.1}Co_{0.9}P$  is further confirmed by ultraviolet photoelectron spectroscopy (UPS, **Figure 1-1(d)**). The DOS results reveal the modulated electronic states after Ni participation (**Figure 1-1(e)**). Additionally, they found that the prepared  $Ni_{0.1}Co_{0.9}P$  not only exhibits a small  $\Delta G_{H^*}$  resulting in enhanced HER performance, but also demonstrates a decreased  $\Delta G_3$ , which is related to the rate determining step (RDS) that processes the formation of activated  $*OOH$  intermediates, leading to an improved OER activity (**Figure 1-1(f, g)**). In another study, Xu and coauthors found that the OER performance of TMP can be boosted by the introduction of elements resulting in bi-/tri- metallic TMP, and that their OER activities follow the trend  $FeP < NiP < CoP < FeNiP < FeCoP < CoNiP < FeCoNiP$ .<sup>[28]</sup>

Impressively, Cheng et al. prepared NiAl<sub>8</sub>P array with Al vacancies exhibiting outstanding bifunctional performance for both the OER and the HER in electrolytes with a wide pH range (0-14).<sup>[29]</sup> The Al defect has significantly lowered the  $\Delta G_{H^*}$  and increased the H<sub>2</sub>O adsorption ability, thus benefiting to the HER and OER performance, respectively.

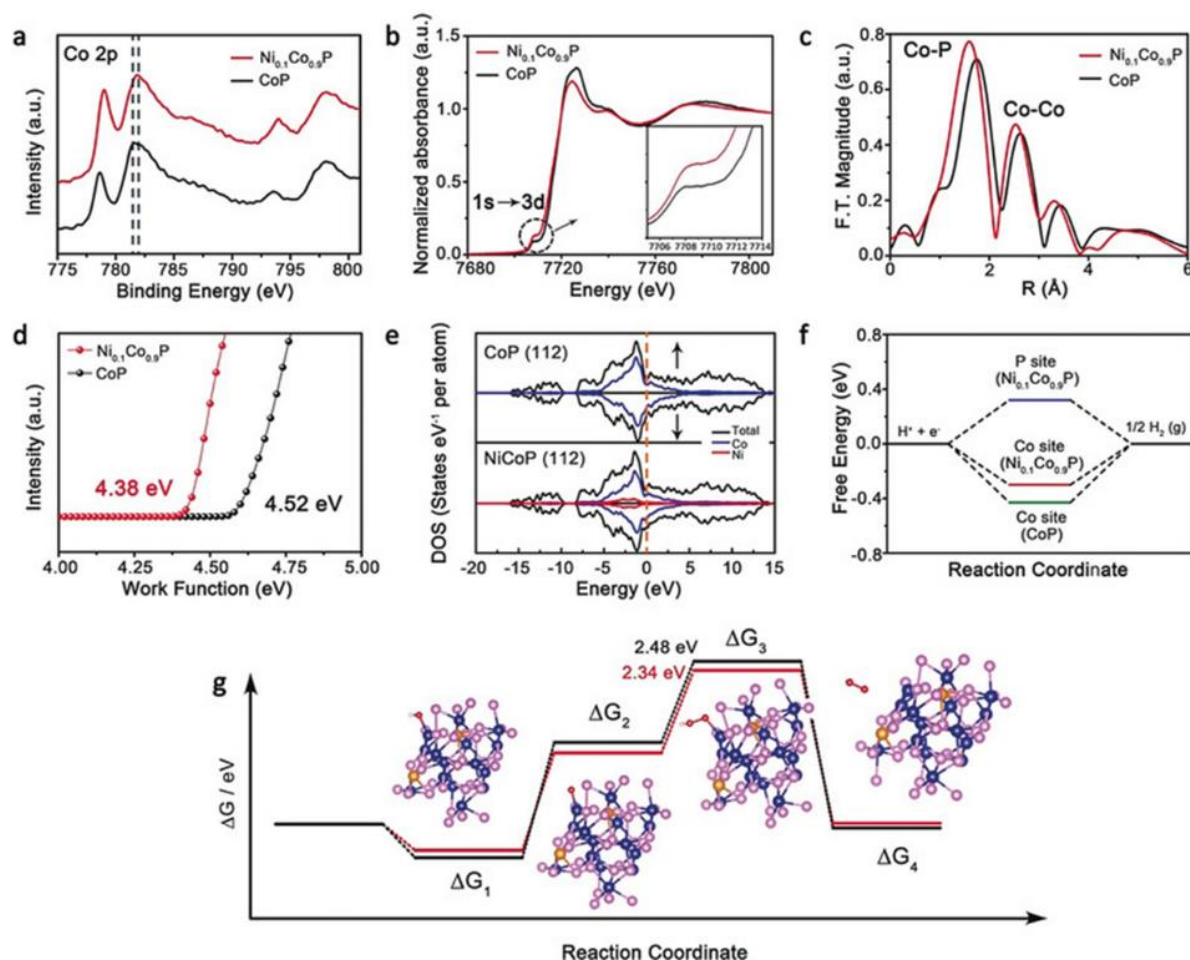


Figure 1-1. (a) Co 2p XPS spectra of Ni<sub>0.1</sub>Co<sub>0.9</sub>P and CoP catalysts. (b) Co K-edge X-ray absorption near-edge spectra and (c) corresponding k<sub>3</sub>-weighted Fourier transform spectra of Ni<sub>0.1</sub>Co<sub>0.9</sub>P and CoP catalysts. (d) Ultraviolet-photoelectron spectra of Ni<sub>0.1</sub>Co<sub>0.9</sub>P and CoP catalysts. (e) Calculated densities of states (DOS) of Ni<sub>0.1</sub>Co<sub>0.9</sub>P and CoP with the Fermi levels aligned at 0 eV. (f) Free energy diagrams for hydrogen adsorption at different sites on the (112) surface of Ni<sub>0.1</sub>Co<sub>0.9</sub>P and CoP. (g) Gibbs free energy change diagram of the OER process on the surface of CoP (black line) and Ni<sub>0.1</sub>Co<sub>0.9</sub>P (red line), including the corresponding intermediates for each step; Blue balls represent Co, orange Ni, pink P, red O and white H atoms. Reproduced with permission.<sup>[26]</sup> Copyright 2018, Wiley-VCH Verlag GmbH & Co. KGaA, Weinheim.

### 1.1.1.3 Doping

Atomic doping is another efficient approach to adjust the electronic structure in order to optimize the adsorption/desorption ability of intermediates of TMP-based electrocatalysts

resulting in enhanced HER/OER activity.<sup>[30]</sup> According to the doping element, the atomic doping can be divided into metal atom doping and nonmetal atom doping. For example, Pan and coauthors studied the doping effects of CoP with various metal atom doping and found that the HER activity of those catalysts follow the trend Ni-CoP/HPFs > Mn-CoP/HPFs > Fe-CoP/HPFs (HPFs, hollow polyhedron frames), owing to the different electronic structure and *d*-band center after doping.<sup>[31]</sup> Wu et al. revealed that Mo dopants can dramatically improve the HER and OER performance of CoP, requiring a potential of 1.56 V to deliver a current density of 10 mA/cm<sup>2</sup> (Figure 1-2(a) and (e)).<sup>[32]</sup> Theoretical calculations indicate that Mo-dopants reduce the  $\Delta G_{H^*}$  to a value close to 0 eV (Figure 1-2 (b-c)) and that the P-3p orbital of the P-sites shifts upwards, leading to a strengthened H-P bond (Figure 1-2 (d)), thus enhancing the HER activity. Mo dopants also reduce the free energy of the RDS from 1.95 eV to 1.82 eV (Figure 1-2 (f-g)) and the Bader charge (Figure 1-2 (h), the energy of atoms calculated by Bader charge analysis) of Co and H, resulting in an improvement of the OER performance. The prepared Mo-CoP only needs 1.56 V to deliver a current density of 10 mA/cm<sup>2</sup> in an alkaline electrolyte (Figure 1-2 (e)). The same phenomenon also is observed for Mo-doped Ni<sub>2</sub>P.<sup>[33]</sup> The highest performance of metal-doped TMP was achieved by Fe-doped CoP requiring 1.49 V (10 mA cm<sup>-2</sup>) for overall water splitting.<sup>[34]</sup>

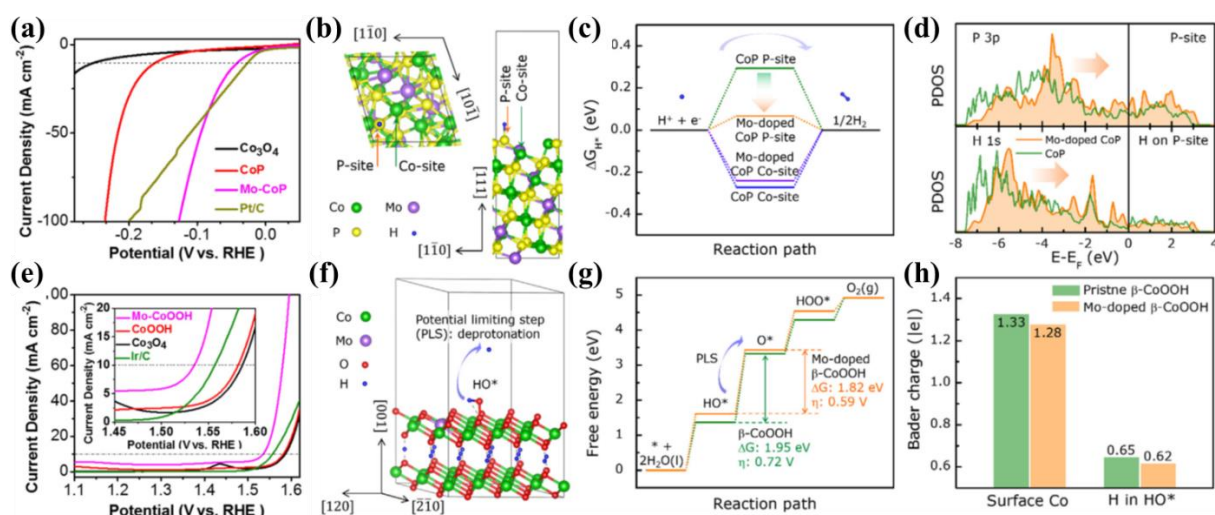


Figure 1-2. (a) Polarization curves of Mo-doped CoP for HER activity. (b) A model of the atomic structure of a Mo-doped CoP (111) surface with H adsorption on the P-site. (c) HER free energy diagrams for the P- and Co-sites on pristine and Mo-doped CoP (111) surfaces. (d) Projected density of states (PDOS) plots of the P 3p and H 1s orbitals for the P-site and for an H atom on pristine (green) and Mo-doped (orange) CoP (111) surfaces. (e)

Polarization curves of Mo-doped CoP for OER activity. (f) A model of the atomic structure of a Mo-doped  $\beta$ -CoOOH (001) surface with HO\* adsorption on an O-site. (g) Standard free energy diagrams for the OER path on pristine (green) and Mo-doped (orange)  $\beta$ -CoOOH (001) surfaces. (h) Bader charge analysis for surface Co ions and H in HO\* adsorption on pristine and Mo-doped  $\beta$ -CoOOH (001) surfaces. Reproduced with permission.<sup>[32]</sup> Copyright 2018, Elsevier Ltd.

For the case of nonmetal doping, Liu et al. revealed that O dopants in Ni<sub>0.75</sub>Fe<sub>0.25</sub>P not only accelerate the change of active sites, but also efficiently reduce the energy barrier of the RDS for the OER.<sup>[35]</sup> Ganesan and coauthors prepared 2D porous O-doped CoP exhibiting overpotentials of 280 and 158 mV at 10 mA cm<sup>-2</sup> for the OER and the HER, respectively, in 1 M KOH.<sup>[36]</sup> The prepared CoPO only required 1.52 V to export 10 mA cm<sup>-2</sup> for overall water splitting. Besides O, S-doped CoP (S: CoP) and Co<sub>2</sub>P (S: Co<sub>2</sub>P), and N-doped CoP (N-CoP) also show significantly improved OER/HER performances.<sup>[37,38]</sup>

#### 1.1.1.4 Morphology

The morphology of electrocatalysts demonstrates a significant influence on their physicochemical properties thus tuning the water splitting activity. A nanostructured hierarchical structure endows TMP-based electrocatalysts with a larger specific surface area to expose more active sites and to enhance the mass transfer during the electrolysis, thus enhancing the catalytic activities. For example, CoP<sub>2</sub> nanocubes ( $\eta_{10} = 39$  mV,  $32$  mV dec<sup>-1</sup>)<sup>[39]</sup> demonstrated a higher HER performance than CoP<sub>2</sub> nanoparticles ( $\eta_{10} = 200$  mV,  $84.0$  mV dec<sup>-1</sup>).<sup>[40]</sup> Similarly, CoP nanorods grown on NF ( $\eta_{10}=54$  mV,  $51$  mV dec<sup>-1</sup>)<sup>[41]</sup> exhibited a better HER activity comprised to CoP nanowires ( $\eta_{10}=100$  mV,  $64$  mV dec<sup>-1</sup>).<sup>[42]</sup> In addition, Beltrán-Suito et al. found that amorphous CoP prepared by a hot-injection method outperformed the crystalline CoP synthesized by a pyrolysis approach with a 130 mV lower cell voltage for overall water splitting, owing to its unique electronic properties and surface characteristics.<sup>[43]</sup> The prepared amorphous CoP exhibited an approximately 2.7 times larger electrochemical surface area (ECSA) than that of crystalline CoP. Therefore, morphology of the samples would have a great influence on the exposure of active sites and mass transfer and the catalytic activities of as-prepared samples can be enhanced by rational morphology structure.

### 1.1.2 3D Electrodes Preparation

There are two general ways to prepare working electrodes for the assessment of the water-splitting performance: (1) casting powder electrocatalysts on a conductive substrate and (2) directly growing electrocatalysts on substrates, resulting in three-dimensional (3D) electrodes (also being called binder-free electrodes). Recently, the second approach has become more and more popular owing to the obtained high current densities and improved conductivity. The substrate used as 3D electrode not only offers more surface area for active sites, but also facilitates the mass and charge transfer, subsequently leading to an enhanced reaction activity. Therefore, the ideal substrate should

- (1) demonstrate excellent conductivity to reduce the overpotential required to overcome the ohmic resistance.
- (2) be stable during the electrolysis, including both compositional and mechanical stability, to maintain the structural stability of the entire electrode.
- (3) be conveniently modified for the incorporation of highly active electrocatalysts with a strong synergistic effect.
- (4) be flexible to meet the shape requirement in the practical application.
- (5) be abundant to reduce the overall costs.

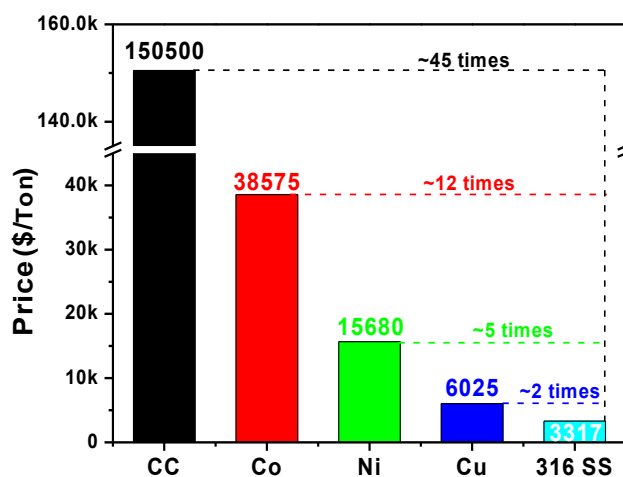


Figure 1-3. Comparison of raw material prices of Ni,<sup>[44]</sup> Cu,<sup>[44]</sup> Co,<sup>[44]</sup> CC,<sup>[45]</sup> and SS (AISI 316).<sup>[46]</sup> (Up to 13 November 2019)

According to those requirements, carbon-based substrates (e.g. carbon cloth (CC) or carbon fiber paper (CFP or CP)) and metal-based substrates (e.g. nickel foam (NF) or Cu foam/foil) are widely used in the preparation of binder-free electrodes for water splitting. For instance, CoP electrodeposited on NF exhibits improved HER and OER performances when compared with CoP on FTO.<sup>[43]</sup> Benefiting from the larger surface area of NF, CoFeP<sub>x</sub> electrodeposited on NF demonstrates a significantly enhanced overall water splitting activity than CoFeP<sub>x</sub> deposited on Cu foil.<sup>[47]</sup> S:CoP deposited on different substrates shows different overall water splitting performances and potentials required to drive 100 mA cm<sup>2</sup> following the trend S:CoP NPs-S:CoP@NF (1.78 V) < S:CoP NPs-S:CoP@CC (1.82 V) < S:CoP NPs-S:CoP@NG (1.85 V, NG: N-doped graphene).<sup>[37]</sup> Therefore, the substrate effects play an important role to determine the intrinsic activity of TMP and the abundant conductive substrate with the larger surface area is preferred to be used to increase the efficiency and reduce the cost for water splitting. Recently, stainless steel (SS), which is intrinsically robust and abundant, has been investigated as a new class of binder-free electrodes with excellent OER performance.<sup>[48]</sup> As shown in Figure 1-3, the price of SS is significantly lower than that of other widely used substrates, which shows a promising potential to further reduce the cost of electrode preparation for water electrolysis. However, the extremely stable characteristic of SS makes it inconvenient to be coupled with highly active electrocatalysts to further improve the (bifunctional) catalytic activity. In Chapter 4 and 5, a method will be introduced to circumvent this disadvantage of SS as a substrate for water electrolysis.

## 1.2 Thesis Scope and Outline

This thesis is focused on the design and preparation of 3D electrodes for efficient water splitting. It comprises the development of highly efficient and abundant electrocatalysts to increase the efficiency of water splitting and exploring cheaper and robust substrates to reduce the cost for the preparation of 3D electrodes (Figure 1-4).

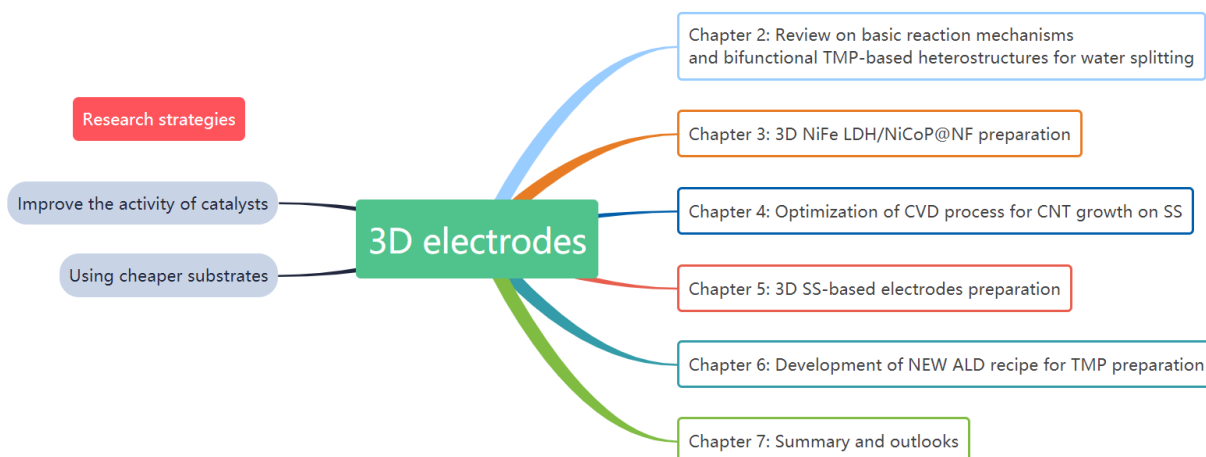


Figure 1-4. Research strategy and outline of this thesis.

Firstly, the basic knowledge of electrochemical water splitting and the related reaction mechanism are summarized and discussed in detail in Chapter 2 (Figure 1-5). Subsequently, the recent progress of the design and preparation of bifunctional TMP-based heterostructures is reviewed and the corresponding mechanisms of the synergistic effect of the heterostructure toward overall water splitting is also discussed in detail. A summary and perspective for further opportunities and challenges are provided at the end of this chapter.

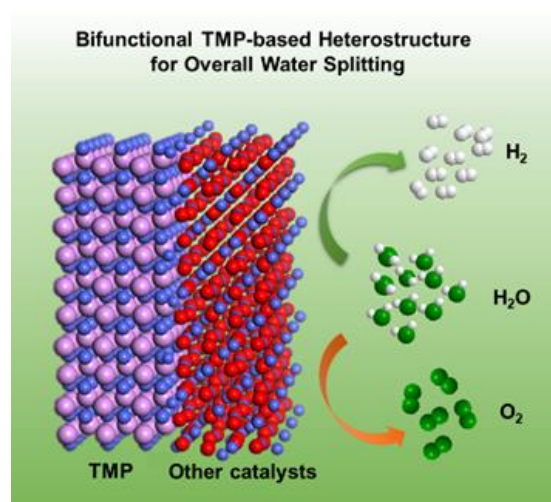


Figure 1-5. The strategy of bifunctional TMP-based heterostructures for efficient overall water splitting.<sup>[49]</sup>

Secondly, a NiFe-layered double hydroxide (NiFe-LDH)/NiCoP heterostructure was designed and directly grown on the surface of NF for the preparation of 3D electrodes with excellent activity and stability for efficient overall water splitting (Figure 1-6 and Chapter 3). The as-synthesized bifunctional heterostructure NiFe LDH@NiCoP/NF electrodes exhibit an



excellent activity for both the HER ( $\eta_{10} = 120$  mV) and the OER ( $\eta_{10} = 220$  mV) in 1 M KOH, owing to the synergistic effect of the heterostructure. For overall water splitting, it just needs a voltage of 1.57 V to reach a current density of 10 mA/cm<sup>2</sup>, which was stable for at least 100 h.

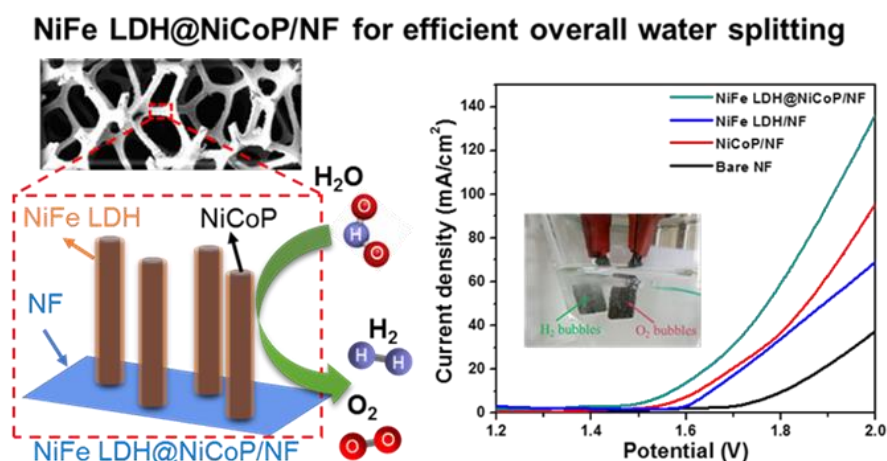


Figure 1-6. Bifunctional NiFe LDH@NiCoP heterostructure grown on NF for efficient overall water splitting.<sup>[50]</sup>

Afterwards, in order to solve the previously discussed issue of the modification of SS, I developed a universal approach to couple highly active electrocatalysts with SS by employing *in-situ* grown carbon nanotubes (CNTs) as the interfacial material for the preparation of 3D SS-based electrodes (denoted as CNT/SS). The grown CNTs on the surface of SS not only act as a highway for fast charge transfer, but also extremely enlarge the specific surface area for the modification of highly active electrocatalysts. The recipe for the CVD process for the growth of CNTs on SS is optimized and discussed in detail in Chapter 4 (Figure 1-7). Those results show that the optimized CNT/SS with the best HER activity is prepared at 700 °C, which can be attributed to the higher number of defects and the higher content of pyrrolic N obtained at this temperature.

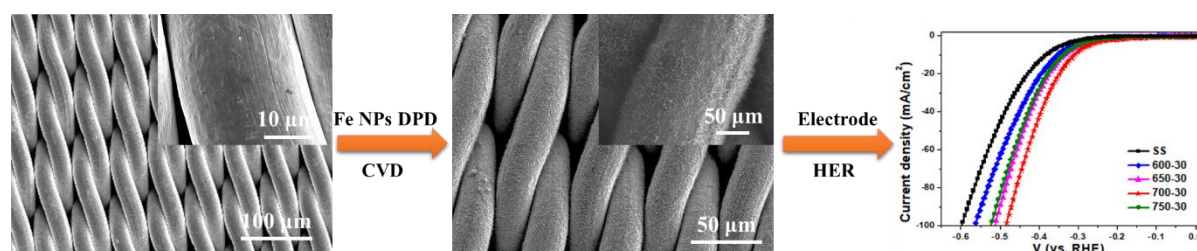


Figure 1-7. Optimization of the CVD process for growing CNTs on the surface of SS.<sup>[51]</sup>



In Chapter 5, the prepared CNT/SS electrodes were further modified by the state-of-the-art catalysts, Pt and RuO<sub>2</sub>, for electrochemical water splitting (Figure 1-8). The recipe for *in-situ* oxidation of CNTs on the surface of SS without destroying the structure of the 3D electrode is also developed. The as-prepared Pt/OxCNT/SS and RuO<sub>2</sub>/OxCNT/SS demonstrated excellent HER and OER activities in various electrolytes with a wide pH range. This strategy shows a promising potential application to combine highly active electrocatalysts with SS for various electrochemical areas.

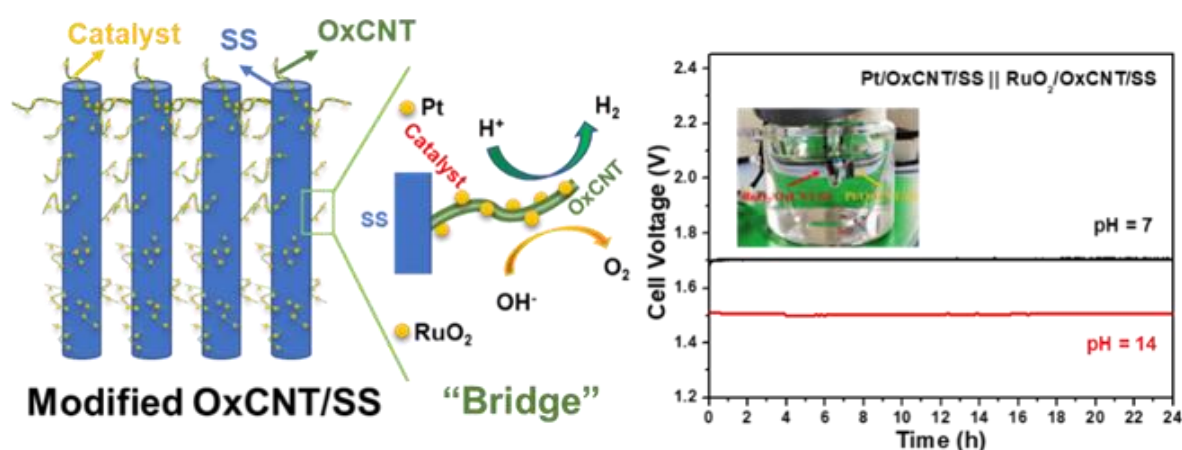


Figure 1-8. Modifying SS with the state-of-the-art catalysts by using CNT as the interface material.<sup>[52]</sup>

Furthermore, TMP-based ultrathin films are prepared by atomic layer deposition (ALD) for the first time. The improved ALD recipe is shown in Figure 1-9 and discussed in Chapter 6. The CoP film was deposited by using PH<sub>3</sub> plasma as the phosphorus source and H<sub>2</sub> plasma to remove excess P in the deposited film. The optimized ALD process demonstrated a self-limited layer-by-layer growth behavior and produced highly pure, smooth and well-crystallized CoP films. The CoP films deposited via this optimized ALD recipe exhibited a higher electrochemical and photoelectrochemical HER activity than that prepared by the traditional post-phosphorization method and can be uniformly deposited on deep narrow trenches. Those results highlight the broad and promising potential application for coating TMP-based ultrathin films on complex 3D structures.

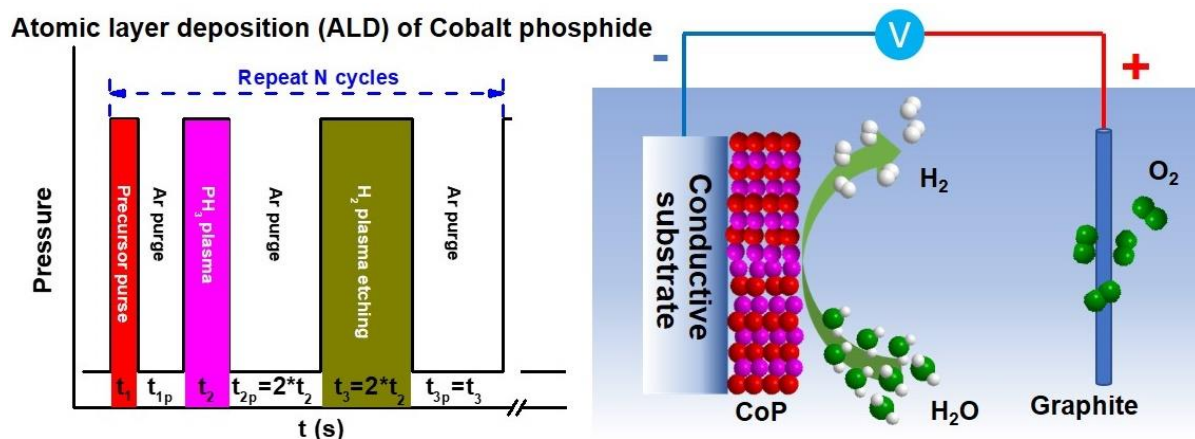


Figure 1-9. Improved ALD process for the preparation of stable CoP.<sup>[53]</sup>

In the end, an outlook and acknowledgments are provided in Chapter 7 and Chapter 8 to give a future perspective of this work and thank the people who contributed to this work.

### 1.3 References

- [1] S. Chu, A. Majumdar, *Nature* **2012**, 488, 294.
- [2] International Energy Agency **2018**, <https://www.iea.org/weo2018/>.
- [3] J. Limberger, T. Boxem, M. Pluymaekers, D. Bruhn, A. Manzella, P. Calcagno, F. Beekman, S. Cloetingh, J.-D. van Wees, *Renewable Sustainable Energy Rev.* **2018**, 82, 961.
- [4] R. J. P. Schmitt, S. Bizzi, A. Castelletti, G. M. Kondolf, *Nat. Sustain.* **2018**, 1, 96.
- [5] J.-Y. Son, K. Ma, *Proc. IEEE* **2017**, 105, 2116.
- [6] N. Kannan, D. Vakeesan, *Renewable Sustainable Energy Rev.* **2016**, 62, 1092.
- [7] International Energy Agency, *The Future of Hydrogen*, Japan **2019**.
- [8] *Global Hydrogen Generation Market Size | Industry Report, 2018-2025* **2018**.
- [9] Committee on Climate Change, *Hydrogen in a low-carbon economy*, UK **2018**.
- [10] A. Ursua, L. M. Gandia, P. Sanchis, *Proc. IEEE* **2012**, 100, 410.
- [11] L. Han, S. Dong, E. Wang, *Adv. Mater.* **2016**, 28, 9266.
- [12] M. Shalom, D. Ressnig, X. Yang, G. Clavel, T. P. Fellingner, M. Antonietti, *J. Mater. Chem. A* **2015**, 3, 8171.
- [13] X. Jia, Y. Zhao, G. Chen, L. Shang, R. Shi, X. Kang, G. I. N. Waterhouse, L.-Z. Wu, C.-H. Tung, T. Zhang, *Adv. Energy Mater.* **2016**, 6, 1502585.
- [14] Y. Pei, Y. Cheng, J. Chen, W. Smith, P. Dong, P. M. Ajayan, M. Ye, J. Shen, *J. Mater. Chem. A* **2018**, 6, 23220.
- [15] H. Zhao, Z. Y. Yuan, *Catal. Sci. Technol.* **2017**, 7, 330.
- [16] K. N. Dinh, Q. H. Liang, C. F. Du, J. Zhao, A. L. Y. Tok, H. Mao, Q. Y. Yan, *Nano Today* **2019**, 25, 99.
- [17] N. Han, K. R. Yang, Z. Lu, Y. Li, W. Xu, T. Gao, Z. Cai, Y. Zhang, V. S. Batista, W. Liu, X. Sun, *Nat. Commun.* **2018**, 9, 924.

- [18] S. Chandrasekaran, L. Yao, L. Deng, C. Bowen, Y. Zhang, S. Chen, Z. Lin, F. Peng, P. Zhang, *Chem. Soc. Rev.* **2019**, *48*, 4178.
- [19] C. Tang, N. Y. Cheng, Z. H. Pu, W. Xing, X. P. Sun, *Angew. Chem. Int. Edit.* **2015**, *54*, 9351.
- [20] H. Du, R.-M. Kong, X. Guo, F. Qu, J. Li, *Nanoscale* **2018**, *10*, 21617.
- [21] J. F. Callejas, C. G. Read, C. W. Roske, N. S. Lewis, R. E. Schaak, *Chem. Mat.* **2016**, *28*, 6017.
- [22] P. W. Menezes, A. Indra, C. Das, C. Walter, C. Göbel, V. Gutkin, D. Schmeißer, M. Driess, *ACS Catal.* **2016**, *7*, 103.
- [23] J. Kibsgaard, C. Tsai, K. Chan, J. D. Benck, J. K. Nørskov, F. Abild-Pedersen, T. F. Jaramillo, *Energy Environ. Sci.* **2015**, *8*, 3022.
- [24] J. Y. Li, M. Yan, X. M. Zhou, Z. Q. Huang, Z. M. Xia, C. R. Chang, Y. Y. Ma, Y. Q. Qu, *Adv. Funct. Mater.* **2016**, *26*, 6785.
- [25] J. Yu, Q. Q. Li, Y. Li, C. Y. Xu, L. Zhen, V. P. Dravid, J. S. Wu, *Adv. Funct. Mater.* **2016**, *26*, 7644.
- [26] R. Wu, B. Xiao, Q. Gao, Y. R. Zheng, X. S. Zheng, J. F. Zhu, M. R. Gao, S. H. Yu, *Angew. Chem. Int. Edit.* **2018**, *57*, 15445.
- [27] J. Kibsgaard, T. F. Jaramillo, *Angewandte Chemie (International ed. in English)* **2014**, *53*, 14433.
- [28] J. Xu, J. Li, D. Xiong, B. Zhang, Y. Liu, K.-H. Wu, I. Amorim, W. Li, L. Liu, *Chem. Sci.* **2018**, *9*, 3470.
- [29] W. R. Cheng, H. Zhang, X. Zhao, H. Su, F. M. Tang, J. Tian, Q. H. Liu, *J. Mater. Chem. A* **2018**, *6*, 9420.
- [30] J. Liu, S. Hou, W. Li, A. S. Bandarenka, R. A. Fischer, *Chemistry, an Asian journal* **2019**.
- [31] Y. Pan, K. Sun, Y. Lin, X. Cao, Y. Cheng, S. Liu, L. Zeng, W.-C. Cheong, Di Zhao, K. Wu, Z. Liu, Y. Liu, D. Wang, Q. Peng, C. Chen, Y. Li, *Nano Energy* **2019**, *56*, 411.
- [32] C. Guan, W. Xiao, H. Wu, X. Liu, W. Zang, H. Zhang, J. Ding, Y. P. Feng, S. J. Pennycook, J. Wang, *Nano Energy* **2018**, *48*, 73.
- [33] Q. Wang, H. Zhao, F. Li, W. She, X. Wang, L. Xu, H. Jiao, *J. Mater. Chem. A* **2019**, *7*, 7636.
- [34] L.-M. Cao, Y.-W. Hu, S.-F. Tang, A. Iljin, J.-W. Wang, Z.-M. Zhang, T.-B. Lu, *Adv. Sci.* **2018**, *5*, 1800949.
- [35] K. Liu, F. Wang, P. He, T. A. Shifa, Z. Wang, Z. Cheng, X. Zhan, J. He, *Adv. Energy Mater.* **2018**, *8*, 1703290.
- [36] G. Anandhababu, Y. Y. Huang, D. D. Babu, M. X. Wu, Y. B. Wang, *Adv. Funct. Mater.* **2018**, *28*, 10.
- [37] M. A. R. Anjum, M. S. Okyay, M. Kim, M. H. Lee, N. Park, J. S. Lee, *Nano Energy* **2018**, *53*, 286.
- [38] M. A. R. Anjum, M. D. Bhatt, M. H. Lee, J. S. Lee, *Chem. Mat.* **2018**, *30*, 8861.
- [39] H. Li, P. Wen, D. S. Itanze, M. W. Kim, S. Adhikari, C. Lu, L. Jiang, Y. Qiu, S. M. Geyer, *Adv. Mater.* **2019**, *31*, e1900813.
- [40] M. Wang, C. L. Dong, Y. C. Huang, S. H. Shen, *J. Catal.* **2019**, *371*, 262.
- [41] Y.-P. Zhu, Y.-P. Liu, T.-Z. Ren, Z.-Y. Yuan, *Adv. Funct. Mater.* **2015**, *25*, 7337.

- [42] B. L. Qiu, A. Han, D. C. Jiang, T. T. Wang, P. W. Du, *ACS Sustain. Chem. Eng.* **2019**, *7*, 2360.
- [43] R. Beltran-Suito, P. W. Menezes, M. Driess, *J. Mater. Chem. A* **2019**, *7*, 15749.
- [44] *London Metal Exchange*, <https://www.lme.com/>.
- [45] *Carbon fiber paper*, <https://www.compositeshop.de/xoshop/lng/en/fibers/carbon-fiber/woven-carbon-fiber-fabric/unidirectional/woven-carbon-fiber-fabric-ud-3k-140gm.html>.
- [46] *Stainless Steel Prices*, <http://www.meps.co.uk/Stainless%20Prices.htm>.
- [47] N. Kornienko, N. Heidary, G. Cibin, E. Reisner, *Chem. Sci.* **2018**, *9*, 5322.
- [48] H. Schäfer, M. Chatenet, *ACS Energy Lett.* **2018**, *3*, 574.
- [49] H. Zhang, A. W. Maijenburg, X. Li, S. L. Schweizer, R. B. Wehrspohn, *Adv. Funct. Mater.* **2020**, *30*, 2003261.
- [50] H. Zhang, X. P. Li, A. Hahnel, V. Naumann, C. Lin, S. Azimi, S. L. Schweizer, A. W. Maijenburg, R. B. Wehrspohn, *Adv. Funct. Mater.* **2018**, *28*, 10.
- [51] H. Zhang, J. Martins de Souza e Silva, C. Santos de Oliveira, X. Lu, S. L. Schweizer, A. W. Maijenburg, M. Bron, R. B. Wehrspohn, *MRS Adv.* **2020**.
- [52] H. Zhang, J. M. de Souza e Silva, X. Lu, C. S. de Oliveira, B. Cui, X. Li, C. Lin, S. L. Schweizer, A. W. Maijenburg, M. Bron, R. B. Wehrspohn, *Adv. Mater. Interfaces* **2019**, *6*, 1900774.
- [53] H. Zhang, D. J. Hagen, X. Li, A. Graff, F. Heyroth, B. Fuhrmann, I. Kostanovskiy, S. L. Schweizer, F. Caddeo, A. W. Maijenburg, S. Parkin, R. B. Wehrspohn, *Angew. Chem. Int. Edit.* **2020**, 10.1002/anie.202002280.

## 2 Bifunctional Heterostructured Transition Metal Phosphides for Efficient Electrochemical Water Splitting

The innovational strategies for the design and preparation of bifunctional heterostructured transition metal phosphides (TMP) with improved electrocatalytic activity and the related reaction mechanisms have been summarized and discussed in detail. Furthermore, a summary and perspective of the further opportunities and challenges for the development and preparation of highly efficient TMP-based bifunctional heterostructures are provided.

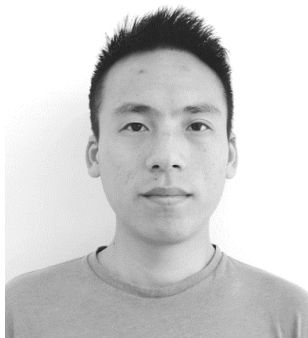
This chapter can be referred to:

Haojie Zhang, A. Wouter Maijenburg, Xiaopeng Li, Stefan L. Schweizer, and Ralf B. Wehrspohn\*, *Advanced Functional Materials*, 2020, 30, 2003261.

## 2.1 Abstract

Reducing green hydrogen production costs is essential for developing a hydrogen economy. Developing cost-effective electrocatalysts for water electrolysis is thus of great research interest. Among various material candidates, transition metal phosphides (TMP) have emerged as robust bifunctional electrocatalysts for both the hydrogen evolution reaction (HER) and the oxygen evolution reaction (OER) due to their various phases and tunable electronic structure. Recently, heterostructured catalysts have exhibited significantly enhanced activities towards HER/OER. The enhancement can be attributed to the increased amount of accessible active sites, accelerated mass/charge transfer and optimized adsorption of intermediates, which arise from the synergistic effects of the heterostructure. Herein, a comprehensive overview of the recent progress of bifunctional TMP-based heterostructure is introduced to provide an insight into their preparation and corresponding reaction mechanisms. It starts with summarizing general fundamental aspects of HER/OER and the synergistic effect of heterostructures for enhanced catalytic activity. Next, the innovational strategies to design and construct bifunctional TMP-based heterostructures with enhanced overall water splitting activity, as well as the related mechanisms, are discussed in detail. Finally, a summary and perspective for further opportunities and challenges are highlighted for the further development of bifunctional TMP-based heterostructures from the points of practical application and mechanistic studies.

## 2.2 Author Biographies



**Haojie Zhang** received his B.S. degree from Zhengzhou University in 2013 and M.S. degree from Shanghai University and Shanghai Advanced Research Institute, CAS in 2016. In November 2016, he started to work as a Ph.D. student at the Institute of physics at the Martin Luther University Halle-Wittenberg under the supervision of Prof. Ralf B. Wehrspohn and Jun.-Prof. A. Wouter Maijenburg. His research is focused on developing efficient catalysts for electrochemical and photoelectrochemical water splitting.



Jun.-Prof. Dr. A. Wouter Maijenburg obtained his Ph.D. degree from the University of Twente (Enschede, The Netherlands) in 2014. After working for 2 years as a postdoctoral researcher at the GSI Helmholtz Centre for Heavy Ion Research (Darmstadt, Germany), in October 2016 he became a Junior Professor at the Martin Luther University Halle-Wittenberg. Here, he holds the chair of Inorganic Functional Materials within the Institute of Chemistry and he is the leader of the Light for Hydrogen group within the Centre for Innovation Competence (ZIK) SiLi-nano. His research is mainly focused on the nanostructure design for solar water splitting.



Prof. Dr. Ralf B. Wehrspohn obtained his Ph.D. degree from École Polytechnique. Afterwards, he habilitated as a post-doctoral at the Max-Planck Institute of Microstructure Physics in Halle before being offered a professorship at the University of Paderborn. In 2006, he started to parallelly work as a professor at Martin Luther University Halle-Wittenberg and director of Fraunhofer Institute for Microstructure of Materials and Systems. In 2019, he has been elected as Executive Vice President at Fraunhofer Gesellschaft. His research interests mainly focus on nanostructured materials and components, such as those used in microelectronics, sensors, photonics, hydrogen technology and photovoltaics.

## 2.3 Introduction

H<sub>2</sub> with a zero-carbon emission is considered as a promising alternative clean energy carrier to tackle the significant threat of serious environmental pollution, global warming and energy crisis caused by fossil fuel combustion.<sup>[1,2]</sup> According to the report from the International Energy Agency, the global energy demand expands by over 25% between 2017 and 2040 and the energy-related CO<sub>2</sub> emission rises gradually to 35.8 Gt/year in 2040.<sup>[3]</sup> Thus, green and sustainable hydrogen generation with a low cost and highly efficient approach is vital to deploy the hydrogen economy in the terawatt scale.<sup>[4]</sup> Otherwise, it is not possible for green hydrogen to compete with “grey” hydrogen from fossil fuels (e.g. methane reforming). Electrochemical water splitting, as a promising hydrogen production method, has attracted great interest in the past decades.<sup>[2]</sup> **Figure 2-1** shows a sustainable pathway for the circulation of hydrogen economy by combining renewable energy and electrochemical water splitting. Water electrolysis consists of hydrogen evolution reaction (HER) on the cathode and the oxygen evolution reaction (OER) on the anode.<sup>[5]</sup> The current state-of-the-art electrolysis requires the use of Pt-based and Ru/Ir-based electrocatalysts as the electrodes for the HER and the OER, respectively.<sup>[6,7]</sup> However, the high cost and scarcity of those precious metals severely restrict the large-scale application of water electrolysis. Therefore, cost-efficient electrocatalysts are urgent to be investigated and developed. Considering the requirement to produce hydrogen in the terawatt scale, earth-abundant elements including Fe, Ni, Co, P and S are suggested to be employed for the development of highly active electrocatalysts.<sup>[4]</sup> Therefore, many different types of transition metal (Ni, Fe, Co, etc.)-based electrocatalysts have been gradually investigated during the past decades as electrocatalysts for efficient water electrolysis due to their earth-abundance and intrinsic activity.<sup>[5,8-10]</sup> Various types of transition metals, including transition metals (TM)<sup>[11]</sup> transition metal oxides (TMO),<sup>[10]</sup> transition metal nitrides (TMN),<sup>[12,13]</sup> transition metal phosphides (TMP),<sup>[14,15]</sup> transition metal carbides (TMC)<sup>[16,17]</sup> and transition metal sulfides (TMS),<sup>[18,19]</sup> have been identified to show high activities towards water electrolysis. In particular, TMP-based electrocatalysts have shown good electrical conductivity, fast charge transfer and improved reaction kinetics, which makes this class of materials



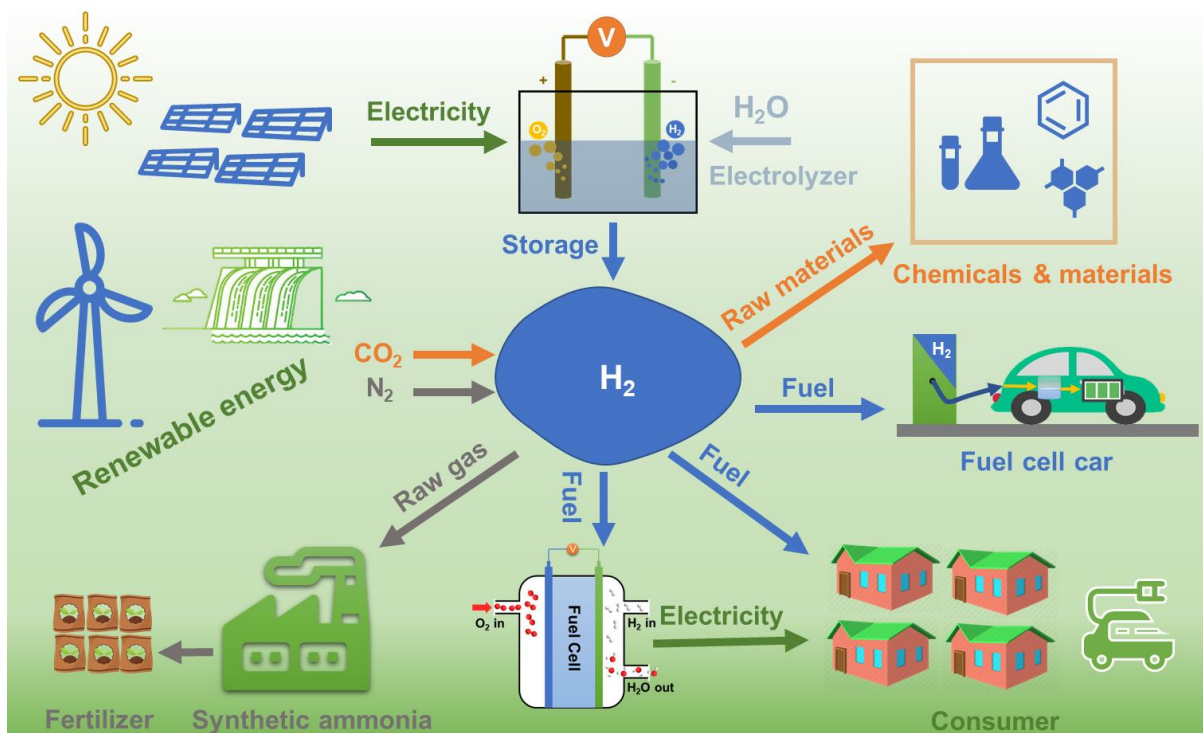


**Figure 2-1.** A sustainable pathway for the circulation of a hydrogen economy by combining renewable energy and electrochemical water splitting.

exceptionally interesting for electrochemical water splitting.<sup>[20,21]</sup> The phosphorus and metal sites in TMP serve as proton acceptor and hydride acceptor sites, respectively.<sup>[22]</sup> The performance of TMP can be further enhanced by tuning the stoichiometric ratio of P and metal (P/M), hetero-atomic doping (metal or nonmetal) or alloying, resulting in enhanced conductivity and increasing the exposure of active sites.<sup>[23,24]</sup> Initially, TMP-based catalysts were mainly used in hydrodesulfurization (HDS).<sup>[25]</sup> The use of TMP-based electrocatalysts for the OER was first reported by Kupka and Budniok in 1990.<sup>[26]</sup> Twenty-three years later, Popczun et al. prepared nanostructured Ni<sub>2</sub>P with a high density of (001) facets, which showed decent HER performance in acidic media.<sup>[27]</sup> Inspired by those promising results, the literature number of TMP electrocatalysts has been rapidly growing in the past decade (**Figure 2-2**). For example, Li et al. reported that phosphorus-rich CoP<sub>2</sub> exhibited higher HER performance than metal-rich TMP, such as CoP and Co<sub>2</sub>P.<sup>[28]</sup> They also extended the application of CoP<sub>2</sub> in photoelectrochemical hydrogen evolution and the prepared p-Si/AZO/TiO<sub>2</sub>/CoP<sub>2</sub> photocathode demonstrated remarkable catalytic activity and stability.<sup>[28]</sup> Chen et al. synthesized NiAl<sub>δ</sub>P nanowall with Al vacancies exhibiting an outstanding bifunctional performance for both the

OER and the HER in a wide pH range of electrolytes (0-14).<sup>[29]</sup> Very recently, Jaramillo's group demonstrated the upscaling of non-precious CoP from a lab-scale application (1 cm<sup>2</sup>) to a commercial scale (86 cm<sup>2</sup>) for its application in a polymer electrolyte membrane (PEM) electrolyzer.<sup>[30]</sup> The performance of the assembled PEM electrolyzer exhibited activity comparable to Pt electrodes, under the same operation conditions (400 psi, 50 °C) with excellent stability for > 1700 h at 1.86 A cm<sup>-2</sup>, which illustrates a potential pathway for using TMP-based electrocatalysts for commercial applications.

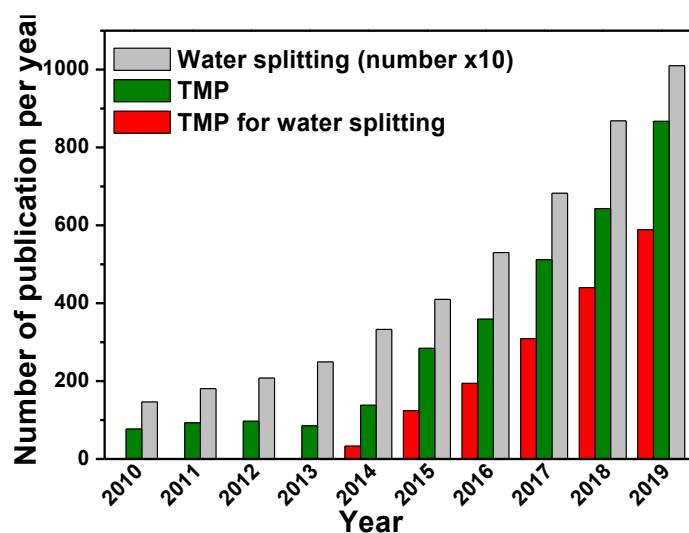


**Figure 2-2.** The number of papers published annually on the topics of TMP, TMP for water splitting and water splitting in general. Data collected from Web of Science (up to 31.12.2019).

The bifunctional electrocatalytic activity is one of the most intriguing properties of TMP-based electrocatalysts. Enormous efforts have been devoted to improving the bifunctional property of TMP, such as tuning the P/M ratio,<sup>[31–34]</sup> alloying,<sup>[35–38]</sup> and metal/nonmetal doping,<sup>[17,39–48]</sup> since employing bifunctional electrocatalyst can further reduce the material production cost. Recently, a variety of TMP-based heterostructured catalysts stand out from the crowd, showing extraordinary bifunctional catalytic performance for overall water splitting.<sup>[23,49–56]</sup> Generally, a heterostructure is defined as the composite structure that couples different solid-state materials with interfacial interaction.<sup>[57]</sup> The heterostructured composites, not only preserve the intrinsic characteristic of both components but also serve to produce novel or enhanced performance, which can be attributed to the synergistic effects arising from the heterointerface (**Figure 2-3**). In addition, well-engineered heterostructures supported by a

conductive substrate, such as Ni foam (NF) and carbon cloth (CC) resulting in a three-dimensional (3D) hierarchical heterostructure, can deliver multiple advantages such as fast mass and charge transfer, improved conductivity and increased amount of active sites.<sup>[58,59]</sup> For example, our group prepared a 3D hierarchical heterostructured electrode by assembling NiFe layered double hydroxides (LDH) nanosheets on NiCoP nanowires with special interfacial engineering and synergetic effects.<sup>[53]</sup> The resulting NiFe LDH/NiCoP/NF electrode exhibited a dramatically improved bifunctional property with low overpotentials for the HER, the OER as well as the overall water splitting, and long-time stability for more than 100 h in basic media. Bu et al. synthesized bimetal phosphide/graphene heterostructure by a metal-organic framework (MOF)-derived method resulting in an enhancement of the overall water splitting performance, which can also be contributed to the synergistic effect of the heterostructure.<sup>[60]</sup> Therefore, employing a proper strategy for designing and constructing heterostructured electrodes is vital to prepare bifunctional TMP-based electrodes with enhanced interfacial effects for efficient overall water splitting.

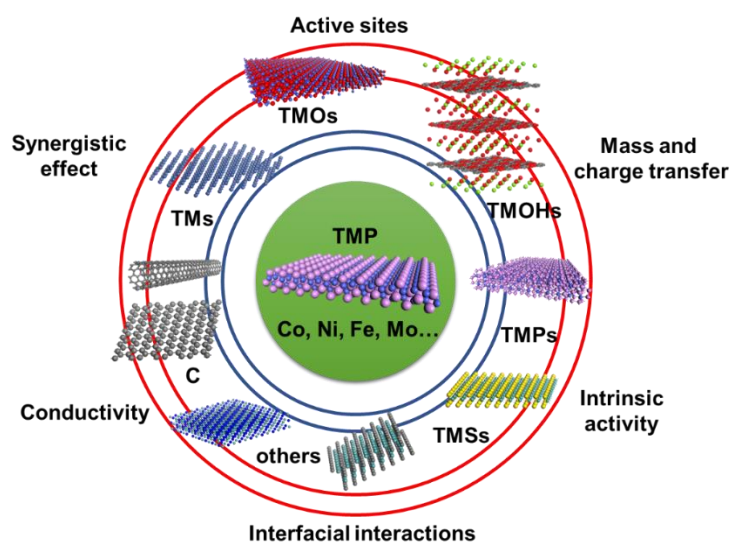


**Figure 2-3.** Heterostructured TMP-based catalysts for water splitting and their superiorities for achieving the enhanced catalytic activity.

To date, several groups have reviewed the development of TMP-based electrocatalysts for water splitting from different aspects.<sup>[14–16,20,21,23,25,57,61–71]</sup> However, the progress in the preparation of heterostructured bifunctional TMP-based electrocatalysts for efficient overall water splitting has not yet been summarized. Also, a unified and comprehensive understanding

of the reaction mechanism is still not achieved. Thus, regarding the rapidly increasing amount of reports on heterostructures as well as their potential to be applied in other research areas as well, it is urgent to review the latest progress and discuss the related reaction mechanism for the further development of heterostructured bifunctional electrocatalysts. Therefore, this review will focus on the recent development of bifunctional heterostructured TMP-based electrocatalysts for overall water splitting. In this review, we intend to provide a comprehensive analysis and understanding of the relationship between the heterostructure and its bifunctional performance for efficient water electrolysis. We start by briefly reviewing the OER and the HER reaction mechanisms and the synergistic effects of heterostructures on both HER and OER. In addition, we will introduce the state-of-the-art bifunctional heterostructured TMP-based electrocatalysts, with an emphasis on the design and preparation strategies and the mechanisms for enhanced electrocatalytic performance. In the end, we will highlight the challenges and perspectives in the development of bifunctional heterostructured TMP-based electrocatalysts for overall water splitting.

## **2.4 Mechanism of the Water Splitting Reactions**

The theoretical thermodynamic potential of overall water splitting is 1.23 V. However, extra overpotentials are always required. Although the HER is more favorable in an acidic environment, overall water splitting is usually performed in an alkaline electrolyte owing to the serious corrosion of OER electrocatalysts and metal cell components in acid. Therefore, this review will focus on the summary of the reaction mechanism of the HER and the OER as well as that of overall water splitting in alkaline electrolytes.

### **2.4.1 General Mechanisms of the HER and the OER in Alkaline Electrolytes**

#### **2.4.1.1 Mechanism of the HER in alkaline electrolytes**

It is generally accepted that the HER occurring on a cathode follows a two-step process in alkaline media.<sup>[23,70,72]</sup> At the beginning of the HER, H<sup>\*</sup> is adsorbed on the active sites (M) of the electrodes by H<sub>2</sub>O dissociation combined with one electron transferred from the electrode

surface, which is named as the Volmer step (Equation 1). Subsequently, there are two possible pathways to form H<sub>2</sub>: one is the reaction of the absorbed H\* with one electron transferred from the electrode surface and one proton from the electrolyte, resulting in one H<sub>2</sub> molecule, which is named as the Heyrovsky step (Equation 2). The other possibility is a faster pathway called the Tafel step (Equation 3), which invokes that two adsorbed H\* directly combine together to form one H<sub>2</sub> molecule. In addition, the Tafel slope obtained by the experimental measurement is usually used to reveal the reaction mechanism of the HER appearing on the electrode surface.<sup>[73]</sup> The lower Tafel slopes indicate faster kinetics.<sup>[74–76]</sup> More specifically, if the adsorption of H<sub>2</sub>O on the catalyst surface is too weak, the Volmer step will be the rate-determining step (RDS), resulting in a Tafel slope of approximately 120 mV dec<sup>-1</sup>. However, when the adsorption of H\* is too strong on the catalyst surface, the overall reaction kinetics will be controlled by the desorption of hydrogen (Heyrovsky or Tafel step). If the concentration of intermediate H\* is low on the surface, the Heyrovsky step would control the reaction kinetics and then the Tafel slope will be approximately 40 mV dec<sup>-1</sup>. In contrast, a high concentration of H\* atoms adsorbed on the catalyst surface allows them to combine directly, resulting in the generation of molecular hydrogen that is released from the surface. In this case, the overall reaction kinetics will follow the Tafel step with a Tafel slope value of approximately 30 mV dec<sup>-1</sup>.

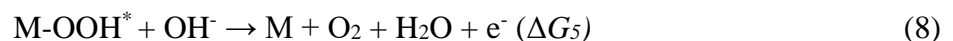
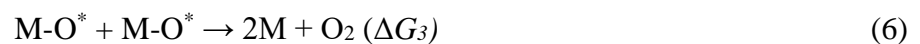
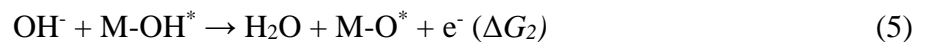
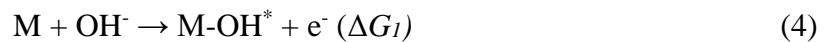


The HER activity of electrocatalysts can also be evaluated by theoretical calculation of the adsorption of H ( $\Delta E_H$ ) and the free energy of H\* ( $\Delta G_{H^*}$ ), which indicates the bond strength between H\* and active sites as well as the adsorption ability of H\* on the active sites, respectively.<sup>[70]</sup> If  $\Delta G_{H^*}$  is more positive, the adsorption of H\* would be too weak and the RDS will be the Volmer step. On the other hand, when  $\Delta G_{H^*}$  is more negative, the adsorption of H\*

will be too strong and the Heyrovsky or Tafel step will be the RDS. Therefore, a good HER catalyst should exhibit a  $\Delta G_{H^*}$  with a value near 0.

#### 2.4.1.2 Mechanism of the OER in alkaline electrolytes

The OER is a 4-electron process with a more complicated mechanism and slower kinetic than the HER. Matsumoto and Sato<sup>[77]</sup> reviewed the OER mechanism on various transition metal oxides in acidic and alkaline electrolytes, including the Krasil'shchikov path,<sup>[78]</sup> the Bochriss path,<sup>[79]</sup> the Yeager's path,<sup>[80]</sup> oxide and electrochemical oxide path.<sup>[81]</sup> In alkaline media, all of the mechanisms begin with the necessary step of hydroxide coordination (Equation 4) to the active sites and followed by other intermediate formations including the oxidation of  $-OH^*$  to  $-O^*$  and  $-O^*$  to  $-OOH^*$ .<sup>[82]</sup> However, the oxygen evolution step can be divided into two categories:<sup>[82]</sup> one is direct generating molecular oxygen from two  $M-O^*$  species, which follows the pathway of Equation (4)  $\rightarrow$  (5)  $\rightarrow$  (6). And the other one is forming the  $M-OOH^*$  intermediate first, which then reacts with another  $OH^-$  from the electrolyte to produce  $O_2$  following the pathway of Equation (4)  $\rightarrow$  (5)  $\rightarrow$  (7)  $\rightarrow$  (8). It is generally recognized that the OER process goes through the second pathway.<sup>[73]</sup> The overpotential required to accomplish the OER is associated with the kinetic barrier of every elementary step and the RDS can also be determined by measuring the Tafel slope in order to understand the reaction mechanism.<sup>[76,83]</sup> In more details, a Tafel slope of  $120 \text{ mV dec}^{-1}$  is obtained when the overall reaction kinetic is determined by the hydroxide coordination step (Equation (4)). Otherwise, the Tafel slope is lower than  $120 \text{ mV dec}^{-1}$ . In particular, when the RDS is the reaction (5) or reaction (7), a Tafel slope of  $30 \text{ mV dec}^{-1}$  is observed with high coverage of empty sites.



Theoretical calculations have also been employed to gain insight into the mechanism of the OER process. Rossmeisl et al. defined the reaction energy for each step as the difference of the Gibbs free energy ( $\Delta G_i$ ;  $i = 1, 2, 4, 5$ ) between two adsorbed intermediates.<sup>[84]</sup> The theoretical overpotential is determined by the step with the highest  $\Delta G$  and the magnitude of  $\Delta G_{OER}$  is given by Equation (9) for the four-step process. Man et al. have studied the thermodynamics of the OER mechanism on the surface of oxides.<sup>[85]</sup> The theoretical overpotential can be calculated by Equation (10) at the ideal condition with  $U = 0$  vs. the standard hydrogen electrode (SHE). And the ideal value of  $G_{OER}$  for OER catalysts is 1.23 eV when  $\eta_{OER} = 0$ .

$$\Delta G_{OER} = \max (\Delta G_1, \Delta G_2, \Delta G_4, \Delta G_5) \quad (9)$$

$$\eta_{OER} = (G_{OER}/e) - 1.23 \text{ eV} \quad (10)$$

Hence, the total overpotential ( $\eta_{total}$ ) for overall water splitting during electrolysis is the sum of the kinetic overpotentials for HER ( $\eta_{HER}$ ), OER ( $\eta_{OER}$ ), the concentration overpotential ( $\eta_{con}$ ) and the overpotential required to overcome the ohmic resistance ( $\eta_{\Omega}$ ) as shown in Equation (11).<sup>[86]</sup> Consequently, developing high-active electrocatalysts to reduce the kinetic overpotentials for the HER and the OER is the key for efficient water splitting.

$$\eta_{total} = \eta_{OER} + \eta_{HER} + \eta_{\Omega} + \eta_{con} \quad (11)$$

#### **2.4.2 Insight into the Synergistic Effects of Heterostructures on the Improved HER/OER and Overall Water Splitting Activities in Alkaline Electrolytes**

According to the concept of the heterostructure, one active catalyst coupled with another may significantly boost its catalytic activity due to the synergistic effect of the interface between the two components. However, the synergistic effects that occur on the heterointerface are complicated with multiple contributing factors including bubble formation and release, wettability, amount active sites, and electronic structure of the heterointerface.<sup>[87,88]</sup> Many researchers have intended to understand the synergistic effects of the heterostructures by the meticulous experimental design and the theoretical calculations.

### 2.4.2.1 Synergistic Effects of heterostructures on the enhanced HER activity

The discovery of the synergy in heterostructures for water splitting started with classical 3d metal hydroxides. Markovic et al. designed a heterostructure of Pt/Ni(OH)<sub>2</sub> by depositing nanometer-scale Ni(OH)<sub>2</sub> clusters on a Pt electrode, whereas the deposited Ni(OH)<sub>2</sub> offers active sites for water dissociation and the generated H\* intermediates were then adsorbed on the nearby Pt surface, which were subsequently combined to molecular H<sub>2</sub>.<sup>[89]</sup> The synergistic effect of the prepared Pt/Ni(OH)<sub>2</sub> heterostructure improves the drawback of the Volmer step on the Pt surface and can be further enhanced *via* Li<sup>+</sup>-induced destabilization of the HO-H bond. Such a synergistic effect generally exists in the Ni(OH)<sub>2</sub>-metal system according to their survey of 9 different metal substrates (both precious and non-precious metals).<sup>[90]</sup> Their results prove that the HER performance of the prepared heterostructures in alkaline media was enhanced as compared to the corresponding metals alone.

A different synergistic effect was reported to exist on the surface of noble metal phosphide-based heterostructures. For example, Mu's group prepared a series of P-rich noble metal diphosphides embedded within an ultrathin nitrogen-doped carbon layer (e.g. IrP<sub>2</sub>@NC, RhP<sub>2</sub>@NC and Pd<sub>5</sub>P<sub>2</sub>@NC).<sup>[91]</sup> The prepared IrP<sub>2</sub>@NC heterostructure demonstrated the highest HER activity among all studied TMP-based electrocatalysts and commercial Pt/C with ultralow overpotentials ( $\eta_{10} = 8$  and 28 mV in 0.5 M H<sub>2</sub>SO<sub>4</sub> and 1 M KOH, respectively) owing to the synergistic effect between NC and IrP<sub>2</sub>. Afterwards, they further synthesized a novel heterostructure with RuP<sub>2</sub> encapsulated in an N-,P-dual-doped carbon shell (RuP<sub>2</sub>@NPC).<sup>[92]</sup> RuP<sub>2</sub>@NPC demonstrated a Pt-like HER activity ( $\eta_{10} = 38$  mV in 0.5 M H<sub>2</sub>SO<sub>4</sub>, 57 mV in 1.0 M PBS and 52 mV in 1.0 M KOH) and superior stability at all pH values, which can be attributed to the synergistic effect between the RuP<sub>2</sub> NPs core and the NPC shell that reduces the charge-transfer resistance at the catalyst/electrolyte interface and increases the electrochemical conductivity. DFT calculation revealed that after coupling with NPC, the  $\Delta G_{H^*}$  is optimized with a smaller value of 0.233 eV than that of NPC and RuP<sub>3</sub> alone.



Non-precious metal TMP-based heterostructures also demonstrated synergistic effects. For example, Liu et al. prepared heterostructured Ni<sub>2</sub>P-NiP<sub>2</sub> hollow nanoparticle polymorphs which outperform the corresponding single components.<sup>[93]</sup> DFT calculation demonstrated that the Ni<sub>2</sub>P-NiP<sub>2</sub> heterostructure exhibited a smaller  $\Delta G_{H^*}$  value compared to pure Ni<sub>2</sub>P and NiP<sub>2</sub> (**Figure 2-4(a, b)**). The Bader charge analysis further revealed that a strong charge redistribution occurred at the interface, as the average valance charge of P (in NiP<sub>2</sub>) near the Ni<sub>2</sub>P-NiP<sub>2</sub> interfaces was reduced from 5.22 eV to 5.05 eV (Figure 2-4(c)). Therefore, the valence electron state of active sites could be optimized and the electronic conductivity of catalysts may also be improved due to the presence of heterointerface. Synergy between TMP and carbon was also found. Li et al. reported that a similar charge redistribution occurred on the heterointerface of a MoP@C heterostructure.<sup>[94]</sup> The formed Mo-C and P-C bonds substantially optimized the free energy barriers and accelerated the charge transfer of the heterointerface, thus promoting the dissociation of water to H<sup>\*</sup> with a faster Volmer process. Furthermore, Zhao et al. investigated the synergistic effect of a MoP@NCHSs heterostructure comprising MoP nanoparticles encapsulated in N-doped carbon hollow spheres with enhanced HER activity.<sup>[95]</sup> Their results reveal that the synergistic effect primarily results from the interaction of MoP with pyridinic N. DFT calculation demonstrated that the pyridinic-N-MoP with a higher electron density on the N-doped support has a lower energy barrier for the adsorption of H<sub>2</sub>O molecules ( $\Delta E_{H_2O}$ ) and the smallest  $|\Delta E_{H^*}|$ , which can accelerate the Volmer and Heyrovsky process on the heterointerface (Figure 2-4(d, e)). Moreover, the OH<sup>\*</sup> adsorption energy ( $\Delta E_{OH^*}$ ) is much lower than that on pyrrolic and graphitic N, indicating the faster desorption ability of hydroxyl species and accelerating the re-adsorption of H<sub>2</sub>O molecules on the active sites (right panel in Figure 2-4(e)). Consequently, the pyridinic-N-MoP sites are identified as the real active sites for the enhanced catalytic HER process. Therefore, the synergistic effect originating from heterostructures (including noble metal phosphide- and TMP-based heterostructures) can enlarge the surface area and tune the electronic structure of the heterostructure to expose more active sites and accelerate the mass/charge transfer. The synergy from the heterostructure can also optimize the adsorption of intermediates at the

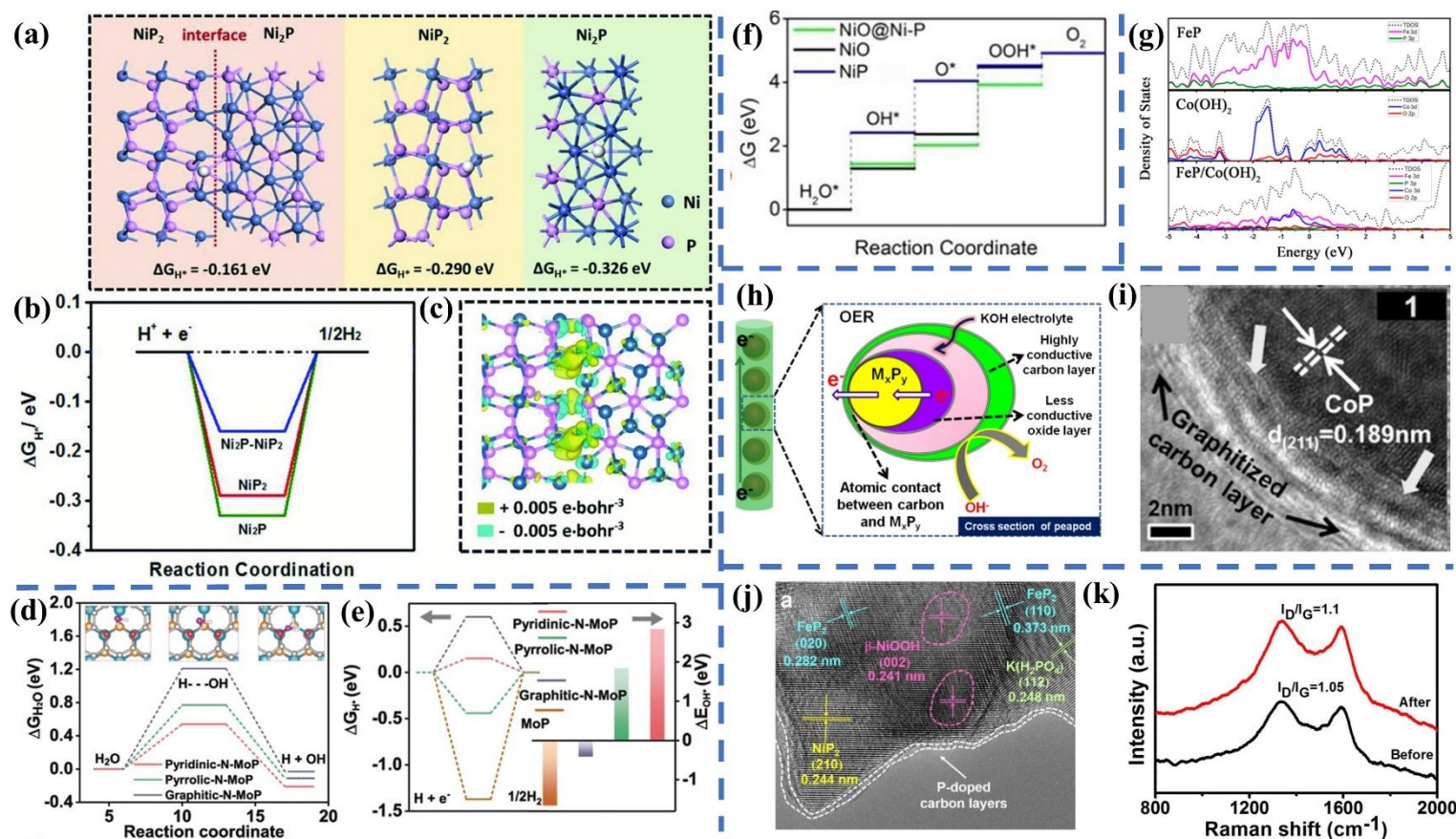


**Figure 2-4.** (a) Top view of the schematic models of the optimized  $\text{Ni}_2\text{P-NiP}_2$  polymorph, and pure  $\text{NiP}_2$  as well as  $\text{Ni}_2\text{P}$  with  $\text{H}^*$  adsorbed on their surfaces. (b) HER free-energy diagram calculated at the equilibrium potential for the  $\text{Ni}_2\text{P-NiP}_2$  polymorph, pure  $\text{NiP}_2$  and pure  $\text{Ni}_2\text{P}$ . (c) Charge density difference plot at the  $\text{Ni}_2\text{P-NiP}_2$  interface. Reproduced with permission.<sup>[93]</sup> Copyright 2018 Wiley-VCH Verlag GmbH & Co. KGaA, Weinheim. (d) Free energy diagram of the water dissociation step. Inset: the atomic configurations of

different states of pyridinic-N-MoP. (e)  $\Delta G_{H^*}$  diagram (left) and the chemisorption energies of  $\text{OH}^*$  ( $\Delta E_{\text{OH}^*}$ ) (right). Reproduced with permission.<sup>[95]</sup> Copyright 2019 Wiley-VCH Verlag GmbH & Co. KGaA, Weinheim. (f) The kinetic-energy barrier profiles of intermediates and products on NiO, Ni-P and NiO@Ni-P composites. Reproduced with permission.<sup>[100]</sup> Copyright 2018 Wiley-VCH Verlag GmbH & Co. KGaA, Weinheim. (g) The density of states of FeP,  $\text{Co(OH)}_2$ , and FeP/ $\text{Co(OH)}_2$ . Reproduced with permission.<sup>[102]</sup> Copyright 2019 American Chemical Society. (h) Illustration of the electron transfer process of metallic  $\text{M}_x\text{P}_y$  ( $\text{M} = \text{Co}, \text{Ni}, \text{and Cu}$ ) composites in the OER process. (i) HRTEM image of H-CoP/C after long-time OER measurement. Reproduced with permission.<sup>[105]</sup> Copyright 2017 Wiley-VCH Verlag GmbH & Co. KGaA, Weinheim. (j) HRTEM image of  $\text{FeP}_2\text{-NiP}_2\text{@PC}$  after successive 3000 cycles for the OER stability test. (k) Raman spectra of  $\text{FeP}_2\text{-NiP}_2\text{@PC}$  before and after applying 3000 successive cycles for the OER stability test. Reproduced with permission.<sup>[106]</sup> Copyright 2019 American Chemical Society.

heterointerface to reduce the barrier energy for the RDS resulting in accelerated reaction kinetics and enhanced HER activities. Moreover, the dopant in a heterostructure with the proper doping configuration (e.g. pyridinic-N doping in graphene in a MoP/C heterostructure<sup>[95]</sup>) can also exhibit a synergistic effect with a TMP to work as highly efficient active sites to further improve the catalytic performance. However, the different doping sites in the heterostructure should be investigated in detail to identify the real active sites for the investigated reactions.

#### 2.4.2.2 Synergistic Effects of heterostructures on the enhanced OER activity

Since OER proceeds in a strong oxidative environment, reconstruction of the surface species of TMP-based heterostructures are usually observed, which makes the understanding of the synergistic effect of heterostructure and theoretical calculations challenging. Phase transformation has been frequently observed in TMP-based heterostructures in which TMP is *in-situ* transferred into metal oxy/hydroxides during the OER.<sup>[65]</sup> For example, Li et al. observed an *in-situ* formed CoOOH shell on a Co<sub>2</sub>P core by high-resolution transition electron microscopy (HRTEM) and linear scanning energy-dispersive X-ray spectroscopy (EDS).<sup>[52]</sup> The *in-situ* formed CoOOH shell prevents the complete oxidation of the Co<sub>2</sub>P core and the Co<sub>2</sub>P/CoOOH heterojunction enables efficient OER performance. Menezes et al. also reported similar results on nickel phosphides.<sup>[96]</sup> The prepared Ni<sub>12</sub>P<sub>5</sub> exhibited a much better OER performance than Ni<sub>2</sub>P, which is related to the higher coverage of Ni on the surface that conventional to form more active species, such as NiOOH and Ni(OH)<sub>2</sub>. However, the mechanisms of the electrochemical oxidation are still not fully understood. Many researchers have attributed the enhanced activity to the electrochemical oxidation of TMP-based electrocatalysts, which would enable the increase of accessible active sites. Furthermore, the underlying TMP-based electrocatalysts with high conductivity would accelerate the charge transfer at the interface.<sup>[97,98]</sup>

For the case of TMP-based heterostructures, there are mainly two different types according to the different locations of the TMP-based catalysts in the heterostructure: (i) TMP-based catalysts are supported by other materials (TMP-exposed heterostructure) and (ii) TMP-

based catalysts protected by other materials (TMP-protected heterostructure). In almost all of those cases, the heterostructures with a strong interaction between the different components have a positive contribution to the OER activity.<sup>[99]</sup> For example, in the case of TMP-exposed heterostructures, Liang et al. investigated the synergistic effect of a CNT-supported  $\text{Co}_{0.7}\text{Ni}_{0.3}\text{P}$  heterostructure ( $\text{Co}_{0.7}\text{Ni}_{0.3}\text{P}/\text{CNTs}$ ) with a better OER performance than unsupported  $\text{Co}_{0.7}\text{Ni}_{0.3}\text{P}$ .<sup>[47]</sup> Their results indicated that the  $\text{Co}_{0.7}\text{Ni}_{0.3}\text{P}$  is almost completely transformed into  $\text{Co}_{0.7}\text{Ni}_{0.3}\text{OOH}$ , which serves as the real active sites for the OER after electrochemical oxidation under the oxidative conditions. And the incorporation of  $\text{Co}_{0.7}\text{Ni}_{0.3}\text{P}$  with CNTs could benefit the effective charge transfer on the heterointerface, thus enhancing the catalytic activity. Hao et al. prepared heterostructured  $\text{NiO}@\text{Ni-P}$  core-shell nanosheet arrays with enhanced OER activity as compared to  $\text{NiO}$  and  $\text{Ni-P}$  with similar morphology.<sup>[100]</sup> DFT calculation based on the optimized structural diagram of  $\text{NiO}@\text{Ni-P}$  (Figure 2-4(f)) indicates that the overpotential for the RDS on the  $\text{NiO}@\text{Ni-P}$  heterointerface is smaller than that of  $\text{NiO}$  and  $\text{Ni-P}$ , which is beneficial to the enhanced OER performance. Mu and coauthors explored the catalytic mechanisms on the surface of a Ru-modulated  $\text{Co}_x\text{P}$  ( $\text{Ru-RuP}_x\text{-Co}_x\text{P}$ ) heterostructure.<sup>[101]</sup> DFT calculation indicated that incorporating Ru onto  $\text{Co}_x\text{P}$  can improve the adsorption/desorption ability of O. The  $\text{Ru}/\text{RuO}_2$  and  $\text{Co}_x\text{P}/\text{CoOOH}$  core-shell structures formed during the OER process on the surface of the  $\text{Ru-RuP}_x\text{-Co}_x\text{P}$  heterostructure worked as the actual active sites for the OER. Therefore, coupling TMP-based catalysts with other materials in TMP-exposed heterostructures can result in enhanced OER activities. The enhancement of activities may arise from the increase in the amount of accessible active sites, the accelerated charge transfer and optimal adsorption ability of intermediates originating from the synergistic effect of heterostructures, all of which result in better reaction kinetics and thus improve the catalytic activities. The in-situ formed  $\text{M-OH}/\text{OOH}$  which is transferred from the TMP-based exposed on the surface of heterostructures worked as the real active sites for the OER.

For the case of TMP-protected heterostructures, Ding et al. prepared a heterostructure of  $\text{FeP}$  embedded in  $\text{Co}(\text{OH})_2$ , and the resulting  $\text{FeP}/\text{Co}(\text{OH})_2$  exhibited an improved OER activity.<sup>[102]</sup> The density of states (DOS) (Figure 4(g)) and charge redistribution calculations

reveal the strong interaction that appeared at the CoP/Co(OH)<sub>2</sub> heterointerface, resulting in the enhanced catalytic activity. Similar situations are also reported for heterostructured NiCoP@NiCoPO<sub>x</sub>,<sup>[103]</sup> and NiP-Al<sub>2</sub>O<sub>3</sub>/NF.<sup>[104]</sup> Bai and coauthors synthesized peapod-like M<sub>x</sub>P<sub>y</sub>/C (M = Co, Ni, and Cu) heterostructures with a strengthened synergistic effect (SSE) between metallic M<sub>x</sub>P<sub>y</sub> and the carbon layer resulting in enhanced bifunctional activity and considerable durability.<sup>[105]</sup> After long-time OER measurement, a Co-O layer was formed on the surface of CoP nanoparticle where there were no atomic contact with carbon. The as-formed Co-O/CoP heterostructure acted as the active sites for OER in alkaline electrolyte. But there are still some positions of CoP, where are protected by carbon layer with atomic contact, were not oxidized. Here, the atomic contact of CoP and C not only accelerates the electron transfer near the interface of the heterostructure but also prevents the oxidation of the encapsulated metallic CoP (Figure 4(h, i)), guaranteeing faster reaction kinetics and outstanding durability. Most recently, Mu's group prepared a heterostructure by coupling a double metal diphosphide with P-doped carbon (FeP<sub>2</sub>-NiP<sub>2</sub>@PC) and investigated the oxidation effect on carbon during the long-time OER measurement.<sup>[106]</sup> After 3000 cycles of the OER stability test, β-NiOOH was formed on the surface of the catalysts, which played a key role in the OER (Figure 2-4(j)). Their Raman measurements indicated that the binding energy of the C=O bonds shifted to higher binding energy (0.8 eV) and that the ratio of the intensity (*I<sub>D</sub>/I<sub>G</sub>*) increased from 1.05 to 1.1 (Figure 2-4(k)), which indicates that more defects were generated after the long-time OER measurement. Therefore, they concluded that the application of a high potential in a KOH solution can promote the generation of defects in carbon layers enhancing the exposure of more active sites for the OER. However, the reaction mechanism that occurs upon carbon encapsulation is still not clear, like which is the pathway for the adsorption of O\* and OOH\* on the heterointerface and how to the generated gases escape from the surface of the catalysts. Therefore, more efforts should be carried out to gain a deeper understanding of the reaction mechanism appearing on the heterostructured TMP-based electrocatalysts.

### 2.4.2.3 Synergistic Effects of Heterostructures on the Overall Water Splitting Performance

According to equation (11), the total overpotential ( $\eta_{total}$ ) for overall water splitting consists of the kinetic overpotential of both half-reactions ( $\eta_{HER}$  and  $\eta_{OER}$ ), a concentration-related overpotential ( $\eta_{con}$ ) and an additional overpotential for overcoming the ohmic resistance ( $\eta_{\Omega}$ ). Thus, for a certain electrolyzer, the main energy consumption is used to overcome the kinetic overpotential of both half-reactions. Therefore, in order to address the match between the overpotential of both half-reactions (HER/OER) and the voltage required for overall water splitting, the calculated voltage ( $V_c$ ) can be calculated according to equation (12) and compared with voltages measured with a two-electrode setup ( $V_m$ ) as shown in **Table 2-1**. It should be noted that this comparison can only be carried out between those results measured under similar measurement conditions. In Table 2-1, it can be seen that  $V_c$  matches very well with  $V_m$  for most cases. The small differences observed for some cases can be attributed to the experimental error, data processing (iR compensation) and so on. The consistency of the overpotential obtained for the HER/OER half-reactions with the voltage required for overall water splitting further highlights the advantage of the bifunctional property of TMP-based heterostructures.

$$V_c = 1.23 \text{ V} + \eta_{OER} + \eta_{HER} \quad (12)$$

For overall water splitting, the HER/OER half-reactions happen on the surface of the cathode or the anode simultaneously, but not on one electrode. Bifunctional TMP-based heterostructures demonstrate enhanced half-reaction activities when compared to their single counterparts, thus resulting in an improved overall water splitting performance. The improved catalytic activities can be attributed to the increased amount of accessible active sites owing to the synergistic effect of the heterostructure. For example, Ali et al. prepared a 3D mesoporous CoP/CoCr<sub>2</sub>O<sub>4</sub> heterostructure with a larger surface area to offer more active sites.<sup>[107]</sup> The as-prepared CoP/CoCr<sub>2</sub>O<sub>4</sub> heterostructure demonstrated excellent catalytic activities with a smaller charge transfer resistance ( $R_s$ ) and larger electrochemical surface area (ECSA) for both half-reactions. Wu and coauthors synthesized a bifunctional NiSe<sub>2</sub>-Ni<sub>2</sub>P heterostructure on NF

(NiSe<sub>2</sub>-Ni<sub>2</sub>P/NF) exhibiting a larger ECSA and superior ECSA-normalized OER and HER activities than that of NiSe<sub>2</sub>/NF and Ni<sub>2</sub>P/NF.<sup>[108]</sup> Recently, Ma et al. also reported a similar result for a Ni<sub>2</sub>P@NPC@CC heterostructure.<sup>[109]</sup> Apart from the above discussion, the heterostructure can also change the morphology of the catalyst surface resulting in enhanced bubble detachment and wettability to accelerate the mass transfer during the electrolysis.<sup>[35,75,110]</sup>

Besides the exposure of more active sites, the formation of a heterointerface can also modulate the electronic structure of the heterostructure resulting in improved conductivity and accelerated charge transfer, thus enhancing the activities of both half-reactions and overall water splitting. For example, Lu et al. prepared 3D bead string-like N-doped CoO@CoP arrays (N-CoO@CoP).<sup>[111]</sup> X-ray photoelectron spectroscopy (XPS) revealed that the N-doping in CoO@CoP can lead to a shift of the Co 2P<sub>3/2</sub> and P 2p peaks towards higher binding energies, which can be attributed to the stronger electronegativity of N than Co and P. Therefore, the N dopant attracts electrons from Co and P to alter the electronic structure of CoP, resulting in a tuned electronic structure and enhanced catalytic activities for overall water splitting. Moreover, Ding et al. modulated the electronic interaction of a Co(OH)<sub>2</sub>/FeP heterostructure.<sup>[102]</sup> They found that strong orbital hybridization between Fe and Co species appeared in the density of state ranging from -1.5 to 0 eV, indicating the strong interaction between Fe and Co atoms. Therefore, the hydrated alkaline-metal cations were stabilized by the surface electron accumulation region of Fe atoms because of the strong electronic interaction, which results in enhanced interaction between the heterointerface and water, thus accelerating the reaction kinetics and improving the activity for overall water splitting.

Along with the change of active sites and the electronic structure of TMP-based heterostructure, the adsorption of intermediates on the surface of heterostructure can also be optimized because of the synergistic effect. The optimized adsorption energy of intermediates significantly reduces the energy barrier of the RDS thus speeding up the catalytic kinetics for HER/OER half-reactions as well as for overall water splitting. For example, Mu's group reported a NiSe<sub>2</sub>-Ni<sub>2</sub>P heterostructure on NF (NiSe<sub>2</sub>-Ni<sub>2</sub>P/NF), which demonstrated excellent

catalytic activities towards both the OER ( $\eta_{50} = 220$  mV,  $45$  mV dec<sup>-1</sup>) and the HER ( $\eta_{10} = 102$  mV,  $68$  mV dec<sup>-1</sup>) as well as for overall water splitting ( $1.50$  V @  $10$  mA cm<sup>-2</sup>) in  $1$  M KOH.<sup>[108]</sup> DFT calculation revealed that the NiSe<sub>2</sub>-Ni<sub>2</sub>P heterostructure exhibited a smaller  $\Delta G_{H^*}$  ( $0.01$  eV) and a lower H<sub>2</sub>O adsorption energy ( $\Delta E_{H_2O} = -0.35$  eV) than those of Ni<sub>2</sub>P and NiSe<sub>2</sub>, resulting in a significant reduction of the adsorption energy of intermediates. Benefitting from the optimized hydrogen adsorption energy (HER) and the favorable H<sub>2</sub>O adsorption process (OER), the heterostructured NiSe<sub>2</sub>-Ni<sub>2</sub>P demonstrated an improved overall water splitting activity compared to its counterparts. Similarly, Cao et al. prepared NiCoP embedded in N doped carbon nanowall array (NiCoP@NC NA/NF) with an improved overall water splitting activity ( $V = 1.56$  V @  $20$  mA cm<sup>-2</sup>).<sup>[112]</sup> DFT calculation indicated that the  $\Delta G_{H^*}$  of NiCoP ( $-0.73$  eV) was reduced to as low as  $0.09$  eV after being coupled with C, which is beneficial to the release of hydrogen resulting in an improved HER activity. For the OER, after coupling with C, the corresponding reaction free energy for the RDS was reduced to as low as  $2.19$  eV from  $2.66$  eV resulting in an enhanced OER performance. Similar results were also reported for other TMP-based bifunctional heterostructures such as FeNi-LDH/CoP/CC,<sup>[113]</sup> Ni<sub>2</sub>P-NiP<sub>2</sub>,<sup>[93]</sup> Ni<sub>2</sub>P@NPC@CC<sup>[109]</sup> and CoP@a-CoOx.<sup>[114]</sup>

In summary, a heterostructure with strong interaction between the different components could exhibit effective synergistic effects. The synergistic effects can regulate the morphology, tune the electronic structure of the heterostructure to increase the amount of accessible active sites and accelerate the mass/charge transfer on the heterointerface. The adsorption ability of intermediates can also be optimized owing to the synergistic effects of heterostructures, which results in reduced energy barriers of the RDS, thus accelerating reaction kinetics for both the HER and the OER half-reactions and improving the overall water splitting performance.

### **2.4.3 *In-situ/operando* Measurements for Mechanistic Studies of the Water Splitting Process**

Although the mechanism of the electrochemical water-splitting including the HER and the OER, has been investigated for decades, the identification of the actual active sites and the corresponding reaction mechanisms are still limited.<sup>[115]</sup> For the case of TMP-based electro-



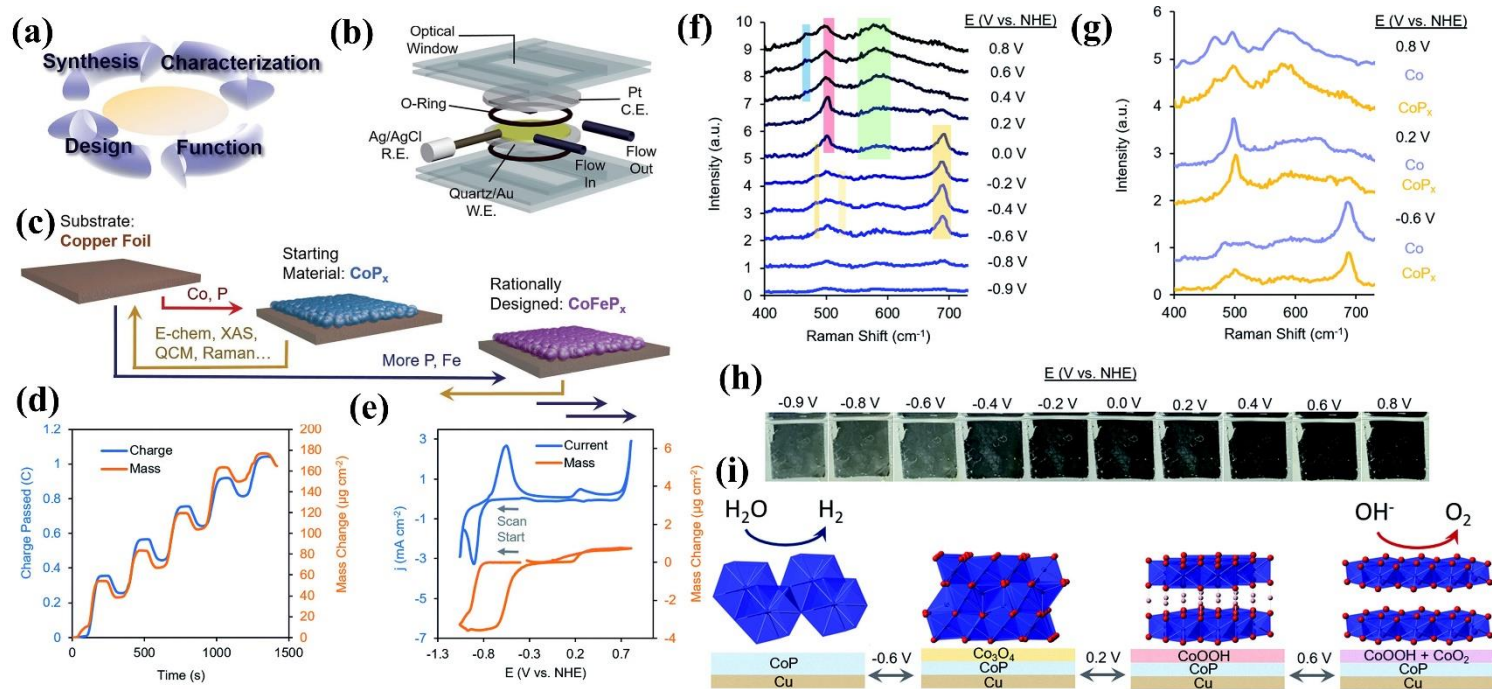


Figure 2-5. (a) An iterative cycle of synthesis, characterization, analysis, and design was employed to develop improved catalysts. (b) Operando measurements of the catalyst were enabled by a QCM setup, which allows for integrated electrochemical, gravimetric and spectroscopic analysis. (c) A bifunctional HER and OER  $\text{CoP}_x$  catalyst was chosen as starting material and improved upon using structure-function relationships derived through operando measurements to yield

a rationally designed  $\text{CoFeP}_x$ . (d) Operando characterization of  $\text{CoP}_x$ . Quartz crystal microbalance-Raman spectroelectrochemical studies enable operando monitoring of mass change and molecular vibrations during an electrochemical measurement. The mass of  $\text{CoP}_x$  deposited on the working electrode was quantified during 5 CV cycles. (e) A CV scan of  $\text{CoP}_x$  in 1.0 M KOH reveals a reversible change of  $\sim 2.0\%$  of the total mass corresponding to a redox wave centered at  $-0.8$  V vs. NHE and a reversible mass change of  $0.3\%$  at  $0.2$  V vs. NHE. (f) Operando Raman spectroscopy, also conducted in 1.0 M KOH at  $25^\circ\text{C}$ , reveals the formation of  $\text{Co}_3\text{O}_4$  from  $0.6$  V to  $0.0$  V vs. NHE,  $\text{CoOOH}$  at  $0$  V vs. NHE and  $\text{CoO}_2/\text{CoO}_x$  at  $0.4$  V vs. NHE. (g) The Raman spectra for  $\text{CoP}_x$  are similar to those of electrodeposited Co under the same conditions, indicating that the spectra of  $\text{CoP}_x$  stem from phases of Co. (h) An electrochromic effect of  $\text{CoP}_x$ , measured on a fluorine-doped tin oxide electrode, also supports the assignment to the film interconversion between metallic, oxide, and oxyhydroxide phases. The dominant surface phase under each voltage range is illustrated in (i). Note: ions and solvent molecules filling in spaces between layers are not shown. Reproduced with permission.<sup>[34]</sup> Reproduced under the terms of the Creative Commons CC-BY License.<sup>[124]</sup> Copyright 2018, N. Kornienko et al., published by the Royal Society of Chemistry.

catalysts, some researchers have demonstrated that the P atoms in TMP incorporated with surrounding metal, work as the active sites for the HER and that *in-situ* formed oxy/hydroxides or phosphates on the surface of TMP serve as the active sites for the OER.<sup>[67,69,116]</sup> However, most of them are based on theoretical calculations, which cannot fully reveal the real reaction mechanism in the actual situation. Therefore, *in-situ*/operando measurements are essential to investigate the intermediates during the reaction process for the confirmation of the results from the theoretical calculation.<sup>[117-122]</sup> For example, Lassalle-Kaiser et al. observed that Mo(III) units with terminal disulfide ligands ( $\eta^2 \text{S}_2^{2-}$ ) were formed at the surface of  $\text{MoS}_x$  during the HER by *in-situ* X-ray absorption spectroscopy and the protonation and reduction of those  $\text{Mo}^{\text{III}}(\text{S}_2)$  sites were identified as the RDS for the HER.<sup>[123]</sup> Most recently, Kornienko and coauthors monitored the mass change and molecular vibration of bifunctional  $\text{CoP}_x$  during the HER/OER processes by combining *in-situ*/operando quartz crystal microbalance (QCM) and Raman spectromicroscopy measurements (**Figure 2-5(a-c)**).<sup>[124]</sup> Their *in-situ* QCM measurement reveals that a relatively small and fully reversible mass change appears on the surface of  $\text{CoP}_x$  rather than a complete bulk transformation during the electrolysis (Figure 2-5(d, e)). Furthermore, operando Raman spectromicroscopy reveals the potential-dependent behavior of  $\text{CoP}_x$  (Figure 2-5(f, g)). Under the reductive potential, the  $\text{CoP}_x$  yielded no obvious peak changes in the Raman spectrum. However, new peaks that can be attributed to  $\text{Co}_3\text{O}_4$  and  $\text{CoOOH}$  arise under the oxidative potential, indicating a phase change of  $\text{CoP}_x \rightarrow \text{Co}_3\text{O}_4 \rightarrow \text{CoOOH}$  along with the increase of potential. The surface reconstruction of the  $\text{CoP}_x$  during the electrolysis is consistent with the results from the theoretical calculation (Figure 2-5(h, i)). Moreover, on-line inductively coupled plasma mass spectrometry (ICP-MS) was also used as an effective tool to investigate the stability of electrocatalysts during the real electrocatalytic process.<sup>[125]</sup> Their results revealed that the prepared Pt-based catalysts are not stable during the oxygen evolution reaction in acidic media. Therefore, *in-situ*/operando measurements are vital to gain an evidential insight into the reaction mechanism and more efforts are required to focus on fundamental studies by employing advanced *in-situ*/operando techniques to provide experimental evidence supporting the general mechanistic hypotheses.

**Table 2-1.** Bifunctional TMP-based heterostructure electrodes for efficient water splitting.

Catalyst	Substrate	Overpotential @ 10 mA cm <sup>-1</sup> (mV) <sup>a</sup>		Voltage for overall @ 10 mA cm <sup>-2</sup> (V) <sup>a</sup>		Tafel slope (mV dec <sup>-1</sup> )		Catalyst loading (mg cm <sup>-2</sup> )	Stability (h)	Electrolyte	Ref.
		$\eta_{HER}$	$\eta_{OER}$	$V_c^h$	$V_m^i$	HER	OER				
Co-P@PC	CFP <sup>b</sup>	76 72 85	282 -- --	1.59 -- --	1.60 -- --	-- 49 --	53 -- --	1	60	1 M KOH 0.5 M H <sub>2</sub> SO <sub>4</sub> 1 M PBS	[138]
Co <sub>x</sub> P/N-doped C	GC <sup>c</sup> CC <sup>d</sup>	187 --	380 --	1.80 --	-- 1.71	58.5 --	68.1 --	0.14 1	-- 10	1 M KOH	[239]
CoP/NPCP	GC CC	150 --	420 --	1.80 --	-- 1.55	20 --	115 --	0.637 1.5	25	1 M KOH	[240]
CoP/NCNHP	GC	115	310	1.66	1.64	66	70	2	36	1 M KOH	[161]
CoP-Co <sub>2</sub> P@PC/PG	NF <sup>e</sup>	39	272 (20)	--	1.567	59	66	10	5000 cycles	1 M KOH	[184]
CoP@NG	GC	114	354	1.70	--	59.6	63.8	--	--	1 M KOH	[241]
CoP-CNT	GC	215	330	1.78	--	56	50	0.285	--	0.1 M NaOH	[179]
CoP <sub>11</sub> /NG	GC	83	262	1.58	1.58	57	54	0.15	65	1 M KOH	[183]
CoP <sub>2</sub> /RGO	GC	115	300	1.65	1.56	50	96	0.285	2.5	1 M KOH	[242]
CoP(MoP)- CoMoO <sub>3</sub> @CN	GC NF	198 --	296 --	1.72 --	-- 1.55	95 --	105 --	1.12(HER) 0.56(OER) 3 (overall)	-- 33	1 M KOH	[243]
Ni <sub>2</sub> P@G	CC	103	275 (20)	--	1.51	56.5	56.3	2.4	24	1 M KOH	[187]
Ni <sub>2</sub> P-NPCM	GC	125	255	1.61	1.62	51	57	1	40	1 M KOH	[162]
Cu <sub>3</sub> P@C	GC	-- 124	300 --	-- --	-- --	-- 24	29 --	0.57	20	1 M KOH 0.5 M H <sub>2</sub> SO <sub>4</sub>	[159]
0.75-NC-Fe <sub>x</sub> P	GC NF	193 --	302 --	1.73 --	-- 1.63	60 --	40 --	0.25 0.39	-- 3.5	1 M KOH	[244]
NiCoFeP/C	CFP	149	270	1.65	1.60	89	65	0.28	18	1 M KOH	[178]
NiP/NiFeP/C	GC	87	250	1.57	1.53	38	58	0.168	20	1 M KOH	[163]
FeNiP/PG	GC CC	173 --	229 --	1.63 --	-- 1.58	50.3 --	49.7 --	0.51 2	10 20	1 M KOH	[60]
FeNiP/SG	GC Bulk	115 --	218 --	1.56 --	-- 1.54	44 --	47 --	--	30 40	1 M KOH	[181]
PrGO/NiCoP	GC NF	106 --	281.3 --	1.62 --	-- 1.56	58.3 --	60.1 --	2	-- 10	1 M KOH	[245]
NiCoP@NC NA/NF	NF	34 37	-- 305	-- 1.57	-- 1.56 (20)	51.8 53.9	-- 70.5	--	15	0.5 M H <sub>2</sub> SO <sub>4</sub> 1 M KOH	[112]
CoFeP/CNT	GC	178	323	1.73	1.74	71	38	0.27	20	1 M KOH	[246]
NiCo <sub>2</sub> P <sub>x</sub> /CNT	GC	47	284	1.56	1.61	67.3	56	0.1	48	1 M KOH	[150]
NCP/G NSs	Ti	119 (100)	400 (100)	1.75 (100)	1.61	62.3	65.9	0.31	10	1 M KOH	[186]
Ni <sub>2</sub> P/Ni/NF	NF	98	200	1.53	1.49	72	--	--	40	1 M KOH	[151]
Ni/NiP	NF	130	270 (30)	--	1.61	58.5	73.2	--	4	1 M KOH	[191]
Ni/NiSP <sub>x</sub> /NF	NF	46	231	1.51	1.82 (100)	86	102	1.35	30	1 M NaOH	[193]

Ni/Ni <sub>2</sub> P@3DNSC	CF <sup>f</sup>	92	231	1.55	1.55	65	67	--	24	1 M KOH	[194]
Ni/Ni <sub>2</sub> P	TiF <sup>g</sup>	73 (20)	331 (20)	1.63 (20)	1.523	76	54	1.9	--	1 M KOH	[192]
Fe:Ni/Ni <sub>2</sub> P		--	285 (20)	--	--	--	48	1.9			
Co/CoP (C)	GC	253 138 178	340 570 (2.6) 570 (1.3)	1.82 -- --	--	90.2 72.3 59.1	--	0.88	12	1 M KOH 1 M PBS 0.5 M H <sub>2</sub> SO <sub>4</sub>	[196]
	NF	--	--	--	1.45 1.51 1.89(1)	--	--	5	12	1 M KOH 1 M PBS 0.5 M H <sub>2</sub> SO <sub>4</sub>	
Co <sub>2</sub> P/Co	Co foil	157	319	1.71	1.71	59	79	--	15	1 M KOH	[195]
Fe <sub>3</sub> O <sub>4</sub> -CoP <sub>x</sub> /TiN	Ti	174	331	1.74	1.75	65	122	--	11	1 M KOH	[168]
Ni <sub>2</sub> P@NiFeAlO <sub>x</sub>	NF	105	210	1.55	1.52	106	106	1	24	1 M KOH	[144]
Ni <sub>2</sub> P@FePO <sub>x</sub>	NF	75	205	1.51	1.51	--	32	1	100	1 M KOH	[145]
NiFeO <sub>x</sub> @NiFeP	Bulk	200 100	220 680	1.65 2.01	1.65 --	85.2 67.2	37 94.0	--	600 --	1 M NaOH 0.5 M H <sub>2</sub> SO <sub>4</sub>	[237]
CuO@Ni-P NA/CF	CF	106 (30)	275 (30)	1.61	1.71 (30)	72.0	124.9	2.9	35	1 M KOH	[202]
Ni <sub>2</sub> P/MoO <sub>2</sub> @MoS <sub>2</sub>	TiF	159	280	1.67	1.82	77	85	--	40	1 M KOH	[247]
NiCo <sub>2</sub> O <sub>4</sub> /Ni <sub>2</sub> P	NF	45	250	1.53	1.59	45	58	1.58	50	1 M KOH	[50]
Co-Pi/CoP/Ti	Ti	68	310	1.61	1.60	--	58	2	24	1 M KOH	[248]
Ni <sub>12</sub> P <sub>5</sub> /Ni <sub>3</sub> (PO <sub>4</sub> ) <sub>2</sub>	GC CFP  Ti	114 --	318 --	1.66 --	-- 1.8 (357.6)	93.1	51.7	0.71 3	10 100	1 M KOH	[167]
CoP@a-CoO <sub>x</sub>	CC	132 --	232 --	1.59 --	-- 1.59	89 --	67 --	3 5	-- 30	1 M KOH	[114]
N-CoO@CoP	NF	201 (100)	332 (100)	1.76	1.79	37	81.5	5.2	50	1 M KOH	[111]
CoP/CoCr <sub>2</sub> O <sub>4</sub>	GC NF	212 --	290 --	1.73 --	-- 1.68	90 --	52 --	0.2 1.0	10 24	1 M KOH	[107]
NC-NiFeO <sub>x</sub> @NiFe-P	GC NF	285 --	237 --	1.75 --	-- 1.59	65 --	48 --	0.2 1	-- 20	1 M KOH	[203]
NiFe LDH/NiCoP/NF	NF	120	220	1.57	1.57	88.2	48.6	2.0	100	1 M KOH	[53]
CoNiP@NiFe LDH	NF	83	216	1.53	1.44	80	45	--	20	1 M KOH	[155]
Co(OH) <sub>2</sub> /Ag/FeP/Ti	TiF	118	236	1.58	1.56	79	56	--	50	1 M KOH	[102]
FeNi-LDH/CoP/CC	CC	135.6 (20)	231 (20)	1.60 (20)	1.617	56.1	33.5	--	18.5	1 M KOH	[113]
Ni <sub>5</sub> P <sub>4</sub> /NiP <sub>2</sub> /NiFe LDH	NF	124	197	1.55	1.52	--	46.6	2	50	1 M KOH	[154]
FeP/Ni <sub>2</sub> P	NF	14	154	1.40	1.42	24.2	22.7	8	40	1 M KOH	[169]
CoP/Co <sub>2</sub> P	GC CFP	103 --	317 --	1.65 --	-- 1.65	61.2 --	58.9 --	0.36	-- 8	1 M KOH	[139]
CoP/CoP <sub>2</sub>	GC	239 (20)	250	--	--	84.2	106.7	0.26	--	1 M KOH	[140]
Co <sub>2</sub> P-Ni <sub>2</sub> P/NF	NF	90	230 (50)	--	1.47	65.3	73	1.51	11	1 M KOH	[59]




Cu <sub>3</sub> P-Co <sub>2</sub> P	NF	124.6 (20)	334 (20)	1.69 (20)	1.55	65	132	2	14	1 M KOH	[142]
CoP-FeP	CC	30 71	-- 250	-- 1.55	--	42 67	-- 131	2.7	24	0.5 M H <sub>2</sub> SO <sub>4</sub> 1 M KOH	[217]
FeP <sub>2</sub> -NiP <sub>2</sub> @PC	GC	179	248	1.66	1.7	65	54	1	--	1 M KOH	[106]
Ni <sub>2</sub> P-Ni <sub>5</sub> P <sub>4</sub>	CC	-- 102	-- 290(20)	--	1.69	69 83	--	-- 109	24	1 M PBS 1 M KOH	[143]
MoP/Ni <sub>2</sub> P/NF	NF	75	309 (20)	--	1.55	100.2	77.6	--	15	1 M KOH	[218]
NiCoP@Cu <sub>3</sub> P	CF	54	309	1.59	--	72	42	--	1000 CV	1 M KOH	[219]
f-CoP/CoP <sub>2</sub> /Al <sub>2</sub> O <sub>3</sub>	GC	138	300	1.67	1.65	73	63	0.2	24	1 M KOH	[249]
NiPS <sub>3</sub> /Ni <sub>2</sub> P	GC NF	85 --	260 --	1.58 --	-- 1.65 (50)	82 --	78 --	0.56 1.0	-- 10	1 M KOH	[226]
Ni <sub>2</sub> P/Ni <sub>3</sub> S <sub>2</sub> /NF	NF	80	210	1.52	1.50	65	62	--	36	1 M KOH	[146]
NiS/Ni <sub>2</sub> P/CC	CC	111	265	1.61	1.67	78.1	41.3	5.68	10	1 M KOH	[147]
Ni-Co-S/Ni-Co-P	NF	110 (20)	240 (50)	--	1.49	62.0	83.4	--	48	1 M KOH	[227]
NiSe <sub>2</sub> -Ni <sub>2</sub> P/NF	NF	102	183	1.52	1.50	88	45	--	25	1 M KOH	[108]
Co/CoN/Co <sub>2</sub> P-NPC	GC	99	272	1.60	1.60	51	62	0.35	48	1 M KOH	[235]
Fe <sub>2</sub> P/Fe <sub>4</sub> N@C	GC	232	410	1.87	--	130	177	1.5	2000 CV	1 M KOH	[250]
Co <sub>2</sub> P/CoN-in-NCNTs	GC CFP	98 --	-- 420	--	-- 1.64	57 --	--	0.2 0.1	--	0.5 M H <sub>2</sub> SO <sub>4</sub> 0.1 M KOH	[55]
CoP-Mo <sub>2</sub> C@NC/CC	CC	74 107	265 330	1.57 1.67	1.64 --	79.4 --	71.6 --	1.8	40 8	1 M KOH 0.5 M H <sub>2</sub> SO <sub>4</sub>	[56]

<sup>a</sup> If not mentioned specially, the overpotentials for HER/OER and the voltages for overall water splitting are taken at 10 mA cm<sup>-2</sup>. Otherwise, the current density is noted in the brackets. <sup>b</sup> CFP, carbon fiber paper; <sup>c</sup> GC, glassy carbon; <sup>d</sup> CC, carbon cloth; <sup>e</sup> NF, nickel foam; <sup>f</sup> CF, Cu foil; <sup>g</sup> TiF, Ti foil; <sup>h</sup> V<sub>c</sub>, calculated voltage for overall water splitting using equation:  $V_c = 1.23 \text{ V} + \eta_{OER} + \eta_{HER}$ ; <sup>i</sup> V<sub>m</sub>, voltage measured for overall water splitting by a two-electrode electrolyzer.

## 2.5 Synthetic Methods for the Preparation of TMP-Based Heterostructures

The preparation of TMP is a very important step for the preparation of TMP-based heterostructure electrocatalysts. Generally, there are four main approaches to prepare TMP-based electrocatalysts with different synthesis strategies: **(a) Solution-phase reaction**, which usually uses *tri-n-octylphosphine* (TOP) and other P-contained organic chemicals as the P source at a temperature range from 220 to 385 °C.<sup>[31,97]</sup> **(b) Solid-phase reaction**, where the P-containing organic chemicals and metal salts were mixed together followed by a high temperature treatment (400-1000 °C) for reduction or a pyrolysis reaction.<sup>[126,127]</sup> **(c) Gas-solid reaction**, which normally starts with the preparation of a metal or metal oxide and followed by a phosphorization treatment with red phosphorus or sodium dihydrogen phosphate ( $\text{NaH}_2\text{PO}_2 \cdot \text{H}_2\text{O}$ ) as the P source in a furnace equipped with a quartz tube at a relatively lower temperature (e.g. 300 °C) when compared to (a). The M/P ratios of the prepared TMP can be adjusted by optimizing the temperature, pressure, and dosage of the P source during the phosphorization process.<sup>[128–132]</sup> **(d) Electrodeposition**, with which the TMP can be directly grown on various conductive substrates with a high specific surface area by reducing the metal ion and  $\text{H}_2\text{PO}_2$ <sup>[35,133]</sup> **(e) Other emerging methods**. Recently, several new innovational methods that emerged for the preparation of TMP, such as the  $\text{PH}_3$  plasma-assisted method,<sup>[134]</sup> aerosol-spray,<sup>[135]</sup> melt spinning<sup>[136]</sup> and chemical vapor deposition (CVD).<sup>[137]</sup> All those methods discussed above are also employed to produce bifunctional TMP-based heterostructures. With innovational strategies, many types of TMP-based heterostructures have been designed and prepared, including the carbon/TMP (C/TMP), transition metals/TMP (TM/TMP), transition metal oxides/TMP (TMO/TMP), transition metal hydroxides/TMP (TMH/TMP), TMP/TMP, transition metal sulfides (TMS)/TMP and other heterostructured TMP-based electrocatalysts. According to the location of TMP-based catalysts in the heterostructures, the TMP-based heterostructures can be classified as TMP-exposed and TMP-protected heterostructures, where TMP-based catalysts are exposed to the surface directly and protected by other catalysts, respectively (**Table 2-2**). The preparation strategies for every type of TMP-based heterostructures will be summarized and discussed in the following.

**Table 2-2.** Overview of the available strategies for the preparation of TMP-based heterostructures.

	Method	Morphology of the heterostructure		Experiment methods		Comments		
		Structure feature	Heterostructure type	Pre-material	Phosphorization	Advantages	Disadvantages	
TMP-based heterostructures	Growth-phosphorization (GP)	TMP-exposed	 <p>TMP exposed on the surface</p>	C/TMP M/TMP TMO/TMP TMP/TMP etc.	Hydrothermal, precipitation, electrodeposition, etc.	(b) (c)	<ol style="list-style-type: none"> <li>1. Sample forms are flexible (powder, bulk, coupled with substrates, etc.).</li> <li>2. TMP exposed at the surface, which can offer more active sites for reactions.</li> </ol>	The stability for the OER may be limited owing to oxidation of the TMP during long-time measurements.
	Growth-phosphorization-modification (GPM)	TMP-protected	 <p>TMP protected by other materials</p>	TMH/TMP etc.	Hydrothermal, electrodeposition, etc.	(c)	<ol style="list-style-type: none"> <li>1. Suitable for the preparation of binder free electrodes.</li> <li>2. The performance and stability of both the HER and the OER can be enhanced.</li> </ol>	Sample forms are limited and it is difficult to prepare the sample in powder form.
	Metal-organic framework (MOF)-derived	TMP-protected	 <p>TMP encapsulated in a carbon shell</p>	C/TMP etc.	Solvothermal, hydrothermal, etc.	(b) (c)	<ol style="list-style-type: none"> <li>1. Material morphology can be controlled by using different MOFs.</li> <li>2. The OER performance and stability can be enhanced due to its protection by C.</li> </ol>	<ol style="list-style-type: none"> <li>1. Organic solutions and high temperatures (&gt; 500 °C) are usually used in the preparation and carbonization of MOFs.</li> <li>2. Sample forms are limited and it is not suitable for preparing binder-free electrodes.</li> </ol>
	Other methods	--	--	C/TMP TMS/TMP TMN/TMP TMC/TMP etc.	Template-assisted method, CVD, one-pot, etc.	(a) (b) (c) (d)	They can meet some specific requirements in the preparation or application.	They may have a high demand for the preparation conditions or required equipment, such as CVD.

### 2.5.1 Growth-Phosphorization (GPM) Method

This GP method is usually used to synthesize TMP-exposed heterostructures and the phosphorization methods (b) and (c) are widely employed. In this case, the metal (hydro)oxides or other metal-containing compounds were directly grown on other types of catalysts by numerous methods followed by phosphorization. As an example of method (b), Wu et al. prepared a TMP@C heterostructure by pyrolyzing a one-dimensional (1D) cobalt phosphonate complex (**Figure 2-6(a)**).<sup>[138]</sup> Firstly, 1D cobalt phosphonate (Co/HEDP-MP) was synthesized by a self-assembly method. Subsequently, the obtained Co/HEDP-MP was used as the precursor to prepare cobalt phosphide nanoparticles decorated P-doped carbon fibers (Co-P@PCs) by one-step calcination. The P in the organic ligands successfully phosphorized the Co and doped the porous carbon matrix. The prepared Co-P@PC heterostructure exhibited excellent bifunctional activity and stability for the HER and the OER, which is associated with the synergistic effect between the active Co-P and the P-doped carbon matrix.

For the case of method (c), Deng et al. prepared a Co<sub>2</sub>P-Ni<sub>2</sub>P heterostructure on Ni foam (Co<sub>2</sub>P-Ni<sub>2</sub>P/NF) using a hydrothermal-phosphorization process.<sup>[59]</sup> As shown in Figure 2-6(b), the CoNi-precursor was first grown on NF by a hydrothermal reaction. Subsequently, the grown CoNi-precursor was phosphorized with NaH<sub>2</sub>PO<sub>2</sub> as the phosphorus source at 400 °C. This method enables the *in-situ* growth of TMP-based heterostructures on conductive substrates. Other types of TMP/TMP heterostructures were also reported to be prepared by a hydrothermal-phosphorization process, such as CoP/Co<sub>2</sub>P,<sup>[139]</sup> CoP/CoP<sub>2</sub>,<sup>[140]</sup> Ni<sub>2</sub>P-VP<sub>2</sub>/NF,<sup>[141]</sup> Cu<sub>3</sub>P-Co<sub>2</sub>P/NF<sup>[142]</sup> and Ni<sub>2</sub>P-Ni<sub>5</sub>P<sub>4</sub>/CC.<sup>[143]</sup> Furthermore, TMO/TMP heterostructures of Ni<sub>2</sub>P/NiFeAlO<sub>x</sub><sup>[144]</sup> and Ni<sub>2</sub>P/FePO<sub>x</sub>,<sup>[145]</sup> as well as TMS/TMP heterostructures of Ni<sub>2</sub>P/Ni<sub>3</sub>S<sub>2</sub>/NF,<sup>[146]</sup> NiS/Ni<sub>2</sub>P/CC<sup>[147]</sup> and CP/Ni<sub>2</sub>P/NiS<sup>[148]</sup> were also synthesized via the hydrothermal-phosphorization process.



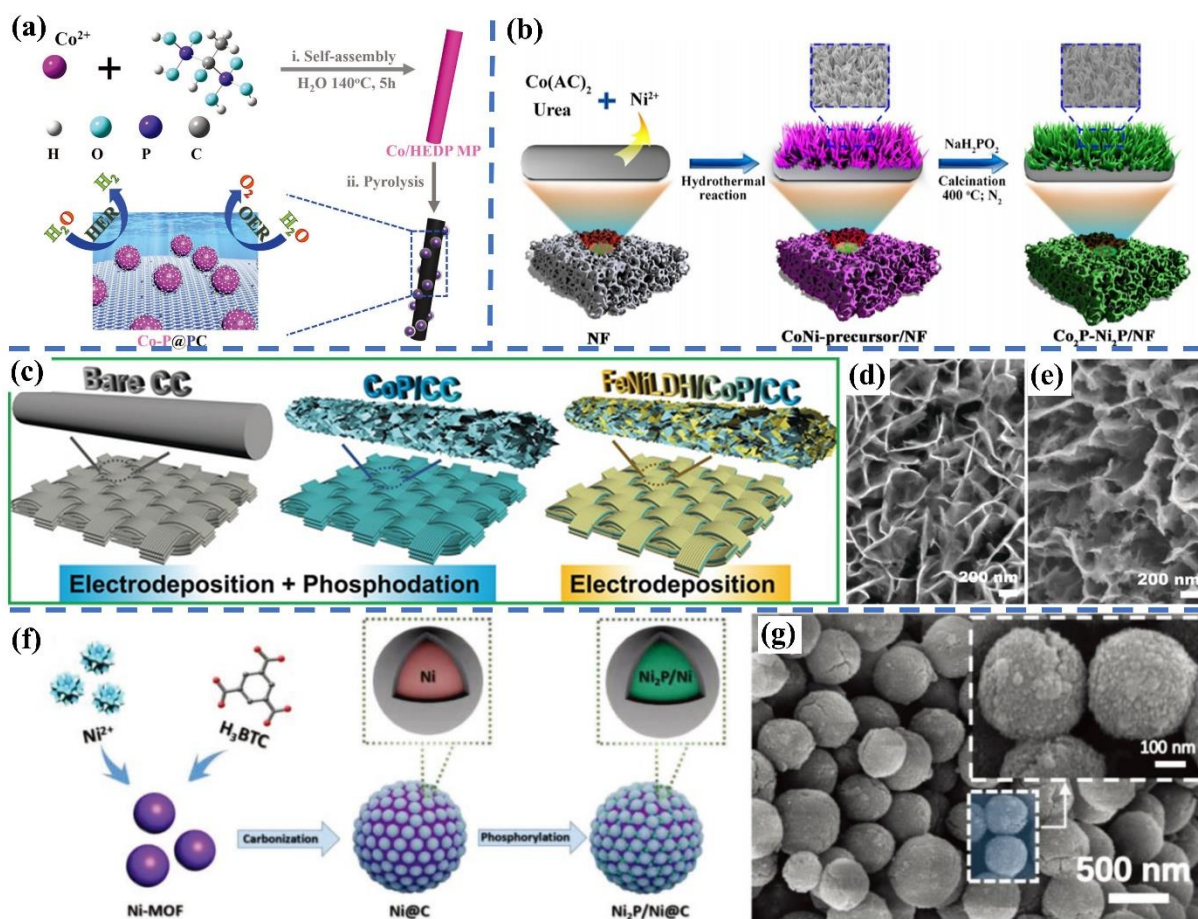


**Figure 2-6.** (a) Schematic illustration of the eco-friendly TMP-derived strategy for constructing Co-P@PC through converting the Co-based TMP upon calcination. Reproduced with permission.<sup>[138]</sup> Copyright 2019 Wiley-VCH Verlag GmbH & Co. KGaA, Weinheim. (b) Illustration of the synthetic procedure of Co<sub>2</sub>P-Ni<sub>2</sub>P/NF. Reproduced with permission.<sup>[59]</sup> Copyright 2019 Elsevier Ltd. (c) Illustration exhibiting the preparation process of FeNi-LDH/CoP/CC composite electrodes. (d, e) SEM images of CoP NSAs (d) and FeNi-LDH/CoP NSAs (e). Reproduced with permission.<sup>[113]</sup> Copyright 2019 Wiley-VCH Verlag GmbH & Co. KGaA, Weinheim. (f) Schematic illustration of the synthesis process of micro-/nanostructured Ni<sub>2</sub>P/Ni@C hybrids. (g) SEM image of Ni<sub>2</sub>P/Ni@C. Reproduced with permission.<sup>[157]</sup> Copyright 2019 Wiley-VCH Verlag GmbH & Co. KGaA, Weinheim.

Apart from the hydrothermal reaction, other effective methods have also been used to prepare the metal precursor. For example, Hu and coauthors prepared a TMO/TMP heterostructure of Fe-CoP/CoO by calcining a molten NaOH with the corresponding metal components.<sup>[149]</sup> The synthesized metal precursor was subsequently phosphorized using NaH<sub>2</sub>PO<sub>4</sub> as the phosphorus source. Huang et al. prepared a NiCo<sub>2</sub>P/CNTs heterostructure via a precipitation method followed with a solid-gas phosphorization treatment.<sup>[150]</sup> You et al. deposited 3D porous Ni microspheres on NF by electrodeposition.<sup>[151]</sup> Afterwards, the

electrodeposited Ni microspheres were converted to NiP by electrochemical conversion, thus building a NiP/Ni heterostructure on NF.

In summary, the GP method is an effective process for preparing TMP-exposed heterostructures, where the TMP-based catalysts are directly exposed to the electrolyte during the water splitting measurement. A large amount of different types of TMP-based heterostructures have been synthesized as discussed above, and the obtainable forms of these samples are flexible which can be powder, bulk or coupled with substrates for the preparation of binder-free electrodes. However, the OER stability for samples prepared by the GP method may be limited due to the oxidation of TMP-based catalysts during long-time OER measurements. Therefore, in order to further increase their long-term stability, extra co-catalysts would need to be coupled as the protective layer for TMP-exposed heterostructures. co-catalyst would need to be coupled as the protective layer for TMP-based heterostructures.

### **2.5.2 Growth-Phosphorization-Modification (GPM) Method**

When TMP-based catalysts are protected by other types of materials, the preparation could follow the GPM process. Therefore, the state-of-the-art method to prepare TMP-protected heterostructures is to first grow certain morphologic metal precursors (nanowires, nanorods, nanosheets and so on) followed by phosphorization to form the TMP-based catalysts. Subsequently, TMP-protected heterostructures are obtained with an extra modification step on the prepared TMP-based catalysts. The phosphorization method (c) is widely used in the GPM process. For example, He et al. prepared a TMH/TMP heterostructure on carbon cloth (CC) using the GPM process.<sup>[113]</sup> As shown in Figure 2-6(c), the Co(OH)<sub>2</sub> nanosheet arrays (NSAs) were first grown on the CC by electrodeposition. Subsequently, the grown Co(OH)<sub>2</sub> nanosheets were converted to CoP by phosphorization with NaH<sub>2</sub>PO<sub>2</sub> as the P source. Finally, the FeNi-layered double hydroxides (LDH) was electrodeposited on the CoP/CC yielding heterostructured FeNi-LDH/CoP/CC. The morphology of the as-prepared CoP NSAs and FeNi-LDH NSAs are shown in Figure 2-6(d, e). Similarly, a NiFe LDH/NiCoP heterostructure consisting of NiFe LDH nanosheets enfolded NiCoP nanowires prepared using the

hydrothermal-phosphorization-hydrothermal process was also reported.<sup>[153]</sup> Other TMH/TMP heterostructures, such as NiFe LDH/Cu<sub>3</sub>P,<sup>[152,153]</sup> Ni<sub>5</sub>P<sub>4</sub>/NiP<sub>2</sub>/NiFe LDH<sup>[154]</sup> and CoNiP@NiFe-LDH<sup>[155]</sup> were also synthesized with the GMP process. The GMP method is widely used to prepare TMH/TMP heterostructures and suitable to couple TMP-based heterostructures with conductive substrates for the preparation of binder-free electrodes. The prepared heterostructures demonstrate enhanced bifunctional activities and the OER stability can also be improved thanks to the protection of coupled catalysts. However, samples prepared by the GMP method are limited to binder-free electrodes and it is difficult to prepare those samples in the powder form.

### 2.5.3 Metal-Organic Framework (MOF)-Derived Method

With this strategy, C/TMP heterostructures comprising TMP encapsulated in the carbon matrix can be obtained through the MOF-derived method, where the morphology and facets can be tuned by using different MOFs.<sup>[156]</sup> In this case, the phosphorization methods (b) and (c) are normally employed. For example, Liu et al. reported a heterostructured Ni<sub>2</sub>P/Ni encapsulated into porous carbon by the MOF-derived method.<sup>[157]</sup> As shown in Figure 2-6(f), the microspherical Ni-MOF with a smooth surface was first synthesized by a facile solvothermal method. After carbonization under high temperature, the Ni ions turned into metallic Ni and the organic ligands of the MOF were transformed into carbon, thus resulting in the formation of Ni@C with a rougher surface. Subsequently, a C/TMP heterostructure consisting of Ni<sub>2</sub>P/Ni@C was obtained through an extra phosphorization treatment with NaH<sub>2</sub>PO<sub>2</sub> as the phosphorus source. The resulting Ni<sub>2</sub>P/Ni@C heterostructure inherits the morphological characteristics of Ni@C (Figure 6(g)), and its excellent stability for water electrolysis is benefited from the high oxidation resistance of the Ni<sub>2</sub>P/Ni surface protected by the coated C. Chandra Shit et al. designed and prepared a FeP@C heterostructure by a similar strategy using Fe-MIL-88B as the template.<sup>[158]</sup> Rong and coauthors produced a Cu<sub>3</sub>P@C heterostructure by phosphorizing Cu-BDC directly without high-temperature carbonization.<sup>[159]</sup> The morphology of the resulting heterostructure can be controlled by tuning the temperature used for the preparation of Cu-BDC.

Meanwhile, the doping of carbon-based materials can optimize their electronic structure and active sites, thus improving the corresponding catalytic activity.<sup>[160]</sup> Therefore, doped C/TMP heterostructures were also prepared by the MOF-derived method. For example, Pan et al. reported a novel heterostructure with CoP nanoparticles embedded in the N-doped carbon nanotube hollow polyhedrons (NCNHP) derived from ZIF-8@ZIF67 through a pyrolysis-oxidation-phosphorization process.<sup>[161]</sup> The resulting CoP/NCNHP heterostructure exhibited an enhanced bifunctional performance for overall water splitting. Furthermore, Yan and coauthors prepared Ni<sub>2</sub>P nanocrystals encapsulated in an N, P-codoped porous carbon matrix through direct pyrolysis of CUP-1-Ni MOFs without post phosphorization, which can avoid the release of flammable and detrimental PH<sub>3</sub> gas.<sup>[162]</sup> Guo et al. synthesized a Co<sub>2</sub>P/CoN-in-NCNTs heterostructure containing Co<sub>2</sub>P/CoN core-shell nanoparticles encapsulated in N-doped CNTs using the same strategy.<sup>[55]</sup> Recently, Weng et al. prepared a heterostructure of NiP/NiFeP encapsulated by heteroatom-doped carbon *via* direct pyrolysis of MOF precursors without post phosphorization.<sup>[163]</sup> A longer ligand was used to optimize the poor metal distribution during the pyrolysis.

The MOF-derived method is especially used to prepare TMP-protected heterostructures with TMP-based catalysts embedded in carbon. The morphology of the samples can be controlled by using different ligands for the preparation of different MOFs. The OER activity and stability can be enhanced, which can be attributed to the protection of carbon. However, the form of samples prepared by the MOF-derived method is restricted to powder and it is not easy to grow MOFs on a substrate for the preparation of binder-free electrodes. Moreover, organic solutions are usually used for the preparation of MOF-based pre-materials and a high temperature (> 500 °C) treatment is needed for the carbonization of MOFs.

#### **2.5.4 Other Methods**

Other novel strategies have also been used to develop TMP-based heterostructures. For example, Sun et al. synthesized Ni<sub>2</sub>P nanoparticles supported on a 3D ordered Co-N-doped carbon matrix by using silica opals as the template.<sup>[164]</sup> The resulting Ni<sub>2</sub>P/OMM-CoN-C

heterostructure demonstrated a 3D ordered interconnected macro/mesoporous structure, which can provide a larger surface area and facilitate the mass/charge diffusion on the heterointerface. Zhang et al. reported a simple and effective approach to prepare well-dispersed, highly active TMP nanoparticles incorporated in a nonporous carbon matrix with P-containing biomass as the phosphorous source.<sup>[165]</sup> For this, metal oxide nanoparticles were first grown on the carbonaceous matrix by a hydrothermal reaction, and then the C/TMP heterostructures were obtained by pyrolysis at high temperatures. With this strategy, a variety of C/TMP heterostructures were prepared, such as  $\text{Co}_2\text{P}/\text{C}$ ,  $\text{Mn}_2\text{P}/\text{C}$ ,  $\text{Ni}_2\text{P}/\text{C}$  and  $\text{Zn}_3\text{P}_2/\text{C}$ , which all demonstrate high activity and stability for the HER. Zhou et al. prepared a  $\text{Ni}_3\text{S}_2/\text{Ni}_2\text{P}$  heterostructure on NF by simultaneous phosphorization and sulfurization of the NF at low temperature using a mixture of  $\text{NaPO}_2\text{H}_2 \cdot \text{H}_2\text{O}$  and S as the phosphorous and sulfurs source, respectively.<sup>[166]</sup> Chang and coauthors synthesized heterostructured  $\text{Ni}_{12}\text{P}_5/\text{Ni}_3(\text{PO}_4)_2$  hollow spheres ( $\text{Ni}_{12}\text{P}_5/\text{Ni}_3(\text{PO}_4)_2\text{-HS}$ ) by a hydrothermal reaction.<sup>[167]</sup> Furthermore, Zhou et al. prepared a bilayered Ni-Co-S/Ni-Co-P heterostructure on NF by a simple electrodeposition method.<sup>[227]</sup> The efficient contact at the Ni-Co-P/NF interface along with the porous Ni-Co-S surface leads to a faster charge transfer, thus improving the catalytic activity. Similar results were also reported for the construction of heterostructured  $\text{NiCoP}@ \text{NNCs}$  (NNCs: nickel nanocones)<sup>[38]</sup> and  $\text{Fe}_3\text{O}_4\text{-CoP}_x/\text{TiN}$ .<sup>[168]</sup> Meanwhile, Yu et al. prepared a  $\text{FeP}/\text{Ni}_2\text{P}$  heterostructure on NF by chemical vapor deposition (CVD).<sup>[169]</sup> The mass loading of the TMP-based heterostructures on the NF can be controlled by changing the amount of the immersion-phosphorization cycles used.

In this case, some preparation methods may meet the specific requirements in the preparation and application of TMP-based heterostructures, such as ordered structure, mild preparation conditions and certain sample forms (e.g. films). But they may have a higher demand for the preparation conditions or required equipment, such as room temperature and CVD. It should be mentioned that atomic layer deposition (ALD) has received numerous attention owing to its specific advantage of conformal deposition of ultrathin films on the flat

as well as complex 3D substrates with strong interaction.<sup>[170,171]</sup> Unfortunately, TMP-based electrocatalysts prepared by ALD have not yet been reported up to now.

## **2.6 Bifunctional TMP-Based Heterostructures for Efficient Water Splitting**

In this section, the latest progress of the preparation of TMP-based heterostructures and their bifunctional properties, as well as the involved reaction mechanisms for overall water splitting with enhanced catalytic activities will be summarized and discussed in detail according to the different materials classes that were coupled with TMP-based catalysts in the heterostructure.

### **2.6.1 C/TMP Heterostructures**

Recently, carbon-based materials employed as electrocatalysts for water splitting have shown fascinating prospects for this field owing to its excellent conductivity, tunable molecular structures and composition chemistry.<sup>[172–175]</sup> However, carbon-based catalysts still suffer from insufficient activity compared with metal-based electrocatalysts, requiring a higher overpotential to deliver a standard current density of  $10 \text{ mA cm}^{-2}$ . However, carbon-based materials do play a vital role in carbon/transition metals phosphides (C/TMP) heterostructured catalysts to improve the catalytic activity, which can increase the accessible active sites, accelerate the electron and mass transfer and optimize the adsorption of intermediates. Generally, C/TMP heterostructures can be divided into two categories according to the morphology and composition of the prepared heterostructure: i) TMP catalysts encapsulated in carbon-based materials and ii) TMP anchored on the surface of carbon-based materials. For example, Pu et al. reported a general strategy for the synthesis of a series of TMP ( $\text{Fe}_2\text{P}$ ,  $\text{FeP}$ ,  $\text{Co}_2\text{P}$ ,  $\text{CoP}$ ,  $\text{Ni}_2\text{P}$ , and  $\text{Ni}_{12}\text{P}_5$ ) nanoparticles (NPs) embedded in an N-doped carbon (NC) matrix by a pyrolysis method.<sup>[176]</sup> The prepared C/TMP heterostructures demonstrated improved activities and durability for both the HER and the OER as compared to their TMP counterparts due to the synergistic effect of the C/TMP heterostructure and effective protection against corrosion by C. Among those prepared phases, the  $\text{Ni}_2\text{P}@NC$  exhibits the best performance with an overpotential of  $\sim 138 \text{ mV}$  for HER in  $0.5 \text{ M H}_2\text{SO}_4$  and  $\sim 320 \text{ mV}$  for OER in  $1 \text{ M}$

KOH. Subsequently, Pan and coauthors synthesized MOF-derived CoP nanoparticles embedded in an N-doped carbon nanotube hollow polyhedron (CoP/NCNHP) as shown in **Figure 2-7(a)**.<sup>[161]</sup> The heterostructured CoP/NCNHP catalyst demonstrated an outstanding bifunctional electrocatalytic performance for both the HER and the OER as well as a cell voltage of 1.64 V was required to achieve a current density of 10 mA cm<sup>-2</sup> for full water splitting. X-ray absorption near edge structure (XANES) spectra (Figure 2-7(b)) indicates that Co in the CoP/NCNHP heterostructure carried a positive charge with a valence state between 2+ and 3+, and the extended X-Ray absorption fine structure (EXAFS) spectra further confirmed the formation of CoP embedded in the NCNHP. The DOS (Figure 2-7(c)) and charge transfer images (Figure 2-7(d, e)) obtained by DFT calculation show that the electron transfer from NCNHP to CoP increases the electronic states of the Co *d*-orbital around the Fermi level, which benefits the adsorption of H\*. The  $\Delta G_{H^*}$  of CoP/NCNHP was calculated to be -0.22 eV, which favors the adsorption and desorption steps (Figure 2-7(f)) thus facilitating the catalytic activity. Bai and coauthors prepared H-CoP/C heterostructure demonstrated the best bifunctional activity for HER ( $\eta_{10}$  (overpotential at 10 mA cm<sup>-1</sup>) = 111 mV in 0.5 M H<sub>2</sub>SO<sub>4</sub>) and OER ( $\eta_{10}$  = 210 mV in 1 M KOH).<sup>[105]</sup> Additionally, the Ni-Co bimetallic phosphide nanoflakes encapsulated in N-doped graphene (FCP@NG)<sup>[177]</sup> and porous honeycomb Ni-Co-Fe trimetallic phosphide embedded in amorphous carbon (NiCoFeP/C)<sup>[178]</sup> were also been prepared and exhibited excellent bifunctional electrocatalytic activity for OER and HER.

For the case of TMP anchored on the surface of carbon-based material, Hou et al. reported that the bifunctional property for overall water splitting of CoP nanoparticles can be enhanced by coupling with N-doped CNTs (CoP-CNT).<sup>[179]</sup> The prepared CoP-CNT presented improved HER ( $\eta_{10}$  = 215 mV) and OER ( $\eta_{10}$  = 330 mV) activity in 0.1 M NaOH electrolyte owing to the synergistic effect between CoP and CNT resulting in increased amount of accessible active sites and accelerated charge transfer near the heterostructure interface. Subsequently, Huang et al. prepared ultrathin Ni-Co bimetallic nanosheets anchored on carbon nanotubes (NiCo<sub>2</sub>P<sub>x</sub>/CNTs) according to the process shown in Figure 2-7(g).<sup>[150]</sup> The obtained NiCo<sub>2</sub>P<sub>x</sub>/CNTs demonstrated a remarkably enhanced bifunctional activity for HER ( $\eta_{10}$  = 47



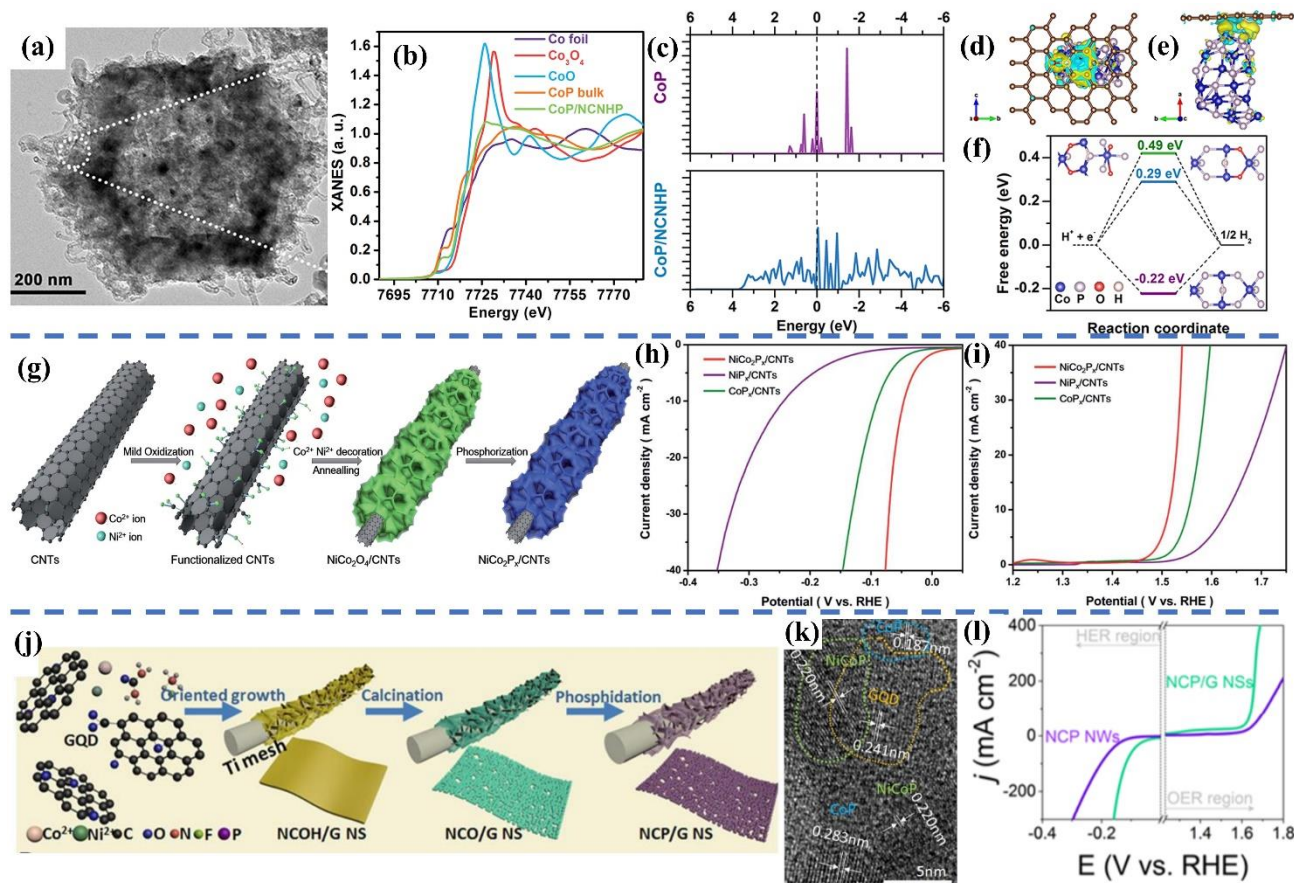


**Figure 2-7.** (a) TEM image of the CoP/NCNHP catalyst. (b) XANES spectra of at the Co K-edge of the CoP/NCNHP, CoP bulk, CoO, and  $\text{Co}_3\text{O}_4$  samples, and Co foil. (c) Calculated DOS curves for pure CoP and CoP/NCNHP. (d, e) Charge density distribution images of CoP/NCNHP: (d) top and (e) side views. (f) Calculated free energy diagram of the HER on CoP, surface-oxidized 50% CoP, and surface-oxidized 100% CoP, respectively. Reproduced with permission.<sup>[189]</sup> Copyright 2018, American Chemical Society. (g) Schematic illustration of the synthetic route for  $\text{NiCo}_2\text{P}_x/\text{CNTs}$ . (h, i) LSV for the HER (h) and the OER (i) of  $\text{NiCo}_2\text{P}_x/\text{CNTs}$ ,  $\text{NiP}_x/\text{CNTs}$  and  $\text{CoP}_x/\text{CNTs}$ . Reproduced with permission.<sup>[179]</sup> Copyright 2018, The Royal Society of Chemistry. (j) Schematic illustration of the fabrication procedure of NCP/G NSs on TiM. (k) High-resolution TEM images of NCP/G nanosheet. (l) Polarization curves of NCP/G NSs and NCP NWs with a scan rate of  $2 \text{ mV s}^{-1}$  in  $1.0 \text{ M KOH}$ . Reproduced with permission.<sup>[212]</sup> Copyright 2018, Elsevier Ltd.



mV,  $67.03 \text{ mV dec}^{-1}$ ) and OER ( $\eta_{10} = 284 \text{ mV}$ ,  $56 \text{ mV dec}^{-1}$ ) as compared to NiP<sub>x</sub>/CNTs and CoP<sub>x</sub>/CNTs (Figure 2-7(h, i)) owing to the synergetic effect of Ni and Co in the NiCo<sub>2</sub>P<sub>x</sub>/CNTs heterostructure. The enhanced performance of heterostructured NiCo<sub>2</sub>P<sub>x</sub>/CNTs also indicates that the alloying of TMP is an effective way to improve their bifunctional activity of C/TMP heterostructures. Similarly, the NiCoP was coupled with reduced graphene oxide (rGO) and the resulted heterostructured NiCoP/rGO exhibited an enhanced bifunctional activity with a cell voltage of  $1.59 \text{ V}$  (@  $10 \text{ mA cm}^{-2}$ ) and remarkable durability of  $75 \text{ h}$  for overall water splitting in basic media.<sup>[180]</sup> Li et al. also anchored the Fe-Ni bimetallic phosphide on 3D strutted graphene (FeNiP/SG).<sup>[181]</sup> The electrolyzers employing FeNiP/SG as cathode and anode demonstrated excellent overall water splitting performance with a potential of  $1.54 \text{ V}$  to deliver a current density of  $10 \text{ mA cm}^{-2}$ , which resulted from the shifted-up *d* states caused by iron incorporation and the synergistic effect between FeNiP and SG.

The performance of C/TMP heterostructure can be further enhanced by nonmetal doping on carbon-based materials. For example, Zhang et al. prepared mixed TMP embedded in N-doped carbon.<sup>[182]</sup> The introduction of N into the carbon matrix leads to a slight charge transfer from C to N and an increased conductivity of the carbon matrix, thus resulting in enhanced OER activity. Yu et al. synthesized hollow CoP nanoparticle/N-doped graphene (CoP<sub>h</sub>/NG) heterostructure as highly active and stable bifunctional catalysts for overall water splitting.<sup>[183]</sup> Compared to the case without N doping, the prepared CoP<sub>h</sub>/NG showed an enhanced activity for HER ( $\eta_{10} = 83 \text{ mV}$ ) and OER ( $\eta_{10} = 262 \text{ mV}$ ). The N doping not only increases the interfacial effect between CoP and N-doped graphene facilitating charge transfer near the interface but also provides additional active sites of Co-N for OER/HER. Similar to N doping, the P and S doping were also been investigated and were found to effectively tuning the electronic structure of C/TMP for enhanced OER/HER activity.<sup>[184,185]</sup>

Additionally, the preparation of heterostructures by combining TMP with macroscopic conductive substrates can further increase the amount of accessible active sites and accelerate the mass transfer, thus enhancing the bifunctional catalytic activity. For example, Tian et al. coupled their graphene quantum dot (GQD) modified NiCo<sub>2</sub>P<sub>2</sub> heterostructure (NCP/G NSs)

with a Ti mesh according to the preparation process shown in Figure 2-7(j).<sup>[186]</sup> The heterostructured NCP/G nanosheets are shown in Figure 2-7(k). The prepared NCP/G/Ti heterostructure catalysts demonstrated an outstanding bifunctional activity for HER ( $\eta_{100} = 119$  mV) and OER ( $\eta_{100} = 400$  mV), which is better than the NCP/Ti counterpart (Figure 2-7(l)). The enhanced bifunctional performance is benefited from the synergistic effect between NCP and GQD and enhanced mass transfer resulting from the Ti mesh substrate. Subsequently, Ni<sub>2</sub>P encapsulated in graphene on carbon cloth (CC) was also prepared via a simple annealing treatment of designed deep eutectic solvent.<sup>[187]</sup> The obtained heterostructured Ni<sub>2</sub>P@G/CC catalysts showed excellent overall water splitting performance with a cell voltage of 1.51 V to reach a current density of 10 mA cm<sup>-2</sup>. Similarly, Ahn and coauthors directly grew nickel-rich bimetallic phosphide encapsulated in N-doped carbon (NiBMP/@N<sub>x</sub>C) on nickel foam (NF).<sup>[188]</sup> The as-prepared heterostructured NiBMP/@N<sub>x</sub>C inhibited excellent bifunctional activity for HER ( $\eta_{20} = 67$  mV), OER ( $\eta_{20} = 201$  mV) and overall water splitting (1.46 V @ 10 mA cm<sup>-2</sup>) in alkaline media, which is superior to other C/TMP based electrocatalysts as summarized in Table 2-1. Very recently, Cao et al. reported similar results obtained by Ni<sub>x</sub>Co<sub>2-x</sub>P@NC (0 < x < 2) nanowall arrays (NA) on NF.<sup>[112]</sup> The optimized NiCoP@NC/NF demonstrated outstanding performance for both the HER ( $\eta_{10} = 37$  mV) and the OER ( $\eta_{50} = 305$  mV) owing to the special morphological and structural design, and electronic structure engineering. Therefore, coupling TMP-based electrocatalysts with carbon-based materials is an effective approach for the synthesis of advanced bifunctional catalysts for overall water splitting. The incorporation of carbon-based materials can increase the active sites, facilitate the charge transfer and optimize the adsorption of intermediates on the heterostructure interface thus leading to improved catalytic activities. The combination of C/TMP heterostructures with macrostructure conductive substrates can further improve the water splitting performance of the heterostructure owing to the increased number of active sites, accelerated mass transfer and strong interaction between C/TMP and the conductive substrates.

## 2.6.2 TM/TMP Heterostructures

Beyond the nonmetal-based electrocatalysts, transition metals (TM)-based electrocatalysts have been regarded as the promising alternative to replace noble metal-based electrocatalysts for efficient water splitting.<sup>[189,190]</sup> Compared to other metal compounds, pure TM normally demonstrates a worse performance for water splitting owing to their intrinsic active sites, electronic structure, crystallinity and adsorption ability of intermediates. However, pure TM exhibits excellent conductivity, which makes them very suitable to be used as activators for enhanced conductivity, accelerated charge and mass transfer and tuning the interface interaction. Therefore, the water splitting performance of TMP-based electrocatalysts can be enhanced by coupling with TM. For example, Chen et al prepared bifunctional Ni/NiP electrodes by direct phosphorization of NF.<sup>[191]</sup> The HRTEM image and selected area electron diffraction (SAED) confirm the formation of crystalline Ni<sub>8</sub>P<sub>3</sub> on the surface of NF (**Figure 2-8(a)**). Compared to Ni/NiS, the prepared Ni/NiP electrode demonstrated better activities for the HER ( $\eta_{10}=130$  mV,  $58.5$  mV dec<sup>-1</sup>), the OER ( $\eta_{30}=270$  mV,  $73.2$  mV dec<sup>-1</sup>) and overall water splitting ( $1.61$  V @  $10$  mA cm<sup>-2</sup>) in  $1$  M KOH (Figure 2-8(b)). The higher valence state of Ni in Ni/NiP can be beneficial to the adsorption of OH<sup>-</sup> and H<sup>\*</sup> and reduction of the energy barrier for the rate-determining step (RDS) during the HER and OER processes (Figure 2-8(c)). The larger bond length in Ni/NiP can facilitate more electron localization on P thus favoring the adsorption of H<sup>\*</sup> (Figure 2-8(d)). Similarly, You and coauthors synthesized a Ni<sub>2</sub>P/Ni/NF heterostructure by electrodeposition of Ni microsphere followed by phosphorization.<sup>[151]</sup> The prepared heterostructured Ni<sub>2</sub>P/Ni/NF demonstrates enhanced HER ( $\eta_{10}=98$  mV), OER ( $\eta_{10}=200$  mV) and overall water splitting ( $1.49$  V @  $10$  mA cm<sup>-2</sup>) performances in basic media, owing to the higher amount of accessible active sites originating from the nanostructured catalysts and the intimate interaction between the catalysts and the NF. Liu et al. prepared a Ni<sub>2</sub>P/Ni heterostructure with carbon coating (Ni<sub>2</sub>P/Ni@C) obtained by a MOF-template assisted method (Figure 2-8(e)) with enhanced HER activity.<sup>[157]</sup> The schematic model of the Ni<sub>2</sub>P/Ni heterointerface is shown in Figure 8(f). The corresponding DFT calculation reveals that the Ni<sub>2</sub>P/Ni heterostructure exhibits a lower  $\Delta G_{H^*}$  than Ni<sub>2</sub>P and Ni (Figure 2-8(g)) and

DOS calculation demonstrates that the Ni<sub>2</sub>P/Ni heterostructure is in a metallic state comprised with Ni<sub>2</sub>P and Ni with enhanced carrier density near the Fermi level (Figure 2-8(h)). Therefore, the strong synergistic effect between Ni<sub>2</sub>P and Ni could optimize the electronic structure, thus enhancing the electrocatalytic activity. Subsequently, Zhou et al. prepared an inverse opal architecture containing a Ni/Ni<sub>2</sub>P heterostructure with accelerated mass transfer for an improved bifunctional property, where the OER activity can be further enhanced by Fe doping (Fe:Ni<sub>2</sub>P).<sup>[192]</sup> In contrast, Chen et al. prepared an S-doped Ni/NiSP<sub>x</sub> heterostructure on NF (Ni/NiSP<sub>x</sub>/NF), which optimized the electronic structure of Ni active sites.<sup>[193]</sup> The prepared Ni/NiSP<sub>x</sub>/NF heterostructure electrodes required low overpotentials of only 46 and 231 mV for the HER and the OER, respectively, to reach a current density of 10 mA cm<sup>-2</sup>, in alkaline media. Except for NF, TM/TMP heterostructures were also formed on other 3D substrates with strong interaction. For instance, Sun et al. synthesized a Ni/Ni<sub>2</sub>P heterostructure on a 3D N, S dual modified microporous carbon framework (Ni/Ni<sub>2</sub>P@3DNSC).<sup>[194]</sup> The obtained Ni/Ni<sub>2</sub>P@3DNSC electrodes exhibited an enhanced catalytic activity with low overpotential of 92 and 231 mV for HER and OER, respectively, which can be attributed to the strongly coupled interface of Ni and Ni<sub>2</sub>P, synergistic effect between the Ni/Ni<sub>2</sub>P core and the graphitic carbon shell, and the unique 3D morphology. Moreover, CoP was also grown on Co foil (CoP/Co) by phosphorization of the oxidized Co foil which requires 1.71 V (@10 mA cm<sup>-2</sup>) for overall water splitting in an alkaline electrolyte.<sup>[195]</sup> Subsequently, Xue and coauthors prepared a Janus heterostructure of Co/CoP coated with C by a controllable vacuum-diffusion method, where the bifunctional activity of the prepared Co/CoP heterostructure can be tuned *via* controlling the amount of NaH<sub>2</sub>PO<sub>2</sub> used in the phosphorization process.<sup>[196]</sup> As shown in Figure 2-8(i), the optimized ratio of NaH<sub>2</sub>PO<sub>2</sub>/Co is 5 (denoted as Co/CoP-5), which exhibits the best bifunctional activity for the HER and the OER. The EDS line profile reveals the asymmetric distribution of P atoms along with the whole Co/CoP-5 nanoparticles (Figure 2-8(j)), the HRTEM image exhibits a clear interface between the Co “facet” and the CoP “facet” within one nanoparticle (Figure 2-8(k)). The electronic structure scheme (Figure 8(l)) indicates the electron redistribution at the interface of the Co/CoP heterostructure due to the Mott-Schottky effect,

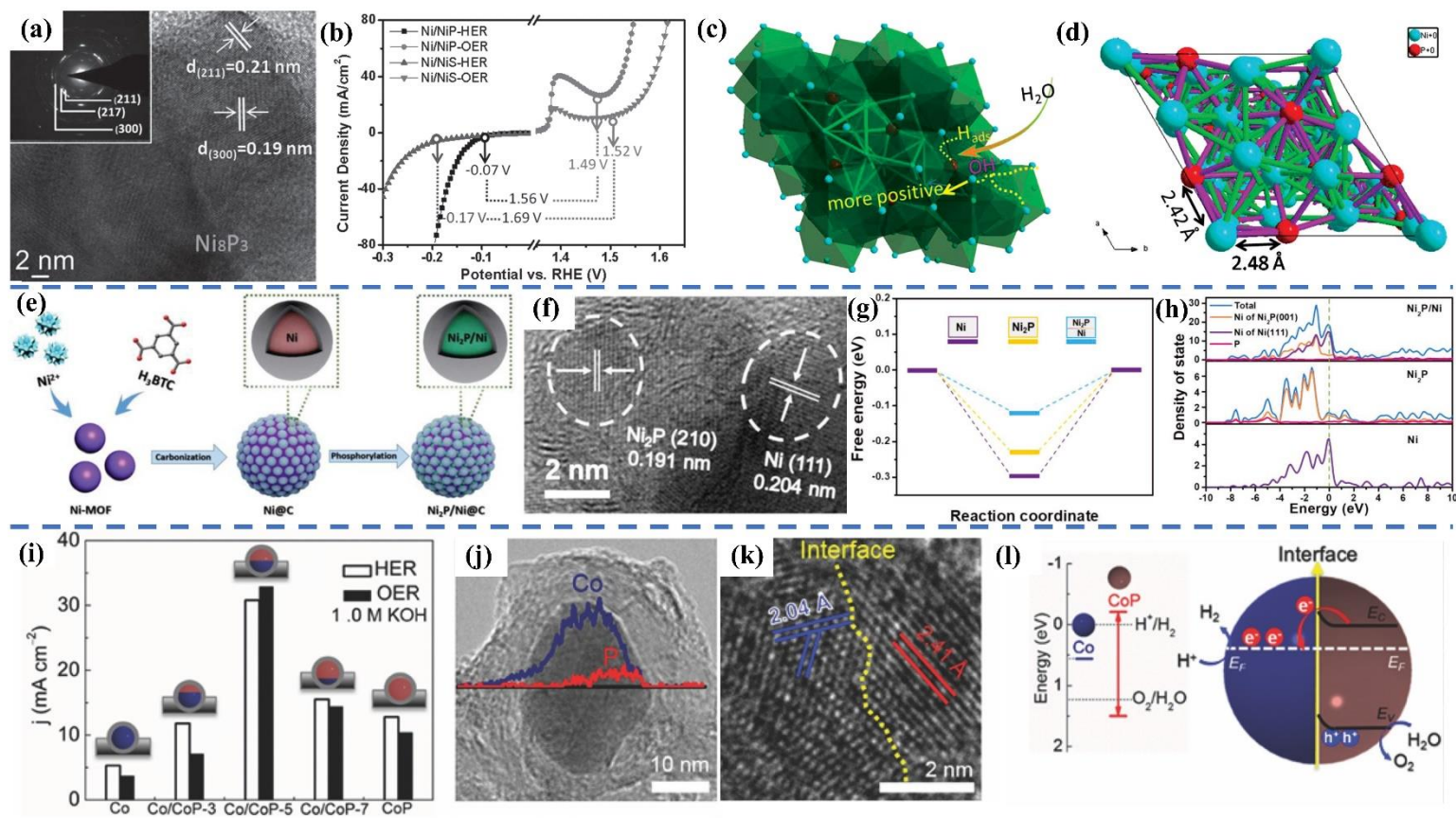


**Figure 2-8.** (a) HRTEM image of Ni/NiP and the corresponding SAED pattern (inset). (b) LSV curves of Ni/NiP and Ni/NiS for both HER and OER in the three-electrode alkaline system. (c) Schematic representation of the Volmer pathway mechanism in a unit cell of rhombohedral Ni<sub>3</sub>P<sub>3</sub> (d) Ni-P bond lengths in the unit cell edge as possible active sites. Reproduced with permission.<sup>[191]</sup> Copyright 2016, Wiley-VCH Verlag GmbH & Co. KGaA, Weinheim. (e) High-resolution TEM images of

Ni<sub>2</sub>P/Ni@C. (f) Schematic model of the Ni<sub>2</sub>P/Ni hybrid structure. (g) Calculated Gibbs free-energy diagram of Ni<sub>2</sub>P, Ni, and Ni<sub>2</sub>P/Ni hybrid-structure surfaces. (h) Calculated DOS curves for Ni<sub>2</sub>P/Ni, Ni<sub>2</sub>P and Ni. Reproduced with permission.<sup>[157]</sup> Copyright 2019, Wiley-VCH Verlag GmbH & Co. KGaA, Weinheim. (i) Current densities of Co, Co/CoP-x and CoP samples in a 1.0 M KOH electrolyte at -0.30 and 1.60 V versus RHE for HER and OER, respectively. (j) TEM image and compositional line profile EDS of a typical Co/CoP-5 nanoparticle. (k) The HRTEM image of a typical Co/CoP-5 nanoparticle, where the interface of Co (blue) and CoP (red) was marked with a yellow dashed line. (l) Electronic structures of metallic Co, CoP, and the Co/CoP based Mott-Schottky contact ( $E_f$ : work function;  $E_c$ : conduction band;  $E_v$ : valence band). Reproduced with permission.<sup>[196]</sup> Copyright 2017, Wiley-VCH Verlag GmbH & Co. KGaA, Weinheim.

which promotes the HER and OER performances of the Co/CoP heterostructure. It should be mentioned, that the prepared Co/CoP heterostructure not only demonstrates excellent overall water splitting in alkaline (1.45 V @ 10 mA cm<sup>-2</sup>) and neutral (1.51 V @ 10 mA cm<sup>-2</sup>) electrolytes but also shows a superior overall water splitting activity (1.89 V@1 mA cm<sup>-2</sup>) and stability (> 12 h) in acidic media. Accordingly, coupling TM with TMP is an effective approach to improve the interfacial synergistic effect, optimize the electronic structure, and to enhance the adsorption/desorption of intermediates resulting in significant promotion of the water splitting performance.

### 2.6.3 TMO/TMP Heterostructures

Transition metal oxides (TMO)-based electrocatalysts exhibiting excellent OER activity for efficient water splitting have attracted great research interest in this field.<sup>[5,197]</sup> However, TMO-based catalysts demonstrate limited HER performance due to their low conductivity, restricted electronic structure, and unfavorable adsorption ability of H\*.<sup>[198,199]</sup> Therefore, great efforts have been made to shape TMO into TMP for enhanced HER activities, which turned these engineered TMO into good candidates for overall water splitting. For example, Huang et al. prepared heterostructured FeO<sub>x</sub>/FeP nanorod (**Figure 2-9(a)**) with an improved HER activity in a wide-pH range electrolyte ( $\eta_{10} = 96, 79$  and  $128$  mV in neutral, acidic and alkaline electrolyte, respectively).<sup>[200]</sup> DFT calculations indicated that the prepared FeO<sub>x</sub>/FeP heterostructure with strong interaction not only facilitates the water adsorption and dissociation but is also optimal for the adsorption of H\* with the smallest value of  $\Delta G_{H^*}$  (Figure 2-9(b)), thus leading to an improved HER activity. Subsequently, Xu et al. performed a controllable surface reorganization of CoP nanowire arrays with O<sub>2</sub> plasma, and the resulted CoP@CoO<sub>x</sub> heterostructure realized a great improvement by decreasing the overpotential by 180 mV in order to reach a current density of 100 mA cm<sup>-2</sup>.<sup>[49]</sup> Meanwhile, the OER activity of TMO-based electrocatalysts can be also enhanced after coupled with TMP-based electrocatalysts. Hu and coauthors synthesized a Fe containing cobalt phosphide/cobalt oxide (Fe-CoP/CoO) heterostructure with superior OER activity ( $\eta_{10} = 219$  mV in 1 M KOH) owing to the optimized electronic structure and activated electronic coupling interface of the Fe-CoP/CoO

heterostructure (Figure 2-9(c)).<sup>[149]</sup> The DFT calculation further indicated that the redistribution of electrons (Figure 2-9(d)) and the facilitated OH<sup>-</sup> adsorption near the interface of the Fe-CoP/CoO heterostructure thus optimizes the Gibbs free energies of the RDS for the OER. Recently, Li et al. also reported similar results by directly growing a NiP-Al<sub>2</sub>O<sub>3</sub> heterostructure on NF (NiP-Al<sub>2</sub>O<sub>3</sub>/NF).<sup>[104]</sup> The as-prepared heterostructured NiP-Al<sub>2</sub>O<sub>3</sub>/NF exhibited excellent OER activity with an overpotential of 193 mV at 10 mA cm<sup>-2</sup> in a 1 M KOH electrolyte. Cheng et al. studied the enhanced OER activity of a Fe<sub>2</sub>O<sub>3</sub>@Ni<sub>2</sub>P/Ni(PO<sub>3</sub>)<sub>2</sub> heterostructure by operando Raman spectroscopy. They found that the in-situ formed amorphous NiOOH and FeOOH structures on the surface of the heterostructure acted as the active phases and contributed to the obtained high performance during the OER process.<sup>[201]</sup> Afterwards, Yu et al. synthesized heterostructured CoP nanoclusters encapsulated in an amorphous CoO<sub>x</sub> plate (CoP@a-CoO<sub>x</sub>).<sup>[114]</sup> Due to the synergistic effect between the CoP nanoclusters and the amorphous CoO<sub>x</sub> in the prepared heterostructure, the CoP@a-CoO<sub>x</sub> electrodes exhibit excellent bifunctional HER/OER activities and the electrolyzers using CoP@a-CoO<sub>x</sub> as both cathode and anode electrode delivered 1.66 V to reach a current density of 10 mA cm<sup>-2</sup> in an alkaline electrolyte. A self-supported amorphous Ni-P alloy on CuO nanowire arrays on Cu foam (CuO@Ni-P NA/CF) was prepared by Chang et al.<sup>[202]</sup> The core-shell heterostructure of CuO@Ni-P is shown in Figure 2-9(e, f). The resulting CuO@Ni-P NA/CF heterostructure exhibits enhanced HER ( $\eta_{30} = 106$  mV) and OER ( $\eta_{30} = 275$  mV) activity in 1 M KOH as compared to CuO NA/CF and Ni-P/CF (Figure 2-9(g, h)) due to the synergistic effect of CuO and Ni-P. A cell voltage of 1.71 V was required to reach a current density of 30 mA cm<sup>-2</sup> by water electrolyzers employing CuO@Ni-P NA/CF as both cathode and anode. Subsequently, a more active Ni<sub>2</sub>P@FePO<sub>x</sub> heterostructure was synthesized by extracting Ni from NiFe-LDH.<sup>[145]</sup> Figure 2-9(i) demonstrates the heterostructure morphology of prepared Ni<sub>2</sub>P@FePO<sub>x</sub>. DFT calculation suggests that the heterostructured Ni<sub>2</sub>P@FePO<sub>x</sub> interface decreased the  $\Delta G_{H^*}$  to a value close to zero (Figure 2-9(j)), and thus increased the HER activity. They further calculated the difference in binding energy between OH and O ( $\Delta E_{OH} - \Delta E_O$ ) as the descriptor to investigate the catalytic mechanism and the resulting volcano



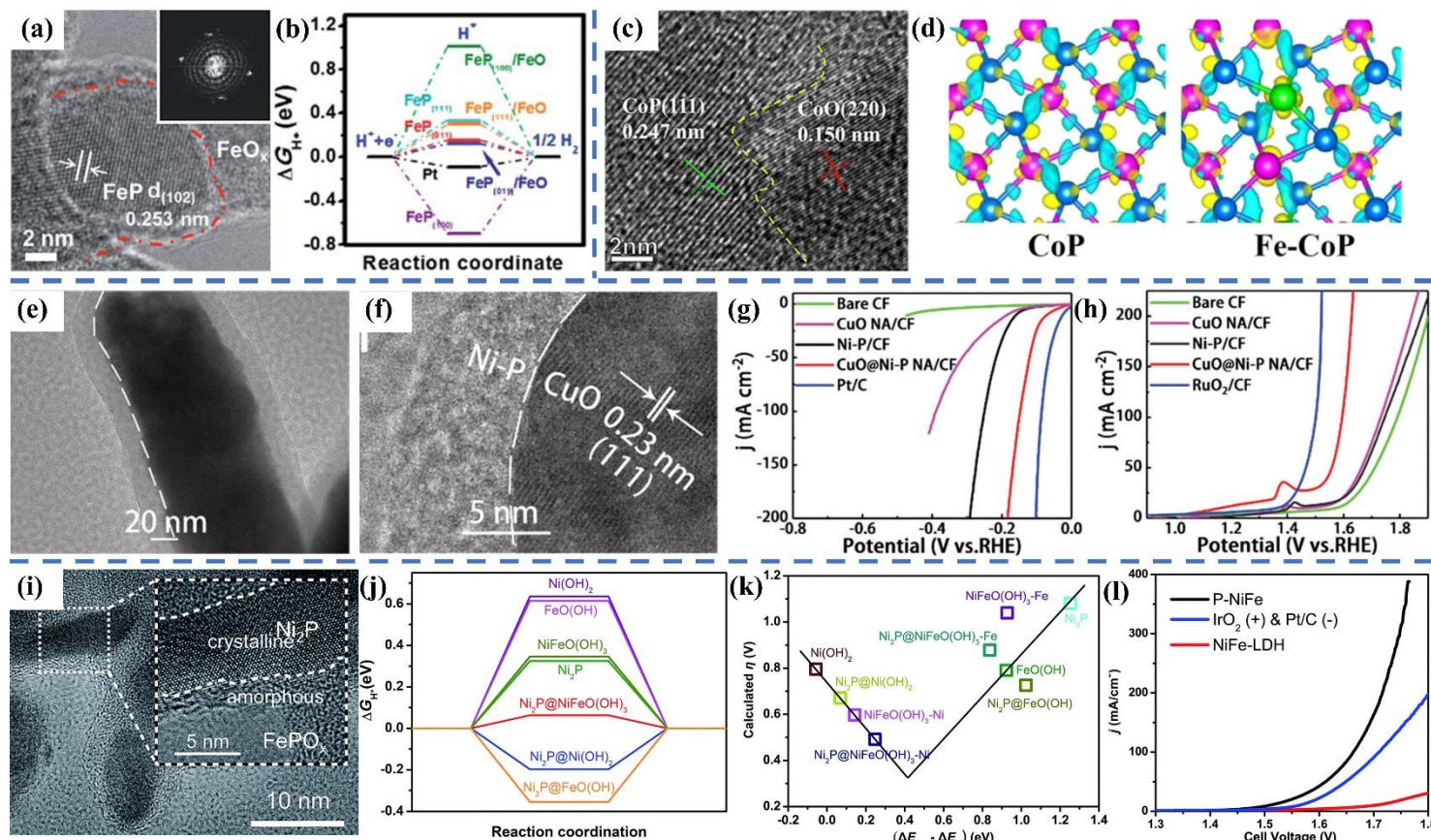


**Figure 2-9.** (a) HRTEM image of Fe-O-P NRs. The inset shows the FFT pattern. (b) The  $\Delta G_{H^*}$  diagrams for the FeP/FeO interface. Reproduced with permission.<sup>[200]</sup> Copyright 2018, The Royal Society of Chemistry. (c) HRTEM images of Fe-CoP/CoO (the green and red dotted areas represent the CoP domains and CoO domains, respectively. the interface between CoP and CoO is labeled with a yellow imaginary line). (d) The charge density distributions of CoP and Fe-CoP, respectively. Reproduced with permission.<sup>[149]</sup> Copyright 2018, Elsevier Ltd. (e, f) TEM and HRTEM images of a CuO@Ni-P nanowire array on Cu foam (NA/CF). (g, h) LSV curves

of CuO@Ni-P NA/CF for the HER (g) and the OER (h) in 1.0 M KOH with a scan rate of  $5 \text{ mV s}^{-1}$ . Reproduced with permission.<sup>[202]</sup> Copyright 2018, The Royal Society of Chemistry. (i) TEM image of a  $\text{Ni}_2\text{P}@FePO_x$  sample. (j) Free energy of  $H^*$  adsorption on different catalysts by DFT calculations. (k) A volcano plot of calculated overpotential *versus* the differences in binding energies between OH and O on the simulated surfaces of different catalysts:  $\text{NiFeO}(\text{OH})_3\text{-Ni}$  and  $\text{Ni}_2\text{P}@NiFeO}(\text{OH})_3\text{-Ni}$  represent the catalytic active sites for Ni, while  $\text{NiFeO}(\text{OH})_3\text{-Fe}$  and  $\text{Ni}_2\text{P}@NiFeO}(\text{OH})_3\text{-Fe}$  represent the catalytic active sites for Fe. (l) LSV curves of P-NiFe (black) and NiFe-LDH (red) as HER and OER bifunctional catalysts in 1.0 M KOH solution for overall water splitting.  $\text{IrO}_2$  and Pt/C as OER and HER benchmarks were measured for comparison (blue). Reproduced with permission.<sup>[145]</sup> Reproduced under the terms of the Creative Commons CC-BY License.<sup>[145]</sup> Copyright 2018, F. Zhang et al., published by the Royal Society of Chemistry.



plot of overpotential *versus*  $\Delta E_{OH}-\Delta E_o$  is shown in Figure 2-9(k). According to the calculated results, the Ni<sub>2</sub>P@NiFeO(OH)<sub>3</sub> heterostructure is closest to the volcano summit, indicating that this heterostructure processes optimal binding energies with the intermediates for improving its OER activity (Figure 2-9(l)). Excellent overall water splitting performance was achieved by heterostructured Ni<sub>2</sub>P@FePO<sub>x</sub> electrocatalysts with a cell voltage of 1.5 V at 10 mA cm<sup>-2</sup> in an alkaline electrolyte. Furthermore, the bimetallic NiCoO<sub>x</sub>/Ni<sub>2</sub>P<sup>[50]</sup> and NC-NiFeO<sub>x</sub>@NiFe-P,<sup>[203]</sup> as well as trimetallic Ni<sub>2</sub>P@NiFeAlO<sub>x</sub><sup>[144]</sup> were also prepared with excellent bifunctional catalytic activities for overall water splitting. Therefore, constructing TMO/TMP is an effective strategy for tuning the electronic structure and optimizing the intermediates adsorption thus improving the bifunctional property for overall water splitting. This strategy may offer a new way to combine recently reported acid-resistant metal oxide-based OER catalysts<sup>[204–207]</sup> with TMP to improve the overall water splitting in acidic media.

#### 2.6.4 TMH/TMP Heterostructures

Transition metal hydroxides (TMH) have been seen as a promising type of electrocatalyst to replace noble metal-based electrocatalysts for efficient water splitting. Among those TMH, the layered double hydroxides (LDH) attracted increasing attention in the fields of electrochemical energy storage and conversion owing to their facile tunability in composition and morphology.<sup>[208]</sup> For example, NiFe LDH electrocatalysts are regarded as one of the best performing non-noble metal OER electrocatalysts in basic media with excellent stability in alkaline electrolytes.<sup>[209]</sup> The high OER activity of NiFe LDH electrocatalysts is generally attributed to the synergistic effect of the incorporation of Fe into NiOOH.<sup>[210]</sup> Although NiFe LDH has also been reported to exhibit HER performance, it is still not comparable to the state-of-the-art nonprecious HER electrocatalysts.<sup>[211]</sup> As discussed above, metal oxide/(oxy)hydroxide *in-situ* generated on the TMP surface enables the high OER performance of TMP-based electrocatalysts. Meanwhile, the NiFe LDH has been successfully combined with NiCo<sub>2</sub>O<sub>4</sub>, NiCo<sub>2</sub>S<sub>4</sub>, and CoSe<sub>0.85</sub>.<sup>[212–214]</sup> The resulting heterostructured NiCo<sub>2</sub>O<sub>4</sub>/NiFe LDH/NF, NiCo<sub>2</sub>S<sub>4</sub>/NiFe LDH/NF and EG/CoSe<sub>0.85</sub>/NiFe LDH (EG: exfoliated graphene foil) demonstrated improved bifunctional performance for both the HER and the OER. DFT

calculation revealed a strong interaction and charge transfer between both counterparts, which tune the interfacial electronic structure and surface reactivity.<sup>[212]</sup> Therefore, coupling the OER-preferred TMH with TMP through heterostructure design with strong interaction and favored interfacial engineering may offer a new strategy to improve the bifunctional property and stability of TMP-based electrocatalysts for efficient water splitting. Inspired by this, our group prepared a bifunctional heterostructure assembly of NiFe LDH nanosheets on NiCoP nanowires as shown in **Figure 2-10(a-b)**.<sup>[53]</sup> The as-prepared NiFe LDH@NiCoP/NF electrodes have a well-established heterostructure with more intensive interface engineering to offer more surface area and to accelerate the mass transfer during OER/HER. Benefiting from the synergistic effect of the heterostructure, the NiFe LDH@NiCoP/NF electrodes required overpotentials of only 120 and 220 mV to reach current densities of 10 mA cm<sup>-2</sup> for the HER and the OER, respectively. Additionally, a cell voltage of 1.57 V (@10 mA cm<sup>-2</sup>) was required for overall water splitting in 1 M KOH (Figure 2-10(c)) with excellent stability for at least 100 h. After the long-term measurement, the NiFe LDH@NiCoP/NF can maintain the morphology and crystalline phase of the NiCoP nanowires owing to the synergistic effect and the strong interface interaction in the heterostructure (Figure 2-10(d)). The surface of NiFe LDH@NiCoP was enriched with hydroxides and oxides/oxyhydroxides during the HER and the OER, which served as the active sites enabling the superior activities. Similar results have also been reported by Zhou et al. by coupling the NiFe LDH with NiCoP nanosheet arrays by an electrosynthesis method.<sup>[155]</sup> The optimized CoNiP@NiFe-LDH/NF electrodes required a cell voltage of only 1.44 V to reach a current density of 10 mA cm<sup>-2</sup>, which is superior to other nonprecious electrocatalysts summarized in Table 2-1. Yu and coauthors prepared amorphous NiFe LDH nanosheets decorated with 3D Ni<sub>5</sub>P<sub>4</sub>/NiP<sub>2</sub> nanoarrays.<sup>[154]</sup> The prepared Ni<sub>5</sub>P<sub>4</sub>/NiP<sub>2</sub>/NiFe LDH heterostructure simultaneously offers a better conductivity for faster charge transfer, larger surface areas for exposing more active sites, and a hierarchical heterostructure for rapid release of gas bubbles, thus contributing to outstanding overall water splitting performance with a cell voltage of 1.52 V (@10 mA cm<sup>-2</sup>) in alkaline media. Recently, He et al. modulated the electron density of a TMH/TMP heterostructure using the semiconductor charge redistribution

concept.<sup>[113]</sup> Here, a p-n junction was formed by CoP nanosheets arrays around by amorphous FeNi-LDH (FeNi-LDH/CoP/CC) prepared by an electrodeposition-phosphorization-electrodeposition process (Figure 2-10(e)). The large difference of  $E_f$  (Fermi energy) between FeNi-LDH and CoP attributes to a larger energy level shifting, which generates a strong space-charge region with a built-in potential of 1.45 V (Figure 2-10(f)). The formed strong space-charge region can work as the driving force to accelerate the electron transfer derived from  $\text{OH}^-$  in the basic electrolyte to the VB of FeNi-LDH. As a result, the prepared FeNi-LDH/CoP/CC demonstrated an improved OER performance of  $350 \text{ mA cm}^{-2}$  ( $\eta = 254 \text{ mV}$ ), which is 10- and 100-fold higher than that of FeNi-LDH/CC and CoP/CC, respectively (Figure 2-10(g)). Apart from LDH, a heterostructure constructed by coupling  $\text{Co}(\text{OH})_2$  with FeP was also reported by Ding et al.<sup>[102]</sup> DFT calculation indicated that the  $\text{Co}(\text{OH})_2/\text{FeP}$  heterointerface favors the dissociation of  $\text{H}_2\text{O}$ , which can be the reason for the enhanced HER and OER activities. Furthermore, the bifunctional activity can also be enhanced by the incorporation of Ag. The morphology of the prepared  $\text{Co}(\text{OH})_2/\text{Ag}/\text{FeP}/\text{Ti}$  heterostructure electrode is shown in (Figure 2-10(h)) and the HRTEM image confirms the existence of FeP, Ag and  $\text{Co}(\text{OH})_2$  (Figure 2-10(i)). The prepared  $\text{Co}(\text{OH})_2/\text{Ag}/\text{FeP}/\text{Ti}$  electrode demonstrated improved OER and HER performance ( $\eta_{10} = 118 \text{ mV}$  for the HER and  $\eta_{10} = 236 \text{ mV}$  for the OER) in an alkaline electrolyte, which is superior to that of other counterparts (Figure 2-10(j, k)). Recently, the negative charging of TMH/TMP heterostructures has been modulated by You et al.<sup>[215]</sup> Their DFT calculation revealed that the TMH/TMP heterostructure demonstrated strong electronic coupling that renders the TMP negatively charged, which facilitates the destabilization of water adsorption and dissociation. The optimal  $\text{sc-Ni}_2\text{P}^\delta/\text{NiHO}$  heterostructure exhibited a low overpotential of 138 mV to reach a current density of  $100 \text{ mA cm}^{-2}$  for HER in alkaline electrolyte. Accordingly, constructing a heterostructure with TMH- and TMP-based electrocatalysts is an attractive strategy to design and produce efficient nonprecious bifunctional electrocatalysts for overall water splitting. Thus, more effects should be focused on the exploration of more TMH/TMP heterostructures for efficient water splitting.

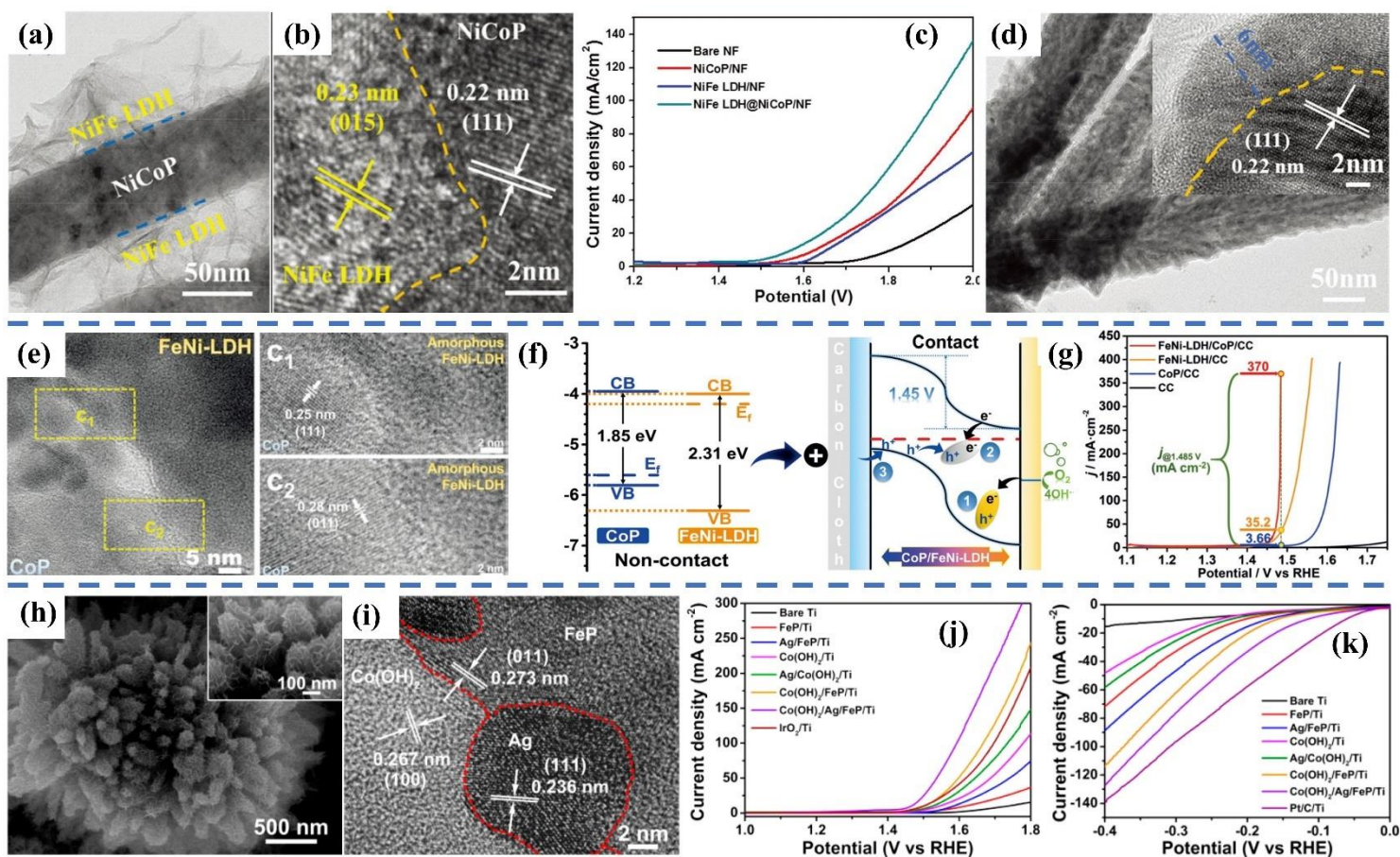


**Figure 2-10.** (a) TEM image of a NiFe LDH@NiCoP nanowire. (b) The HRTEM image of the NiFe LDH@NiCoP nanowire highlighting the interface between nanowire and nanosheets. (c) Polarization curve of the as-prepared electrocatalysts for overall water splitting in 1 M KOH. (d) TEM and HRTEM (inset) images of the NiFe LDH@NiCoP heterostructure after OER investigation. Reproduced with permission.<sup>[53]</sup> Copyright 2018, Wiley-VCH Verlag GmbH & Co. KGaA, Weinheim. (e) HRTEM image of FeNi-LDH/CoP NSs with (c<sub>1</sub>) and (c<sub>2</sub>) the corresponding lattice fringe images of FeNi-LDH/CoP NSs. (f) The energy diagrams of CoP and FeNi-LDH and the proposed mechanism for the electrocatalytic OER in the FeNi-LDH/CoP/CC p-n junction under the condition of applying enough potential via the external circuit. (g) LSV curves for the OER in the presence of FeNi-LDH/CoP/CC (red), FeNi-LDH/CC (orange), and CoP/CC (blue) in 1 M KOH electrolyte at a scan rate of 5 mV s<sup>-1</sup>. Reproduced with permission.<sup>[113]</sup> Copyright 2019, Wiley-VCH Verlag GmbH & Co. KGaA, Weinheim. (h) SEM images of Co(OH)<sub>2</sub>/Ag/FeP on Ti foil. (i) HRTEM image of Co(OH)<sub>2</sub>/Ag/FeP/Ti. (j, k) Electrocatalytic properties of different electrodes for the OER (j) and the HER (k) without iR correction. Reproduced with permission.<sup>[102]</sup> Copyright 2019, Wiley-VCH Verlag GmbH & Co. KGaA, Weinheim.

(a) TEM image of a NiFe LDH@NiCoP nanowire. (b) The HRTEM image of the NiFe LDH@NiCoP nanowire highlighting the interface between nanowire and nanosheets. (c) Polarization curve of the as-prepared electrocatalysts for overall water splitting in 1 M KOH. (d) TEM and HRTEM (inset) images of the NiFe LDH@NiCoP heterostructure after OER investigation. Reproduced with permission.<sup>[53]</sup> Copyright 2018, Wiley-VCH Verlag GmbH & Co. KGaA, Weinheim. (e) HRTEM image of FeNi-LDH/CoP NSs with (c<sub>1</sub>) and (c<sub>2</sub>) the corresponding lattice fringe images of FeNi-LDH/CoP NSs. (f) The energy diagrams of CoP and FeNi-LDH and the proposed mechanism for the electrocatalytic OER in the FeNi-LDH/CoP/CC p-n junction under the condition of applying enough potential via the external circuit. (g) LSV curves for the OER in the presence of FeNi-LDH/CoP/CC (red), FeNi-LDH/CC (orange), and CoP/CC (blue) in 1 M KOH electrolyte at a scan rate of 5 mV s<sup>-1</sup>. Reproduced with permission.<sup>[113]</sup> Copyright 2019, Wiley-VCH Verlag GmbH & Co. KGaA, Weinheim. (h) SEM images of Co(OH)<sub>2</sub>/Ag/FeP on Ti foil. (i) HRTEM image of Co(OH)<sub>2</sub>/Ag/FeP/Ti. (j, k) Electrocatalytic properties of different electrodes for the OER (j) and the HER (k) without iR correction. Reproduced with permission.<sup>[102]</sup> Copyright 2019, Wiley-VCH Verlag GmbH & Co. KGaA, Weinheim.

## 2.6.5 TMP/TMP Heterostructures

TMP/TMP heterostructures are also reported to have enhanced performances for the HER and the OER with strong synergistic effects. For example, Boppella et al. prepared a CoP/NiCoP/NC heterostructure that demonstrated an improved HER performance in electrolytes with a wide pH range ( $\eta_{10} = 60, 123$  and  $75$  mV in  $0.5$  M  $\text{H}_2\text{SO}_4$ ,  $1$  M PBS and  $1$  M KOH), respectively, which is superior to its counterparts.<sup>[216]</sup> Liu et al. prepared a  $\text{Ni}_2\text{P}$ - $\text{NiP}_2$  heterostructure with extremely enhanced HER performance ( $\eta_{10} = 59.7$  mV) in alkaline media.<sup>[93]</sup> DFT calculation indicated that  $\text{Ni}_2\text{P}$ - $\text{NiP}_2$  heterostructure exhibits a smaller  $\Delta G_{H^*}$  than the  $\text{Ni}_2\text{P}$  and  $\text{NiP}_2$  counterparts, enabling a preferable  $\text{H}^*$  adsorption. Correspondingly, Yan et al. synthesized a  $\text{Ni}_2\text{P}$ - $\text{VP}_2$ /NF heterostructure, which demonstrates an enhanced OER activity ( $\eta_{50} = 306$  mV,  $46$  mV  $\text{dec}^{-1}$ ).<sup>[141]</sup> DFT calculation revealed that the  $\text{Ni}_2\text{P}/\text{VP}_2$  heterostructure demonstrates a lower O species adsorption energy barrier ( $0.79$  eV) than that for  $\text{Ni}_2\text{P}$  ( $1.46$  eV), indicating a facilitated reaction kinetic on  $\text{Ni}_2\text{P}/\text{VP}_2$ .

Subsequently, Yu et al. prepared a bifunctional FeP/ $\text{Ni}_2\text{P}$  heterostructure electrocatalysts as shown in **Figure 2-11(a)**.<sup>[169]</sup> The as-prepared FeP/ $\text{Ni}_2\text{P}$  demonstrated an enhanced bifunctional property for water splitting that excellently drives both HER ( $\eta_{10} = 14$  mV) and OER ( $\eta_{10} = 154$  mV) in basic media (Figure 2-11(b, c)). Most importantly, an electrolyzer equipped with heterostructured FeP/ $\text{Ni}_2\text{P}$  electrodes as both the cathode and the anode simultaneously, required a cell voltage of  $1.42$  V to deliver a current density of  $10$  mA  $\text{cm}^{-2}$ , which outperforms the state-of-the-art  $\text{IrO}_2 \parallel \text{Pt}$  configuration and other TMP/TMP heterostructure electrocatalysts (Figure 2-11(d) and Table 2-1). Liu and coauthors further investigated the charge transfer and interfacial effect of a  $\text{Cu}_3\text{P}$ - $\text{Co}_2\text{P}$  heterostructure by DFT theoretical calculation.<sup>[142]</sup> The HRTEM image of the  $\text{Cu}_3\text{P}$ - $\text{Co}_2\text{P}$  heterostructure is shown in Figure 2-11(e). The crystal structures of  $\text{Cu}_3\text{P}$  with a quasi-layer structure in the  $[010]$  direction and  $\text{Co}_2\text{P}$  with polar planes in  $(001)$  obtained from the DFT calculation are shown in Figure 2-11(f, g). In the  $\text{Co}_2\text{P}$ - $\text{Cu}_3\text{P}$  heterostructure, the positive charge on the Cu atoms is increased from  $0.12$  to  $0.15$ - $0.16$  eV, whereas that on the Co atoms decreased from  $0.15$  to  $0.03$ - $0.04$  eV indicating a charge transfer from the Cu atoms to the Co atoms (Figure 2-11(h-j)). A lower

value of  $\Delta G_{H^*}$  was obtained at the interface of the Co<sub>2</sub>P-Cu<sub>3</sub>P heterostructure, revealing an optimized H<sup>\*</sup> adsorption ability (Figure 11(k)). Thus, the charge transfer from Cu<sub>3</sub>P to Co<sub>2</sub>P successfully tunes the electronic structure of the Co<sub>2</sub>P-Cu<sub>3</sub>P heterostructure and enhances its bifunctional activity for water splitting. Similar charge transfer and interfacial engineering were also reported for a CoP-FeP branched heterostructure.<sup>[217]</sup> Here, the electrons transfer from CoP to FeP owing to the built-in electric field originating from the lower work function of CoP and the bandgap arrangement of both materials (Figure 2-11(l, m)). The morphology change of the TMP/TMP heterostructures after long-time HER/OER measurements were investigated by Deng et al.<sup>[59]</sup> The initial morphology of their Co<sub>2</sub>P-Ni<sub>2</sub>P heterostructure is shown in Figure 2-11(n). Similar crystal fringes corresponding to Co<sub>2</sub>P and Ni<sub>2</sub>P were observed in the Co<sub>2</sub>P-Ni<sub>2</sub>P heterostructure after 3000 cycles of HER (Figure 2-11(o)). After long-time OER measurement (1000 cycles CV), an amorphous (ox)hydroxides layer with a thickness of ~8.7 nm was formed on the surface of the Co<sub>2</sub>P-Ni<sub>2</sub>P heterostructure (Figure 2-11(p)). The surface roughening and the *in-situ* formation of M-P-O and MOOH during HER/OER enabled the high catalytic performance of the Co<sub>2</sub>P-Ni<sub>2</sub>P/NF heterostructure. Other TMP/TMP heterostructure electrocatalysts, such as CoP/Co<sub>2</sub>P,<sup>[139]</sup> MoP/Ni<sub>2</sub>P/NF,<sup>[218]</sup> NiCoP@Cu<sub>3</sub>P/CF<sup>[219]</sup>, Ni<sub>2</sub>P-Ni<sub>5</sub>P<sub>4</sub><sup>[143]</sup> and so on were also prepared with enhanced overall water splitting performances. From the discussion above, the synergistic effect of the heterointerface could effectively tune the electronic structure and optimize the adsorption ability of intermediates on the interface of TMP/TMP heterostructures, thus remarkably enhancing the performance of TMP/TMP heterostructures for overall water splitting. It should be mentioned that the water splitting activities of heterostructured TMP/TMP electrocatalysts can be further enhanced by employing the strategies for improving the bifunctional property of TMP-based electrocatalyst.<sup>[23]</sup> More efforts should be made to design and prepare TMP/TMP electrocatalysts with remarkably enhanced overall water splitting activity and to study the surface reconstruction engineering in order to improve the stability of the heterostructured TMP/TMP electrocatalysts.



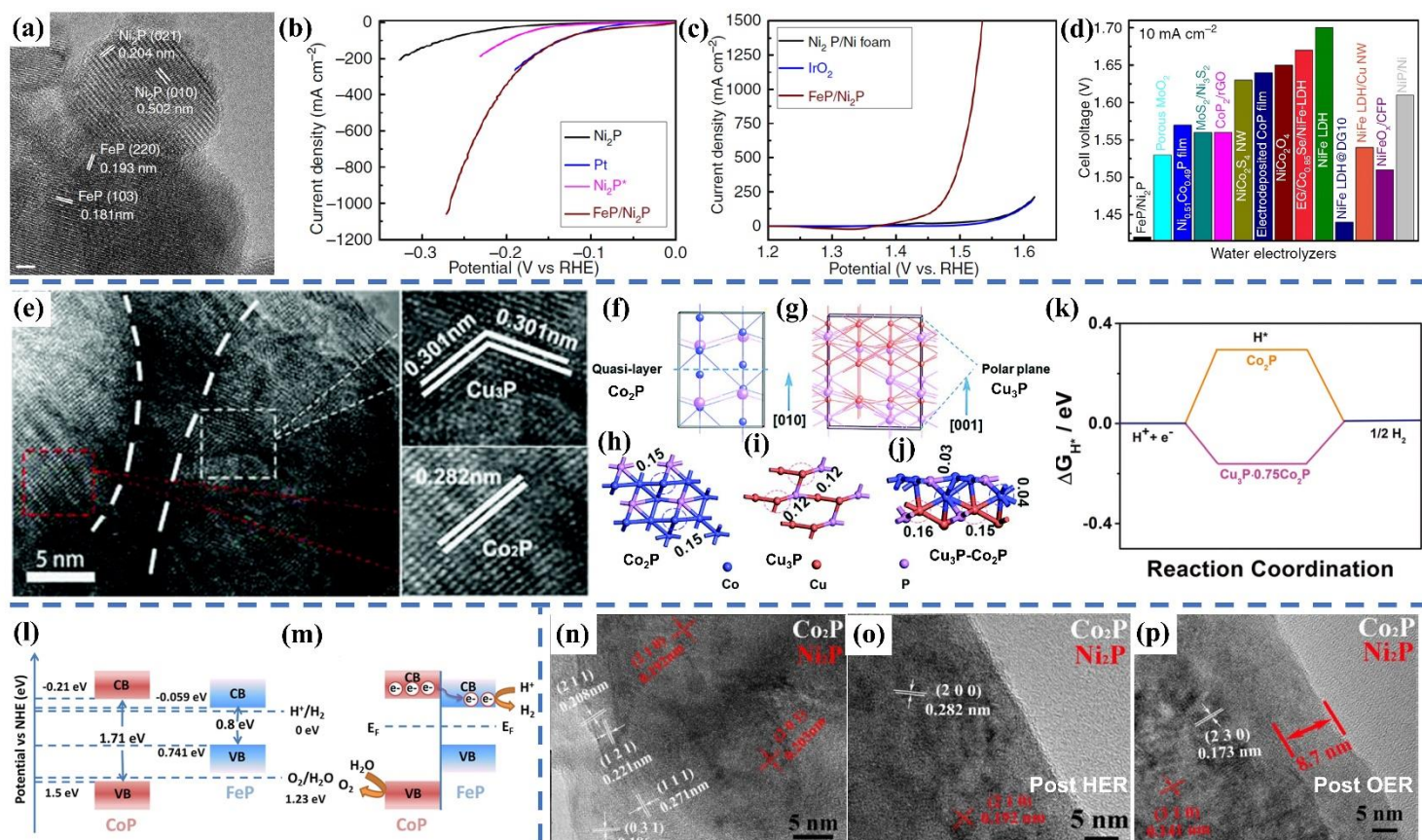


**Figure 2-11.** (a) A typical HRTEM image taken from the FeP/Ni<sub>2</sub>P catalysts. Scale bar, 2 nm. (b, c) Polarization curves recorded on different catalysts for the OER and the HER, respectively. (d) Comparison of the cell voltages to achieve 10 mA cm<sup>-2</sup> among different water alkaline electrolyzers in alkaline electrolytes. Reproduced under the terms of the Creative Commons CC-BY License.<sup>[169]</sup> Copyright 2018, F. Yu et al., published by Springer Nature. (e) The HRTEM image of a Cu<sub>3</sub>P·0.75Co<sub>2</sub>P heterostructure. (f, g) Crystal structure of (f) Co<sub>2</sub>P, indicating a quasi-layer structure in the [010] direction, and (g) Cu<sub>3</sub>P, showing polar planes in the [001] direction.

(h-j) The charge distribution in the theoretical models of (h) pure Co<sub>2</sub>P, (i) pure Cu<sub>3</sub>P and (j) Cu<sub>3</sub>P-Co<sub>2</sub>P nanocomposite, revealing charge transfer from Cu<sub>3</sub>P to Co<sub>2</sub>P. (k) HER free energy diagrams for Co<sub>2</sub>P and Cu<sub>3</sub>P·0.75Co<sub>2</sub>P. Reproduced with permission.<sup>[142]</sup> Copyright 2019, The Royal Society of Chemistry. (l) Schematic illustrations of the band structure of FeP and CoP before contact. (m) Charge transfer at the interface between CoP and FeP in the CoP-FeP heterostructure. Reproduced with permission.<sup>[217]</sup> Copyright 2018 American Chemical Society. (n) The HRTEM image of a single Co<sub>2</sub>P-Ni<sub>2</sub>P nanoparticle before HER and OER investigation. (o) HRTEM image of Co<sub>2</sub>P-Ni<sub>2</sub>P/NF after 3000 cycles of the HER. (p) HRTEM image of Co<sub>2</sub>P-Ni<sub>2</sub>P/NF after 1000 cycles of the OER. Reproduced with permission.<sup>[59]</sup> Copyright 2019 Elsevier Ltd.

### 2.6.6 TMS/TMP Heterostructures

Recently, earth-abundant transition metal sulfides (TMS) have attracted enormous attention as promising electrocatalysts for water splitting due to their tunable electronic, physical and chemical properties.<sup>[18,220,221]</sup> Compared to metal oxides and hydroxides, TMS exhibit a higher conductivity, which is crucial for electrochemical reactions.<sup>[222]</sup> Up to now, plenty of TMS-based electrocatalysts have been prepared and investigated, including MS, M<sub>2</sub>S, M<sub>3</sub>S<sub>4</sub>, MS<sub>2</sub>, bimetal sulfides (A<sub>1-x</sub>B<sub>x</sub>S<sub>y</sub>) and so on, where M represents the transient metal of Co, Ni, Cu, Fe, W, Mo, etc.; A and B are different metals; x and y are integers.<sup>[18,221]</sup> Similar to TMP-based electrocatalysts, some of the TMS-based electrocatalysts were also been evidenced to perform a bifunctional activity for overall water splitting.<sup>[223–225]</sup> Accordingly, heterostructures formed by coupling TMS-based and TMP-based electrocatalysts may demonstrate higher bifunctional electrochemical activities for overall water splitting. For example, Sun et al. prepared a high-active Ni<sub>2</sub>P/NiS heterostructure on carbon fiber paper (CP/Ni<sub>2</sub>P/NiS) through a facile hydrothermal seed growth process.<sup>[148]</sup> The Ni<sub>2</sub>P/NiS heterostructure not only provides a higher electrochemical surface area (ECSA) with more active sites, but also improves the surface wettability, thus benefiting to the HER. The prepared CP/Ni<sub>2</sub>P/NiS heterostructure demonstrated higher HER performance with an overpotential  $\eta_{10} = 103$  mV, which is superior to the single counterparts of Ni<sub>2</sub>P ( $\eta_{10} = 183$  mV) and Ni(OH)<sub>2</sub>/NiS ( $\eta_{10} = 268$  mV). Zhou et al. performed the DFT calculations to investigate the synergistic effect between Ni<sub>3</sub>S<sub>2</sub> and Ni<sub>2</sub>P in the heterostructure.<sup>[166]</sup> The DFT results indicated the strong coupling interactions between Ni<sub>3</sub>S<sub>2</sub> and Ni<sub>2</sub>P with lower  $\Delta G_{H^*}$  and H<sub>2</sub>O adsorption energy ( $\Delta E_{H_2O}$ ) and better conductivity than their single counterparts.

Subsequently, Zeng and coauthors grew 3D networked heterogeneous Ni<sub>2</sub>P/Ni<sub>3</sub>S<sub>2</sub> on NF *via* a typically GP (hydrothermal-phosphorization) method (**Figure 2-12(a)**).<sup>[146]</sup> An HRTEM image and corresponding SAED pattern of the Ni<sub>2</sub>P/Ni<sub>3</sub>S<sub>2</sub> heterostructure are shown in **Figure 2-12(b)**. The prepared heterostructured Ni<sub>2</sub>P/Ni<sub>3</sub>S<sub>2</sub>/NF exhibited superior bifunctional activity for HER ( $\eta_{10} = 80$  mV,  $65$  mV dec<sup>-1</sup>), OER ( $\eta_{10} = 210$  mV,  $62$  mV dec<sup>-1</sup>), and overall water splitting ( $V_{10} = 1.5$  V) activities in alkaline media (**Figure 2-12(c, d)**). The synergistic effect of Ni<sub>2</sub>P/Ni<sub>3</sub>S<sub>2</sub>



with strong electronic interaction contributes to the optimal  $\Delta G_{H^*}$  and  $\Delta E_{H_2O}$ , thus accelerating the whole electrochemical reaction kinetics. Very recently, Liang et al. further explored the interfacial engineering by building a NiPS<sub>3</sub>/Ni<sub>2</sub>P heterojunction with well-matched lattice *via* an *in-situ* epitaxial growth method.<sup>[226]</sup> The discontinued and randomly distributed interfaces of the NiPS<sub>3</sub>/Ni<sub>2</sub>P heterostructure at the nanoscale are revealed by HRTEM as indicated by the yellow dashed line in Figure 2-12(e, f) with the dominantly exposed (001) facets. The colored HRTEM image (Figure 2-12(g)) presents the nanoscale interface of NiPS<sub>3</sub> and Ni<sub>2</sub>P. The electrodes prepared through coating the heterostructured NiPS<sub>3</sub>/Ni<sub>2</sub>P electrocatalysts on GC (glassy carbon) or NF demonstrated excellent bifunctional activities for the HER (GC with 0.56 mg cm<sup>-2</sup>,  $\eta_{10} = 85$  mV, 85 mV dec<sup>-1</sup>), the OER (GC with 0.56 mg cm<sup>-2</sup>,  $\eta_{10} = 260$  mV, 78 mV dec<sup>-1</sup>) and the overall water splitting (NF with 1 mg cm<sup>-2</sup>,  $V_{50} = 1.65$  V) in 1 M KOH. These activities are all superior to their single counterparts as shown in Figure 2-12(h, i). DFT calculation based on the models as shown in Figure 2-12(j) indicated that the NiPS<sub>3</sub>/Ni<sub>2</sub>P heterostructure has a much smaller  $|\Delta G_{H^*}|$  than that of the pristine Ni<sub>2</sub>P and NiPS<sub>3</sub> (Figure 2-12(k)) and lower energy barrier for H<sup>\*</sup> adsorption (Figure 2-12(k), inset), which can be associated with the synergetic effect arising from the heterostructure interfaces. Calculation of the charge redistribution near the epitaxial interface of the NiPS<sub>3</sub>/Ni<sub>2</sub>P heterostructure indicated that a built-in electric field is achieved by the electron transfer from metallic Ni<sub>2</sub>P to NiPS<sub>3</sub> (Figure 2-12(l)), which further accelerates the electron transfer near the interface. They also concluded that the improved electrocatalytic activity of the heterostructure is related to the epitaxial interfacial area rather than the amount of secondary phase. Besides monometallic TMS, bimetallic bifunctional heterostructured Ni-Co-S/Ni-Co-P was synthesized on NF by Zhou et al. *via* a simple electrodeposition method.<sup>[227]</sup> The as-prepared Ni-Co-S/Ni-Co-P heterostructure required a lower cell potential of 1.49 V to deliver 10 mA cm<sup>-2</sup> for overall water splitting in a basic electrolyte and a solar water splitting efficiency of 10.8% was achieved when driven by three ordinary Si solar cells. The MoS<sub>2</sub>/MoP heterostructure was also prepared and further incorporated with carbon demonstrating enhanced HER performance.<sup>[228,229]</sup> Therefore, the TMS/TMP heterostructures usually increase the number of active sites owing to its well-

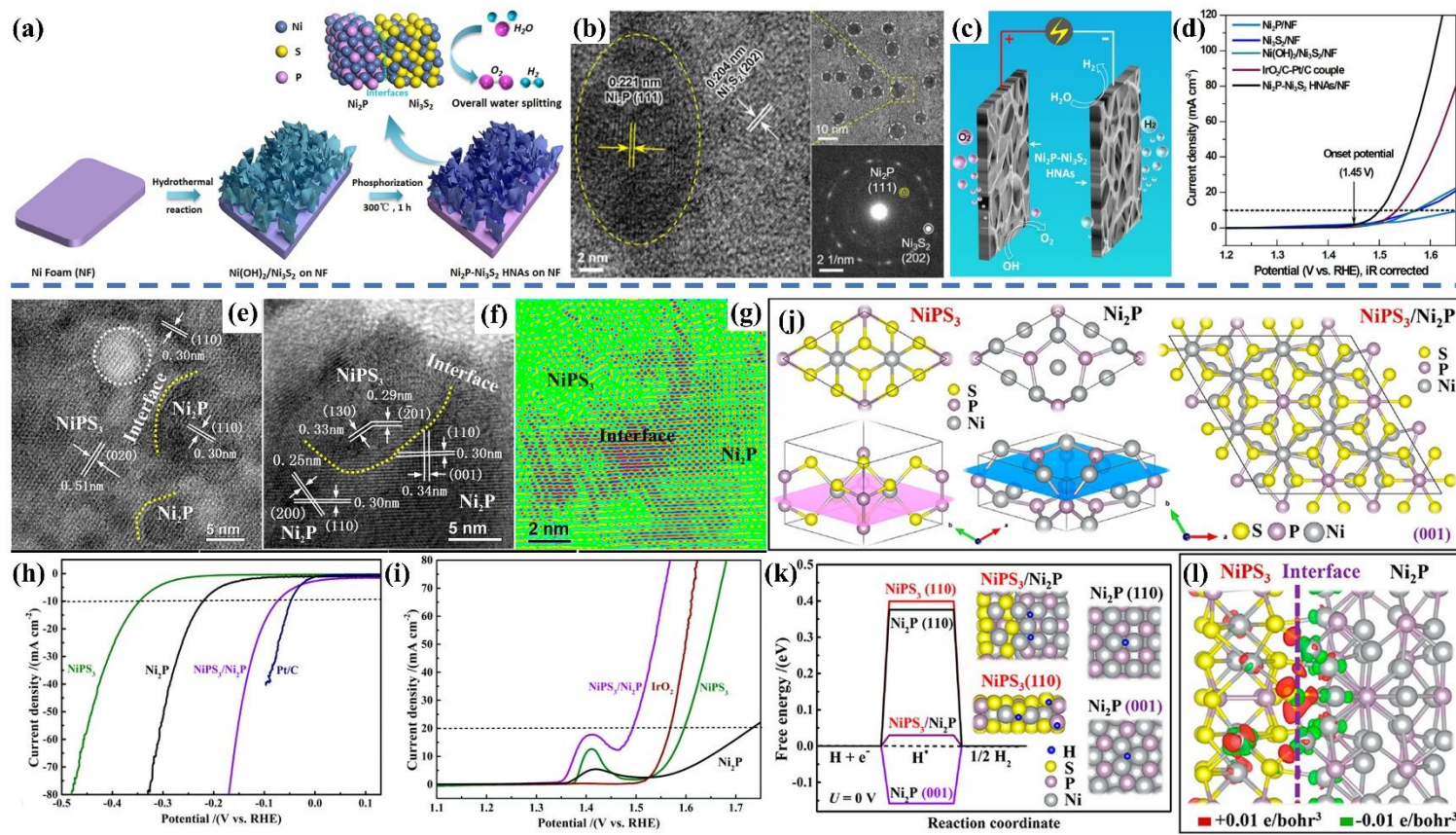


**Figure 2-12.** (a) Illustration of the fabrication of 3D-networked heterostructured  $\text{Ni}_2\text{P-Ni}_3\text{S}_2$  HNAs/NF composites. (b) High-resolution TEM images and SAED pattern of  $\text{Ni}_2\text{P-Ni}_3\text{S}_2$  HNAs/NF. (c) Schematic illustration of the two-electrode cells using  $\text{Ni}_2\text{P-Ni}_3\text{S}_2$  HNAs/NF as both the anode and the cathode for overall water splitting. (d) IR-corrected polarization curves recorded at  $1 \text{ V s}^{-1}$  of  $\text{Ni}_2\text{P/NF}$ ,  $\text{Ni}_3\text{S}_2/\text{NF}$ ,  $\text{Ni(OH)}_2/\text{Ni}_3\text{S}_2/\text{NF}$  and  $\text{IrO}_2/\text{C-Pt/C}$  couple on NF for comparison. Reproduced with permission.<sup>[146]</sup> Copyright 2018 Elsevier Ltd. (e-g) TEM (e) and HRTEM (f), and corresponding

color-filtered HRTEM (g) images of the  $\text{NiPS}_3/\text{Ni}_2\text{P}$  heterostructure. (h) LSV profiles of  $\text{NiPS}_3$ ,  $\text{Ni}_2\text{P}$ ,  $\text{NiPS}_3/\text{Ni}_2\text{P}$ , and  $\text{Pt/C}$  electrocatalysts for the HER. (i) LSV profiles of the  $\text{NiPS}_3$ ,  $\text{Ni}_2\text{P}$ ,  $\text{NiPS}_3/\text{Ni}_2\text{P}$ , and  $\text{IrO}_2$  electrocatalyst used for the OER. (j) Schematic models to illustrate the lattice matching between  $\text{NiPS}_3$  and  $\text{Ni}_2\text{P}$ . (k)  $\Delta G_{H^*}$  calculated at the equilibrium potential ( $U = 0 \text{ V}$ ) for the  $\text{NiPS}_3/\text{Ni}_2\text{P}$ ,  $\text{Ni}_2\text{P}$  (001),  $\text{Ni}_2\text{P}$  (110), and  $\text{NiPS}_3$  (110); The insets are the corresponding optimized configurations of  $\text{H}^*$  adsorption calculated by DFT. (l) Distribution of charge density difference at the  $\text{NiPS}_3/\text{Ni}_2\text{P}$  interface, where the red and green areas represent electron accumulation ( $\Delta\rho = +0.01 \text{ e} \times \text{bohr}^{-3}$ ) and depletion ( $\Delta\rho = -0.01 \text{ e} \times \text{bohr}^{-3}$ ), respectively. The Ni, S, P and H atoms are marked in gray, yellow, purple, and blue, respectively. Reproduced with permission.<sup>[226]</sup> Copyright 2019, American Chemical Society.

established heterostructure and the synergistic effect as well as strong electron interaction near the interface of the TMS/TMP heterostructure thus contributing to the enhanced bifunctional activity for the HER and the OER. Moreover, the bifunctional activity of these TMS/TMP heterostructures can be further promoted by hybridization with carbon-based materials or coupling with conductive substrates, which not only increase the amount active sites but also enable the rapid mass transfer.

### 2.6.7 Other Heterostructured TMP-Based Catalysts

During the exploration of high-active, cost-efficient and durable catalysts for water splitting, transition metal nitrides (TMN) and transition metal carbides (TMC) also draw enormous attention due to their elemental abundance and catalytic activity.<sup>[230–233]</sup> Therefore, there are also TMN/TMP and TMC/TMP heterostructures reported as bifunctional catalysts for overall water splitting and most of these investigations attributed to enhanced catalytic activity due to the massive amount of exposed active sites, interfacial interactions and synergistic effect of the heterostructure. For example, Zhong et al. firstly reported sandwich-architecture heterostructured Co<sub>2</sub>P/Co<sub>x</sub>N nanoparticles embedded in N-doped carbon (NC) and uniformly dispersed on the N-doped graphene sheets (CoNP@NC/NG).<sup>[234]</sup> The resulted CoNP@NC/NG heterostructure demonstrated an excellent OER performance ( $\eta_{10} = 390$  mV in 0.1 M KOH) benefitting from the synergistic effect originating from the Co<sub>2</sub>P/Co<sub>x</sub>N heterostructure. Subsequently, Guo et al. prepared heterostructured Co<sub>2</sub>P/CoN nanoparticles encapsulated in N-doped CNTs (Co<sub>2</sub>P/CoN-in-NCNTs) as shown in **Figure 2-13(a)**.<sup>[55]</sup> The prepared Co<sub>2</sub>P/CoN-in-NCNTs heterostructure showed excellent HER ( $\eta_{10} = 98$  mV in 0.5 M H<sub>2</sub>SO<sub>4</sub> (Figure 2-13(b)) and OER ( $\eta_{10} = 420$  mV in 0.1 M KOH) performance. DFT calculation revealed that the Co<sub>2</sub>P/CoN-in-NCNTs heterostructure exhibited the smallest  $\Delta GH^*$  value of 0.25 eV among Co-in-NCNTs (0.55 eV), N-doped CNT (1.85 eV) and graphene (0.91 eV), indicating favored adsorption of H<sup>\*</sup> on the heterointerface. The pyrrole nitrogen coupled with Co<sub>2</sub>P is identified as the active sites for HER and the Co-N-C sites existing on the interfaces of CoN and N-doped carbon are responsible for the OER activity. Therefore, the Co<sub>2</sub>P/CoN-in-NCNTs heterostructure possessed a good electrocatalytic activity for Zn–air battery-driven water



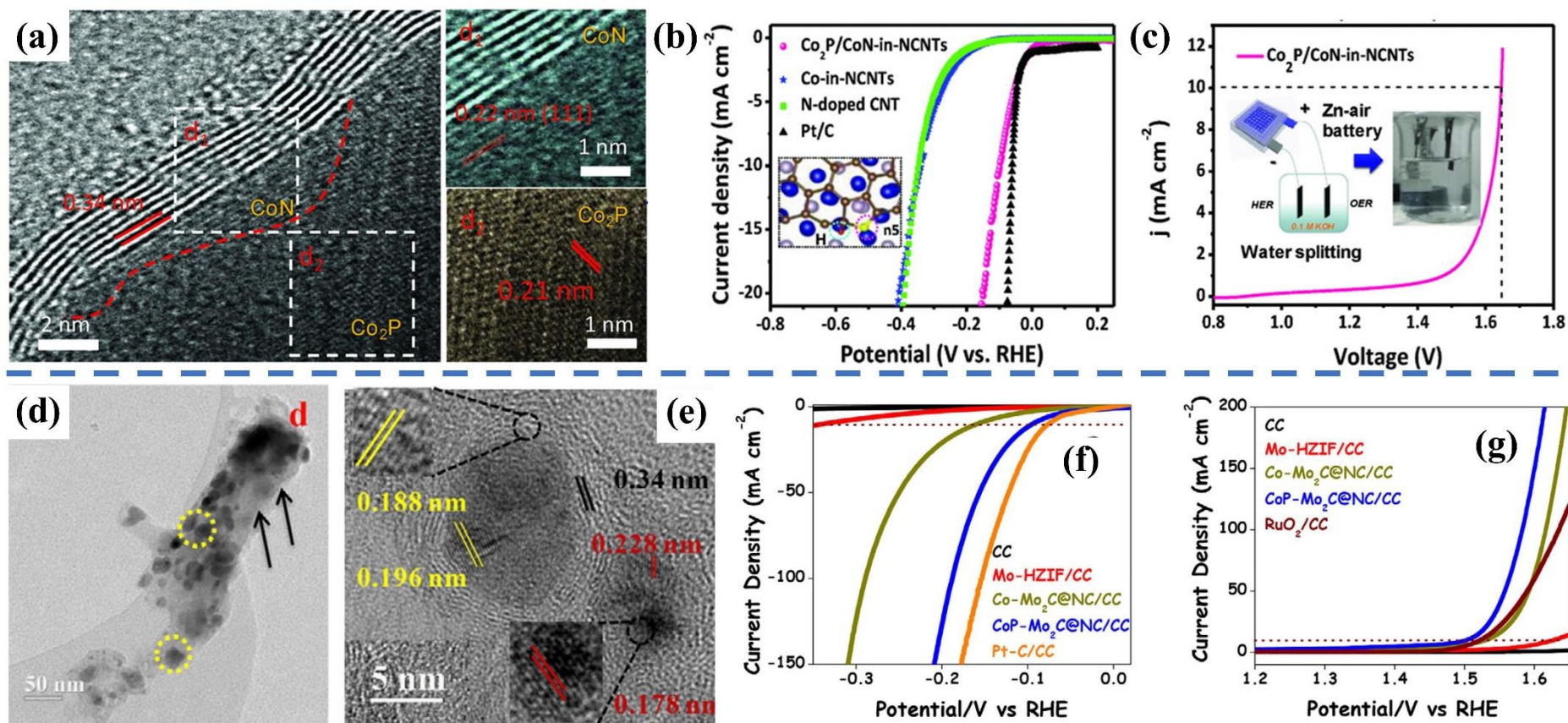


**Figure 2-13.** (a) TEM and HRTEM images of  $\text{Co}_2\text{P}/\text{CoN-in-NCNTs}$ . (b) Polarization curves of  $\text{Co}_2\text{P}/\text{CoN-in-NCNTs}$ ,  $\text{Co-in-NCNTs}$ , and  $\text{Pt/C}$  in a 0.5 M  $\text{H}_2\text{SO}_4$  solution at a scan rate of  $5 \text{ mV s}^{-1}$ . The inset shows the  $\text{H}^*$  adsorbed at  $\text{Co}_2\text{P-n5-H}$  sites. (c) Illustration scheme, photo, and polarization curves of a Zn-air battery-driven water-splitting device in 0.1 M KOH (the catalyst loading on the carbon paper was  $0.1 \text{ mg cm}^{-2}$ ). Reproduced with permission.<sup>[55]</sup> Copyright 2018, Wiley-VCH Verlag GmbH & Co. KGaA, Weinheim. (d) TEM and (e) HRTEM images of  $\text{CoP-Mo}_2\text{C@NC}$ . (f, g) The iR-corrected polarization curves of Mo-HZIF/CC, Co-Mo<sub>2</sub>C@NC/CC, CoP-Mo<sub>2</sub>C@NC/CC, and Pt@C/CC electrodes for the HER (f) and OER (g), respectively. Reproduced with permission.<sup>[56]</sup> Copyright 2018, Wiley-VCH Verlag GmbH & Co. KGaA, Weinheim.

splitting in 0.1 M KOH with a cell voltage of 1.64 V to deliver a current density of 10 mA cm<sup>-2</sup> (Figure 2-13(c)). Similar results were also reported by Hu and coauthors.<sup>[235]</sup>

For the case of TMC/TMP heterostructures, Gao et al. prepared heterostructured Co<sub>2</sub>C/WC covered with N-doped carbon by a one-step annealing process (Co<sub>2</sub>P/WC@NC).<sup>[236]</sup> Co<sub>2</sub>P/WC@NC demonstrated enhanced HER activity in acidic media with an overpotential of 91 mV required to reach a current density of 10 mA cm<sup>-2</sup>. Subsequently, Dutta et al. synthesized heterostructured CoP-Mo<sub>2</sub>C incorporated in N-doped carbon nanosheets on CC (CoP-Mo<sub>2</sub>C@NC/CC).<sup>[56]</sup> The TEM and HRTEM images (Figure 2-13(d, e)) indicated that the CoP-Mo<sub>2</sub>C heterostructure demonstrated a pea-like morphology, in which spherical CoP nanoparticles (~10 nm) encapsulated in N-doped carbon enriched with Mo<sub>2</sub>C nanoparticles. The composition engineering and synergistic effect of the heterostructure boosted the electrochemical water splitting with overpotentials of 94 and 265 mV for the HER and the OER, respectively, in 1M KOH, which are superior to their counterparts as shown in Figure 2-13(f, g). A cell voltage of 1.64 V (@10 mA cm<sup>-2</sup>) was achieved by an electrolyzer employing a CoP-Mo<sub>2</sub>C@NC/CC || CoP-Mo<sub>2</sub>C@NC/CC configuration and kept stable for 40 h. Impressively, the as-prepared CoP-Mo<sub>2</sub>C@NC/CC also demonstrated remarkable HER ( $\eta_{10}$  = 107 mV) and OER ( $\eta_{10}$  = 303 mV) activities in 0.5 M H<sub>2</sub>SO<sub>4</sub> due to the protection of the carbon shell.

## 2.7 Conclusions and Perspectives

This review summarizes the recent progress on bifunctional heterostructured TMP-based electrocatalysts with enhanced OER and HER activities for efficient overall water splitting. The rational strategies to couple TMP-based electrocatalysts with other highly active electrocatalysts forming TMP-based bifunctional heterostructures for highly efficient overall water splitting, as well as the related mechanisms of enhanced activity, are discussed in detail. Specifically, TMP-based heterostructures can be classified as TMP-exposed and TMP-protected heterostructures according to the heterostructure morphology. For the TMP-exposed heterostructures, direct exposition of the TMP may offer more active sites for the OER or the HER. But, the OER stability may be limited due to oxidation of the TMP during long-term operation. This type of heterostructure is usually prepared by using the growth-phosphorization (GP) method, including C/TMP (TMP supported on carbon), TM/TMP, TMO/TMP, TMS/TMP, TMC/TMP, TMN/TMC, etc. On the other hand, TMP-protected heterostructures are usually synthesized by the growth-phosphorization-modification (GPM) and MOF-derived methods, including C/TMP (TMP encapsulated in carbon), TMH/TMP, etc. In this case, the bifunctional activities for both the HER and the OER as well as the stability for the OER can be enhanced owing to the synergistic effect of the heterointerface and protection of TMP by the coating.

The overall water splitting activities of as-prepared TMP-based heterostructures are determined by various factors, including sample forms (e.g. powder or binder-free electrodes) and the corresponding measurement methods, different types of heterostructures (active sites). In the case of sample forms, binder-free electrodes, in which heterostructures are coupled with conductive substrates (CC, NF, etc.), would demonstrate a higher overall water splitting performance when compared to other sample forms (e.g. powder or bulk). In the case of different heterostructures, a comparison just can only be made for samples measured under similar conditions. According to Table 2-1, it can be concluded that TMP-protected heterostructures may achieve higher water splitting activities and better stabilities than other types of heterostructures. However, it should be noted that the activity of TMP-based heterostructures is mostly dependent on the heterostructure morphology with a strong

synergistic effect. Additionally, the preparation of electrodes based on TMP-based heterostructures for large-scale applications also needs to take the requirements of commercial electrolyzers into account.

In summary, the enhanced overall water splitting activity of TMP-based heterostructures can be attributed to the increased amount of active sites, the improved conductivity, the accelerated mass/charge transfer, as well as the optimized adsorption of intermediates, all of which are associated with tuning the electronic structure and the synergistic effect between the heterostructured components. However, there are still several challenges that exist in the design and construction of TMP-based bifunctional heterostructures for efficient and durable overall water splitting. These challenges will be discussed in the following.

- (1) Enhancement of the overall water splitting performance. Enhancing the efficiency is vital to reduce the cost of the hydrogen generation, when using TMP-based heterostructure for the preparation of electrodes used in commercial electrolyzers for efficient overall water splitting. According to the summary in Table 2-1, most of the optimized TMP-based heterostructures exhibit an overall water splitting activity with a cell voltage of  $\sim 1.50$  V to reach a current density of  $10 \text{ mA cm}^{-2}$  in alkaline media. Therefore, innovational strategies for the preparation of bifunctional TMP-based bifunctional heterostructures with remarkably enhanced HER and OER activity should urgently be explored. Meanwhile, in order to compare the activities between different publications and groups, recommended and unified protocols should be employed to evaluate the water splitting performance, which should be explained in detail to avoid inaccurate information.
- (2) Besides performance, stability is another important aspect. As discussed through this review, surface reconstruction and dissolution of catalysts usually occurred on the surface of TMP-based electrocatalysts during the HER and OER process. The *in-situ* formed species on the surface may work as the real active sites to enable high activity. However, many of them degrade quickly and this low stability seriously restricts their large-scale application. Therefore, *in-situ/operando* methods are necessary to assess the stability and gain insight into the activity degradation mechanism. More efforts should also be devoted

to establishing an effective strategy to improve the intrinsic stability of TMP-based bifunctional heterostructures for large-scale practical applications.

- (3) Development of a cost-efficient and easily scalable synthesis method is still one of the biggest barriers for the industrial application of heterostructured catalysts. Although many of the discussed TMP-based heterostructures demonstrated excellent bifunctional activities for overall water splitting, most of the reported synthesis methods are still restricted to the lab-scale. Therefore, developing an abundant and scalable preparation strategy plays a vital role in the realization of the large-scale commercial application of bifunctional electrocatalysts.
- (4) Development of non-precious bifunctional catalysts for overall water splitting in acidic electrolytes. Although the TMP-based electrocatalysts and their corresponding heterostructures show bifunctionality for water splitting in alkaline electrolytes and excellent HER activity in acidic electrolytes, their OER activity in acidic media is still restricted owing to the serious corrosion of metal-based catalysts in acid. At present, efficient OER activity at low pH is still hard to be realized without the assistance of noble metal-based catalysts. Therefore, more efforts should be conducted in the search for acid-resistant non-noble metal OER catalysts and explore the possibility to couple these with TMP-based electrocatalysts for the preparation of bifunctional electrocatalysts for efficient overall water splitting in acidic media.
- (5) Preparation of 3D binder-free electrodes by coupling bifunctional TMP-based heterostructures with macrostructure conductive substrates. The employment of 3D conductive substrates would not only improve the conductivity of the entire electrode, but also increase the mass loading of the highly active catalysts, thus leading to higher current densities and lower overpotentials as compared to that of electrodes prepared with binders. Inspired by this issue, many efforts have been devoted to the direct growth of efficient heterostructures on 3D conductive substrates, such as NF, CC and CFP. Meanwhile, the cost of 3D binder-free electrodes can be further reduced by employing cheaper substrates such as stainless steel.<sup>[238]</sup> Therefore, the possibility of coupling TMP-based



heterostructures with cheaper substrates is also recommended for the exploration of cost-efficient overall water splitting.

- (6) Development of *in-situ/operando* high-resolution characterization methodologies is vital to gain insight into the reaction mechanism behind the improved catalytic performance. Even though theoretical calculations offer a comprehensive understanding and prediction of the activity of TMP-based heterostructures, resulting in the conclusion that the enhanced performance was attributed to the synergistic effect arising from the heterostructure, the real mechanism of this synergistic effect is still not clear. Therefore, more *in-situ/operando* measurements and theoretical calculations need to be carried out to investigate the active sites and the reaction process. More importantly, a combination of experimental work, theoretical calculations and *in-situ/operando* measurements will increase our understanding of the reaction mechanism and benefit to the design and construction of more efficient bifunctional TMP-based heterostructures for efficient overall water splitting.

When these challenges can be overcome during the coming decade, we foresee a high potential for the commercial applicability of TMP-based heterostructured bifunctional electrocatalysts for overall water splitting.

## 2.8 Acknowledgment

This work was financially supported by the Bundesministerium für Bildung und Forschung (BMBF)-project Struktursolar. A.W.M. also thanks the BMBF (grant no. FKZ:03Z22HN11) for financial support. X. Li thanks the support from National Science Foundation of China (Grant No. 21972163), the Fundamental Research Funds for the Central Universities and Donghua university (DHU) Distinguished Young Professor Program.

## 2.9 References

- [1] S. Chu, A. Majumdar, *Nature* **2012**, 488, 294.
- [2] X. Zou, Y. Zhang, *Chem. Soc. Rev.* **2015**, 44, 5148.

- [3] International Energy Agency **2018**, <https://www.iea.org/weo2018/>, accessed at 19.05.2020.
- [4] P. C. K. Vesborg, T. F. Jaramillo, *RSC Adv.* **2012**, *2*, 7933.
- [5] I. Roger, M. A. Shipman, M. D. Symes, *Nat. Rev. Chem.* **2017**, *1*, 928.
- [6] A. Ursua, L. M. Gandia, P. Sanchis, *Proc. IEEE* **2012**, *100*, 410.
- [7] O. Schmidt, A. Gambhir, I. Staffell, A. Hawkes, J. Nelson, S. Few, *Int. J. Hydrog. Energy* **2017**, *42*, 30470.
- [8] K. E. Dalle, J. Warnan, J. J. Leung, B. Reuillard, I. S. Karmel, E. Reisner, *Chemical reviews* **2019**, *119*, 2752.
- [9] A. Li, Y. Sun, T. Yao, H. Han, *Chemistry* **2018**, *24*, 18334.
- [10] L. Han, S. Dong, E. Wang, *Adv. Mater.* **2016**, *28*, 9266.
- [11] J. Zhang, T. Wang, P. Liu, Z. Liao, S. Liu, X. Zhuang, M. Chen, E. Zschech, X. Feng, *Nat. Commun.* **2017**, *8*, 15437.
- [12] M. Shalom, D. Ressnig, X. Yang, G. Clavel, T. P. Fellingner, M. Antonietti, *J. Mater. Chem. A* **2015**, *3*, 8171.
- [13] X. Jia, Y. Zhao, G. Chen, L. Shang, R. Shi, X. Kang, G. I. N. Waterhouse, L.-Z. Wu, C.-H. Tung, T. Zhang, *Adv. Energy Mater.* **2016**, *6*, 1502585.
- [14] Y. Pei, Y. Cheng, J. Chen, W. Smith, P. Dong, P. M. Ajayan, M. Ye, J. Shen, *J. Mater. Chem. A* **2018**, *6*, 23220.
- [15] H. Zhao, Z. Y. Yuan, *Catal. Sci. Technol.* **2017**, *7*, 330.
- [16] K. N. Dinh, Q. H. Liang, C. F. Du, J. Zhao, A. L. Y. Tok, H. Mao, Q. Y. Yan, *Nano Today* **2019**, *25*, 99.
- [17] N. Han, K. R. Yang, Z. Lu, Y. Li, W. Xu, T. Gao, Z. Cai, Y. Zhang, V. S. Batista, W. Liu, X. Sun, *Nat. Commun.* **2018**, *9*, 924.
- [18] S. Chandrasekaran, L. Yao, L. Deng, C. Bowen, Y. Zhang, S. Chen, Z. Lin, F. Peng, P. Zhang, *Chem. Soc. Rev.* **2019**, *48*, 4178.
- [19] C. Tang, N. Y. Cheng, Z. H. Pu, W. Xing, X. P. Sun, *Angew. Chem. Int. Edit.* **2015**, *54*, 9351.
- [20] H. Du, R.-M. Kong, X. Guo, F. Qu, J. Li, *Nanoscale* **2018**, *10*, 21617.
- [21] J. F. Callejas, C. G. Read, C. W. Roske, N. S. Lewis, R. E. Schaak, *Chem. Mat.* **2016**, *28*, 6017.
- [22] P. Liu, J. A. Rodriguez, *J. Am. Chem. Soc.* **2005**, *127*, 14871.
- [23] Y. Wang, B. Kong, D. Y. Zhao, H. T. Wang, C. Selomulya, *Nano Today* **2017**, *15*, 26.
- [24] P. E. R. Blanchard, A. P. Grosvenor, R. G. Cavell, A. Mar, *Chem. Mat.* **2008**, *20*, 7081.
- [25] Y. Shi, B. Zhang, *Chem. Soc. Rev.* **2016**, *45*, 1529.
- [26] J. Kupka, A. Budniok, *J. Appl. Electrochem.* **1990**, *20*, 1015.
- [27] E. J. Popczun, J. R. McKone, C. G. Read, A. J. Biacchi, A. M. Wiltrout, N. S. Lewis, R. E. Schaak, *J. Am. Chem. Soc.* **2013**, *135*, 9267.
- [28] H. Li, P. Wen, D. S. Itanze, M. W. Kim, S. Adhikari, C. Lu, L. Jiang, Y. Qiu, S. M. Geyer, *Adv. Mater.* **2019**, *31*, e1900813.
- [29] W. R. Cheng, H. Zhang, X. Zhao, H. Su, F. M. Tang, J. Tian, Q. H. Liu, *J. Mater. Chem. A* **2018**, *6*, 9420.

- [30] L. A. King, M. A. Hubert, C. Capuano, J. Manco, N. Danilovic, E. Valle, T. R. Hellstern, K. Ayers, T. F. Jaramillo, *Nat. Nanotechnol.* **2019**, *14*, 1071.
- [31] J. Y. Li, J. Li, X. M. Zhou, Z. M. Xia, W. Gao, Y. Y. Ma, Y. Q. Qu, *ACS Appl. Mater. Interfaces* **2016**, *8*, 10826.
- [32] X. G. Wang, W. Li, D. H. Xiong, D. Y. Petrovykh, L. F. Liu, *Adv. Funct. Mater.* **2016**, *26*, 4067.
- [33] Y. Dang, J. He, T. Wu, L. Yu, P. Kerns, L. Wen, J. Ouyang, S. L. Suib, *ACS Appl Mater Interfaces* **2019**, *11*, 29879.
- [34] Z. Jin, P. Li, D. Xiao, *Green Chem.* **2016**, *18*, 1459.
- [35] G. B. Darband, M. Aliofkhaezai, S. Hyun, A. S. Rouhaghdam, S. Shanmugam, *J. Power Sources* **2019**, *429*, 156.
- [36] Y. M. Du, H. Q. Qu, Y. R. Liu, Y. Han, L. Wang, B. Dong, *Appl. Surf. Sci.* **2019**, *465*, 816.
- [37] X. Liu, L. Zhou, L. Huang, L. Chen, L. Long, S. Wang, X. Xu, M. Liu, W. Yang, J. Jia, *Electrochim. Acta* **2019**, *318*, 883.
- [38] K. Wang, K. Sun, T. Yu, X. Liu, G. Wang, L. Jiang, G. Xie, *J. Mater. Chem. A* **2019**, *7*, 2518.
- [39] J. H. Chen, Y. F. Zhang, H. Q. Ye, J. Q. Xie, Y. M. Li, C. Z. Yan, R. Sun, C. P. Wong, *ACS Appl. Energ. Mater.* **2019**, *2*, 2734.
- [40] M. A. R. Anjum, M. S. Okyay, M. Kim, M. H. Lee, N. Park, J. S. Lee, *Nano Energy* **2018**, *53*, 286.
- [41] W. Liu, E. Hu, H. Jiang, Y. Xiang, Z. Weng, M. Li, Q. Fan, X. Yu, E. I. Altman, H. Wang, *Nat. Commun.* **2016**, *7*, 10771.
- [42] G. Anandhababu, Y. Y. Huang, D. D. Babu, M. X. Wu, Y. B. Wang, *Adv. Funct. Mater.* **2018**, *28*, 10.
- [43] W. Xi, G. Yan, Z. Lang, Y. Ma, H. Tan, H. Zhu, Y. Wang, Y. Li, *Small* **2018**, *14*, e1802204.
- [44] Q. Qin, H. Jang, L. Chen, P. Li, T. Wei, X. Liu, J. Cho, *ACS Appl. Mater. Interfaces* **2019**, *11*, 16461.
- [45] L. Partanen, M. Hakala, K. Laasonen, *Phys. Chem. Chem. Phys.* **2018**, *21*, 184.
- [46] Y. J. Li, H. C. Zhang, M. Jiang, Q. Zhang, P. L. He, X. M. Sun, *Adv. Funct. Mater.* **2017**, *27*, 8.
- [47] X. Zhang, X. Zhang, H. Xu, Z. Wu, H. Wang, Y. Liang, *Adv. Funct. Mater.* **2017**, *27*, 1606635.
- [48] Y. Q. Wu, X. Tao, Y. Qing, H. Xu, F. Yang, S. Luo, C. H. Tian, M. Liu, X. H. Lu, *Adv. Mater.* **2019**, *31*, 9.
- [49] K. Xu, H. Cheng, H. Lv, J. Wang, L. Liu, S. Liu, X. Wu, W. Chu, C. Wu, Y. Xie, *Adv. Mater.* **2018**, *30*, 1703322.
- [50] L. Y. Wang, C. D. Gu, X. Ge, J. L. Zhang, H. Y. Zhu, J. P. Tu, *Adv. Mater. Interfaces* **2017**, *4*, 10.
- [51] H. Guo, Q. Feng, K. Xu, J. Xu, J. Zhu, C. Zhang, T. Liu, *Adv. Funct. Mater.* **2019**, *29*, 1903660.

- [52] H. Li, Q. Li, P. Wen, T. B. Williams, S. Adhikari, C. Dun, C. Lu, D. Itanze, L. Jiang, D. L. Carroll, G. L. Donati, P. M. Lundin, Y. Qiu, S. M. Geyer, *Adv. Mater.* **2018**, *30*, 170596.
- [53] H. J. Zhang, X. P. Li, A. Hahnel, V. Naumann, C. Lin, S. Azimi, S. L. Schweizer, A. W. Maijenburg, R. B. Wehrspohn, *Adv. Funct. Mater.* **2018**, *28*, 10.
- [54] J. Y. Chen, C. Fan, X. Y. Hu, C. Wang, Z. H. Huang, G. T. Fu, J. M. Lee, Y. W. Tang, *Small* **2019**, *15*, 8.
- [55] Y. Guo, P. Yuan, J. Zhang, H. Xia, F. Cheng, M. Zhou, J. Li, Y. Qiao, S. Mu, Q. Xu, *Adv. Funct. Mater.* **2018**, *28*, 1805641.
- [56] S. Dutta, A. Indra, H. Han, T. Song, *ChemSusChem* **2018**, *11*, 3956.
- [57] G. Zhao, K. Rui, S. X. Dou, W. Sun, *Adv. Funct. Mater.* **2018**, *28*, 1803291.
- [58] Y. F. Cheng, F. Liao, W. Shen, L. B. Liu, B. B. Jiang, Y. Q. Li, M. W. Shao, *Nanoscale* **2017**, *9*, 18977.
- [59] B. L. Deng, L. S. Zhou, Z. Q. Jiang, Z. J. Jiang, *J. Catal.* **2019**, *373*, 81.
- [60] F. X. Bu, W. S. Chen, M. F. A. Aboud, I. Shakir, J. J. Gu, Y. X. Xu, *J. Mater. Chem. A* **2019**, *7*, 14526.
- [61] Y. Lu, T. Wang, X. Li, G. Zhang, H. Xue, H. Pang, *RSC Adv.* **2016**, *6*, 87188.
- [62] M. Sun, H. Liu, J. Qu, J. Li, *Adv. Energy Mater.* **2016**, *6*, 1600087.
- [63] J. Wang, Z. Liu, Y. Zheng, L. Cui, W. Yang, J. Liu, *J. Mater. Chem. A* **2017**, *5*, 22913.
- [64] J. Z. Su, J. L. Zhou, L. Wang, C. Liu, Y. B. Chen, *Sci. Bull.* **2017**, *62*, 633.
- [65] W. Li, D. H. Xiong, X. F. Gao, L. F. Liu, *Chem. Commun.* **2019**, *55*, 8744.
- [66] A. Dutta, N. Pradhan, *J. Phys. Chem. Lett.* **2017**, *8*, 144.
- [67] L. S. Peng, S. S. A. Shah, Z. D. Wei, *Chin. J. Catal.* **2018**, *39*, 1575.
- [68] P. Xiao, W. Chen, X. Wang, *Adv. Energy Mater.* **2015**, *5*, 1500985.
- [69] B. Owens-Baird, Y. V. Kolen'ko, K. Kovnir, *Chemistry* **2018**, *24*, 7298.
- [70] J. Joo, T. Kim, J. Lee, S.-I. Choi, K. Lee, *Adv. Mater.* **2019**, *31*, e1806682.
- [71] Y. Lv, X. Wang, *Catal. Sci. Technol.* **2017**, *7*, 3676.
- [72] Y. Jiao, Y. Zheng, M. Jaroniec, S. Z. Qiao, *Chem. Soc. Rev.* **2015**, *44*, 2060.
- [73] S. Anantharaj, S. R. Ede, K. Sakthikumar, K. Karthick, S. Mishra, S. Kundu, *ACS Catal.* **2016**, *6*, 8069.
- [74] D. Strmcnik, P. P. Lopes, B. Genorio, V. R. Stamenkovic, N. M. Markovic, *Nano Energy* **2016**, *29*, 29.
- [75] G. B. Darband, M. Aliofkhazraei, S. Shanmugam, *Renewable Sustainable Energy Rev.* **2019**, *114*, 109300.
- [76] T. Shinagawa, A. T. Garcia-Esparza, K. Takanabe, *Sci. Rep.* **2015**, *5*, 13801.
- [77] Y. Matsumoto, E. Sato, *Mater. Chem. Phys.* **1986**, *14*, 397.
- [78] A. I. Krasil'shchikov, *Zh. Fiz. Khim.* **1963**, *37*, 273.
- [79] J. O.'M. Bockris, *J. Electrochem. Soc.* **1984**, *131*, 290.
- [80] W. O'Grady, C. Iwakura, E. Yeager, *Am. Soc. Mech. Eng.* **1976**, *76 - ENAs - 37*, 1.
- [81] J. O.'M. Bockris, *The Journal of Chemical Physics* **1956**, *24*, 817.
- [82] X. Rong, J. Parolin, A. M. Kolpak, *ACS Catal.* **2016**, *6*, 1153.
- [83] S. Giménez, J. Bisquert, *Photoelectrochemical solar fuel production: From basic principles to advanced devices*, Springer, Cham Switzerland **2016**.

- [84] J. Rossmeisl, Z.-W. Qu, H. Zhu, G.-J. Kroes, J. K. Nørskov, *J. Electroanal. Chem.* **2007**, *607*, 83.
- [85] I. C. Man, H. - Y. Su, F. Calle - Vallejo, H. A. Hansen, J. I. Martínez, N. G. Inoglu, J. Kitchin, T. F. Jaramillo, J. K. Nørskov, J. Rossmeisl, *ChemCatChem* **2011**, *3*, 1159.
- [86] C. Xiang, K. M. Papadantonakis, N. S. Lewis, *Mater. Horiz.* **2016**, *3*, 169.
- [87] J. Wei, M. Zhou, A. Long, Y. Xue, H. Liao, C. Wei, Z. J. Xu, *Nano-micro letters* **2018**, *10*, 75.
- [88] W. Yang, Z. Wang, W. Zhang, S. Guo, *Trends in Chemistry* **2019**, *1*, 259.
- [89] R. Subbaraman, D. Tripkovic, D. Strmcnik, K.-C. Chang, M. Uchimura, A. P. Paulikas, V. Stamenkovic, N. M. Markovic, *Science* **2011**, *334*, 1256.
- [90] N. Danilovic, R. Subbaraman, D. Strmcnik, K.-C. Chang, A. P. Paulikas, V. R. Stamenkovic, N. M. Markovic, *Angew. Chem. Int. Edit.* **2012**, *51*, 12495.
- [91] Z. Pu, J. Zhao, I. S. Amiinu, W. Li, M. Wang, D. He, S. Mu, *Energ Environ Sci* **2019**, *12*, 952.
- [92] Z. Pu, I. S. Amiinu, Z. Kou, W. Li, S. Mu, *Angew. Chem. Int. Edit.* **2017**, *56*, 11559.
- [93] T. Liu, A. Li, C. Wang, W. Zhou, S. Liu, L. Guo, *Adv. Mater.* **2018**, *30*, e1803590.
- [94] G. Li, Y. Sun, J. Rao, J. Wu, A. Kumar, Q. N. Xu, C. Fu, E. Liu, G. R. Blake, P. Werner, B. Shao, K. Liu, S. Parkin, X. Liu, M. Fahlman, S.-C. Liou, G. Auffermann, J. Zhang, C. Felser, X. Feng, *Adv. Energy Mater.* **2018**, *8*, 1801258.
- [95] Di Zhao, K. Sun, W.-C. Cheong, L. Zheng, C. Zhang, S. Liu, X. Cao, K. Wu, Y. Pan, Z. Zhuang, B. Hu, D. Wang, Q. Peng, C. Chen, Y. Li, *Angew. Chem. Int. Edit.* **2019**, 10.1002/anie.201908760.
- [96] P. W. Menezes, A. Indra, C. Das, C. Walter, C. Göbel, V. Gutkin, D. Schmeißer, M. Driess, *ACS Catal.* **2016**, *7*, 103.
- [97] W. Li, X. F. Gao, X. G. Wang, D. H. Xiong, P. P. Huang, W. G. Song, X. Q. Bao, L. F. Liu, *J. Power Sources* **2016**, *330*, 156.
- [98] K. Liu, C. Zhang, Y. Sun, G. Zhang, X. Shen, F. Zou, H. Zhang, Z. Wu, E. C. Wegener, C. J. Taubert, J. T. Miller, Z. Peng, Y. Zhu, *ACS Nano* **2018**, *12*, 158.
- [99] Y. Liang, Y. Li, H. Wang, H. Dai, *J. Am. Chem. Soc.* **2013**, *135*, 2013.
- [100] S. Hao, N. Chen, Q. Liu, Y. Xie, H. Fu, Y. Yang, *Chem. Asian J.* **2018**, *13*, 944.
- [101] L. Wang, Q. Zhou, Z. Pu, Q. Zhang, X. Mu, H. Jing, S. Liu, C. Chen, S. Mu, *Nano Energy* **2018**, *53*, 270.
- [102] X. Ding, Y. Xia, Q. Li, S. Dong, X. Jiao, D. Chen, *ACS Appl. Mater. Interfaces* **2019**, *11*, 7936.
- [103] M. X. Jin, Y. L. Pu, Z. J. Wang, Z. Zhang, L. Zhang, A. J. Wang, J. J. Feng, *ACS Appl. Energ. Mater.* **2019**, *2*, 4188.
- [104] M. Li, L. Chen, S. Ye, G. Fan, L. Yang, X. Zhang, F. Li, *J. Mater. Chem. A* **2019**, *7*, 13695.
- [105] Y. J. Bai, L. Fang, H. T. Xu, X. Gu, H. J. Zhang, Y. Wang, *Small* **2017**, *13*, 11.
- [106] P. Ji, H. Jin, H. Xia, X. Luo, J. Zhu, Z. Pu, S. Mu, *ACS Appl. Mater. Interfaces* **2020**, *12*, 727.

- [107] A. Saad, H. Shen, Z. Cheng, Q. Ju, H. Guo, M. Munir, A. Turak, J. Wang, M. Yang, *ACS Appl. Energ. Mater.* **2020**, 10.1021/acsaem.9b02155.
- [108] P. Wang, Z. Pu, W. Li, J. Zhu, C. Zhang, Y. Zhao, S. Mu, *J. Catal.* **2019**, 377, 600.
- [109] B. Ma, X. Duan, W. Han, X. Fan, Y. Li, F. Zhang, G. Zhang, W. Peng, *J. Colloid Interface Sci.* **2020**, 567, 393.
- [110] C. Huang, Z. Guo, *Nanoscale* **2018**, 10, 19659.
- [111] M. Lu, La Li, D. Chen, J. Li, N. I. Klyui, W. Han, *Electrochim. Acta* **2020**, 330, 135210.
- [112] B. Cao, Y. Cheng, M. Hu, P. Jing, Z. Ma, B. Liu, R. Gao, J. Zhang, *Adv. Funct. Mater.* **2019**, 414, 1906316.
- [113] K. He, T. Tadesse Tsega, X. Liu, J. Zai, X.-H. Li, X. Liu, W. Li, N. Ali, X. Qian, *Angew. Chem. Int. Edit.* **2019**, 58, 11903.
- [114] J. Yu, Y. Zhong, X. Wu, J. Sunarso, M. Ni, W. Zhou, Z. Shao, *Adv. Sci.* **2018**, 5, 1800514.
- [115] X. Du, J. Huang, J. Zhang, Y. Yan, C. Wu, Y. Hu, C. Yan, T. Lei, W. Chen, C. Fan, J. Xiong, *Angew. Chem. Int. Edit.* **2019**, 58, 4484.
- [116] Y.-P. Zhu, Y.-P. Liu, T.-Z. Ren, Z.-Y. Yuan, *Adv. Funct. Mater.* **2015**, 25, 7337.
- [117] A. I. Chumakov, Y. Shvyd'ko, I. Sergueev, D. Bessas, R. Rüffer, *Phys. Rev. Lett.* **2019**, 123, 315.
- [118] B. Lassalle-Kaiser, S. Gul, J. Kern, V. K. Yachandra, J. Yano, *J. Electron Spectrosc. Relat. Phenom.* **2017**, 221, 18.
- [119] J. Li, R. Güttinger, R. Moré, F. Song, W. Wan, G. R. Patzke, *Chem. Soc. Rev.* **2017**, 46, 6124.
- [120] O. Kasian, S. Geiger, K. J. J. Mayrhofer, S. Cherevko, *Chemical record* **2018**, 18, 1.
- [121] Y. Ye, C. H. Wu, L. Zhang, Y.-S. Liu, P.-A. Glans-Suzuki, J. Guo, *J. Electron Spectrosc. Relat. Phenom.* **2017**, 221, 2.
- [122] Z. W. Seh, J. Kibsgaard, C. F. Dickens, I. Chorkendorff, J. K. Nørskov, T. F. Jaramillo, *Science* **2017**, 355.
- [123] B. Lassalle-Kaiser, D. Merki, H. Vrubel, S. Gul, V. K. Yachandra, X. Hu, J. Yano, *J. Am. Chem. Soc.* **2015**, 137, 314.
- [124] N. Kornienko, N. Heidary, G. Cibin, E. Reisner, *Chem. Sci.* **2018**, 9, 5322.
- [125] S. Cherevko, G. P. Keeley, N. Kulyk, K. J. J. Mayrhofer, *J. Electrochem. Soc.* **2016**, 163, H228-H233.
- [126] G. Zhang, G. C. Wang, Y. Liu, H. J. Liu, J. H. Qu, J. H. Li, *J. Am. Chem. Soc.* **2016**, 138, 14686.
- [127] Y.-J. Tang, Y. Chen, H.-J. Zhu, A.-M. Zhang, X.-L. Wang, L.-Z. Dong, S.-L. Li, Q. Xu, Y.-Q. Lan, *J. Mater. Chem. A* **2018**, 6, 21969.
- [128] T. Wu, M. Pi, D. Zhang, S. Chen, *J. Power Sources* **2016**, 328, 551.
- [129] C. Y. Son, I. H. Kwak, Y. R. Lim, J. Park, *Chem. Commun.* **2016**, 52, 2819.
- [130] X. Yang, A.-Y. Lu, Y. Zhu, S. Min, M. N. Hedhili, Y. Han, K.-W. Huang, L.-J. Li, *Nanoscale* **2015**, 7, 10974.
- [131] M. Wang, C. L. Dong, Y. C. Huang, S. H. Shen, *J. Catal.* **2019**, 371, 262.
- [132] Y. Pan, Y. Liu, J. Zhao, K. Yang, J. Liang, D. Liu, W. Hu, D. Liu, Y. Liu, C. Liu, *J. Mater. Chem. A* **2015**, 3, 1656.
- [133] N. Jiang, B. You, M. L. Sheng, Y. J. Sun, *Angew. Chem. Int. Edit.* **2015**, 54, 6251.

- [134] H. Liang, A. N. Gandi, D. H. Anjum, X. Wang, U. Schwingenschlögl, H. N. Alshareef, *Nano Lett.* **2016**, *16*, 7718.
- [135] H. L. Jia, R. B. Jiang, W. Z. Lu, Q. F. Ruan, J. F. Wang, J. C. Yu, *J. Mater. Chem. A* **2018**, *6*, 4783.
- [136] Y. W. Tan, F. Zhu, H. Wang, Y. Tian, A. Hirata, T. Fujita, M. W. Chen, *Adv. Mater. Interfaces* **2017**, *4*, 7.
- [137] C. Ye, M. Q. Wang, G. Chen, Y. H. Deng, L. J. Li, H. Q. Luo, N. B. Li, *J. Mater. Chem. A* **2017**, *5*, 7791.
- [138] J. Wu, D. Wang, S. Wan, H. Liu, C. Wang, X. Wang, *Small* **2019**, 1900550.
- [139] L. Y. Chen, Y. Y. Zhang, H. F. Wang, Y. X. Wang, D. Z. Li, C. Y. Duan, *Nanoscale* **2018**, *10*, 21019.
- [140] S. P. Li, G. Zhang, X. M. Tu, J. H. Li, *ChemElectroChem* **2018**, *5*, 701.
- [141] H. Yan, Y. Xie, A. Wu, Z. Cai, L. Wang, C. Tian, X. Zhang, H. Fu, *Adv. Mater.* **2019**, *31*, e1901174.
- [142] L. Liu, L. Ge, Y. Sun, B. Jiang, Y. Cheng, L. Xu, F. Liao, Z. Kang, M. Shao, *Nanoscale* **2019**, *11*, 6394.
- [143] Y. Yan, J. Lin, K. Bao, T. Xu, J. Qi, J. Cao, Z. Zhong, W. Fei, J. Feng, *J. Colloid Interface Sci.* **2019**, *552*, 332.
- [144] Z. Gao, F.-Q. Liu, L. Wang, F. Luo, *Inorg. Chem.* **2019**, *58*, 3247.
- [145] F. S. Zhang, J. W. Wang, J. Luo, R. R. Liu, Z. M. Zhang, C. T. He, T. B. Lu, *Chem. Sci.* **2018**, *9*, 1375.
- [146] L. Y. Zeng, K. A. Sun, X. B. Wang, Y. Q. Liu, Y. Pan, Z. Liu, D. W. Cao, Y. Song, S. H. Liu, C. G. Liu, *Nano Energy* **2018**, *51*, 26.
- [147] X. Xiao, D. Huang, Y. Fu, M. Wen, X. Jiang, X. Lv, M. Li, L. Gao, S. Liu, M. Wang, C. Zhao, Y. Shen, *ACS Appl. Mater. Interfaces* **2018**, *10*, 4689.
- [148] J. M. Sun, Y. J. Chen, Z. Y. Ren, H. Y. Fu, Y. T. Xiao, J. E. Wang, G. H. Tian, *ChemElectroChem* **2017**, *4*, 1341.
- [149] X. Hu, S. Zhang, J. Sun, L. Yu, X. Qian, R. Hu, Y. Wang, H. Zhao, J. Zhu, *Nano Energy* **2019**, *56*, 109.
- [150] C. Huang, T. Ouyang, Y. Zou, N. Li, Z.-Q. Liu, *J. Mater. Chem. A* **2018**, *6*, 7420.
- [151] B. You, N. Jiang, M. L. Sheng, M. W. Bhushan, Y. J. Sun, *ACS Catal.* **2016**, *6*, 714.
- [152] P. Zhao, H. Nie, Z. Zhou, J. Wang, G. Cheng, *ChemistrySelect* **2018**, *3*, 8064.
- [153] H. Wang, T. Zhou, P. Li, Z. Cao, W. Xi, Y. Zhao, Y. Ding, *ACS Sustain. Chem. Eng.* **2018**, *6*, 380.
- [154] L. Yu, H. Q. Zhou, J. Y. Sun, I. K. Mishra, D. Luo, F. Yu, Y. Yu, S. Chen, Z. F. Ren, *J. Mater. Chem. A* **2018**, *6*, 13619.
- [155] L. Zhou, S. Jiang, Y. K. Liu, M. F. Shao, M. Wei, X. Duan, *ACS Appl. Energ. Mater.* **2018**, *1*, 623.
- [156] J. Liu, S. Hou, W. Li, A. S. Bandarenka, R. A. Fischer, *Chemistry, an Asian journal* **2019**, *14*, 3474.
- [157] X. Liu, W. Li, X. Zhao, Y. Liu, C.-W. Nan, L.-Z. Fan, *Adv. Funct. Mater.* **2019**, *7*, 1901510.

- [158] S. C. Shit, I. Mondal, S. Pendem, L. Y. Bai, J. Y. Park, J. Mondal, *ChemElectroChem* **2018**, *5*, 2842.
- [159] J. Rong, J. Xu, F. Qiu, Y. Zhu, Y. Fang, J. Xu, T. Zhang, *Adv. Mater. Interfaces* **2019**, *401*, 1900502.
- [160] C. Hu, L. Dai, *Adv. Mater.* **2019**, *31*, e1804672.
- [161] Y. Pan, K. Sun, S. Liu, X. Cao, K. Wu, W.-C. Cheong, Z. Chen, Y. Wang, Y. Li, Y. Liu, D. Wang, Q. Peng, C. Chen, Y. Li, *J. Am. Chem. Soc.* **2018**, *140*, 2610.
- [162] L. T. Yan, H. M. Jiang, Y. Wang, L. J. Li, X. Gu, P. C. Dai, D. D. Liu, S. F. Tang, G. M. Zhao, X. B. Zhao, K. M. Thomas, *Electrochim. Acta* **2019**, *297*, 755.
- [163] B. C. Weng, X. M. Wang, C. R. Grice, F. H. Xu, Y. F. Yan, *J. Mater. Chem. A* **2019**, *7*, 7168.
- [164] T. T. Sun, J. Dong, Y. Huang, W. Ran, J. F. Chen, L. B. Xu, *J. Mater. Chem. A* **2018**, *6*, 12751.
- [165] T.-Q. Zhang, J. Liu, L.-B. Huang, X.-D. Zhang, Y.-G. Sun, X.-C. Liu, D.-S. Bin, X. Chen, A.-M. Cao, J.-S. Hu, L.-J. Wan, *J. Am. Chem. Soc.* **2017**, *139*, 11248.
- [166] Y. Zhou, T. T. Li, S. Q. Xi, C. He, X. G. Yang, H. J. Wu, *ChemCatChem* **2018**, *10*, 5487.
- [167] J. F. Chang, Q. Lv, G. Q. Li, J. J. Ge, C. P. Liu, W. Xing, *Appl. Catal. B-Environ.* **2017**, *204*, 486.
- [168] B. Guo, J. Sun, X. Hu, Y. Wang, Y. Sun, R. Hu, L. Yu, H. Zhao, J. Zhu, *ACS Appl. Nano Mater.* **2019**, *2*, 40.
- [169] F. Yu, H. Q. Zhou, Y. F. Huang, J. Y. Sun, F. Qin, J. M. Bao, W. A. Goddardiii, S. Chen, Z. F. Ren, *Nat. Commun.* **2018**, *9*, 9.
- [170] B. C. Mallick, C.-T. Hsieh, K.-M. Yin, Y. A. Gandomi, K.-T. Huang, *ECS J. Solid State Sci. Technol.* **2019**, *8*, N55-N78.
- [171] D. J. Hagen, M. E. Pemble, M. Karppinen, *Appl. Phys. Rev.* **2019**, *6*, 41309.
- [172] H. Huang, M. Yan, C. Yang, H. He, Q. Jiang, L. Yang, Z. Lu, Z. Sun, X. Xu, Y. Bando, Y. Yamauchi, *Adv. Mater.* **2019**.
- [173] Y. Jiao, Y. Zheng, K. Davey, S.-Z. Qiao, *Nat Energy* **2016**, *1*, 43.
- [174] Y. Zheng, Y. Jiao, Y. Zhu, L. H. Li, Y. Han, Y. Chen, A. Du, M. Jaroniec, S. Z. Qiao, *Nat. Commun.* **2014**, *5*, 3783.
- [175] Y. Zhao, F. Zhao, X. Wang, C. Xu, Z. Zhang, G. Shi, L. Qu, *Angew. Chem. Int. Edit.* **2014**, *53*, 13934.
- [176] Z. Pu, C. Zhang, I. S. Amiinu, W. Li, L. Wu, S. Mu, *ACS Appl. Mater. Interfaces* **2017**, *9*, 16187.
- [177] D. Yang, W. Hou, Y. Lu, W. Zhang, Y. Chen, *Nanoscale* **2019**, *11*, 12837.
- [178] X. Wei, Y. Zhang, H. He, P. Li, S. Xiao, Y. Shuangrui, P. Xiao, *Chem. Commun.* **2019**.
- [179] C.-C. Hou, S. Cao, W.-F. Fu, Y. Chen, *ACS Appl. Mater. Interfaces* **2015**, *7*, 28412.
- [180] J. Y. Li, M. Yan, X. M. Zhou, Z. Q. Huang, Z. M. Xia, C. R. Chang, Y. Y. Ma, Y. Q. Qu, *Adv. Funct. Mater.* **2016**, *26*, 6785.
- [181] R.-Q. Li, B.-L. Wang, T. Gao, R. Zhang, C. Xu, X. Jiang, J. Zeng, Y. Bando, P. Hu, Y. Li, X.-B. Wang, *Nano Energy* **2019**, *58*, 870.
- [182] L. Zhang, C. Chang, C. W. Hsu, C. W. Chang, S. Y. Lu, *J. Mater. Chem. A* **2017**, *5*, 19656.



- [183] X. B. Yu, S. Zhang, C. Y. Li, C. L. Zhu, Y. J. Chen, P. Gao, L. H. Qi, X. T. Zhang, *Nanoscale* **2016**, *8*, 10902.
- [184] J. Yang, D. Guo, S. Zhao, Y. Lin, R. Yang, D. Xu, N. Shi, X. Zhang, L. Lu, Y.-Q. Lan, J. Bao, M. Han, *Small* **2019**, *15*, e1804546.
- [185] P. Li, H. C. Zeng, *Chem. Commun.* **2017**, *53*, 6025.
- [186] J. Q. Tian, J. Chen, J. Y. Liu, Q. H. Tian, P. Chen, *Nano Energy* **2018**, *48*, 284.
- [187] H. Mou, J. Wang, D. Yu, D. Zhang, F. Lu, L. Chen, D. Wang, T. Mu, *J. Mater. Chem. A* **2019**, *7*, 13455.
- [188] S. H. Ahn, A. Manthiram, *J. Mater. Chem. A* **2019**, *7*, 8641.
- [189] F. Lyu, Q. Wang, S. M. Choi, Y. Yin, *Small* **2019**, *15*, e1804201.
- [190] Z. Chen, X. Duan, W. Wei, S. Wang, B.-J. Ni, *J. Mater. Chem. A* **2019**, *7*, 14971.
- [191] G. F. Chen, T. Y. Ma, Z. Q. Liu, N. Li, Y. Z. Su, K. Davey, S. Z. Qiao, *Adv. Funct. Mater.* **2016**, *26*, 3314.
- [192] Q. W. Zhou, J. Pu, X. L. Sun, C. Zhu, J. C. Li, J. Wang, S. Z. Chang, H. G. Zhang, *J. Mater. Chem. A* **2017**, *5*, 14873.
- [193] X. Chen, Q. Li, Q. Che, Y. Chen, Y. Tan, X. Xu, *ACS Sustain. Chem. Eng.* **2019**, *7*, 11778.
- [194] Y. Q. Sun, T. Zhang, X. Y. Li, Y. Bai, X. J. Lyu, G. Q. Liu, W. P. Cai, Y. Li, *Adv. Mater. Interfaces* **2018**, *5*, 9.
- [195] C. Z. Yuan, S. L. Zhong, Y. F. Jiang, Z. K. Yang, Z. W. Zhao, S. J. Zhao, N. Jiang, A. W. Xu, *J. Mater. Chem. A* **2017**, *5*, 10561.
- [196] Z.-H. Xue, H. Su, Q.-Y. Yu, B. Zhang, H.-H. Wang, X.-H. Li, J.-S. Chen, *Adv. Energy Mater.* **2017**, *7*, 1602355.
- [197] M. S. Burke, L. J. Enman, A. S. Batchellor, S. Zou, S. W. Boettcher, *Chem. Mat.* **2015**, *27*, 7549.
- [198] T. Zhang, M.-Y. Wu, D.-Y. Yan, J. Mao, H. Liu, W.-B. Hu, X.-W. Du, T. Ling, S.-Z. Qiao, *Nano Energy* **2018**, *43*, 103.
- [199] L. Yang, H. Zhou, X. Qin, X. Guo, G. Cui, A. M. Asiri, X. Sun, *Chem. Commun.* **2018**, *54*, 2150.
- [200] J. Huang, Y. Su, Y. Zhang, W. Wu, C. Wu, Y. Sun, R. Lu, G. Zou, Y. Li, J. Xiong, *J. Mater. Chem. A* **2018**, *6*, 9467.
- [201] X. Cheng, Z. Pan, C. Lei, Y. Jin, B. Yang, Z. Li, X. Zhang, L. Lei, C. Yuan, Y. Hou, *J. Mater. Chem. A* **2019**, *7*, 965.
- [202] B. Chang, S. Hao, Z. Ye, Y. Yang, *Chem. Commun.* **2018**, *54*, 2393.
- [203] Q. Hu, X. F. Liu, C. Y. Tang, L. D. Fan, X. Y. Chai, Q. L. Zhang, J. H. Liu, C. X. He, *Sustain. Energ. Fuels* **2018**, *2*, 1085.
- [204] Y. Lin, Z. Tian, L. Zhang, J. Ma, Z. Jiang, B. J. Deibert, R. Ge, L. Chen, *Nat. Commun.* **2019**, *10*, 162.
- [205] T. Reier, H. N. Nong, D. Teschner, R. Schlögl, P. Strasser, *Adv. Energy Mater.* **2017**, *7*, 1601275.
- [206] L. Yang, G. Yu, X. Ai, W. Yan, H. Duan, W. Chen, X. Li, T. Wang, C. Zhang, X. Huang, J.-S. Chen, X. Zou, *Nat. Commun.* **2018**, *9*, 5236.
- [207] H. Jin, J. Joo, N. K. Chaudhari, S. - I. Choi, K. Lee, *ChemElectroChem* **2019**, *6*, 3244.

- [208] Y. Wang, D. Yan, S. El Hankari, Y. Zou, S. Wang, *Adv. Sci.* **2018**, *5*, 1800064.
- [209] M. Gong, Y. Li, H. Wang, Y. Liang, J. Z. Wu, J. Zhou, J. Wang, T. Regier, F. Wei, H. Dai, *J. Am. Chem. Soc.* **2013**, *135*, 8452.
- [210] L. Trotochaud, S. L. Young, J. K. Ranney, S. W. Boettcher, *J. Am. Chem. Soc.* **2014**, *136*, 6744.
- [211] J. Luo, J.-H. Im, M. T. Mayer, M. Schreier, M. K. Nazeeruddin, N.-G. Park, S. D. Tilley, H. J. Fan, M. Grätzel, *Science* **2014**, *345*, 1593.
- [212] J. Liu, J. Wang, B. Zhang, Y. Ruan, L. Lv, X. Ji, K. Xu, L. Miao, J. Jiang, *ACS Appl. Mater. Interfaces* **2017**, *9*, 15364.
- [213] Y. Hou, M. R. Lohe, J. Zhang, S. Liu, X. Zhuang, X. Feng, *Energy Environ. Sci.* **2016**, *9*, 478.
- [214] C. Xiao, Y. Li, X. Lu, C. Zhao, *Adv. Funct. Mater.* **2016**, *26*, 3515.
- [215] B. You, Y. Zhang, Y. Jiao, K. Davey, S. Z. Qiao, *Angew. Chem. Int. Edit.* **2019**, *58*, 11796.
- [216] R. Boppella, J. Tan, W. Yang, J. Moon, *Adv. Funct. Mater.* **2019**, *29*, 1807976.
- [217] Z. Niu, C. Qiu, J. Jiang, L. Ai, *ACS Sustain. Chem. Eng.* **2019**, *7*, 2335.
- [218] C. C. Du, M. X. Shang, J. X. Mao, W. B. Song, *J. Mater. Chem. A* **2017**, *5*, 15940.
- [219] X. Ma, Y. Chang, Z. Zhang, J. Tang, *J. Mater. Chem. A* **2018**, *6*, 2100.
- [220] X. Y. Yu, X. W. David Lou, *Adv. Energy Mater.* **2018**, *8*, 1701592.
- [221] C. Tan, Z. Lai, H. Zhang, *Adv. Mater.* **2017**, *29*, 1701392.
- [222] X. Wang, X. Gan, T. Hu, K. Fujisawa, Y. Lei, Z. Lin, B. Xu, Z.-H. Huang, F. Kang, M. Terrones, R. Lv, *Adv. Mater.* **2017**, *29*, 1603617.
- [223] L.-L. Feng, G. Yu, Y. Wu, G.-D. Li, H. Li, Y. Sun, T. Asefa, W. Chen, X. Zou, *J. Am. Chem. Soc.* **2015**, *137*, 14023.
- [224] Y. Wu, G.-D. Li, Y. Liu, L. Yang, X. Lian, T. Asefa, X. Zou, *Adv. Funct. Mater.* **2016**, *26*, 4839.
- [225] M. S. Faber, R. Dziejczak, M. A. Lukowski, N. S. Kaiser, Q. Ding, S. Jin, *J. Am. Chem. Soc.* **2014**, *136*, 10053.
- [226] Q. H. Lian, L. X. Zhong, C. F. Du, Y. B. Luo, J. Zhao, Y. Zheng, J. W. Xu, J. M. Ma, C. T. Liu, S. Z. Li, Q. Y. Yan, *ACS Nano* **2019**, *13*, 7975.
- [227] X. Zhou, J. Zhou, G. Huang, R. Fan, S. Ju, Z. Mi, M. Shen, *J. Mater. Chem. A* **2018**, *6*, 20297.
- [228] J.-Q. Chi, Y.-M. Chai, X. Shang, B. Dong, C.-G. Liu, W. Zhang, Z. Jin, *J. Mater. Chem. A* **2018**, *6*, 24783.
- [229] Z. Wu, J. Wang, K. Xia, W. Lei, X. Liu, D. Wang, *J. Mater. Chem. A* **2018**, *6*, 616.
- [230] R. Michalsky, Y.-J. Zhang, A. A. Peterson, *ACS Catal.* **2014**, *4*, 1274.
- [231] Y. Zhong, X. Xia, F. Shi, J. Zhan, J. Tu, H. J. Fan, *Adv. Sci.* **2016**, *3*, 1500286.
- [232] T. Meng, M. Cao, *Chemistry* **2018**, *24*, 16716.
- [233] X. Peng, C. Pi, X. Zhang, S. Li, K. Huo, P. K. Chu, *Sustain. Energ. Fuels* **2019**, *3*, 366.
- [234] X. Zhong, Y. Jiang, X. L. Chen, L. Wang, G. L. Zhuang, X. N. Li, J. G. Wang, *J. Mater. Chem. A* **2016**, *4*, 10575.
- [235] L. Hu, Y. W. Hu, R. Liu, Y. C. Mao, M. S. Balogun, Y. X. Tong, *Int. J. Hydrog. Energy* **2019**, *44*, 11402.

- [236] Y. Gao, Z. L. Lang, F. Y. Yu, H. Q. Tan, G. Yan, Y. H. Wang, Y. Y. Ma, Y. G. Li, *ChemSusChem* **2018**, *11*, 1082.
- [237] F. Hu, Y. Zhang, X. Shen, J. Tao, X. Yang, Y. Xiong, Z. Peng, *J. Power Sources* **2019**, *428*, 76.
- [238] H. Zhang, J. M. de Souza e Silva, X. Lu, C. S. de Oliveira, B. Cui, X. Li, C. Lin, S. L. Schweizer, A. W. Maijenburg, M. Bron, R. B. Wehrspohn, *Adv. Mater. Interfaces* **2019**, *6*, 1900774.
- [239] J. S. Li, L. X. Kong, Z. X. Wu, S. Zhang, X. Y. Yang, J. Q. Sha, G. D. Liu, *Carbon* **2019**, *145*, 694.
- [240] L. H. Li, L. Song, H. R. Xue, C. Jiang, B. Gao, H. Gong, W. Xia, X. L. Fan, H. Guo, T. Wang, J. P. He, *Carbon* **2019**, *150*, 446.
- [241] Y. J. Lu, W. Q. Hou, D. X. Yang, Y. F. Chen, *Electrochim. Acta* **2019**, *307*, 543.
- [242] J. M. Wang, W. R. Yang, J. Q. Liu, *J. Mater. Chem. A* **2016**, *4*, 4686.
- [243] L. Yu, Y. Xiao, C. L. Luan, J. T. Yang, H. Y. Lbw, Y. Wang, X. Zhang, X. P. Dai, Y. Yang, H. H. Zhao, *ACS Appl. Mater. Interfaces* **2019**, *11*, 6890.
- [244] J. H. Tong, T. Li, L. L. Bo, W. Y. Li, Y. L. Li, Y. Zhang, *ChemElectroChem* **2019**, *6*, 3437.
- [245] T. Dong, X. Zhang, P. Wang, H. S. Chen, P. Yang, *Carbon* **2019**, *149*, 222.
- [246] D. Yang, W. Hou, Y. Lu, X. Wang, W. Zhang, Y. Chen, *ACS Sustain. Chem. Eng.* **2019**, *7*, 13031.
- [247] Y. Wang, T. Williams, T. Gengenbach, B. Kong, D. Zhao, H. Wang, C. Selomulya, *Nanoscale* **2017**, *9*, 17349.
- [248] L. H. Ai, Z. G. Niu, J. Jiang, *Electrochim. Acta* **2017**, *242*, 355.
- [249] W. Li, S. L. Zhang, Q. N. Fan, F. Z. Zhang, S. L. Xu, *Nanoscale* **2017**, *9*, 5677.
- [250] X. H. Fan, F. T. Kong, A. G. Kong, A. L. Chen, Z. Q. Zhou, Y. K. Shan, *ACS Appl. Mater. Interfaces* **2017**, *9*, 32840.

### **3 Bifunctional Heterostructure Assembly of NiFe LDH Nanosheets on NiCoP Nanowires for Highly Efficient and Stable Overall Water Splitting**

The as-synthesized bifunctional heterostructure NiFe LDH@NiCoP/NF electrodes exhibit an excellent activity for both HER and OER as defined by a low overpotential, Tafel slope, charge transfer resistance and a superior stability for at least 100 h owing to the special interface engineering and synergistic effects. NiFe LDH@NiCoP/NF is further used for overall water splitting with a cell voltage of 1.57 V ( $j=10 \text{ mA/cm}^2$ ) and an outstanding stability for at least 100 h without any noticeable loss of activity.

This chapter can be referred to:

Haojie Zhang, Xiaopeng Li, Angelika Hähnel, Volker Naumann, Chao Lin, Sara Azimi, Stefan L. Schweizer, A. Wouter Maijenburg,\* and Ralf B. Wehrspohn,\* *Advanced Functional Materials* 2018, 28, 10.

### 3.1 Abstract

3D hierarchical heterostructure NiFe LDH@NiCoP/NF electrodes have been prepared successfully on nickel foam with special interface engineering and synergistic effects. Our research finds that the as-prepared NiFe LDH@NiCoP/NF electrodes have a more sophisticated inner structure and intensive interface than simply physical mixture. The NiFe LDH@NiCoP/NF electrodes required an overpotential as low as 120 mV and 220 mV to deliver 10 mA/cm<sup>2</sup> for the HER and OER in 1 M KOH, respectively. Tafel and electrochemical impedance spectroscopy (EIS) further reveal the favorable kinetic during the electrolysis. Specifically, the NiFe LDH@NiCoP/NF electrodes were simultaneously used as cathode and anode for overall water splitting, which requires a cell voltage of 1.57 V at 10 mA/cm<sup>2</sup>. Furthermore, the synergistic effect of heterostructure improved the structure stability and promoted the generation of active phases during HER and OER, resulting in excellent stability over 100 h continuous operation. Moreover, the strategy and interface engineering of the introduced heterostructure can also be used to prepare other bifunctional and cost-efficient electrocatalysts for various applications.

### 3.2 Introduction

Developing earth-abundant, easily scalable, binder-free, stable and bifunctional electrocatalysts with excellent activity for overall water splitting is a promising strategy for the storage and transport of renewable energy in order to address the increasing energy demands and associated environmental crisis.<sup>[1]</sup> Electrochemical water splitting to produce H<sub>2</sub> and O<sub>2</sub> is one of the most efficient and large-scale energy storage and transport strategies, which transforms electric energy into chemical energy and which can be easily integrated with other renewable energies (e.g. solar and wind).<sup>[2]</sup> However, this process has not been widely used in industrial applications. Water electrolysis consists of two half reactions, namely the oxygen evolution reaction (OER) and the hydrogen evolution reaction (HER), which normally require two types of catalysts to cover the large overpotential necessary to generate H<sub>2</sub> and O<sub>2</sub>.<sup>[3]</sup> The state-of-the-art electrocatalysts are currently the noble metal Pt based catalysts for the HER and Ru and Ir based catalysts for the OER.<sup>[4]</sup> However, their large-scale and widespread applications are seriously limited by the global reserve scarcity and exorbitant price of these noble metals. Driven by these challenges, recently an enormous amount of research efforts have been devoted to develop cost-efficient and easily scalable electrocatalysts for improving the electrolytic efficiency and minimizing the dynamic overpotential.<sup>[5]</sup> On the other hand, practical utilization of particle catalysts involves the usage of binder additives for firmly attaching particles onto the current collector, resulting in limited activity and stability. Therefore, there are considerable efforts focusing on preparing binder-free and bifunctional electrodes that are cost efficient and obtain high catalytic activity by reduction of the overpotential for HER and OER.<sup>[6]</sup> Furthermore, the binder-free and bifunctional electrodes can simplify the design and construction of the electrolysis device.

Previous research has indicated that adequate structure design not only accelerates the performance of electrolysis by improving the charge transfer capability between catalysts and substrate, but also provides the possibility to combine two different kinds of catalysts for the preparation of bifunctional electrocatalysts for overall water splitting.<sup>[7]</sup> For instance, Yang et al. prepared MoS<sub>2</sub>-Ni<sub>2</sub>S<sub>2</sub> heteronanorods on nickel foam (NF), which exhibited a cell voltage

of 1.50 V at 10 mA/cm<sup>2</sup> for overall water splitting.<sup>[8]</sup> Xiao et al. electrodeposited amorphous NiFe nanosheets on NiCo<sub>2</sub>O<sub>4</sub> nanoflakes as a bifunctional electrocatalyst for HER and OER.<sup>[9]</sup> Hou et al. prepared ternary hybrid CoSe/NiFe LDH/EG by depositing NiFe LDH (layered double hydroxide) on the *in-situ* grown NiSe nanosheets vertically oriented on exfoliated graphene foil.<sup>[10]</sup> Wang et al. molecularly coupled NiFe LDH nanosheets on NiCo<sub>2</sub>O<sub>4</sub> nanowire arrays on a NF substrate, which was used as a bifunctional electrocatalyst for overall water splitting.<sup>[11]</sup> Zhang et al. studied the interface engineering of the MoS<sub>2</sub>/Ni<sub>3</sub>S<sub>2</sub> heterostructure as a bifunctional electrocatalyst with accelerated overall water splitting performance.<sup>[7]</sup> Furthermore, Liu et al. fabricated the heterostructure by combining NiFe LDH nanosheets with *in-situ* grown NiCo<sub>2</sub>S<sub>4</sub> nanotubes on NF with an enhanced overall water splitting activity.<sup>[12]</sup> Previous approaches revealed that electrocatalysts with appropriate design of the heterostructure can result in promising bifunctional activity for water splitting. On the other hand, metal phosphides have recently attracted extensive research interest owing to their high activity.<sup>[13]</sup> However, their relatively poor OER performance, compared to state-of-the-art non-noble metal OER catalysts such as NiFe LDH, limited their application as bifunctional electrocatalysts for water splitting and only a few bifunctional heterostructure metal phosphides have been reported so far.<sup>[14]</sup> Therefore, it is expected that the formation of a heterostructure by combining metal phosphides with NiFe LDH, which is a promising electrocatalyst for OER, will be a promising strategy for the preparation of active bifunctional electrocatalysts for water splitting.

Herein, we present a 3D hierarchical heterostructure NiFe LDH@NiCoP/NF constructed by coupling ultrathin NiFe LDH with NiCoP nanowires by a simple three-step hydrothermal-phosphorization-hydrothermal process at low temperature. This structure showed a synergistically enhanced performance for HER and OER. For the preparation of these 3D hierarchical NiFe LDH@NiCoP/NF heterostructures, we first hydrothermally grew NiCo hydroxide nanowires on the NF, which had a porous 3D structure beneficial for releasing the formed H<sub>2</sub> and O<sub>2</sub> gas bubbles and which can be used as the current collector. Afterward, these NiCo hydroxide nanowires were phosphatized for the formation of NiCoP nanowires. Finally,

NiFe LDH nanosheets were grown on top of these NiCoP nanowires by an additional hydrothermal reaction. The as-synthesized NiFe LDH@NiCoP/NF electrodes with engineered interface exhibited synergistic effects toward electrocatalytic reactions. Therefore, the NiFe LDH@NiCoP/NF required overpotentials as low as 120 mV and 220 mV to achieve 10 mA/cm<sup>2</sup> for HER and OER, respectively, and excellent stability for 100 h. The NiFe LDH@NiCoP/NF electrodes also possessed a lower Tafel slope, smaller charge transfer resistance ( $R_{ct}$ ), and higher electrochemical active surface area (ECSA) as compared to NiFe LDH/NF and NiCoP/NF. Specifically, the NiFe LDH@NiCoP/NF electrodes were used as cathode and anode for overall water splitting resulting in a cell voltage of 1.57 V to achieve 10 mA/cm<sup>2</sup> with outstanding durability for 100 h, making it become one of the most efficient earth-abundant bifunctional electrocatalysts for overall water splitting. Overall, 3D hierarchical heterostructure electrodes made of earth-abundant metals were prepared successfully for overall water splitting. Additionally, we also provided mechanistic insights into the impact of heterostructure interfaces.

### 3.3 Experimental Section

**Materials and Chemicals.** Iron nitrate nonahydrate ( $\text{Fe}(\text{NO}_3)_3 \cdot 9\text{H}_2\text{O}$ , ACS Reagent grade) and nickel nitrate hexahydrate ( $\text{Ni}(\text{NO}_3)_2 \cdot 6\text{H}_2\text{O}$ , ACS Reagent grade) were purchased from Merck KGaA. Nickel chloride hexahydrate ( $\text{NiCl}_2 \cdot 6\text{H}_2\text{O}$ ,  $\geq 98\%$ ), cobalt chloride hexahydrate ( $\text{CoCl}_2 \cdot 6\text{H}_2\text{O}$ ,  $\geq 98\%$ ), ammonium fluoride ( $\text{NH}_4\text{F}$ ,  $\geq 99.9\%$ ), urea ( $\text{CO}(\text{NH}_2)_2$ , ACS Reagent grade), sodium hypophosphite monohydrate ( $\text{NaH}_2\text{PO}_2 \cdot \text{H}_2\text{O}$ ,  $\geq 99\%$ ), 20wt% Pt/C and Ruthenium(IV) oxide ( $\text{RuO}_2$ , 99.9%) were purchased from Sigma-Aldrich. All the chemicals were used as received without further purification. Nickel foam (NF) with a thickness of 1.6 mm was purchased from Shanghai Tankii Alloy Material Co., Ltd. and used as the substrate. Ultrapure water with a resistance of 18.2 M $\Omega$ , which was purified by a Millipore system (JWT GmbH), was used throughout all experiments.

**Synthesis of NiCoP Nanowires on NF (NiCoP/NF).** NiCoP nanowires on NF were prepared by a hydrothermal reaction followed by phosphorization. Firstly, 1 mmol  $\text{CoCl}_2 \cdot 6\text{H}_2\text{O}$ ,



0.5 mmol  $\text{NiCl}_2 \cdot 6\text{H}_2\text{O}$ , 5 mmol urea and 2.5 mmol  $\text{NH}_4\text{F}$  were dissolved in 17.5 mL of water under vigorous stirring for 15 min in order to obtain a clear solution. Secondly, this solution was transferred to a Teflon-lined stainless steel autoclave and reacted at 120 °C for 6 h with a piece of Ni foam (2.4 cm $\times$ 2.4 cm), which was cleaned with acetone, ethanol, a 3 M HCl solution and pure water under ultrasonication for 15 min each. After reaction, the Teflon-lined stainless steel autoclave was cooled naturally to room temperature and the NF was taken out, washed with water and ethanol, and then dried with a  $\text{N}_2$  gun. Finally, for phosphorization, 1 g  $\text{NaH}_2\text{PO}_2 \cdot \text{H}_2\text{O}$  was placed at the upstream side of a tube furnace (Carbolite Gero, model E3216) and the NF was placed at the downstream side. Subsequently, the sample was heated to 300 °C in a 500 mL/min stream of  $\text{N}_2$  gas for 2 h resulting in NiCoP nanowires on the NF (NiCoP/NF).

**Synthesis of NiFe LDH@NiCoP heterostructure on Ni Foam (NiFe LDH@NiCoP/NF).** The NiFe Layered double hydroxide (LDH) was hierarchically grown on the surface of NiCoP/NF nanowires by employing a second hydrothermal reaction. Typically, the obtained NiCoP/NF was immersed in a 17.5 mL aqueous solution containing 0.25 mmol  $\text{Fe}(\text{NO}_3)_2 \cdot 6\text{H}_2\text{O}$ , 0.75 mmol  $\text{Ni}(\text{NO}_3)_2 \cdot 6\text{H}_2\text{O}$  and 1.25 mmol urea in a Teflon-lined stainless steel autoclave, which was hydrothermally treated at 120 °C for 10 h for the growth of the NiFe LDH nanosheets on the surface of the NiCoP nanowires. After the reaction, the autoclave was cooled naturally and the sample was taken out, washed with water and ethanol, and dried with a stream of  $\text{N}_2$  gas in order to yield the desired heterostructure. The catalyst loadings were determined by weighting the mass of the NF electrodes before and after catalyst growth. For NiFe LDH@NiCoP/NF in this report, the catalyst loading was approximately 2 mg/cm<sup>2</sup>.

**Synthesis of NiFe LDH/NF.** For comparison, the NiFe LDH was also directly grown on NF. In a typical procedure, a piece of NF (2.4 cm  $\times$  2.4 cm) was cleaned with acetone, ethanol, a 3M HCl solution and pure water under ultrasonication for 15 min each, and then dried with a  $\text{N}_2$  gun. Then, it was immersed in a 17.5 mL aqueous solution containing 0.25 mmol  $\text{Fe}(\text{NO}_3)_2 \cdot 6\text{H}_2\text{O}$ , 0.75 mmol  $\text{Ni}(\text{NO}_3)_2 \cdot 6\text{H}_2\text{O}$  and 1.25 mmol urea in a Teflon-lined stainless steel autoclave, which was hydrothermally treated at 120 °C for 10 h for the growth of NiFe LDH nanosheets on the surface of the NF (NiFe LDH/NF).

**Preparation of 20 wt% Pt/C/NF and RuO<sub>2</sub>/NF.** Samples containing 20 wt% Pt/C and RuO<sub>2</sub> were chosen as the benchmark electrocatalyst for the HER and OER for comparison of the H<sub>2</sub> and O<sub>2</sub> generation activity following the recipe reported previously.<sup>[30]</sup> Briefly, 5 mg of catalyst was added to a solution containing 750  $\mu$ L water, 250  $\mu$ L isopropyl alcohol and 16  $\mu$ L 5% Nafion. The obtained suspension was ultrasonicated for 30 min in order to obtain a scattered uniform ink solution. Subsequently, 400  $\mu$ L of the ink solution was coated on the NF (1x1 cm<sup>2</sup>) resulting in a catalyst loading of approximately 2 mg/cm<sup>2</sup>. Finally, the samples were dried with hot air.

**Characterization.** All samples were characterized by X-ray diffraction (XRD) using a Bruker D8 diffractometer, with Cu  $K_{\alpha}$  radiation ( $\lambda = 1.541874 \text{ \AA}$ ). Scanning electron microscopy (SEM) characterizations were carried out with a FEI Quanta 650 FEG scanning electron microscope equipped with an X-ray detector for energy dispersive X-ray spectroscopy (EDX, Oxford). The morphology of the samples was further characterized by transmission electron microscopy (TEM) on a FEI Tecnai F20 transmission electron microscope equipped with an EDX (Oxford). X-ray photoelectron spectroscopy (XPS) data was obtained by a Kratos Axis Ultra DLD X-ray photoelectron spectrometer equipped with a monochromatic Al  $K_{\alpha}$  X-ray source. All XPS spectra were calibrated by shifting the C 1s peak to 248.8 eV.

**Electrochemical Measurements.** All electrochemical measurements were conducted using an Autolab PGSTAT302N Potentiostat/galvanostat in a typical three-electrode configuration, using a Pt wire and Ag/AgCl reference electrode (3 M KCl) as counter and reference electrode, respectively. The working electrodes were pre-treated by 20 cycles of cyclic voltammetry scans from -1.5 V to 1.0 V vs. Ag/AgCl (3M KCl) at 50 mV/s in 1 M KOH. For the HER and OER performance, the polarization curves were recorded by linear sweep voltammetry at a scan rate of 10 mV/s in 1 M KOH. For overall water splitting, the prepared electrodes were directly used as cathode and anode in a two-electrode configuration in 1 M KOH at room temperature. For this, the polarization curves were recorded by linear sweep voltammetry from 1.0 to 2.0 V versus the counter electrode at a scan rate of 10 mV/s. Chronopotentiometry measurements were performed at a constant current density of 10

mA/cm<sup>2</sup> for 100 h for all relevant reactions: HER, OER and overall water splitting. The electrochemically active surface areas (ECSA) were estimated by cyclic voltammetry and calibrated according to the method reported by Liang et. al.<sup>[14b]</sup> In short, the  $C_{dl}$  was used to indicate the active surface areas for comparison. We measured the currents in a narrow potential window without faradaic processes. Subsequently, the double layer capacitance ( $C_{dl}$ ) can be estimated by the half slope of the linearly fitted curve of the capacitive current ( $\Delta j = j_{anodic} - j_{cathodic}$ ) plotted against the scan rate. The electrochemical impedance spectroscopy (EIS) measurements were recorded at -1.2 V vs. Ag/AgCl (3 M KCl) for the HER and 0.55 V vs. Ag/AgCl (3 M KCl) for the OER, with a frequency range from 100 kHz to 0.1 Hz and a 10 mV AC dither. All polarization curves were not corrected for iR drop throughout the system. All overpotentials were acquired by chronopotentiometry measurements at a constant current density of 10 mA/cm<sup>2</sup> for HER, OER and overall water splitting. All potentials reported in this study for OER and HER were converted to the corresponding potentials vs. the reversible hydrogen electrode (RHE) using the equation  $E_{RHE} = E_{Ag/AgCl} + 0.197 + 0.059 \times \text{pH}$ , where  $E_{RHE}$  and  $E_{Ag/AgCl}$  are the potentials vs. RHE and the measured potentials vs. Ag/AgCl (3M KCl) reference electrode, respectively.

### 3.4 Results and Discussion

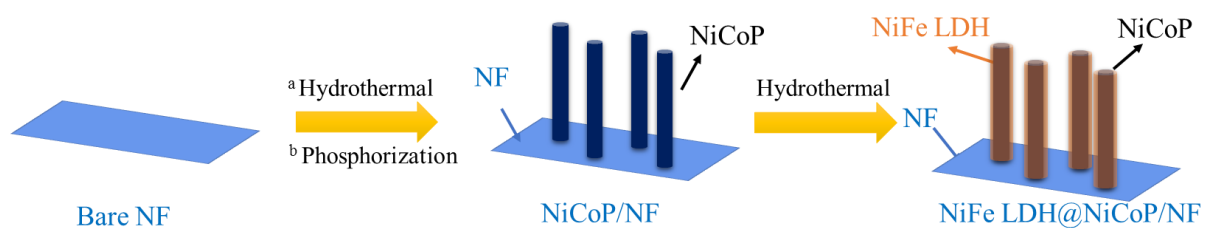


**Figure 3-1.** Schematic representation of the synthesis of 3D hierarchical NiFe LDH@NiCoP/NF electrodes.

The NiFe LDH@NiCoP/NF electrodes were prepared by a simple three-step hydrothermal-phosphorization-hydrothermal method according to previous reports.<sup>[9, 14b]</sup> The schematic diagram in **Figure 3-1** illustrated the processes used for the preparation of the hierarchical heterostructure NiFe LDH@NiCoP supported on NF. NF was used as a 3D porous binder-free substrate which provided sufficient mechanical strength and conductivity. The X-

ray diffraction spectrum (XRD) of the as-prepared NiFe LDH@NiCoP/NF is shown in **Figure 3-2(a)**, together with the bare NF, NiCoP, NiFe LDH/NF as references, for interpreting the structure information. From the pattern of NiFe LDH@NiCoP/NF, the peaks located at  $2\theta = 44.5^\circ$ ,  $51.9^\circ$  and  $76.37^\circ$  can be assigned to the (111), (200) and (220) planes of Ni, respectively (PDF #04-0850), and the peaks at  $2\theta = 40.9^\circ$ ,  $45.6^\circ$ , and  $54.4^\circ$  well matched with the (111), (210) and (300) planes of NiCoP, respectively (PDF #71-2336), while the peaks at  $2\theta = 11.7^\circ$ ,  $23.2^\circ$ ,  $33.2^\circ$ ,  $38.7^\circ$  and  $61.3^\circ$  coincided very well with the (003), (006), (101), (015) and (113) planes of the NiFe LDH, respectively, as observed by NiFe LDH/NF and NiCoP/NF as well.<sup>[11, 14b]</sup>

From the scanning electron microscopy (SEM) images shown in **Figure S 3-1(a-b)**, the revealed NF had a 3D open porous structure with enough space for the release of the generated  $O_2$  and  $H_2$  gas bubbles. Furthermore, the surface of the NF is smooth and the energy dispersive X-ray spectroscopy (EDX) spectrum (Figure S 3-1(c)) indicated that Ni and O were the only elements existing in the NF. After the first hydrothermal reaction, NiCo hydroxide nanowires were uniformly grown on the surface of NF as shown in Figure S 3-1(d-e), and the EDX pattern shown in Figure S 3-1(f) confirmed the presence of Ni and Co. Figure 3-2(b) shows the morphology of the NiCoP nanowires, which was preserved after phosphorization (inset image). The EDX spectrum as shown **Figure S 3-2(a)** and **Table S 3-1** verified the presence of Ni, Co and P. As displayed in Figure 3-2(c), the NiFe LDH@NiCoP nanowires exhibited a heterostructure with ultrathin NiFe LDH nanosheets grown around the surface of the NiCoP nanowires supported on the NF substrate. From the EDX pattern of the as-prepared NiFe LDH@NiCoP/NF, the peaks from Co, Ni, Fe and P were clearly discernible and the ratio of Ni:Co:P:Fe is 33:22:22:1 (as shown in Figure S 3-2(b) and Table S 3-1). In order to further understand the processes of the growth of NiFe LDH nanosheets, samples consisting of NiFe LDH on NF (denoted as NiFe LDH/NF) were also prepared by the same procedure. After hydrothermal reaction, NiFe LDH ultrathin nanosheets were grown on the NF as shown in Figure S 3-1(g-h), for which the XRD pattern matched well with the results reported in the

literature.<sup>[10, 15]</sup> EDX results indicated that the ratio of Ni:Fe is ~ 4:1 as shown in Figure S 3-1(i) and Table S 3-1.

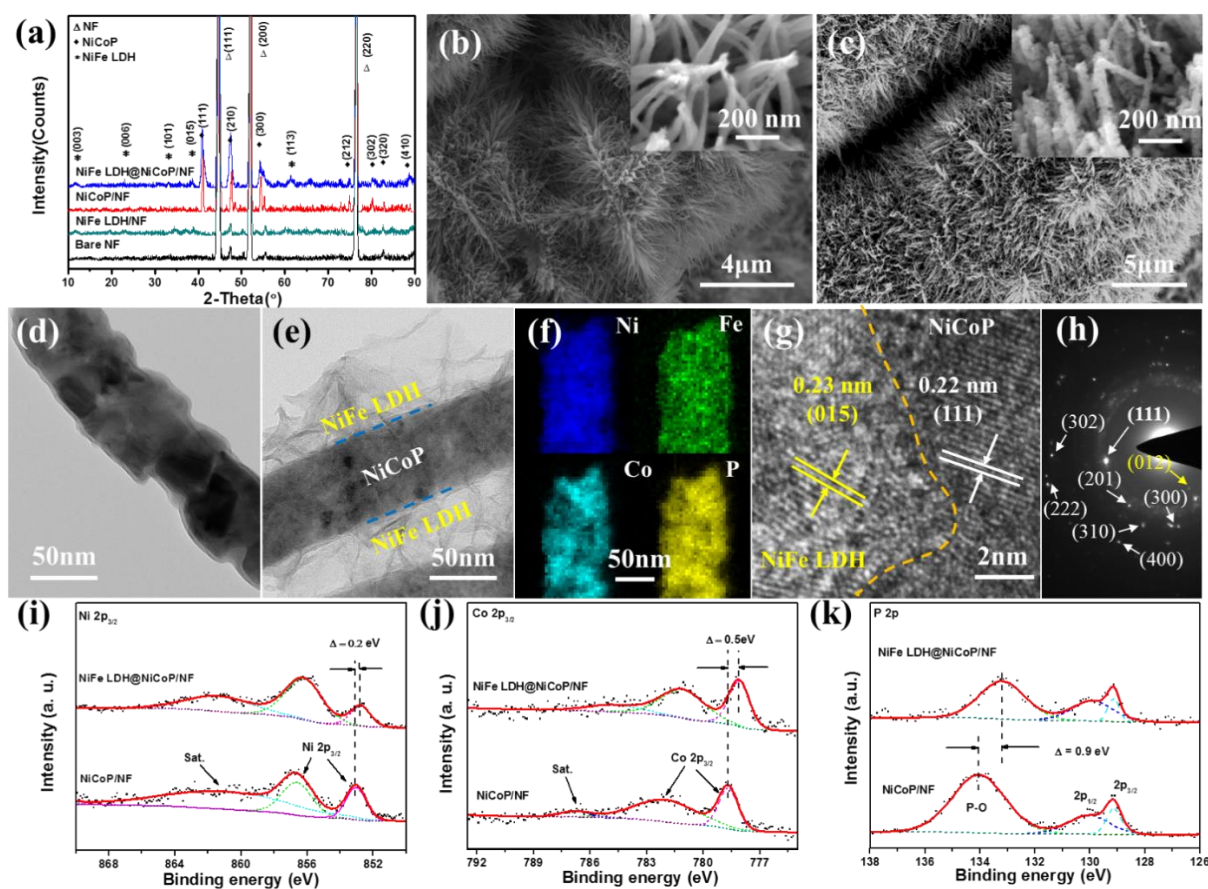


**Figure 3-2.** (a) XRD spectra of the bare NF, NiCoP/NF, NiFe LDH@NiCoP/NF and NiFe LDH/NF; (b) SEM image of the as-synthesized NiCoP/NF nanowires, where the inset shows a high resolution image of the NiCoP nanowires; (c) SEM image of the as-synthesized NiFe LDH@NiCoP/NF nanowires, where the inset shows a high resolution image of the NiFe LDH@NiCoP nanowires; (d) TEM image of a NiCoP nanowire; (e) TEM image of a NiFe LDH@NiCoP nanowire; (f) EDX mapping images of the NiFe LDH@NiCoP nanowire; (g) HRTEM image of the NiFe LDH@NiCoP nanowire highlighting the interface between nanowire and nanosheets. (h) Selected area diffraction (SAD) pattern of the interface of the NiFe LDH@NiCoP. (i-k) XPS patterns of the Ni 2p<sub>3/2</sub>, Co 2p<sub>3/2</sub>, P 2p for NiCoP/NF and NiFe LDH@NiCoP/NF, respectively.

Transmission electron microscopy (TEM) was used to further investigate the morphology as well as the interfaces between the NiCoP nanowires and NiFe LDH nanosheets. As shown in Figure 3-2(d), the TEM image of a NiCoP nanowire revealed its polycrystalline nature. Figure 3-2(e) shows the morphology of a NiFe LDH@NiCoP nanowire and the EDX mapping images (Figure 3-2(f)) evidenced the uniform distribution of the elements Ni, Co, P and Fe throughout the heterostructure. As shown in Figure 3-2(g), the interface of the NiCoP

nanowire and the NiFe LDH exhibited lattice spaces of 0.22 nm and 0.23 nm, respectively, which are consistent with the (111) and (012) planes of NiCoP and NiFe LDH, respectively. Selected area (electro) diffraction (SAD) in Figure 3-2(h) further confirmed the heterostructure, in line with the XRD results. These results indicated that the as-prepared NiFe LDH@NiCoP/NF electrode had a sophisticated inner structure and interaction.

X-ray photoelectron spectroscopy (XPS) was carried out to probe the surface composition, and the corresponding oxidation states of the elements for investigating the synergistic effect of the heterostructure. The Ni 2p<sub>3/2</sub> peaks of the NiCoP/NF are shown in Figure 3-2(i), three peaks at binding energies of 853.0, 856.6 and 861.5 eV were observed, which can be assigned to Ni-P (Ni<sup>2+</sup>), Ni-PO<sub>x</sub> (Ni<sup>3+</sup>) and its satellite peak, respectively.<sup>[14b, 16]</sup> The Ni-P and Ni-PO<sub>x</sub> peaks can also be observed for NiFe LDH@NiCoP/NF, which confirmed that the NiFe LDH nanosheets did not completely block the XPS signal of the NiCoP nanowires in the heterostructure. It is noteworthy that the shoulder peak of Ni 2p<sub>3/2</sub> of NiFe LDH@NiCoP/NF located at 852.8 eV (Figure 3-2(i)), which is very close to that of metallic Ni (852.6 eV). This suggested that part of the Ni<sup>2+</sup> has been further reduced during the growth of NiFe LDH.<sup>[14b, 16]</sup> Similarly, the Co 2p<sub>3/2</sub> spectra (Figure 3-2(j)) of the NiCoP/NF and NiFe LDH@NiCoP/NF displayed an extra peak located at 778.8 and 778.3 eV, respectively, which can be assigned to the formation of Co-P.<sup>[17]</sup> Compared with metallic Co (778.2 eV), this peak shifted to slightly higher binding energy, suggesting the presence of partially charged Co species.<sup>[18]</sup> Moreover, the peaks located at 781.9 eV and 781.2 eV for NiCoP/NF and NiFe LDH@NiCoP/NF, respectively, can be related to Co-PO<sub>x</sub>.<sup>[13c]</sup> After coupling with the NiFe LDH ultrathin nanosheets, the Ni 2p<sub>3/2</sub> and Co 2p<sub>3/2</sub> peaks shifted ~0.2 eV and ~0.5 eV to lower binding energies, respectively, indicating of the strong electronic interactions at the interface between the NiFe LDH nanosheets and the NiCoP nanowires.<sup>[11]</sup> Figure 3-2(k) shows the P 2p spectra of the as-prepared NiCoP/NF and NiFe LDH@NiCoP/NF. The two peaks located at 129.1 and 130.0 eV can be assigned to P<sup>3-</sup>, and the predominant peaks at 134.1 eV for NiCoP/NF and 133.2 eV for NiFe LDH@NiCoP/NF can be attributed to PO<sub>4</sub><sup>3-</sup>.<sup>[19]</sup> Interestingly, the P 2p peak of the NiFe LDH@NiCoP/NF also shifted 0.9 eV toward lower binding energy, again

verifying the charge transfer between NiFe LDH and NiCoP. The interaction between NiFe LDH and NiCoP will be beneficial for the reaction dynamics of both HER and OER.<sup>[13a, 13b]</sup>

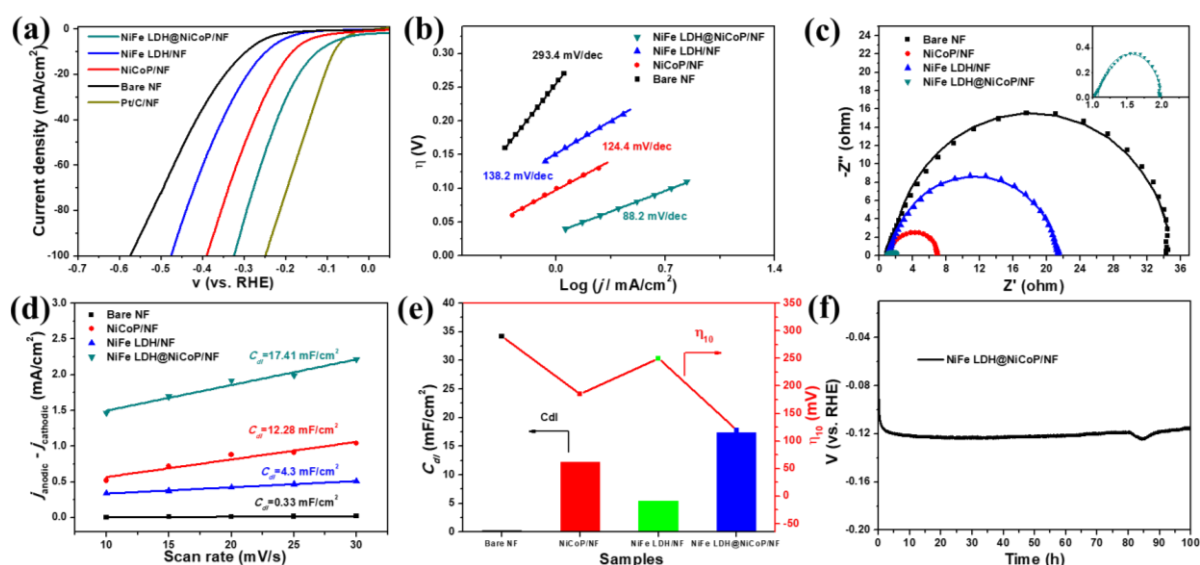
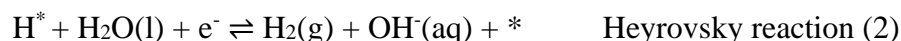
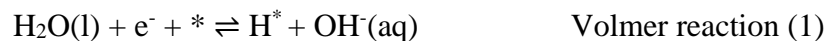


**Figure 3-3.** (a) Polarization curves of the NiFe LDH@NiCoP/NF, NiCoP/NF, NiFe LDH/NF, Bare NF and Pt/C/NF for the HER without iR compensation; (b) Tafel plots and (c) Electrochemical impedance spectroscopy for the corresponding electrocatalysts (the magnified impedance pattern for NiFe LDH@NiCoP/NF is shown as inset); (d) Plots showing the extraction of the double layer capacitance ( $C_{dl}$ ) for the estimation of the electrochemically active surface area (ECSA); (e) The relationship between the  $C_{dl}$  and overpotential ( $\eta$  at a current density of  $-10 \text{ mA/cm}^2$ ); (f) Long-time stability test of the NiFe LDH@NiCoP/NF heterostructure for the HER performed at a constant current density of  $-10 \text{ mA/cm}^2$ .

The electrocatalytic HER performance of the NiFe LDH@NiCoP/NF heterostructure was examined in 1 M KOH using a typical three-electrode configuration. The NiFe LDH@NiCoP/NF heterostructure with a geometric area of  $1 \times 1 \text{ cm}^2$  was directly used as the working electrode, and Ag/AgCl (3 M KCl) and Pt wire were used as reference and counter electrode, respectively. For comparison, bare NF, NiCoP/NF, NiFe LDH/NF and 20 wt% Pt/C supported on bare NF with the same catalyst loading (denoted as Pt/C/NF) were also tested under the same conditions. As shown in **Figure 3-3(a)**, the as-prepared NiFe LDH@NiCoP/NF heterostructure possessed an excellent HER activity. The overpotential required for  $j = -10 \text{ mA/cm}^2$  is as low as 120 mV without iR compensation (acquired from the chronopotentiometry measurement), which is superior to that of bare NF ( $\eta_{10} = 295 \text{ mV}$ ), NiFe LDH/NF ( $\eta_{10} = 250 \text{ mV}$ ), and NiCoP/NF ( $\eta_{10} = 185 \text{ mV}$ ). The significant improvement of the HER activity originated from the strong interaction and efficient synergy between the NiCoP nanowires and

NiFe LDH ultrathin nanosheets. The Tafel slope of 88.2 mV/dec obtained for the NiFe LDH@NiCoP/NF heterostructure (Figure 3-3(b)) also suggested favorable HER kinetics following the Heyrovsky-step-determined Volmer-Heyrovsky mechanism.<sup>[20]</sup>



Where \* denotes a catalytic site and H\* is an adsorbed H- species.

Electrochemical impedance spectroscopy (EIS) measurements were performed to investigate the kinetics of the catalysts at the electrode/electrolyte interface as shown in Figure 3-3(c). All EIS data were fitted with the equivalent circuit as shown in **Figure S 3-3**, consisting of a resistor ( $R_l$ ) in series with a parallel combination of a resistor ( $R_{ct}$ ) and a constant phase element (CPE).<sup>[21]</sup> In this equivalent circuit,  $R_l$  is attributed to the ohmic resistance of the electrolyte, the electrocatalysts as well as all the contacts, and  $R_{ct}$  indicates the charge transfer resistance between the catalysts and the electrolyte. The  $R_{ct}$  is related to electrocatalytic kinetics and a lower  $R_{ct}$  value corresponds to a faster reaction rate. According to the fitted EIS results (**Table S 3-2**), the NiFe LDH@NiCoP/NF heterostructure exhibited the smallest  $R_{ct}$  (2.77  $\Omega$ ), suggesting rapid charge transfer kinetics. This is consistent with the low overpotential and small Tafel slope found for the NiFe LDH@NiCoP/NF. The double layer capacitances ( $C_{dl}$ ) were measured to estimate the electrochemical active surface area (ECSA) of all the samples.<sup>[14b]</sup> As shown in Figure 3-3(d), the  $C_{dl}$  of NiFe LDH@NiCoP/NF is approximately 32 times higher than that of the bare NF, suggesting that the heterostructure contained many more catalytically active surface sites, which can be attributed to the synthesis of two different types of nanostructures on top of the NF. As seen in Figure 3-3(e), the overpotential decreased along with the increase of the  $C_{dl}$ , which confirmed that the heterostructure offered a higher ECSA for the HER. Stability is another important criteria of electrocatalysts. Figure 3-3(f) shows that the NiFe LDH@NiCoP/NF electrode retained its high catalytic activity even after 100 h of continuous operation, which is superior to the activity of most of the recently reported electrocatalysts (usually less than 24 h stability reported). Above results established our NiFe



LDH@NiCoP/NF heterostructure as an outstanding HER catalyst with excellent activity as compared to other recently reported earth-abundant HER catalysts in alkaline media (**Table S 3-3**).<sup>[7, 9-12, 16, 22]</sup>

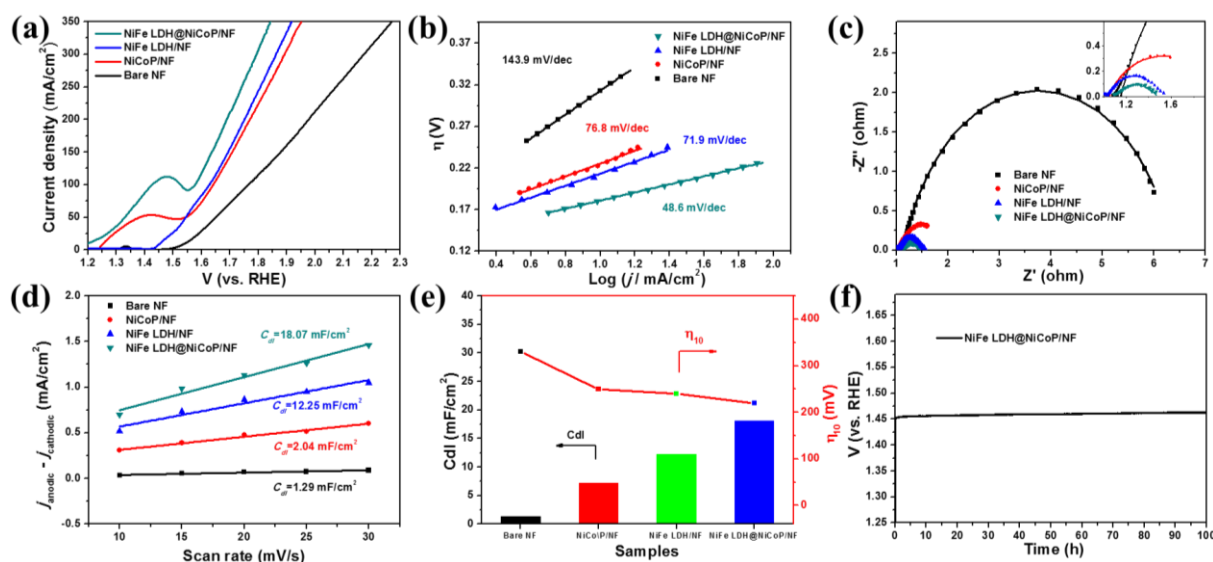


**Figure 3-4.** (a) Polarization curves of NiFe LDH@NiCoP/NF, NiCoP/NF, NiFe LDH/NF and bare NF for the OER without iR compensation; (b) Tafel plots and (c) Electrochemical impedance spectroscopy of the corresponding electrocatalysts, the magnified impedance pattern shown inset; (d) Different current density versus scan rate to assess the double layer capacitances for the estimation of the electrochemically active surface area (ECSA); (e) The relationship between the  $C_{dl}$  and overpotential ( $\eta$  at a current density of 10 mA/cm<sup>2</sup>); (f) Long-term stability test of the NiFe LDH@NiCoP/NF for the OER carried out at a constant current density of 10 mA/cm<sup>2</sup>.

Next to the HER activity, we also investigated the OER activity of the NiFe LDH@NiCoP/NF electrode in 1M KOH. **Figure 3-4(a)** shows the polarization curve of the NiFe LDH@NiCoP/NF without iR compensation (cyan curve). The peaks observed between 1.3 and 1.5 V vs. RHE can be probably correspond to the oxidation of  $M^{2+}$  to  $M^{3+}$  ( $M = Ni, Co$ ) in the NiFe LDH@NiCoP heterostructure, which was also reported for NiCoP nanowires<sup>[23]</sup> and NiFe LDH@NiCoS heterostructures.<sup>[12]</sup> The NiFe LDH@NiCoP/NF electrode exhibited a low overpotential of 220 mV at a current density of 10 mA/cm<sup>2</sup> (acquired from the chronopotentiometry measurement). In contrast, NiFe LDH/NF, NiCoP/NF and bare NF required an overpotential of 240, 250 and 330 mV, respectively. Additionally, the NiFe LDH@NiCoP/NF displayed a better OER performance than the state-of-the-art RuO<sub>2</sub> (**Figure S 3-4**), owing to its smaller contact resistance and faster charge transfer between the catalyst and the substrate.<sup>[24]</sup> The excellent OER performance of NiFe LDH@NiCoP/NF is also better

than recently reported OER catalysts (**Table S 3-4**).<sup>[9-12, 15b, 22, 25]</sup> Figure 3-4(b) shows that the NiFe LDH@NiCoP/NF heterostructure electrode exhibited the smallest Tafel slope of 48.6 mV/dec, indicating that the NiFe LDH@NiCoP/NF proceeded a faster OER kinetic.<sup>[26]</sup> The EIS results (Figure 3-4(c) and Table S 3-2) revealed that the NiFe LDH@NiCoP/NF had the smallest  $R_{ct}$  (0.41  $\Omega$ ) among all the samples, indicating a faster charge transfer and favorable reaction kinetics on the heterostructure. The measured  $C_{dl}$  of NiFe LDH@NiCoP/NF was much higher than that of NiCoP/NF, NiCo hydroxide/NF and bare NF (Figure 3-4(d)). As shown in Figure 3-4(e), the reduced overpotential for the NiFe LDH@NiCoP/NF heterostructure can be assigned to an increase of the ECSA of the heterostructure as compared to the other samples investigated in this work. To assess the stability of the NiFe LDH@NiCoP/NF electrode for the OER, a long- time chronopotentiometry measurement was carried out at a current density of 10 mA/cm<sup>2</sup> for 100 h without observation of degradation (Figure 3-4(f)).

In order to further gain insights into the reaction mechanism, the NiFe LDH@NiCoP/NF electrode after HER and OER was characterized by XRD, SEM, TEM and XPS. For the sample after long term HER measurement, the crystalline and the morphology remained nearly identical as before, which was evidenced by XRD pattern (**Figure S 3-5(a)**), SEM images (Figure S 3-5(b)) and HRTEM images (**Figure 3-5(a)**). The dominant O specie is metal hydroxide (M-OH) as observed with O 1s spectra (Figure 3-5(c)). Meanwhile, the O content (EDX results as shown in Table S 3-1) and the height of the M-OH peak (Figure 3-5(c)) increased dramatically, suggesting the formation of a thin metal hydroxide layer on the surface of the heterostructure.<sup>[27]</sup> It is hard to distinguish this layer from the HRTEM, but it can be validated from the Co 2p<sub>3/2</sub>, Ni 2p<sub>3/2</sub> and P 2p spectra of the NiFe LDH@NiCoP/NF after the long term HER measurement, where the peaks at the low binding energies (Ni, ~852.8 eV, Co ~ 778.1 eV and P, ~129.2 and 129.9 eV) disappeared as shown in Figure 3-5(d-f).<sup>[13a, 14b, 16]</sup> The content of the Fe and P decreased as shown in Table S 3-1, also confirmed the formation of the metal hydroxides.

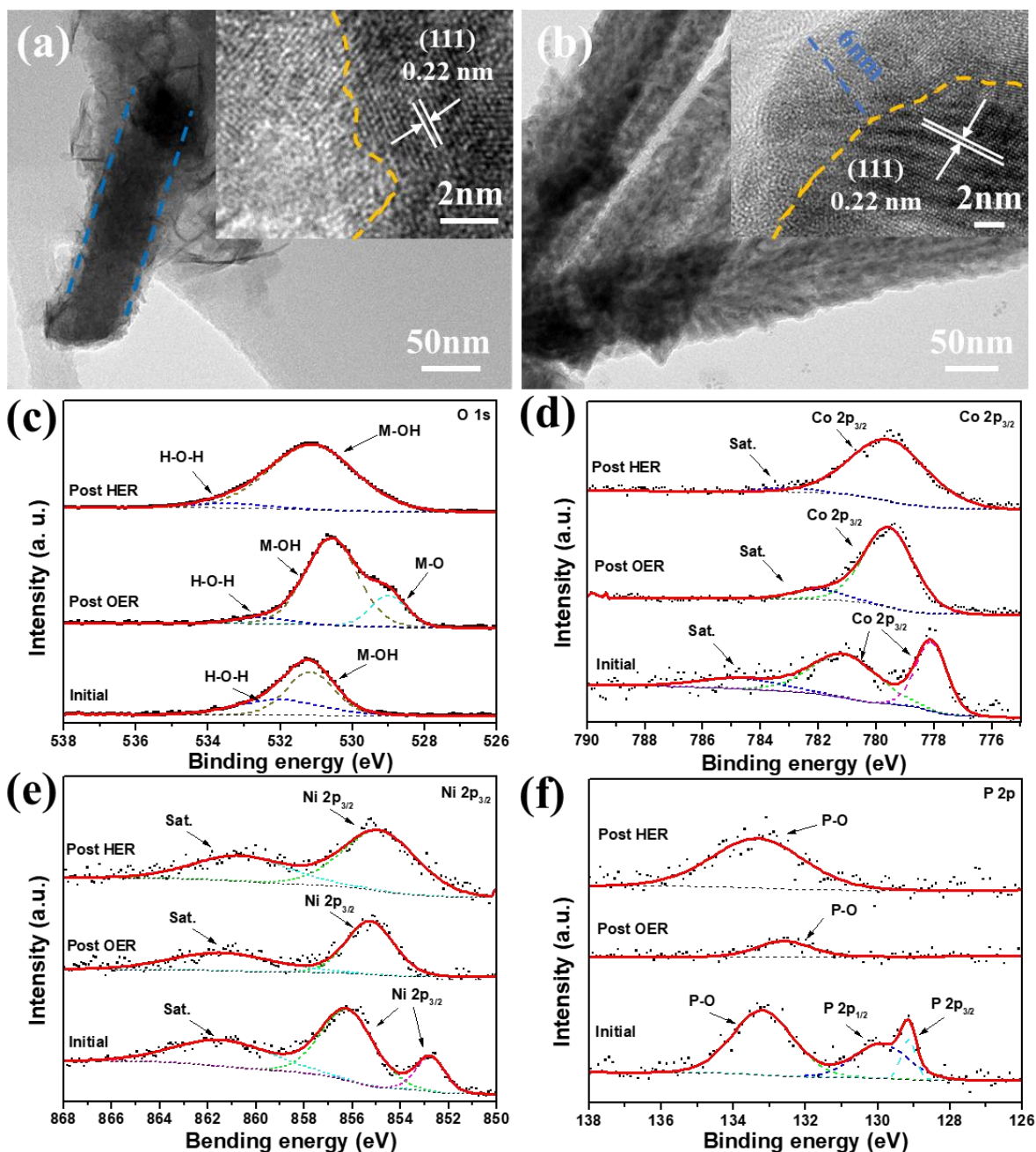


**Figure 3-5.** TEM images of the NiFe LDH@NiCoP heterostructure after (a) HER and (b) OER, the corresponding HRTEM images of the heterostructure were shown in the inset. XPS spectra of the NiFe LDH@NiCoP/NF electrode before reaction, post OER and post HER, (c) O 1s; (d) Co 2p<sub>3/2</sub>; (e) Ni 2p<sub>3/2</sub>; (f) P 2p, respectively.

However, the surface morphology of NiFe LDH@NiCoP/NF changed substantially after long term OER operation. Compared with the HER operating in a reducing potential environment, the strong anodic oxidation in the OER potential range leads to an evident and irreversible phase transformation of metal phosphides to metal oxide/oxyhydroxide. The thickness of the *in-situ* formed oxide/oxyhydroxide layers on the metal phosphides surface was reported in the range of several nanometers.<sup>[13b]</sup> Here, XRD (Figure S 3-5(a)) and SEM (Figure

S 3-5(c)) characterization suggested that the main crystalline phase and morphology of NiCoP remained after long term OER measurement. However, The HRTEM images (as shown in Figure 3-5(b)) revealed that a new rugged layer with a thickness of ~6 nm, was *in-situ* formed on the surface of the heterostructure. The Fe reduced content change from the EDX (Table S 3-1), indicated the NiFe LDH was merged together with the newly formed oxide/oxyhydroxide layer. The EDX mapping of the single NiFe LDH@NiCoP (**Figure S 3-6**) further confirmed the uniform distribution of the Ni, Co Fe, P and O on the surface of nanowire. Meanwhile, the O content increased dramatically (as shown in Table S 3-1) and a new peak arose at 529.0 eV in the O 1s spectra (Figure 3-5(c)) after long term OER measurement, further proving the formation of metal oxide/oxyhydroxides.<sup>[28]</sup> The peaks located at the lower binding energy in the Co 2p<sub>3/2</sub> (Figure 3-5(d)) and Ni 2p<sub>3/2</sub> (Figure 3-5(e)) spectra, disappeared after the OER test, indicating the phase transformation of metal phosphides to metal oxide/oxyhydroxide.<sup>[14b]</sup> Moreover, this phase transformation can be further confirmed by a dramatic decrease in the P content as shown in **Table S 3-1** and the lower binding energy peaks disappear in the P 2p spectra as shown in Figure 3-5(f).<sup>[14b]</sup> These results further confirmed that the surface of NiFe LDH@NiCoP was dominated by the *in-situ* formed metal oxide/oxyhydroxide during OER operation which has been also regarded as the electrocatalytically active phase.<sup>[15b]</sup> Overall, owing to the synergistic effect of the strong interface interaction in the heterostructure, the NiFe LDH@NiCoP/NF can maintain the nanowire architecture and crystalline phase of NiCoP. Meanwhile, the surface of the NiFe LDH@NiCoP were enriched with hydroxides (during HER) and oxides/oxyhydroxides (during OER) transformed from NiCoP, which are known as the electrocatalytically active phases.<sup>[14d]</sup>

According to the results discussed above, the NiFe LDH@NiCoP/NF electrode can serve as an efficient and robust electrocatalyst for HER and OER. Therefore, we also used the NiFe LDH@NiCoP/NF electrodes simultaneously as anode and cathode for overall water splitting as schematically represented in **Figure 3-6(a)**. The digital photograph of the electrolytic cell during operation was illustrated in Figure 3-6(b). The video (in Supporting information) recorded at different constant current densities, clearly showed the formation of

H<sub>2</sub> and O<sub>2</sub> bubbles on the cathode and anode, respectively. The polarization curves (Figure 3-6(c)) indicated that the NiFe LDH@NiCoP/NF electrodes exhibited superior overall water splitting activity. Remarkably, a current density of 10 mA/cm<sup>2</sup> can be achieved with an overpotential as low as 340 mV (calculated from the cell voltage of 1.57 V as acquired during a chronopotentiometry measurement), which is better or comparable to previously reported electrocatalysts (see **Table S 3-5**)<sup>[6b, 9-12, 13d, 14b, 14c, 22, 29]</sup>. Furthermore, the NiFe LDH@NiCoP/NF showed excellent stability during the long-time overall water splitting measurement with only a slight deactivation during the complete 100 h operation (Figure 3-6(d)).

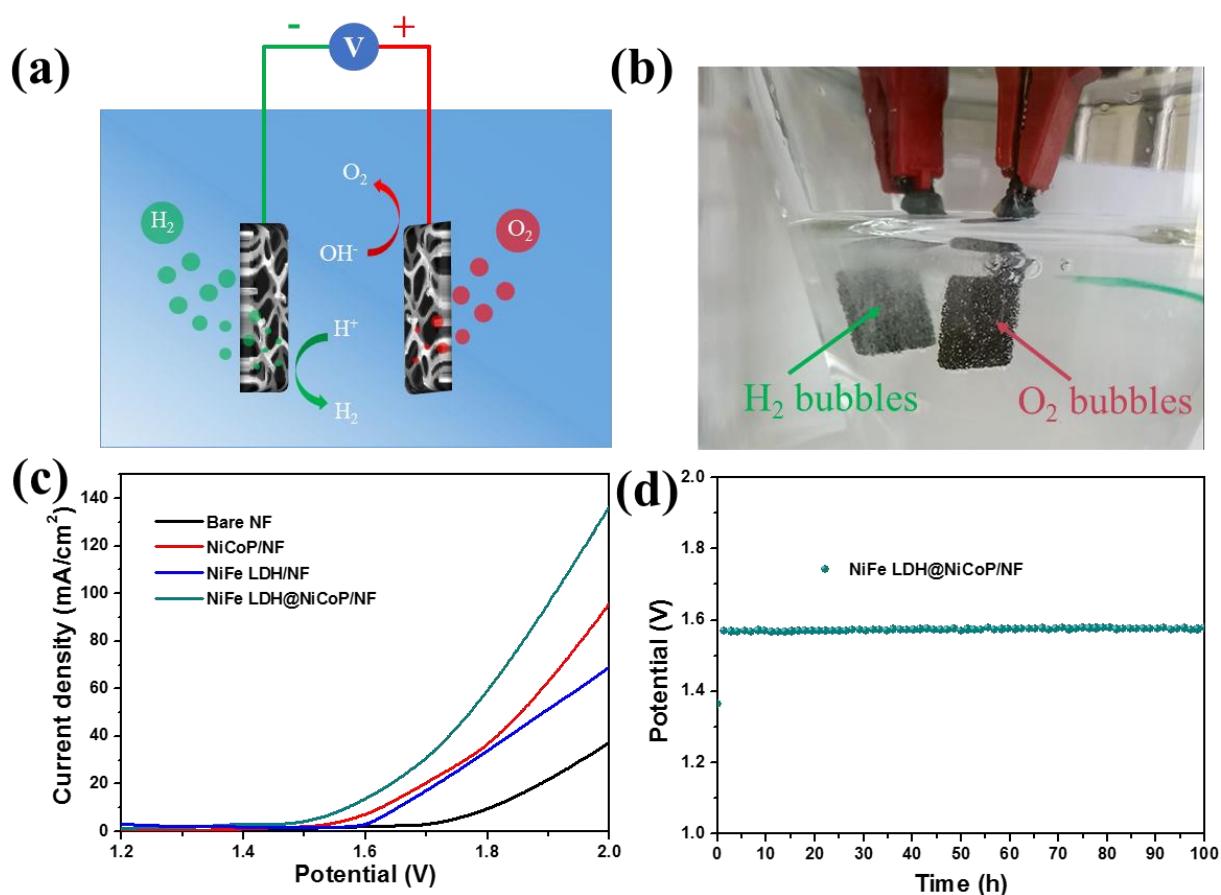


**Figure 3-6.** (a) Schematic representation of the two-electrode configuration in which a NiFe LDH@NiCoP/NF heterostructure was used as both anode and cathode for overall water splitting; (b) Digital photograph of the two-electrodes configuration during operation at a constant current density of 100 mA/cm<sup>2</sup>; (c) Polarization curve of as-prepared electrocatalysts; (d) Long-term stability test of the NiFe LDH@NiCoP/NF for overall water splitting recorded at a current density of 10 mA/cm<sup>2</sup> for 100 h.

### 3.5 Conclusions

In summary, a binder-free bifunctional 3D hierarchical heterostructure electrode consisting of NiFe LDH@NiCoP nanowires on a nickel foam has been successfully prepared through a simple three-step hydrothermal-phosphorization-hydrothermal method for efficient overall water splitting. Our results showed that the NiFe LDH and NiCoP were effectively coupled with strong electronic interaction, leading to facilitated charge transfer and enhanced reaction kinetics. Therefore, this heterostructure can fully utilize the advantage of both components and therefore generate a bifunctional and outstanding electrocatalyst for overall water splitting. The as-prepared NiFe LDH@NiCoP/NF electrodes achieved an excellent performance for both the HER and the OER combined with an outstanding stability in alkaline medium as compared to recently reported earth-abundant electrocatalysts. The enhanced performance of the bifunctional heterostructure was determined by a low overpotential of 120 mV and 220 mV at a current density of 10 mA/cm<sup>2</sup> without iR compensation for the HER and the OER, respectively. The overall water splitting of the NiFe LDH@NiCoP/NF electrodes exhibited a cell voltage of 1.57 V to achieve a current density of 10 mA/cm<sup>2</sup> with excellent stability. According to these results, the heterostructure NiFe LDH@NiCoP/NF electrode is a promising candidate for overall water splitting. Moreover, the synthetic strategy and interface engineering of the heterostructure can also be used to prepare other bifunctional electrocatalysts.

### 3.6 Acknowledgment

This research was financially supported by the BMBF-project Struktursolar. X.L. acknowledges financial support from the China Ministry of Science and Technology (Grant No. 2016YFA0202802) and the National Natural Science Foundation of China (Grant No. 21403280). The authors greatly acknowledge Dr. Frank Heyroth for TEM measurements performed at the Interdisciplinary Center of Materials Science (CMAT) of the Martin Luther University Halle-Wittenberg. The authors also thank Dr. Guowei Li from the Max Planck Institute for Chemical Physics of Solids for SEM-EDX measurements.

### 3.7 References

- [1] H. B. Gray, *Nat. Chem.* **2009**, *1*, 7.
- [2] a) M. Caban-Acevedo, M. L. Stone, J. R. Schmidt, J. G. Thomas, Q. Ding, H. C. Chang, M. L. Tsai, J. H. He, S. Jin, *Nat. Mater.* **2015**, *14*, 1245; b) G. Boyle, *Renewable energy: power for a sustainable future*, Taylor & Francis, 1997.
- [3] C. G. Morales-Guio, L. A. Stern, X. Hu, *Chem. Soc. Rev.* **2014**, *43*, 6555.
- [4] X. Li, X. Hao, A. Abudula, G. Guan, *J. Mater. Chem. A* **2016**, *4*, 11973.
- [5] a) L. Han, S. Dong, E. Wang, *Adv. Mater.* **2016**, *28*, 9266; b) W. Zhang, W. Lai, R. Cao, *Chem. Rev.* **2017**, *117*, 3717.
- [6] a) B. Liu, Y. F. Zhao, H. Q. Peng, Z. Y. Zhang, C. K. Sit, M. F. Yuen, T. R. Zhang, C. S. Lee, W. J. Zhang, *Adv. Mater.* **2017**; b) C. Tang, N. Cheng, Z. Pu, W. Xing, X. Sun, *Angew. Chem. Int. Ed. Engl.* **2015**, *54*, 9351.
- [7] J. Zhang, T. Wang, D. Pohl, B. Rellinghaus, R. Dong, S. Liu, X. Zhuang, X. Feng, *Angew. Chem. Int. Ed. Engl.* **2016**, *55*, 6702.
- [8] Y. Yang, K. Zhang, H. Lin, X. Li, H. C. Chan, L. Yang, Q. Gao, *ACS Catal.* **2017**, *7*, 2357.
- [9] C. Xiao, Y. Li, X. Lu, C. Zhao, *Adv. Funct. Mater.* **2016**, *26*, 3515.
- [10] Y. Hou, M. R. Lohe, J. Zhang, S. Liu, X. Zhuang, X. Feng, *Energy Environ. Sci.* **2016**, *9*, 478.
- [11] Z. Wang, S. Zeng, W. Liu, X. Wang, Q. Li, Z. Zhao, F. Geng, *ACS Appl. Mater. Interfaces* **2017**, *9*, 1488.
- [12] J. Liu, J. Wang, B. Zhang, Y. Ruan, L. Lv, X. Ji, K. Xu, L. Miao, J. Jiang, *ACS Appl. Mater. Interfaces* **2017**, *9*, 15364.
- [13] a) X. Wang, R. Tong, Y. Wang, H. Tao, Z. Zhang, H. Wang, *ACS Appl. Mater. Interfaces* **2016**, *8*, 34270; b) L.-A. Stern, L. Feng, F. Song, X. Hu, *Energy Environ. Sci.* **2015**, *8*, 2347; c) H. Huang, C. Yu, J. Yang, C. Zhao, X. Han, Z. Liu, J. Qiu, *ChemElectroChem* **2016**, *3*, 719; d) A. Han, H. Zhang, R. Yuan, H. Ji, P. Du, *ACS Appl. Mater. Interfaces* **2017**, *9*, 2240.
- [14] a) N. Jiang, B. You, M. L. Sheng, Y. J. Sun, *Angew. Chem. Int. Ed.* **2015**, *54*, 6251; b) H. Liang, A. N. Gandi, D. H. Anjum, X. Wang, U. Schwingenschlogl, H. N. Alshareef, *Nano Lett.* **2016**, *16*, 7718; c) G.-F. Chen, T. Y. Ma, Z.-Q. Liu, N. Li, Y.-Z. Su, K. Davey, S.-Z. Qiao, *Adv. Funct. Mater.* **2016**, *26*, 3314; d) B. You, N. Jiang, M. Sheng, M. W. Bhushan, Y. Sun, *ACS Catal.* **2016**, *6*, 714.
- [15] a) Z. Lu, W. Xu, W. Zhu, Q. Yang, X. Lei, J. Liu, Y. Li, X. Sun, X. Duan, *Chemical communication* **2014**, *50*, 6479; b) J. Chi, H. Yu, B. Qin, L. Fu, J. Jia, B. Yi, Z. Shao, *ACS Appl. Mater. Interfaces* **2017**, *9*, 464.
- [16] R. Zhang, X. Wang, S. Yu, T. Wen, X. Zhu, F. Yang, X. Sun, X. Wang, W. Hu, *Adv. Mater.* **2017**, *29*, 1605502.
- [17] A. W. Burns, K. A. Layman, D. H. Bale, M. E. Bussell, *Appl. Catal. A: Gen.* **2008**, *343*, 68.
- [18] S. Valeri, A. Borghi, G. C. Gazzadi, A. di Bona, *Surf. Sci.* **1999**, *423*, 346.

- [19] R. Ye, P. del Angel-Vicente, Y. Liu, M. J. Arellano-Jimenez, Z. Peng, T. Wang, Y. Li, B. I. Yakobson, S. H. Wei, M. J. Yacaman, J. M. Tour, *Adv. Mater.* **2016**, *28*, 1427.
- [20] a) B. Losiewicz, *Int. J. Hydrogen Energ.* **2004**, *29*, 145; b) A. W. Maijenburg, M. Regis, A. N. Hattori, H. Tanaka, K. S. Choi, J. E. ten Elshof, *ACS Appl. Mater. Interfaces* **2014**, *6*, 2003; c) B. Hinnemann, P. G. Moses, J. Bonde, K. P. Jorgensen, J. H. Nielsen, S. Horch, I. Chorkendorff, J. K. Nørskov, *J. Am. Chem. Soc.* **2005**, *127*, 5308.
- [21] Y. Wu, G.-D. Li, Y. Liu, L. Yang, X. Lian, T. Asefa, X. Zou, *Adv. Funct. Mater.* **2016**, *26*, 4839.
- [22] a) L. L. Feng, G. Yu, Y. Wu, G. D. Li, H. Li, Y. Sun, T. Asefa, W. Chen, X. Zou, *J. Am. Chem. Soc.* **2015**, *137*, 14023; b) M. Ledendecker, S. Krick Calderon, C. Papp, H. P. Steinruck, M. Antonietti, M. Shalom, *Angew. Chem. Int. Ed.* **2015**, *54*, 12361; c) J. Lee, G.-H. Lim, B. Lim, *Chem. Phys. Lett.* **2016**, *644*, 51; d) Q. Liu, S. Gu, C. M. Li, *J. Power Sources* **2015**, *299*, 342; e) J. Luo, J. H. Im, M. T. Mayer, M. Schreier, M. K. Nazeeruddin, N. G. Park, S. D. Tilley, H. J. Fan, M. Gratzel, *Science* **2014**, *345*, 1593; f) Y. Rao, Y. Wang, H. Ning, P. Li, M. Wu, *ACS Appl. Mater. Interfaces* **2016**, *8*, 33601; g) J. Zhang, T. Wang, D. Pohl, B. Rellinghaus, R. Dong, S. Liu, X. Zhuang, X. Feng, *Angew. Chem.* **2016**, *128*, 6814; h) Z. Y. Zhang, S. S. Liu, F. Xiao, S. Wang, *ACS Sustain. Chem. Eng.* **2017**, *5*, 529.
- [23] W. Li, X. Gao, X. Wang, D. Xiong, P.-P. Huang, W.-G. Song, X. Bao, L. Liu, *J. Power Sources* **2016**, *330*, 156.
- [24] a) H. Liang, H. N. Alshareef, *Small Methods* **2017**, *1*, 1700111; b) B. Zhang, Y. H. Lui, H. Ni, S. Hu, *Nano Energy* **2017**, *38*, 553.
- [25] Q. Xiao, Y. Zhang, X. Guo, L. Jing, Z. Yang, Y. Xue, Y. M. Yan, K. Sun, *Chem. Commun.* **2014**, *50*, 13019.
- [26] H. Dau, C. Limberg, T. Reier, M. Risch, S. Roggan, P. Strasser, *ChemCatChem* **2010**, *2*, 724.
- [27] X. Wang, W. Li, D. Xiong, D. Y. Petrovykh, L. Liu, *Adv. Funct. Mater.* **2016**, *26*, 4067.
- [28] X. Liu, W. Liu, M. Ko, M. Park, M. G. Kim, P. Oh, S. Chae, S. Park, A. Casimir, G. Wu, J. Cho, *Adv. Funct. Mater.* **2015**, *25*, 5799.
- [29] a) W. X. Zhu, X. Y. Yue, W. T. Zhang, S. X. Yu, Y. H. Zhang, J. Wang, J. L. Wang, *Chem. Commun.* **2016**, *52*, 1486; b) Y. Yu, P. Li, X. Wang, W. Gao, Z. Shen, Y. Zhu, S. Yang, W. Song, K. Ding, *Nanoscale* **2016**, *8*, 10731; c) R. Xu, R. Wu, Y. Shi, J. Zhang, B. Zhang, *Nano Energy* **2016**, *24*, 103; d) J. Tian, N. Cheng, Q. Liu, X. Sun, Y. He, A. M. Asiri, *J. Mater. Chem. A* **2015**, *3*, 20056; e) T. Liu, Q. Liu, A. M. Asiri, Y. Luo, X. Sun, *Chem. Commun.* **2015**, *51*, 16683; f) D. Liu, Q. Lu, Y. Luo, X. Sun, A. M. Asiri, *Nanoscale* **2015**, *7*, 15122; g) G.-F. Chen, T. Y. Ma, Z.-Q. Liu, N. Li, Y.-Z. Su, K. Davey, S.-Z. Qiao, *Adv. Funct. Mater.* **2016**, *26*, 3314.
- [30] H. Zhang, C. Lin, F. Du, Y. Zhao, P. Gao, H. Chen, Z. Jiao, X. Li, T. Zhao, Y. Sun, *ACS Sustain. Chem. Eng.* **2015**, *3*, 2049.



### 3.8 Supporting Information

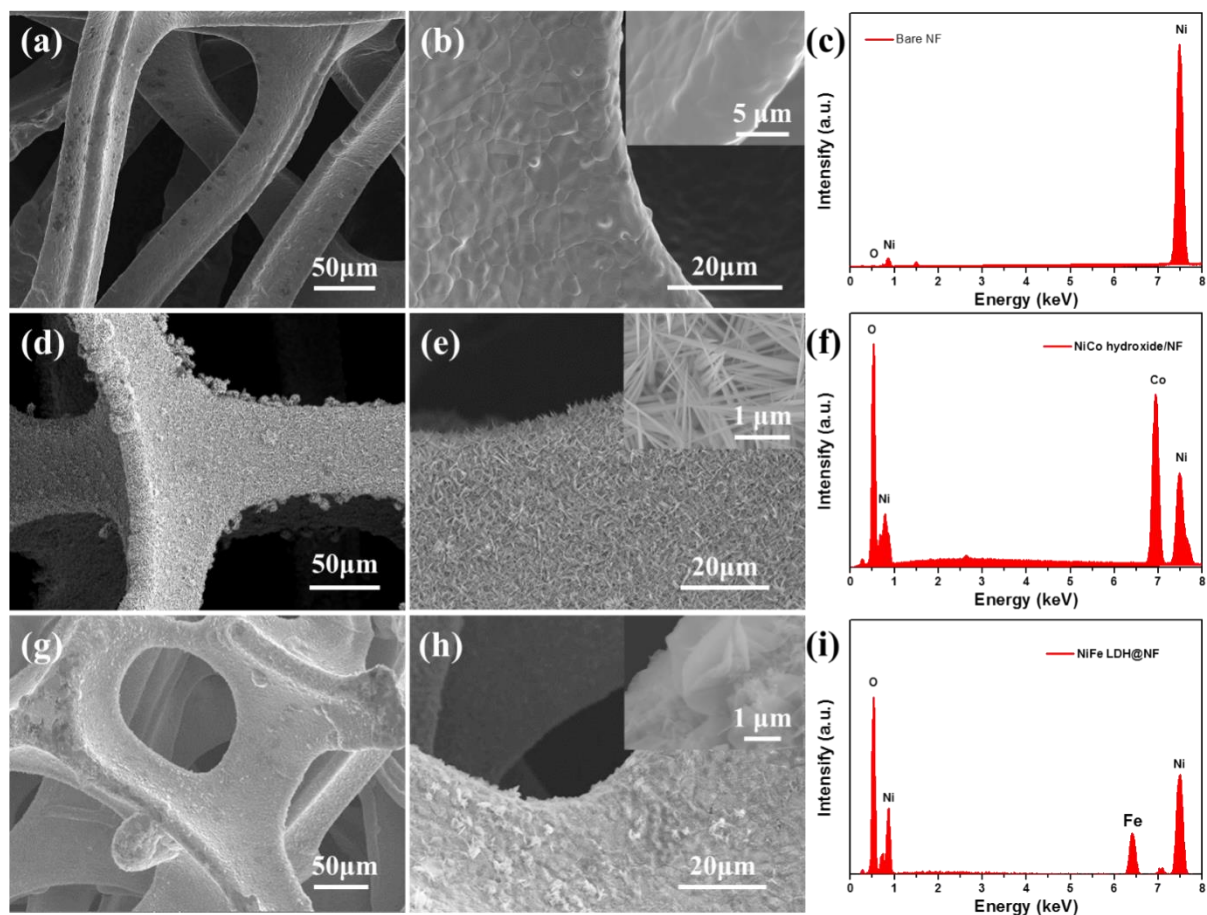


**Figure S 3-1.** (a-b), (d-e) and (g-h) are the SEM images of the bare NF, NiCo hydroxide /NF and NiFe LDH/NF, respectively, whereas the insets show high-resolution images. (c), (f) and (i) are the corresponding EDX spectra of bare NF, NiCo hydroxide /NF and NiFe LDH/NF, respectively.

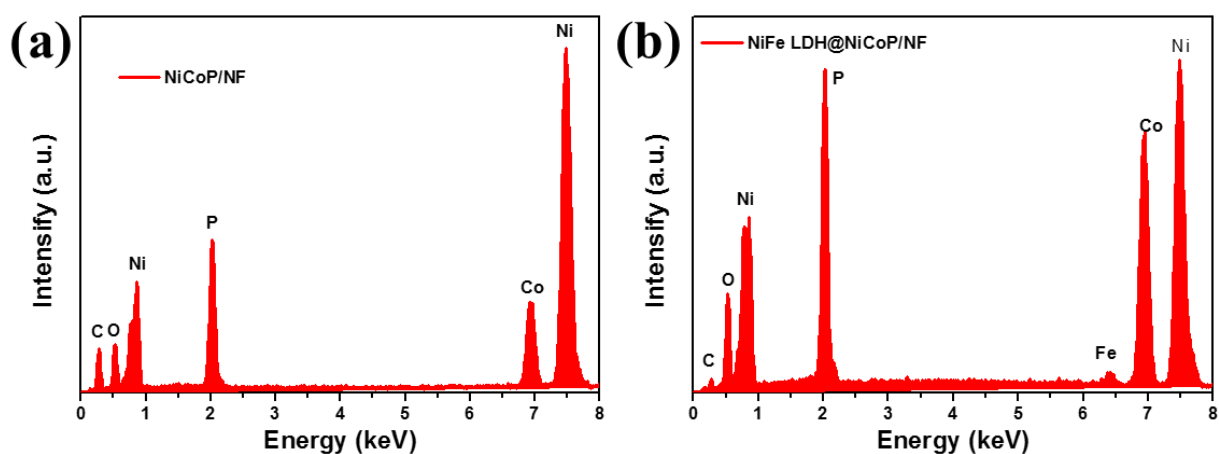


**Figure S 3-2.** EDX spectra of the as-prepared (a) NiCoP/NF and (b) NiFe LDH@NiCoP/NF.

**Table S 3-1.** EDX results of the as-prepared electrocatalysts.

Samples	Ni (atom%)	O (atom%)	Co (atom%)	P (atom%)	Fe (atom%)	K (atom%)
Bare NF	98.96	1.04	--	--	--	--
NiCo hydroxide/NF	17.00	57.13	25.87	--	--	--
NiCoP/NF	53.90	16.68	12.30	17.29	--	--
NiFe LDH/NF	23.05	71.27	--	--	5.69	--
NiFe LDH@NiCoP/NF	33.07	21.61	21.99	22.31	1.02	--
NiFe LDH@NiCoP/NF post HER	32.62	49.57	5.98	10.29	0.74	0.81
NiFe LDH@NiCoP/NF post OER	16.16	68.09	4.88	5.98	0.55	4.35

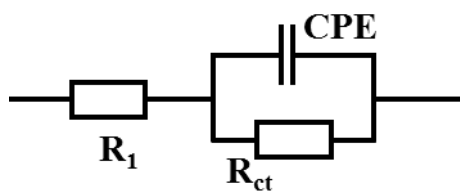


**Figure S 3-3.** The equivalent circuit diagram used for analysis of the EIS curves measured for the OER and the HER

**Table S 3-2.** Summary of the EIS results fitted to the equivalent circuit board as shown in Figure S 3-3.

Sample	Reaction	$R_{ct}$ ( $\Omega$ )	$R_1$ ( $\Omega$ )	CPE	
				$Y_0$ ( $\mu\text{Mho}$ )	n
Bare NF	HER	34.5	1.20	0.625	0.86
	OER	5.39	1.11	0.052	0.811
NiCoP/NF	HER	6.01	1.10	2.29	0.866
	OER	1.39	1.16	1.15	0.994
NiFe LDH/NF	HER	20.80	1.15	1.27	0.851
	OER	0.63	1.10	0.625	0.555
NiFe LDH@NiCoP/NF	HER	2.77	1.20	9.16	0.824
	OER	0.41	1.10	2.08	0.613

**Table S 3-3.** Comparison of the HER performance of our NiFe LDH@NiCoP/NF heterostructure to other reported electrocatalysts in alkaline media.

Catalyst	Electrolyte (KOH)	$\eta_{10}^a$ (mV)	Tafel slope (mV/dec)	Durability (h)	Ref.
NiFe LDH@NiCoP/NF	1 M	120	88.2	100	This work
NiFe/NiCo <sub>2</sub> O <sub>4</sub> /NF <sup>b</sup>	1 M	105	88	10	[S1]
NiFe LDH/NiCo <sub>2</sub> O <sub>4</sub> /NF	1 M	192	59	10	[S2]
NiFe LDH@NiCo <sub>2</sub> S <sub>4</sub> /NF <sup>b</sup>	1 M	200	101.1	12	[S3]
MoS <sub>2</sub> /Ni <sub>3</sub> S <sub>2</sub> /NF <sup>b</sup>	1 M	110	83	10	[S4]
NiO@Ni@Carbon fiber	1 M	153	84	24	[S5]
EG/Co <sub>0.85</sub> Se/NiFe LDH <sup>b</sup>	1 M	260	125	10	[S6]
NiCo <sub>2</sub> P <sub>x</sub> /Carbon felt <sup>b</sup>	1 M	58	34.3	30	[S7]
NiFe LDH/NF	1 M	210	58.9	10	[S8]
Ni <sub>3</sub> P <sub>4</sub> /Ni foil	1 M	150	53	20	[S9]
Ni(OH) <sub>2</sub> /NF	1 M	172	140	24	[S10]
Ni <sub>3</sub> S <sub>2</sub> /NF	1 M	223	--	200	[S11]
Ni(OH) <sub>2</sub> /NF	1 M	298	--	--	[S12]
Cu-P/Cu foam <sup>b</sup>	1 M	98	55	15	[S13]

If not mentioned specifically, all overpotentials were acquired without iR compensation.

<sup>a</sup> Overpotential ( $\eta$ ) at a current density of 10 mA/cm<sup>2</sup>; <sup>b</sup> Overpotential ( $\eta$ ) acquired at a current density of 10 mA/cm<sup>2</sup> with additional iR compensation.

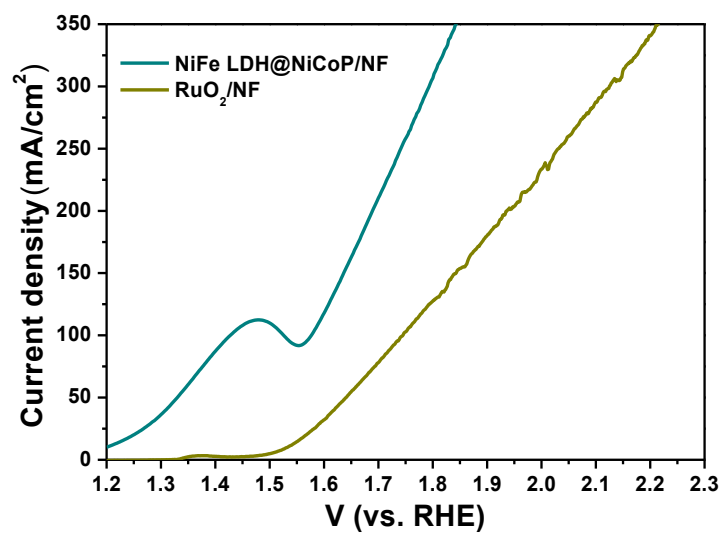


**Figure S 3-4.** Comparison of the as prepared NiFe LDH@NiCoP/NF with RuO<sub>2</sub>/NF for the OER activity.

**Table S 3-4.** Comparison of OER performance for NiFe LDH@NiCoP/NF with other reported electrocatalysts in the alkaline media.

Catalyst	Electrolyte (KOH)	$\eta_{10}^a$ (mV)	Tafel slope (mV/dec)	Stability (h)	Ref.
NiFe LDH@NiCoP/NF	1 M	220	48.6	100	This work
NiFe/NiCo <sub>2</sub> O <sub>4</sub> /NF <sup>b</sup>	1 M	340 <sup>e</sup>	45.5	10	[S1]
NiFe-LDH/NiCo <sub>2</sub> O <sub>4</sub> /NF	1 M	290	53	10	[S2]
NiFe LDH@NiCo <sub>2</sub> S <sub>4</sub> /NF	1 M	201 <sup>d</sup>	46.3	10	[S3]
MoS <sub>2</sub> /Ni <sub>3</sub> S <sub>2</sub> /NF <sup>b</sup>	1 M	218	88	10	[S4]
NiO@Ni@Carbon fiber	1 M	300	60	24	[S5]
NiFe LDHs@FeOOH/NF <sup>b</sup>	1 M	208	42	20	[S14]
NiFe LDH@Co <sub>0.85</sub> Se/NF <sup>b</sup>	1 M	270 <sup>e</sup>	57	10	[S6]
Ni <sub>5</sub> P <sub>4</sub> /Ni foil	1 M	290	40	20	[S9]
Ni(OH) <sub>2</sub> /NF	1 M	330 <sup>d</sup>	150	24	[S10]
NiFe LDH/NF	1 M	240	58.9	--	[S8]
Ni <sub>3</sub> S <sub>2</sub> /NF	1 M	280 <sup>f</sup>	--	200	[S11]
Ni(OH) <sub>2</sub> /NF	1 M	350	--	--	[S12]
Cu-P/Cu foam <sup>b</sup>	1 M	325	120	15	[S13]
RuO <sub>2</sub> <sup>b</sup>	1 M	350	85	--	[S15]
IrO <sub>2</sub> <sup>b</sup>	1 M	350	67	--	[S15]

If not mentioned specifically, all overpotentials were acquired without iR compensation.

<sup>a</sup> Overpotential ( $\eta$ ) at the current density of 10 mA/cm<sup>2</sup>; <sup>b</sup> the overpotential was corrected with iR compensation. <sup>c</sup> Current density at 1200 mA/cm<sup>2</sup> with 65 % iR compensation. <sup>d</sup> Current density at 50 mA/cm<sup>2</sup>. <sup>e</sup> Current density at 150 mA/cm<sup>2</sup>; <sup>f</sup> Current density at 200 mA/cm<sup>2</sup>.

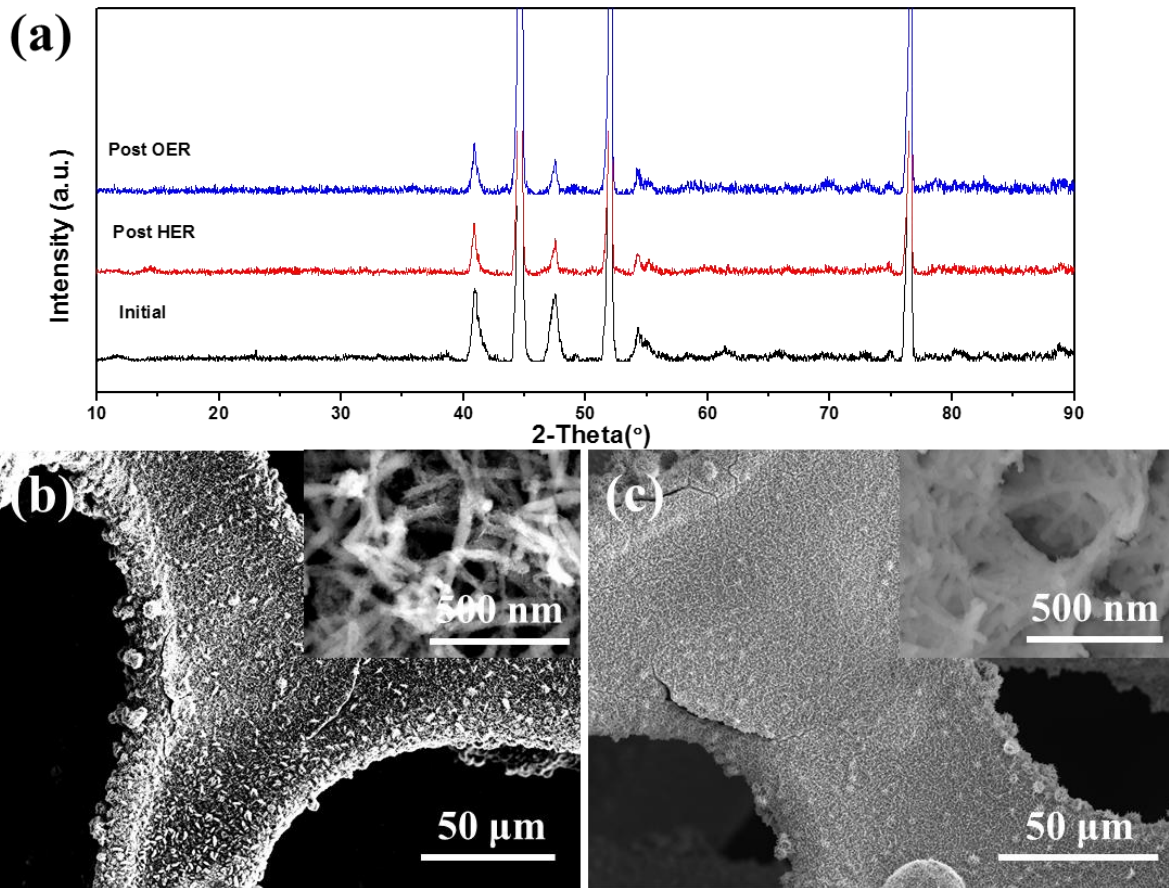


**Figure S 3-5.** (a) XRD pattern comparison of the NiFe LDH@NiCoP, post HER and post OER measurements. SEM images of the NiFe LDH@NiCoP heterostructure after (b) HER and (c) OER measurement, inset images are the corresponding high-resolution SEM images.

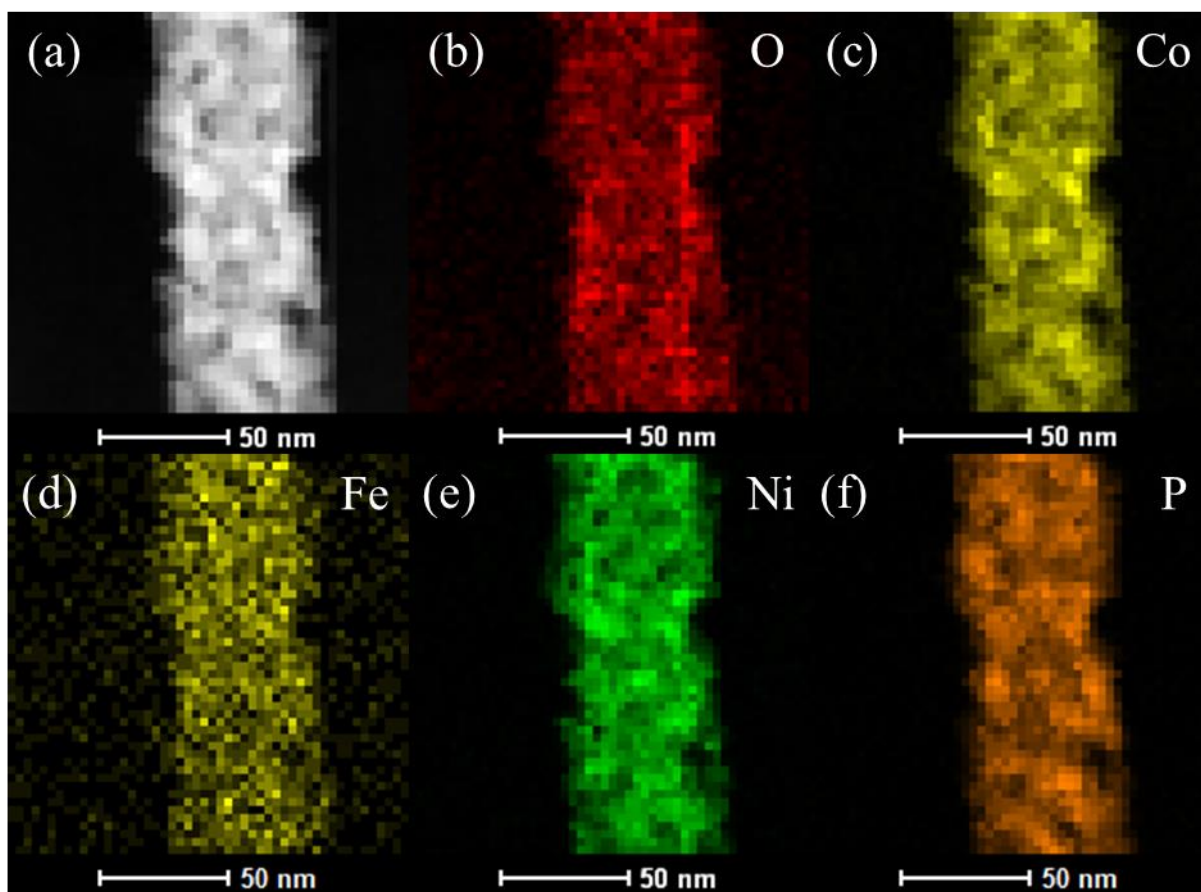


**Figure S 3-6.** EDX mapping of the NiFe LDH@NiCoP/NF after long time OER measurement. (a) TEM image of the NiFe LDH@NiCoP and the corresponding element distribution of (b) O, (c) Co, (d) Fe, (e) Ni and (f) P.



**Table S 3-5.** Comparison of the overall water splitting performance of NiFe LDH@NiCoP/NF with other reported electrocatalysts in alkaline medium.

Catalyst	Electrolyte (KOH)	$\eta_{10}^a$ (mV)	Stability (h)	Ref.
NiFe LDH@NiCoP/NF	1 M	340	100	This work
NiFe/NiCo <sub>2</sub> O <sub>4</sub> /NF	1 M	440	10	[S1]
NiFe LDH/NiCo <sub>2</sub> O <sub>4</sub> /NF	1 M	370	12	[S2]
NiFe LDH@NiCo <sub>2</sub> S <sub>4</sub> /NF	1 M	370	12	[S3]
MoS <sub>2</sub> -Ni <sub>3</sub> S <sub>2</sub> /NF	1 M	330	12	[S4]
NiO@Ni@Carbon fiber	1 M	500 <sup>b</sup>	60	[S5]
NiFe LDH@Co <sub>0.85</sub> Se/NF	1 M	440	10	[S6]
NiFe LDH/NF	1 M	470	3	[S8]
Ni <sub>5</sub> P <sub>4</sub> /NF	1 M	470	20	[S9]
NiCoP/NF	1 M	350	25	[S16]
NiSe/NF	1 M	400	20	[S17]
Ni <sub>3</sub> Se <sub>2</sub> /NF	1 M	380	140	[S18]
NiS/NF	1 M	410	35	[S19]
NiCo <sub>2</sub> S <sub>4</sub> /carbon cloth	1 M	450	10	[S20]
V/NF	1 M	510	24	[S21]
NiP/NF	1 M	380	4.2	[S22]
Ni(OH) <sub>2</sub> /NF	1 M	450	24	[S10]
Ni <sub>3</sub> S <sub>2</sub> /NF	1 M	530	200	[S11]
Ni(OH) <sub>2</sub> /NF	1 M	600	--	[S12]
Ni-P/Cu foam	1 M	450	15	[S13]
NiMo HNRs/Ti mesh	1 M	410	10	[S23]
CoSe/Ti mesh	1 M	430	25	[S24]
NiCo <sub>2</sub> S <sub>4</sub> /Carbon cloth	1 M	450	10	[S20]
Cu <sub>3</sub> P/NF	1 M	440	12	[S25]

<sup>a</sup> Overpotential ( $\eta$ ) at an applied current density of 10 mA/cm<sup>2</sup>; <sup>b</sup> Current density at an applied current density of 20 mA/cm<sup>2</sup>.

## References

- [S1] C. Xiao, Y. Li, X. Lu, C. Zhao, *Adv. Funct. Mater.* **2016**, *26*, 3515.
- [S2] Z. Wang, S. Zeng, W. Liu, X. Wang, Q. Li, Z. Zhao, F. Geng, *ACS Appl. Mater. Interfaces* **2017**, *9*, 1488.
- [S3] J. Liu, J. Wang, B. Zhang, Y. Ruan, L. Lv, X. Ji, K. Xu, L. Miao, J. Jiang, *ACS Appl. Mater. Interfaces* **2017**, *9*, 15364.
- [S4] J. Zhang, T. Wang, D. Pohl, B. Rellinghaus, R. Dong, S. Liu, X. Zhuang, X. Feng, *Angew. Chem.* **2016**, *128*, 6814.
- [S5] Z. Y. Zhang, S. S. Liu, F. Xiao, S. Wang, *ACS Sustain. Chem. Eng.* **2017**, *5*, 529.
- [S6] Y. Hou, M. R. Lohe, J. Zhang, S. Liu, X. Zhuang, X. Feng, *Energy Environ. Sci.* **2016**, *9*, 478.
- [S7] R. Zhang, X. Wang, S. Yu, T. Wen, X. Zhu, F. Yang, X. Sun, X. Wang, W. Hu, *Adv. Mater.* **2017**, *29*, 1605502.
- [S8] J. Luo, J. H. Im, M. T. Mayer, M. Schreier, M. K. Nazeeruddin, N. G. Park, S. D. Tilley, H. J. Fan, M. Gratzel, *Science* **2014**, *345*, 1593.
- [S9] M. Ledendecker, S. Krick Calderon, C. Papp, H. P. Steinruck, M. Antonietti, M. Shalom, *Angew. Chem. Int. Ed.* **2015**, *54*, 12361.
- [S10] Y. Rao, Y. Wang, H. Ning, P. Li, M. Wu, *ACS Appl. Mater. Interfaces* **2016**, *8*, 33601.
- [S11] L. L. Feng, G. Yu, Y. Wu, G. D. Li, H. Li, Y. Sun, T. Asefa, W. Chen, X. Zou, *J. Am. Chem. Soc.* **2015**, *137*, 14023.
- [S12] J. Lee, G.-H. Lim, B. Lim, *Chem. Phys. Lett.* **2016**, *644*, 51.
- [S13] Q. Liu, S. Gu, C. M. Li, *J. Power Sources* **2015**, *299*, 342.
- [S14] J. Chi, H. Yu, B. Qin, L. Fu, J. Jia, B. Yi, Z. Shao, *ACS Appl. Mater. Interfaces* **2017**, *9*, 464.
- [S15] Q. Xiao, Y. Zhang, X. Guo, L. Jing, Z. Yang, Y. Xue, Y. M. Yan, K. Sun, *Chem. Commun.* **2014**, *50*, 13019.
- [S16] H. Liang, A. N. Gandi, D. H. Anjum, X. Wang, U. Schwingenschlogl, H. N. Alshareef, *Nano Lett.* **2016**, *16*, 7718.
- [S17] C. Tang, N. Cheng, Z. Pu, W. Xing, X. Sun, *Angew. Chem. Int. Ed. Engl.* **2015**, *54*, 9351.
- [S18] R. Xu, R. Wu, Y. Shi, J. Zhang, B. Zhang, *Nano Energy* **2016**, *24*, 103.
- [S19] W. X. Zhu, X. Y. Yue, W. T. Zhang, S. X. Yu, Y. H. Zhang, J. Wang, J. L. Wang, *Chem. Commun.* **2016**, *52*, 1486.
- [S20] D. Liu, Q. Lu, Y. Luo, X. Sun, A. M. Asiri, *Nanoscale* **2015**, *7*, 15122.
- [S21] Y. Yu, P. Li, X. Wang, W. Gao, Z. Shen, Y. Zhu, S. Yang, W. Song, K. Ding, *Nanoscale* **2016**, *8*, 10731.
- [S22] G.-F. Chen, T. Y. Ma, Z.-Q. Liu, N. Li, Y.-Z. Su, K. Davey, S.-Z. Qiao, *Adv. Funct. Mater.* **2016**, *26*, 3314.
- [S23] J. Tian, N. Cheng, Q. Liu, X. Sun, Y. He, A. M. Asiri, *J. Mater. Chem. A* **2015**, *3*, 20056.
- [S24] T. Liu, Q. Liu, A. M. Asiri, Y. Luo, X. Sun, *Chem. Commun.* **2015**, *51*, 16683.
- [S25] A. Han, H. Zhang, R. Yuan, H. Ji, P. Du, *ACS Appl. Mater. Interfaces* **2017**, *9*, 2240.

# **4 Optimization of Chemical Vapor Deposition Process for Carbon Nanotubes Growth on Stainless Steel: Towards Efficient Hydrogen Evolution Reaction**

This chapter can be referred to:

**H. Zhang**; J. M. de Souza e Silva; C. S. de Oliveira; X. Lu, S. L. Schweizer, A. W. Maijenburg, M. Bron, R. B. Wehrspohn, Optimization of Chemical Vapor Deposition Process for Carbon Nanotubes Growth on Stainless Steel: Towards Efficient Hydrogen Evolution Reaction. *MRS Advances* 2020.

## 4.1 Abstract

We report a novel strategy to render stainless steel (SS) a more versatile material that is suitable to be used as the substrate for preparing electrodes for efficient hydrogen evolution by interface engineering. Our strategy involves the growth of carbon nanotubes (CNTs) by atmospheric pressure chemical vapor deposition (APCVD) as the interface material on the surface of SS. We optimized the procedure to prepare CNTs/SS and demonstrate a higher activity of the CNTs/SS prepared at 700 °C for the hydrogen evolution reaction (HER) when compared to samples prepared at other temperatures. This can be attributed to the higher number of defects and the higher content of pyrrolic N obtained at this temperature. Our strategy offers a new approach to employ SS as a substrate for the preparation of highly efficient electrodes and has the potential to be widely used in electrochemistry.

## 4.2 Introduction

Stainless steel (SS) is becoming more and more popular to be used in electrochemical water splitting due to its cost-efficiency and excellent stability.[1] SS can be directly used as an electrode for water splitting. In this case, efforts have been devoted to change the composition and morphology of the SS surface in order to expose more active sites and increase its surface area. For example, Schäfer et al. oxidized the surface of AISI 304 steel with  $\text{Cl}_2$ . The oxidized AISI 304 steel exhibited an enhanced oxygen evolution reaction (OER) activity.[2] They also electrochemically oxidized  $\text{Ni}_{42}$  steel.[3] These are efficient approaches to improve the OER activity of SS-based electrodes, but the hydrogen evolution reaction (HER) performances showed only minor improvements. SS can also be used as a substrate for modification with highly active electrocatalysts. For example, Chen et al. prepared NiS-modified SS electrodes that exhibit high OER activity.[4] Ring et al. modified  $\text{Ni}_{42}$  steel with Pt towards enhanced HER performance.[5] However, the interfacial properties of the SS severely restrict the possibility to couple SS with other catalysts to further improve the catalytic activity, especially for the HER. Therefore, depositing an effective interface material is an essential tool for interface engineering of SS to make it more versatile.

Herein, we developed a novel strategy for improving the interface engineering of SS-based electrocatalysts by employing carbon nanotubes (CNTs) as the interface material. The CNTs were grown on the surface of SS by atmospheric pressure chemical vapor deposition (APCVD). The procedure for double pulse deposition (DPD) of Fe nanoparticles, which work as catalysts for CVD growth, and the CVD process for the growth of CNTs were optimized. The optimized CNTs/SS was prepared at  $700\text{ }^\circ\text{C}$  and demonstrated the best HER activity owing to the higher number of defects and the higher content of pyrrolic N in this sample. Our strategy offers a new method to make SS a more versatile material, and thus shows potential to be used in various electrochemical research areas.

## 4.3 Experimental Section

**CVD process of growing CNTs on the surface of SS (CNTs/SS).** CVD process of growing CNTs on the surface of SS (CNTs/SS): CNTs/SS composites were prepared by APCVD as reported in the literature.[6] Firstly, the SS substrate (AISI 316 L) was cleaned with acetone, ethanol and 3 M HCl for 15 min by ultrasonication. Subsequently, the Fe NPs were electrodeposited on the SS by a double pulse deposition (DPD) in a solution containing 0.01 M  $\text{FeSO}_4 \cdot 7\text{H}_2\text{O}$ , 0.1 M  $\text{Na}_2\text{SO}_4$  and 0.015 mM L-Ascorbic acid. An  $\text{Ag}|\text{AgCl}|\text{KCl}_{\text{sat}}$  reference and

a Pt wire were used as the reference electrode and the counter electrode, respectively. Afterwards, the SS with deposited Fe nanoparticles was put into a horizontal tube furnace equipped with a quartz tube. For the growth of CNTs, acetonitrile and H<sub>2</sub>/Ar (50 %, v/v) were used as the carbon source and the reducing gas, respectively. Different CNTs growth temperatures were employed, all of which were reached with a ramping rate of 10 °C/min and the targeted temperature was maintained for 30 min. H<sub>2</sub>/Ar reducing gas was purged through the CVD reactor with a flow rate of 6 L/h throughout the CVD process, including the temperature ramping stage, substrate reducing stage and CNTs growth stage. However, acetonitrile was only injected into the CVD reactor from a saturator by using the H<sub>2</sub>/Ar reducing gas as the carrier gas during the CNTs growth stage. Finally, the sample was cooled down to room temperature in an N<sub>2</sub> atmosphere.

**Characterization.** Scanning electron microscopy (SEM) characterization was carried out with an FEI Quanta 650 FEG scanning electron microscope equipped with an X-ray detector for energy-dispersive X-ray spectroscopy (EDS) and a focused ion beam (FIB). Transmission electron microscopy (TEM) measurements were conducted with a Zeiss Leo 912 Omega TEM. X-ray photoelectron spectroscopy (XPS) data were obtained employing an X-ray Photoelectron Spectrometer System equipped with a monochromatic Al K $\alpha$  X-ray source (Thermo Scientific<sup>TM</sup> K-Alpha<sup>TM</sup>). The C1s peak (248.8 eV) was used as the reference for the calibration of all XPS spectra. Raman spectra were acquired using a LabRAM HR Evolution, HORIBA. X-ray microscopy measurements (XRM) were performed on a Carl Zeiss Xradia 810 Ultra by using Zernike phase-contrast imaging.

**Electrochemical measurements.** All electrochemical measurements were recorded by an Autolab PGSTAT302N Potentiostat in a three-electrode setup by using a Pt wire and an Ag|AgCl|KCl<sub>sat.</sub> as the counter electrode and the reference electrode in 1 M KOH, respectively. Linear sweep voltammograms of the HER activity were recorded with a scan rate of 10 mV s<sup>-1</sup> without iR compensation. The long-time measurement was acquired at a constant current density of -10 mA cm<sup>-2</sup>. All potential values were converted to the reversible hydrogen electrode (RHE) using the equation  $E_{RHE} = E_{Ag|AgCl|KCl_{sat}} + 0.197 + 0.059 \text{ pH}$ .

#### 4.4 Results and Discussion

For the growth of CNTs on the surface of SS, a piece of SS (1 × 2 cm<sup>2</sup>) was put into a tube furnace and heated to 700 °C for 30 min with acetonitrile and H<sub>2</sub>/Ar (50%, v/v) as the carbon source and reducing gas, respectively, as detailed in the experimental section. In this

case, no homogeneous CNT layer was obtained, and a thick layer of carbon was observed (**Figure 4-1(a)**). Therefore, Fe NPs were electrodeposited onto the surface of SS as an additional catalyst for the growth of CNTs by a DPD method (Figure 4-1(b)).[6] The size and number of electrodeposited Fe NPs can be controlled by changing  $t_1$  and  $t_2$  as well as the deposition potentials. In order to simplify the optimization process,  $t_2$  in the DPD process was kept consistent at 10 s and the potentials  $V_1$  and  $V_2$  were kept constant at -3 V and -1 V, respectively. The size of the deposited Fe NPs increased with the increase of  $t_1$  (Figure 4-1(c-e), inset c1, d1, and e1). After the CVD process, the coverage of the surface with CNTs is more homogeneous (Figure 4-1(c-e), inset c2, d2, and e2). When  $t_1$  is 60 s, the obtained CNTs/SS has an improved morphology with a uniform coating of CNTs on the surface of SS (Figure 4-1(e)). The temperature-dependent growth behavior of the CNTs was also evaluated by growing CNTs at different temperatures. As shown in Figure 4-1(e-h), the growth rate of the CNTs was increased along with the increase in temperature, and the temperature window for successful and homogeneous CNT growth can be varied from 600 °C up to at least 750 °C. It should be noted that metal NPs were clearly observed on the top of the CNTs when grown at 650 °C, indicating that the growth of the CNTs follows the tip growth mechanism.[7]

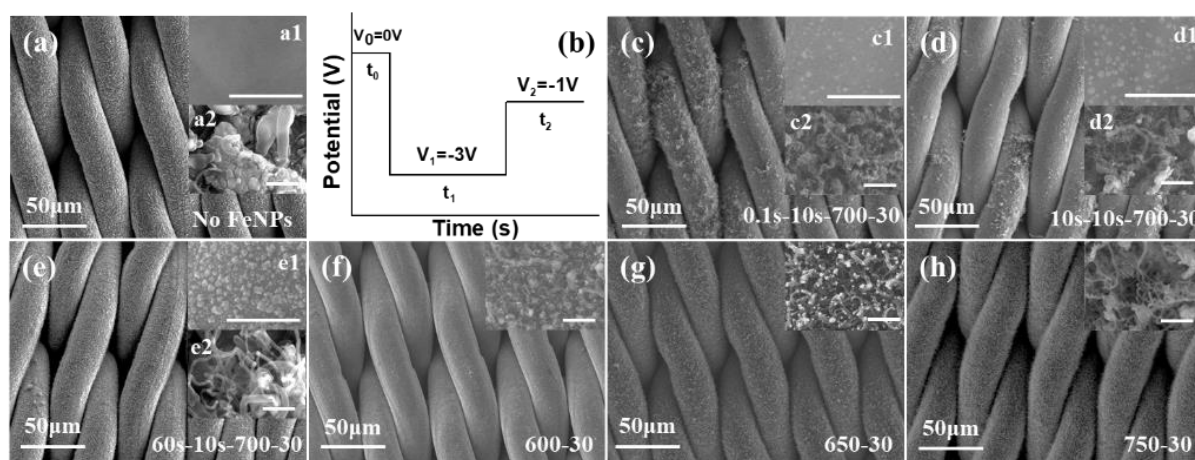


Figure 4-1. (a) SEM images of CNTs/SS grown without any additional catalysts at 700 °C for 30 min. a1 and a2 are the high-resolution SEM images of the surface of SS before and after the growth of the CNTs, respectively. (b) DPD process for the deposition of Fe nanoparticles on the surface of SS. (c-e) SEM images of CNTs/SS prepared at 700 °C for 30 min with different DPD parameters ( $t_1$ - $t_2$ -CVD temperature-time). The corresponding SEM images of the surface of SS before and after CVD are shown in the inset on the top (c1, d1 and e1) and bottom (c2, d2, and e2) of the figure, respectively. (f-h) SEM images of CNTs/SS prepared at different temperatures with the additional Fe nanoparticle catalysts deposited at  $t_1 = 60$  s and  $t_2 = 10$  s. The HRSEM images are shown in the inset. Scale bars are 500 nm, if not stated differently.

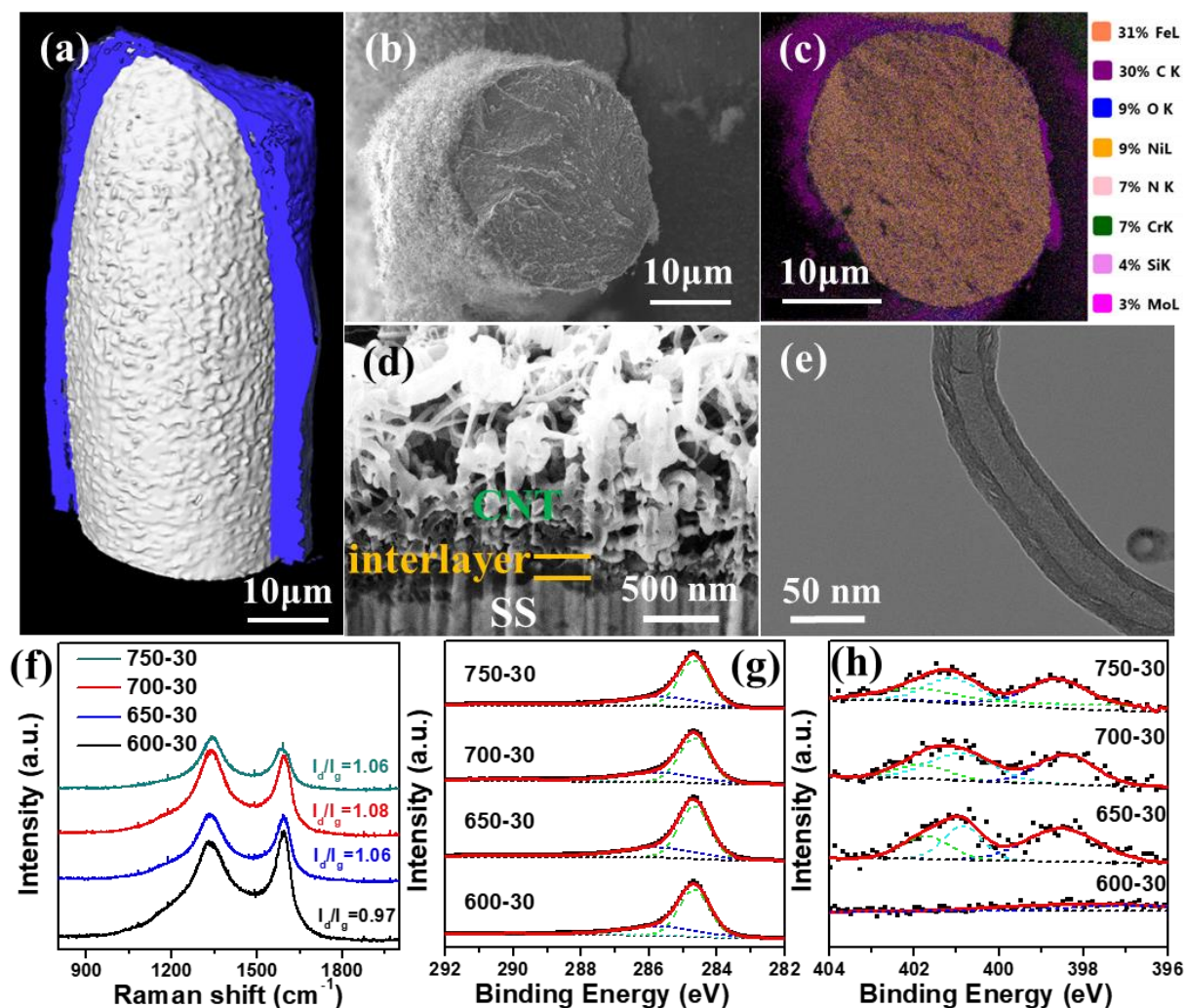


Figure 4-2. (a) 3D representation of the prepared CNTs/SS reconstructed from XRM imaging, showing the CNTs coverage virtually cut and pseudo-colored in blue and SS in grey. (b) Cross-section SEM images of the CNT/SS prepared at 700 °C (c) EDS mapping of the CNTs/SS and the corresponding quantification results shown in the inset. (d) HRSEM image of the cross-section of CNTs/SS prepared by FIB. (e) TEM image of the CNTs grown on the SS. (f) Raman spectra of the CNTs/SS prepared at different temperatures. (g, h) XPS spectra of (g) C 1s and (h) N 1s of the CNTs/SS synthesized at different temperatures.

The interface engineering of the SS using CNTs as interfacial material was further evaluated and **Figure 4-2(a)** shows the 3D model reconstructed by XRM imaging, with a virtual cut showing the growth of CNTs around the SS. The cross-section SEM image of CNTs/SS (Figure 4-2(b)) agrees with the XRM results. The EDS mapping also shows that the grown CNTs are homogeneously distributed on the surface of the SS (Figure 4-2(c)). Furthermore, the high-resolution cross-section view of the CNTs/SS prepared with FIB (Figure 4-2(d)) shows that the grown CNTs are connected to the SS by an interlayer, which most probably consists of Fe and C.<sup>[5]</sup> The grown CNTs exhibit a hollow morphology, as shown by TEM (Figure 4-2(e)).



**Table 4-1.** XPS analysis results of the N 1s for the CNTs/SS synthesized at different temperatures.

Sample	N content (atom %)	Pyridinic N (eV) (atom %)	Pyrrolic N (eV) (atom %)	Graphitic N (eV) (atom %)
600-30	0.9	--	--	--
650-30	2.1	398.52 (49.9%)	400.85 (27.3%)	401.73 (22.7%)
700-30	2.1	398.39 (39.7%)	400.89 (42.3%)	401.89 (18.0%)
750-30	2.9	398.64 (39.1%)	401.14 (34.3%)	401.94 (26.6%)

The CNTs/SS prepared at different temperatures were also characterized by Raman spectroscopy and X-ray photoelectron spectroscopy (XPS). As shown in Figure 4-2(f), two strong characteristic peaks were observed in the Raman spectra for all of the CNTs/SS samples, which correspond to the D-band and the G-band of multi-walled CNTs.[8] The Raman spectra further reveal that the CNTs/SS prepared at 700 °C demonstrated the biggest  $I_d/I_g$  value compared to the other CNTs/SS samples, indicating that more defects were created in this sample during the CVD process.[9] The XPS measurements indicated that the prepared CNTs/SS exhibited similar C 1s spectra, as shown in Figure 4-2(g). However, the N content increased along with the increase in temperature (**Table 4-1**). Furthermore, the CNTs/SS prepared at 700 °C exhibits a higher pyrrolic N content (**Table 4-1** and Figure 4-2(h)) compared to the other samples, which is beneficial for the HER activity with a smaller Gibbs free-energy ( $\Delta G_{H^*}$ ).[10]

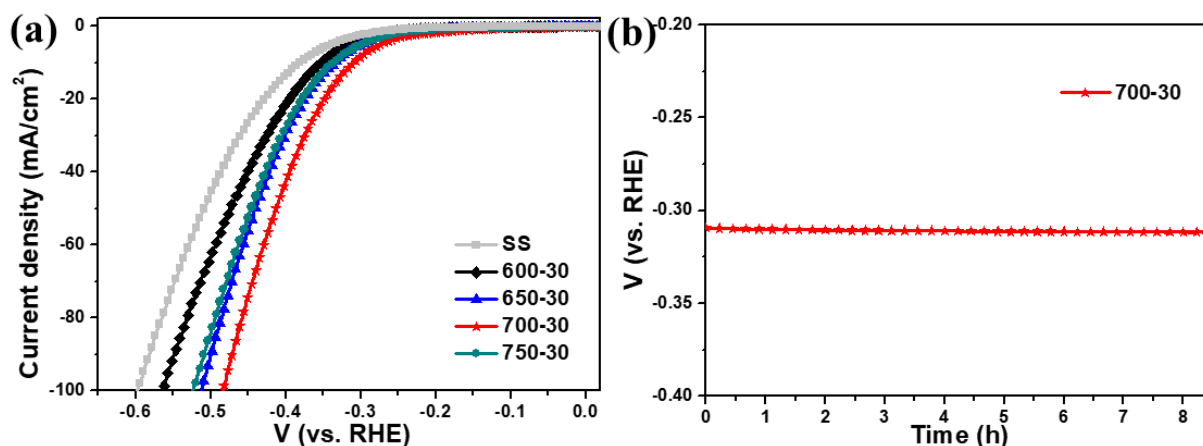


Figure 4-3. (a) LSV curves of the as-prepared CNTs/SS at different temperatures for the HER in 1 M KOH. (b) Long-time measurement of the CNTs/SS prepared at 700 °C recorded at  $-10 \text{ mA cm}^{-2}$ .

The HER activities of the prepared CNTs/SS samples were evaluated in 1 M KOH with a three-electrode electrochemical setup. As shown in **Figure 4-3(a)**, the CNTs/SS prepared at 700 °C demonstrate the best HER activity, with an overpotential of 306 mV to reach a current density of  $-10 \text{ mA cm}^{-1}$ , which is much lower than the value observed for the bare SS (381 mV). **Figure 4-3 (b)** shows that the CNTs/SS prepared at 700 °C demonstrates a good stability for at least 8 h.

## 4.5 Conclusions

CNTs were successfully grown on the surface of SS by APCVD. The CVD process for the growth of the CNTs exhibits a wide temperature window and follows a tip growth mechanism. The optimized CNTs/SS, which were grown with DPD parameters of  $t_1 = 60$  s (@-1 V) and  $t_2 = 10$  s (@-3 V), and at 700 °C for 30 min for the CVD process, demonstrated the best HER activity among all of the prepared samples, with a high stability for at least 8 h. The enhanced HER activity can be possibly attributed to the larger amount of defects and the higher content of pyrrolic N generated during the CVD process. Our strategy on the interface engineering of SS may also have a huge potential for application in other electrochemical areas, such as fuel cells and CO<sub>2</sub> reduction.

## 4.6 Acknowledgment

The authors acknowledge the financial support by the BMBF project Struktursolar. The authors also acknowledge Dr. Frank Heyroth for the support with SEM-EDS and TEM measurements performed at the Interdisciplinary Center of Materials Science-Martin Luther University Halle-Wittenberg (CMAT-MLU). JMSS and RBW acknowledge the DFG and Carl Zeiss for the loan of the phase ring.

## 4.7 References

- [1] H. Schäfer and M. Chatenet, *ACS Energy Lett.* **3**, 574 (2018).
- [2] H. Schafer, S. M. Beladi-Mousavi, L. Walder, J. Wollschlager, O. Kuschel, S. Ichilmann, S. Sadaf, M. Steinhart, K. Kupper, and L. Schneider, *ACS Catal.* **5**, 2671 (2015).
- [3] H. Schäfer, D. M. Chevrier, P. Zhang, J. Stangl, K. Müller-Buschbaum, J. D. Hardege, K. Kuepper, J. Wollschläger, U. Krupp, S. Dühren, M. Steinhart, L. Walder, S. Sadaf, and M. Schmidt, *Adv. Funct. Mater.* **26**, 6402 (2016).
- [4] J. S. Chen, J. Ren, M. Shalom, T. Fellingner, and M. Antonietti, *ACS Appl. Mater. Interfaces* **8**, 5509 (2016).
- [5] L. Ring, B. G. Pollet, M. Chatenet, S. Abbou, K. Küpper, M. Schmidt, M. Huck, A. Gries, M. Steinhart, H. Schäfer, *Angew. Chem. Int. Ed.* **58**, 17383 (2019).
- [6] H. Zhang, J. M. de Souza e Silva, X. Lu, C. S. de Oliveira, B. Cui, X. Li, C. Lin, S. L. Schweizer, A. W. Maijenburg, M. Bron, and R. B. Wehrspohn, *Adv. Mater. Interfaces* **6**, 1900774 (2019).
- [7] A. Gohier, C. P. Ewels, T. M. Minea, and M. A. Djouadi, *Carbon* **46**, 1331 (2008).
- [8] X. Zhang, J. Zhang, J. Quan, N. Wang, and Y. Zhu, *Analyst* **141**, 5527 (2016).
- [9] H. Wang, J. T. Robinson, X. Li, and H. Dai, *J. Am. Chem. Soc.* **131**, 9910 (2009).
- [10] H. Dong, C. Liu, H. Ye, L. Hu, B. Fugetsu, W. Dai, Y. Cao, X. Qi, H. Lu, and X. Zhang, *Sci. Rep.* **5**, 17542 (2015).

## 5 Novel Stable Three-dimensional Stainless Steel-based Electrodes for Efficient Water Splitting

An efficient process to construct highly-stable three-dimensional (3D) stainless steel (SS)-based electrode was successfully developed by employing an interfacial network of carbon nanotubes (CNTs) between SS and the highly-active electrocatalysts. The resulting Pt/OxCNT/SS and RuO<sub>2</sub>/OxCNT/SS 3D electrodes exhibit the best activity for the hydrogen evolution reaction (HER) and a comparable oxygen evolution reaction (OER) when compared to other SS-based electrodes reported in the literature.

This chapter can be referred to:

Haojie Zhang, Juliana Martins de Souza e Silva, Xubin Lu, Cristine Santos de Oliveira, Bin Cui, Xiaopeng Li, Chao Lin, Stefan L. Schweizer, A. Wouter Maijenburg, Michael Bron,\* and Ralf B. Wehrspohn\*, *Advanced Materials Interfaces* 2019, 6, 1900774.

## 5.1 Abstract

The stability of electrocatalysts grown on substrates is a significant challenge for the construction of three-dimensional (3D) stainless-steel (SS) based electrodes for highly-efficient water splitting. This paper presents an efficient and universal process to enhance the interfacial interaction between SS and highly-active electrocatalysts for the preparation of 3D electrodes through the formation of an interfacial network of carbon nanotubes (CNTs) on the SS. Nano-scale X-ray computed tomography and focused ion beam were used to visualize the interface between the CNTs and the SS, and the 3D structure of CNT/SS electrodes prepared through our process. The strongly-interconnected CNTs network increases the surface area of the SS support that benefits the modification of highly-active electrocatalysts and also serves as an electron/charge-conductive highway between the electrocatalysts and the support. The modified electrocatalysts on CNT/SS further improve the hydrogen evolution reaction (HER) and the oxygen evolution reaction (OER) performances, respectively, of the 3D electrodes. While compared to the SS-based electrodes reported in the literature, our Pt/OxCNT/SS shows the best HER activity over wide pH range and RuO<sub>2</sub>/OxCNT/SS exhibits a comparable OER performance in neutral and alkaline electrolyte. We report an efficient approach to combine highly-active electrocatalysts with SS for the preparation of active and stable 3D electrodes that can be further explored in various areas.

## 5.2 Introduction

Electrochemical water splitting is one of the most promising technologies that could meet the increasing energy consumption requirements for the development of human society and achieve the goal of clean renewable energy conversion and storage.<sup>[1]</sup> However, the efficiency of water splitting is to a great extent limited by the intrinsically low kinetics of both anodic and cathodic reactions, which are named as the oxygen evolution reaction (OER) and hydrogen evolution reaction (HER), respectively.<sup>[2]</sup> Motivated by this challenge, many studies were devoted to develop highly-active electrocatalysts for water splitting based on precious metal,<sup>[3]</sup> non-precious metal oxides,<sup>[4]</sup> nitrides,<sup>[5]</sup> sulfides,<sup>[6]</sup> selenides,<sup>[7]</sup> and phosphides,<sup>[8]</sup> to list a few. To fully utilize the potential of these electrocatalysts, new hierarchical three-dimensional (3D) electrodes have been designed for a more efficient charge transport and better kinetics when compared to the traditional electrodes.<sup>[9, 10]</sup> The requirements of these new 3D electrodes are the use of a robust and conductive substrate to support the 3D structure composed of a strongly interconnected and conductive network with enlarged surface area, and the coupling of highly-active electrocatalysts to the support to further increase the activity of the as-prepared 3D electrodes<sup>[10, 11]</sup> Examples of 3D electrodes prepared recently according to this strategy include those based on nickel foam,<sup>[10, 12]</sup> graphene,<sup>[13]</sup> carbon paper<sup>[14]</sup>, and carbon cloth<sup>[15]</sup>. However, further developments of these electrodes are still crucial, to obtain 3D electrodes with much better conductivity and higher corrosion resistance, from abundant, cheaper and flexible sources. Meanwhile, the wide-pH range electrocatalysts exhibit excellent compatibility and flexibility, matching various operating conditions during the commercial application for water splitting. Thus, it is also of great importance to combine wide-pH range electrocatalysts with 3D electrode for the preparation of 3D wide-pH range electrodes for efficient and flexible water splitting.

In this context, stainless steel is the ideal substrate for the construction of 3D electrodes due to its excellent conductivity, great corrosion resistance and robustness.<sup>[16]</sup> For example, Yu et al. reported the direct use of 316L stainless steel as anode for OER.<sup>[17]</sup> Schäfer et al.,<sup>[16, 18, 19, 20]</sup> Tang et al.,<sup>[21]</sup> and Zhong et al.<sup>[22]</sup> have shown that various types of SS can be treated by *in-situ/ex-situ* oxidation or by etching, in processes that cause a morphological and compositional change of the SS surface, resulting in the enhancement of the water splitting performance. Balogun et al. demonstrated the use of N- and P-doping in etched SS for water splitting in an alkaline electrolyte.<sup>[23]</sup> In the context of 3D electrodes production based on SS as the substrate, Liu et al. directly used SS scrubbers with a large specific surface area as the electrode for overall

water splitting.<sup>[24]</sup> Huang et al. used an advanced selective laser melting (SLM) technology to directly print 3D cellular SS for the OER,<sup>[25]</sup> and Chen et al. used a hydrothermal technique to grow NiS on the SS mesh.<sup>[26]</sup> However, none of the works mentioned above report a universal method to couple highly-active electrocatalysts with SS (as the substrate) to construct stable 3D SS-based electrodes for efficient water splitting, especially for the HER. The common problem of lack of stability of the electrocatalysts from the unfavorable interface between the substrate and the modified electrocatalysts deposited on it and is, thus, a challenge for the preparation of stable 3D SS-based electrodes for water splitting.<sup>[10, 16]</sup> Therefore, it is imperative to find an appropriate material that favors the interaction of the SS and the electrocatalysts that can be used on their interface to increase the stability of the final 3D SS-based electrodes to enable their broad use for efficient water splitting.

This material must favor the interfacial interaction between the electrocatalysts and the SS, possess a large surface area, and an excellent conductivity for fast electron/charge transfer. Here, we report an efficient and universal process to overcome the limitations of the 3D SS-based electrodes. Our process allows the synthesis of stable and efficient 3D SS-based electrodes for water splitting. It employs carbon nanotubes (CNTs) as an interfacial material and can be easily scaled up. Our process involves a few steps that begins by modifying the SS surface by growing CNTs on it through atmospheric pressure chemical vapor deposition (APCVD). Then, the grown CNTs are *in-situ* oxidized without damaging the substrate, resulting in OxCNT/SS. Subsequently, the state-of-the-art catalysts Pt and RuO<sub>2</sub> can be successfully anchored onto the OxCNT/SS, forming Pt/OxCNT/SS and RuO<sub>2</sub>/OxCNT/SS 3D electrodes. Nano-scale X-ray computed tomography (nano-CT) was performed to visualize the 3D structure of the CNT/SS electrode prepared by the growth of CNTs on the SS surface and focused ion beam (FIB) was used to study the interface of the grown CNTs and SS. The strong interaction between the modified electrocatalysts and the CNT results in a stable system with high activity for the HER and the OER in a wide pH range. The synthesized Pt/OxCNT/SS and RuO<sub>2</sub>/OxCNT/SS electrodes exhibit the best HER and a comparable OER activities, respectively, when compared to other SS-based electrodes reported in the literature. Additionally, the Pt/OxCNT/SS || RuO<sub>2</sub>/OxCNT/SS configuration needed only 1.50 and 1.70 V to obtain a current density of 10 mA/cm<sup>2</sup> in alkaline and neutral electrolytes, respectively, with a stability for at least 24 h in continuous operation. We therefore show that our new synthetic strategy to grow CNTs on a SS mesh surface is an effective and universal approach to couple highly-active catalysts for the construction of 3D SS-based electrodes, and that it has

the potential to be used in different areas, such as fuel cell, metal-air batteries and supercapacitors.

### 5.3 Experimental Section

**Chemicals.** All chemicals were used as received without any further purification. Stainless steel mesh (SS, 316L) was bought from Sigma-Aldrich and used as the substrate for the preparation of the electrodes. Chloroplatinic acid hexahydrate ( $\text{H}_2\text{PtCl}_6 \cdot 6\text{H}_2\text{O}$ , ACS reagent grade), Iron (II) sulfate heptahydrate ( $\text{FeSO}_4 \cdot 7\text{H}_2\text{O}$ ,  $\geq 99\%$ ), L-Ascorbic acid (99%) and Acetonitrile (99.8%) were obtained from Sigma-Aldrich. Ethylene glycol (EG, 99.8%), Ruthenium (III)-chloride hydrate ( $\text{RuCl}_3 \cdot x\text{H}_2\text{O}$ , 10-15% water), Sodium sulfate ( $\text{Na}_2\text{SO}_4$ ,  $\geq 99\%$ ), Sodium nitrate ( $\text{NaNO}_3$ ,  $\geq 99.0\%$ ), Potassium permanganate ( $\text{KMnO}_4$ ,  $\geq 99\%$ ), Potassium hydroxide ( $\text{KOH}$ ,  $\geq 85\%$ ), Disodium hydrogen phosphate ( $\text{Na}_2\text{HPO}_4$ ,  $\geq 99.5\%$ ) and Sodium dihydrogen phosphate ( $\text{NaH}_2\text{PO}_4$ ,  $\geq 98\%$ ) were purchased from Carl Roth. Deionized water (Millipore,  $18.2 \text{ M}\Omega \cdot \text{cm}$ ) was used for all experiments.

**Growth of CNT on the surface of SS (CNT/SS).** The CNTs were grown on the surface of SS by an atmospheric pressure chemical vapor deposition (APCVD) method, as reported in the literature.<sup>[27, 28]</sup> Briefly, the SS ( $2 \times 1 \text{ cm}^2$ ) was cleaned with acetone, ethanol and 3 M HCl solution under ultrasonication for 15 min each. The Fe nanoparticles deposition was carried out under -3 V for 60 s and then -1.5 V for 10 s in a solution containing 0.01 M  $\text{FeSO}_4 \cdot 7\text{H}_2\text{O}$ , 0.1 M  $\text{Na}_2\text{SO}_4$  and 0.015 mM L-Ascorbic acid using a three-electrode setup using an Ag/AgCl (saturated KCl) and a Pt wire as the reference and counter electrodes, respectively. Subsequently, the SS with Fe nanoparticles was positioned in the center of a horizontal tube furnace (Carbolite Gero) equipped with a quartz tube. For the growth of CNTs,  $\text{H}_2/\text{Ar}$  (50 %, v/v) and acetonitrile were used as reducing gas and carbon source, respectively. First, the SS was heated up to 750 °C with a ramping rate of 10 °C/min and maintained at this temperature for 30 min with a constant reducing gas flow rate of 6 L/h. And then, the gas was kept and humidified with acetonitrile bubbling at 31 °C to growth the CNTs for 1 h. Finally, the system was cooled down to room temperature under an Ar flow of 19 L/h.

**Functionalization of the grown CNTs on the SS surface (OxCNT/SS).** The oxidation of the CNTs grown on the SS surface was carried out by a modified process reported in the literature.<sup>[30]</sup> Typically, one piece of the as-prepared CNT/SS was immersed in 20 mL of concentrated sulfuric acid overnight. Next, the CNT/SS was collected and transferred in 20 mL of a concentrated sulfuric acid solution containing 6 mM  $\text{KMnO}_4$  and 12 mM  $\text{NaNO}_3$  for 30

min at 40 °C. Finally, the oxidized CNT/SS (denoted as OxCNT/SS) was washed with water and dried with a N<sub>2</sub> gun for further use.

**Decoration of the OxCNT/SS with Pt nanoparticles (Pt/OxCNT/SS).** Pt nanoparticles were deposited onto the oxidized CNT/SS by a hydrothermal reaction.<sup>[35]</sup> Firstly, the OxCNT/SS was put into in a 25 mL Teflon autoclave containing 15 mL of EG and the solution was stirred with a glass bar for 15 min. Then, 86 μL of a 38.6 mM H<sub>2</sub>PtCl<sub>6</sub> solution was added to the autoclave and left stirring for 1 h. Subsequently, the autoclave was sealed and heated to 150 °C for 3 h. After this period, the autoclave was cooled down to room temperature and the material obtained was washed with water and dried with the aid of a N<sub>2</sub> gun. Finally, the as-synthesized Pt/OxCNT/SS was reduced with 5% H<sub>2</sub>/Ar for 1 h under 200 °C. For comparison, the 20 wt. % Pt/C with a loading amount of 2 mg/cm<sup>2</sup> was also coated on the SS by a drop casting method (denoted as 20 wt. % Pt/C/SS) as described in the literature.<sup>[42]</sup>

**Decoration of the OxCNT/SS with RuO<sub>2</sub> (RuO<sub>2</sub>/OxCNT/SS).** The RuO<sub>2</sub> decorated OxCNT/SS was prepared by a modified hydrothermal reaction described in the literature.<sup>[39]</sup> Typically, the OxCNT/SS was placed into a 25 mL Teflon autoclave with 15 mL of 3 mM RuCl<sub>3</sub> aqueous solution and stirred for 1 h. Then, a 1 M KOH solution was used to adjust the pH of the solution to 7. Subsequently, the autoclave was sealed and heated to 120 °C for 3 h. Afterwards, the autoclave was cooled down to room temperature and the obtained sample was washed with water and dried at 150 °C for 3 h in an oven. For comparison, RuO<sub>2</sub> with a loading amount of 2 mg/cm<sup>2</sup> was also coated on the pristine SS with a similar drop casting method as the preparation of 20 wt. % Pt/C/SS (denoted as RuO<sub>2</sub>/SS).

**Characterization.** Scanning electron microscopy (SEM) characterization was performed with a FEI Quanta 650 FEG scanning electron microscope equipped with an X-ray detector for energy dispersive X-ray spectroscopy (EDS). The transmission electron microscopy (TEM) measurement was performed in a FEI Tecnai F20 transmission electron microscopy equipped with an EDS detector. X-ray photoelectron spectroscopy (XPS) data were obtained by a Thermo Scientific™ K-Alpha™ X-ray Photoelectron Spectrometer System equipped with a monochromatic Al K $\alpha$  X-ray source. All XPS spectra were calibrated by shifting the C 1s peak to 284.8 eV. The Raman spectrum were collected by a Raman spectrometer (LabRAM HR Evolution, HORIBA). Raman analyses were performed on several locations of the sample to obtain a more reliable value of the  $I_d/I_g$  ratio. The nano-CT X-ray imaging experiments were performed on a Carl Zeiss Xradia 810 Ultra (quasi-monochromatic X-ray Cr source, 5.4 keV) using the Zernike phase-contrast imaging mode.<sup>[43]</sup> One single wire



was glued onto the tip of a metallic pin. For the imaging experiment, the sample was placed on the sample holder and 901 projection images were obtained over 180°, each one with an exposure time of 100 s, detector binning of 1 and a final voxel size of 64 nm. Final projections have a field-of-view (FOV) of 65 x 65  $\mu\text{m}^2$ . Image reconstruction was performed by a filtered back-projection algorithm using the software integrated into the Xradia 810 Ultra and the datasets were exported as a stack of 16-bit TIFF images of 1024 x 1024 pixels. The 3D renderings presented here were created using either the commercial software Thermo Fischer Avizo after image filtering (median filter followed by non-local means filter for the bare SS sample, and only non-local means filter for the SS/NCNT dataset for preservation of surface features). Contrast propagation (using the Avizo magic wand feature) was used for the segmentation of the CNT. Surface area was calculated from the processed images using the surface area volume module in Avizo. The contact angle measurement was carried by dropping 6  $\mu\text{L}$  deionized water on the electrode surface with a dosing rate of 1  $\mu\text{L}/\text{s}$  (Data Physics Optical Contact Angle System OCA 15EC) and the data were analyzed with the SCA20 software. The measurements were conducted more than 3 times per sample to increase the accuracy of the data.

**Electrochemical measurements.** The electrochemical measurements were carried out using an Autolab PGSTAT302N Potentiostat in a three-electrode setup using a Pt wire and an Ag/AgCl reference electrode (saturated KCl) as the counter and reference electrodes, respectively. The different electrolytes of 0.5 M  $\text{H}_2\text{SO}_4$  (pH = 0), 1 M phosphate buffer solution (PBS, pH = 7) and 1 M KOH (pH = 14) were used in the water splitting measurement. The hydrogen evolution reaction (HER) and oxygen evolution reaction (OER) performances were evaluated by linear sweep voltammetry at a scan rate of 10 mV/s. The electrochemical impedance spectroscopy (EIS) was collected at certain voltage with a frequency range from 100 kHz to 0.1 kHz and a 10 mV amplitude for both HER and OER. The overall water splitting activity was recorded with a two-electrode configuration at a scan rate of 10 mV/s. The stability measurements were conducted by chronoamperometric measurements at a constant current density of 10  $\text{mA}/\text{cm}^2$  for a long time. All potential values were converted to *vs.* the reversible hydrogen electrode (RHE) using the equation  $E_{RHE} = E_{Ag/AgCl} + 0.197 + 0.059 \times \text{pH}$ , where  $E_{RHE}$  and  $E_{Ag/AgCl}$  are the potentials *vs.* the RHE and the measured potentials *vs.* the Ag/AgCl (saturate KCl) reference electrodes, respectively, without *iR* compensation.

## 5.4 Results and Discussion

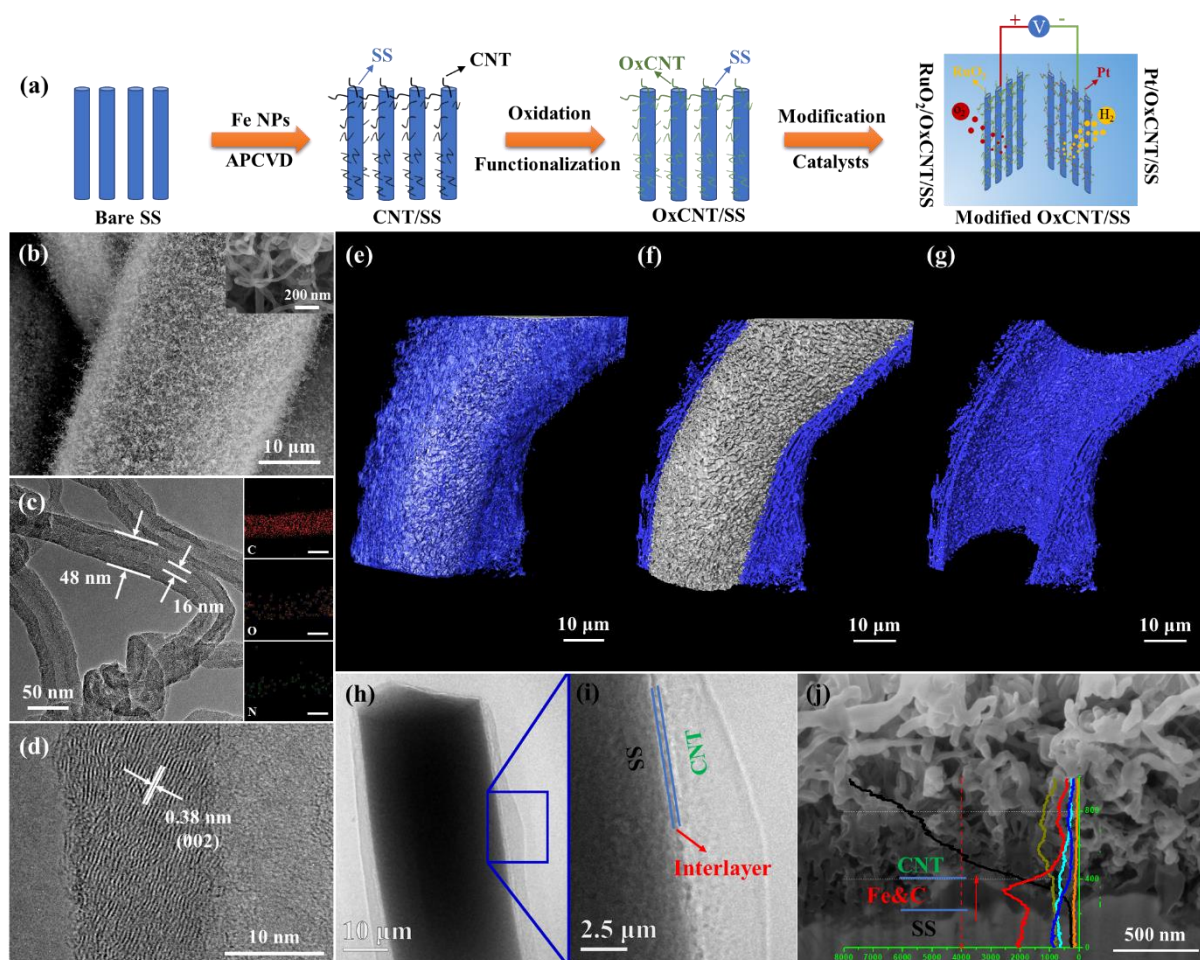


**Figure 5-1.** (a) Illustration of the process to prepare 3D electrodes for the overall water splitting. (b) SEM images of the prepared CNT/SS. The HRSEM image of the grown CNT is shown in the inset. (c) TEM images of the grown CNT and the mapping of C, N and O element along the CNT is shown in the inset (scale bar: 60 nm). (d) HRTEM image of the grown CNT. (e) Nano-CT 3D representations of the SS/CNT. In (f), a virtual cut to remove part of the CNT of the surface of the CNT/SS is shown, and in (g) the CNT grown on SS is shown in more detail. (h) Exemplary nano-CT X-ray projection of one wire of CNT/SS and (i) a high-resolution X-ray projection of the interface of the SS and the CNT. (j) The cross-section of the CNT/SS prepared by FIB, with the linear scan EDS along the red dashed line.

In our work, we used a commercial SS mesh that consists of vertically woven SS fibers with a diameter of 26  $\mu\text{m}$  and a smooth surface (**Figure S 5-1(a-c)**). The synthetic process that we developed for the preparation of 3D electrodes for water splitting requires modifying the SS surface with CNTs to couple highly-active electrocatalysts to the CNTs-modified SS (**Figure 5-1(a)**). In detail, the growth of CNTs onto the SS mesh surface was carried out by a typical APCVD method.<sup>[27, 28]</sup> We made an attempt of growing CNT on the SS by directly inserting the bare SS mesh in a furnace without depositing any catalyst onto its surface. In this case, a thick layer of carbon with a few CNTs was obtained on the surface of the SS (Figure S 5-1(d-f)). In order to increase the coverage of the SS surface with CNT, Fe nanoparticles (FeNPs) were deposited onto the bare SS mesh (FeNPs/SS) by a double pulse deposition (DPD) process

to serve as catalysts for the CNTs growth. The scanning electron microscopy (SEM) images of the FeNPs/SS (Figure S 5-1(g-j)) show that FeNPs were successfully deposited and uniformly distributed onto the bare SS. In the following step, the FeNPs/SS was heated to 750 °C and kept at this temperature for 0.5 h for the reduction of the FeNPs and another 1 h for the growth of CNTs with H<sub>2</sub>/Ar (50 %, v/v) and acetonitrile as reducing gas and carbon source, respectively. The morphology of the CNT/SS was characterized by SEM (**Figure S 5-2(a)**) and it was observed that the general morphology of the SS remained unchanged after the growth of the CNTs. When inspecting one single SS fiber with higher SEM magnification (HRSEM), we verified that the CNTs uniformly grow on the surface of the SS and exhibited an average diameter of 35.8 nm (Figure 5-1(b), inset, and Figure S 5-2(b)). The presence of the CNTs changed the morphology of the SS surface and the CNT/SS have a much rougher surface when compared to the smooth surface of the SS (Figure 5-1(b) vs. Figure S 5-1(a-c)). The elemental distribution of the CNT/SS obtained by scanning electron microscopy energy dispersive X-ray spectroscopy (SEM-EDS) mapping identified carbon as the main element on the surface of the SS (Table S 5-1, Figure S 5-2(c-g)). After the growth of CNT on the SS surface, a change of the properties was observed by a change of the wettability of the CNT/SS sample (**Figure S 5-3(a-b)**). We further characterized the grown CNTs with transmission electron microscopy (TEM) (Figure 5-1(c)) and the diameter of the nanotube is ca. 48 nm, with an inner diameter of approximately 16 nm. Also, the TEM-EDS mapping of a single CNT indicates that carbon is the main element composing the CNT (Figure 5-1(c), inset). The interplanar distance of 0.35 nm as indicated in the high-resolution TEM (HRTEM) image (Figure 5-1(d)) correlates with the crystal plane of (002).<sup>[29]</sup>

We used 3D X-ray computed tomography with nanometric resolution (nano-CT) to inspect the morphology of the SS before and after the growth of CNTs. The 3D representation of one single pristine SS wire imaged using nano-CT shows a smooth outer surface (**Figure S 5-4**). The volumetric representation of the CNT/SS (Figure 5-1(e), with the CNTs pseudo-colored in blue) shows a much rougher surface when compared to that of the pristine SS. The rougher surface results in a surface area almost 7 times larger for the CNT/SS when compared to the pristine SS. Though a much higher surface area is expected when covering the SS with CNTs, the surface area calculation, which is based on the nano-CT datasets, is limited by the resolution of the imaging experiment performed, that resulted in images with a voxel size of 64 nm. When virtually cutting a part of the CNTs in the nano-CT volumetric images, we observed that the CNTs resemble a shell on the SS wire with a thickness varying from 2 to 5 μm (Figure 5-1(f), with the SS pseudo-colored in grey and the CNTs in blue) and the surface of the SS fiber

becomes rougher after the growth of the CNTs. The rougher surface of SS results probably from deposition of the FeNPs on the SS and the further processes performed for the growth of the CNTs.<sup>[28]</sup> By virtually removing the SS wire from the CNT/SS sample, the 3D representation of the CNTs shell further indicates that the CNTs is distributed on the entire surface of the SS wire (Figure 5-1(g)). The X-ray projections of the CNT/SS (Figure 5-1(h) and (i)) show the hierarchical structure of the sample, with a thin interlayer marked in Figure 5-1(i). The cross-section SEM image of the CNT/SS prepared by focused ion beam (FIB, Figure 5-1(j)) further illustrates the interface of the CNTs and the SS with a higher resolution. The linear scanning EDS reveals that the interlayer consists of Fe and C (detail in Figure 5-1(j)), which is consistent with the growth mechanism of the CNTs initiated by the FeNPs.<sup>[28]</sup> The growth of CNTs consumes some of the FeNPs deposited on the SS, creating a rougher surface and the formed mixed Fe&C layer favors the growth of a stable and tightly attached network of CNTs around the SS.<sup>[11]</sup>

For the modification of the CNTs, it is known that oxygen-containing groups, such as hydroxyl and carboxyl, play a key role in the adsorption of other ions.<sup>[30]</sup> Therefore, an additional functionalization step was carried out to oxidize the CNTs on the SS surface, without damaging the substrate. For this, we used a modified version of a process reported in the literature,<sup>[30]</sup> which oxidized the CNTs with  $\text{KMnO}_4$  in concentrated  $\text{H}_2\text{SO}_4$  at 40 °C. First, the effect of the critical oxidation environment on the bare SS was examined by immersing one piece of bare SS in the oxidizing solution to compare the morphology change due to the oxidation process (denoted as OxSS). No change of the weight of the SS mesh is observed after the oxidation procedure to prepare OxSS (**Figure S 5-5(a)**). Moreover, no change of morphology was observed by SEM and HRSEM images of the OxSS (Figure S 5-5(b-c), inset). The SEM and HRSEM images of the OxSS (Figure S 5-5(b-c), inset) show that the morphology of the SS remained constant even after oxidation treatment in the strongly oxidizing environment, because of its high stability. Subsequently, the oxidation of the CNT/SS was carried out using the same procedure as described for the treatment of OxSS. The weight of the CNT/SS reduced approximately 0.3 mg after the oxidation treatment to prepare OxCNT/SS (**Figure S 5-6(a)**). The SEM image and cross section (FIB) image (Figure S 5-6(b-d)) show a difference of morphology between CNT/SS and OxCNT/SS (Figure 5-1(b)). The HRSEM image (inset Figure S 5-6(d)) of CNTs and elemental analysis (Table S 5-1) of the OxCNT show that the nanotubular nature of CNTs deposited on the SS fiber remains constant, though the composition of the CNTs shows a more than 12 times increase in the oxygen content when

compared with that of the CNT/SS. After oxidation treatment of the CNT/SS, a significant change of the surface wettability was observed and the OxCNT/SS is highly-hydrophilic with a contact angle of  $0^\circ$  (Figure S 5-3(c)). The TEM and HRTEM images of one single OxCNT (Figure S 5-6(e, f)), also show the same morphology of the CNTs. The TEM-EDS mapping of one single fiber on the surface of OxCNT/SS shows a uniform distribution and a higher percentage of oxygen when compared to the CNT/SS (Table S 5-1). Raman spectra of CNT/SS and OxCNT/SS (Figure S 5-6(g)) show D-band ( $I_D$ ) and ( $I_G$ ) signals at  $1350$  and  $1590\text{ cm}^{-1}$ , which indicate the disorder in CNTs and the in-plane vibrations of the  $sp^2$  C-C bonds, respectively.<sup>[31]</sup> The intensity ratio of  $I_D/I_G$  of OxCNT/SS increased from 1.06 (CNT/SS) to 1.12, indicating more disorder created during the oxidation process.<sup>[32]</sup> The crystal size ( $L_a$ ) was reduced from 18.1 nm to 17.2 nm (Table S 5-2).<sup>[33]</sup> The XPS C1s and O1s spectra of CNT/SS and OxCNT/SS (Figure S 5-6(h, i)) support the TEM mapping results and indicate the presence of oxygen on the surface of the OxCNT/SS sample. The higher intensity peaks at 286.2 and 288.3 eV that are present in the OxCNT/SS C1s spectrum (Figure S 5-6(h)) are attributed to C-O and C=O, respectively.<sup>[31]</sup> The presence of oxygen in this sample is further evidenced by the O1s spectrum of OxCNT/SS (Figure S 5-6(i)), which consisted of three peaks, which are assigned to C-O (C-O and C-O=C, 533.2 eV), C=O (isolated -OH, C=O, O-C=O, 531.6 eV) and physically absorbed oxygen/carbonate species (530.5 eV).<sup>[34]</sup>

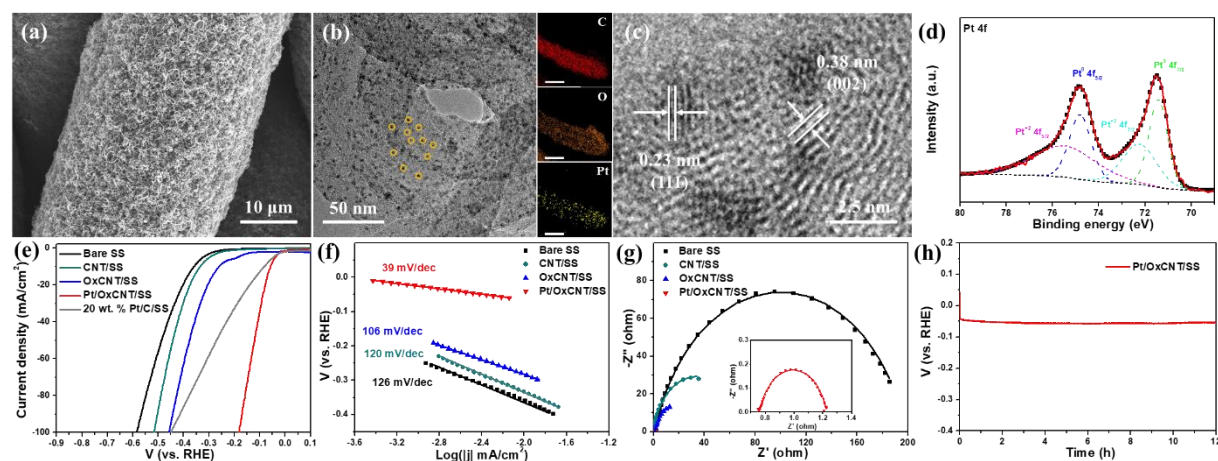


**Figure 5-2.** (a) SEM image of the Pt/OxCNT/SS. (b, c) TEM and HRTEM of the Pt/OxCNT. The corresponding element mapping of the C, O and Pt is shown in the inset of (b) with the scale bar of 50 nm. (d) Pt 4f XPS spectrum of the Pt/OxCNT/SS (e) Polarization curves of bare SS, CNT/SS, OxCNT/SS, Pt/OxCNT/SS and 20 wt. % Pt/C/SS recorded without iR correction for the HER. (f) Tafel plots of the bare SS, CNT/SS, OxCNT/SS and Pt/OxCNT/SS. (g) EIS measurement of the bare SS, CNT/SS, OxCNT/SS and Pt/OxCNT/SS. The EIS curve of Pt/OxCNT/SS is magnified in the inset. (h) Stability measurement of the Pt/OxCNT/SS recorded at a constant current density of  $10\text{ mA/cm}^2$ .

Bare SS exhibits excellent OER catalytic activity, but it has poor HER performance.<sup>[24]</sup> Therefore, in order to increase the HER activity, we deposited Pt, the state-of-the-art HER catalyst, on the surface of OxCNT/SS (denoted as Pt/OxCNT/SS) to benchmark the HER

performance. The Pt/OxCNT/SS was prepared by a modified hydrothermal reaction.<sup>[35]</sup> The Pt/OxCNT/SS has the same interlaced morphology as the base SS (**Figure S 5-2(a)** and **Figure S 5-7(a-b)**). The SEM-EDS elemental analysis of the Pt/OxCNT/SS demonstrates that Pt was successfully deposited and uniformly distributed on the OxCNT/SS (Figure S 5-7(c-e)) with a loading of approximately 9.71 wt% (Table S 5-1). The contact angle measurement of Pt/OxCNT/SS indicates that the modification with Pt does not change the hydrophilicity of the electrode (Figure S 5-3(d)). The morphology of the Pt/OxCNT characterized by TEM shows the uniform distribution of Pt with an average diameter of 2.2 nm (Figure 5-2(b)) and the size distribution of Pt NPs was shown in Figure S7(f). Some Pt nanoparticles are marked as yellow circle as shown in Figure 5-2(b). The element mapping of C, O and Pt shown in the inset of Figure 5-2(b) further evidenced the uniform distribution of Pt along with the OxCNT. The lattice fringes of 0.23 nm and 0.38 nm measured from the HRTEM image (Figure 5-2(c)) correspond well to the (111) lattice and (002) lattice planes of Pt and CNTs, respectively.<sup>[35]</sup> The peaks located at 70.9 eV and 72.2 eV as shown in the XPS spectrum of Pt 4f (Figure 5-2(d)) can be attributed to metallic Pt and Pt-O suggesting an interaction between the Pt and OxCNT.<sup>[35]</sup> The Raman spectra measurement (Table S 5-2) show the  $I_D/I_G$  and  $L_a$  didn't change significantly indicating the modification of Pt didn't affect the defect of the OxCNT.

To examine the HER performance of the synthesized electrode, the Pt/OxCNT/SS 3D electrode was used as the cathode in a three-electrodes electrochemical cell in a 1 M KOH solution with a Pt wire and Ag/AgCl (saturated KCl) reference as the counter and reference electrodes, respectively. The polarization curve (Figure 5-2(e)) indicates that the Pt/OxCNT/SS exhibited an overpotential of 56 mV to reach a current density of 10 mA/cm<sup>2</sup> without iR compensation, which is the lowest overpotential observed when compared with the other samples tested. The OxCNT/SS, CNT/SS, bare SS, and 20 wt. % Pt/C/SS exhibited overpotentials of 257 mV, 334 mV, 359 mV and 82 mV, respectively. The as-prepared Pt/OxCNT/SS exhibits the best HER performance when compared to other SS-based electrodes recently reported in the literature as summarized in **Table S 5-3**.<sup>[20, 23, 24, 36]</sup> From the corresponding Tafel plots (Figure 5-2(f)), the measured values for bare SS, CNT/SS and OxCNT/SS are 126, 120 and 106 mV/dec, respectively. Pt/OxCNT/SS exhibited the smaller Tafel slope of 39 mV/dec indicating the better reaction kinetic. To understand the enhanced activity of the Pt/OxCNT/SS 3D electrode, the effective electrochemical active surface area (ECSA) of the as-prepared electrodes was evaluated by measuring the double layer capacitance ( $C_{dl}$ ), which is proportional to the ESCA.<sup>[37]</sup> The  $C_{dl}$  value of the Pt/OxCNT/SS (**Figure S 5-8**) was almost 1.5 and 50 times higher than that of the OxCNT/SS and SS, respectively, which



suggest that the modification of the SS and coupled with Pt can enlarge the ECSA. Besides that, the  $C_{dl}$  of the OxCNT/SS was higher than that of the CNT/SS, suggesting that the oxygen groups or defects present on the surface of the CNT created by the oxidation step could also enlarge the ECSA for HER.<sup>[38]</sup> We also performed electrochemical impedance spectroscopy (EIS) to investigate the mechanism of the catalysis (Figure 5-2(g), **Figure S 5-9** and **Table S 5-4**). The Pt/OxCNT/SS exhibits a lower  $R_{ct}$  value of  $0.47 \Omega$  than that observed for OxCNT/SS, CNT/SS and bare SS ( $37.70 \Omega$ ,  $65.92 \Omega$  and  $197.50 \Omega$ , respectively). The smaller charge transfer resistance further revealing the fast charge transfer for the HER. Most importantly, the stability of the as-prepared Pt/OxCNT/SS, characterized by chronoamperometry (Figure 5-2(h)), exhibited well stability for at least 12 h of continuous testing.

Although the bare SS already exhibits a superior OER activity,<sup>[16]</sup> we deposited the state-of-the-art OER catalyst,  $\text{RuO}_2$ , on the OxCNT/SS to further enhance its OER catalytic performance. For that,  $\text{RuO}_2$  was deposited on the OxCNT/SS by a modified one-pot hydrothermal reaction as reported elsewhere.<sup>[39]</sup> The process of  $\text{RuO}_2$  deposition to prepare  $\text{RuO}_2/\text{OxCNT}/\text{SS}$  does not cause changes in the mesh morphology (**Figure 5-3(a)** and **Figure S 5-10(a-b)**), though it results in a rougher surface when compared to OxCNT/SS. The HRSEM image of the  $\text{RuO}_2/\text{OxCNT}$  was shown in the inset of Figure 5-3(a). The SEM-EDS mapping of  $\text{RuO}_2/\text{OxCNT}/\text{SS}$  reveals that ruthenium is uniformly distributed on the OxCNT/SS (Figure S 5-10(c-e)) with a Ru loading of approximately 9.79 wt% (Table S 5-1). The hydrophilicity of the  $\text{RuO}_2/\text{CNT}/\text{SS}$  didn't change significantly with the modification of  $\text{RuO}_2$  (Figure S 5-3(e)).

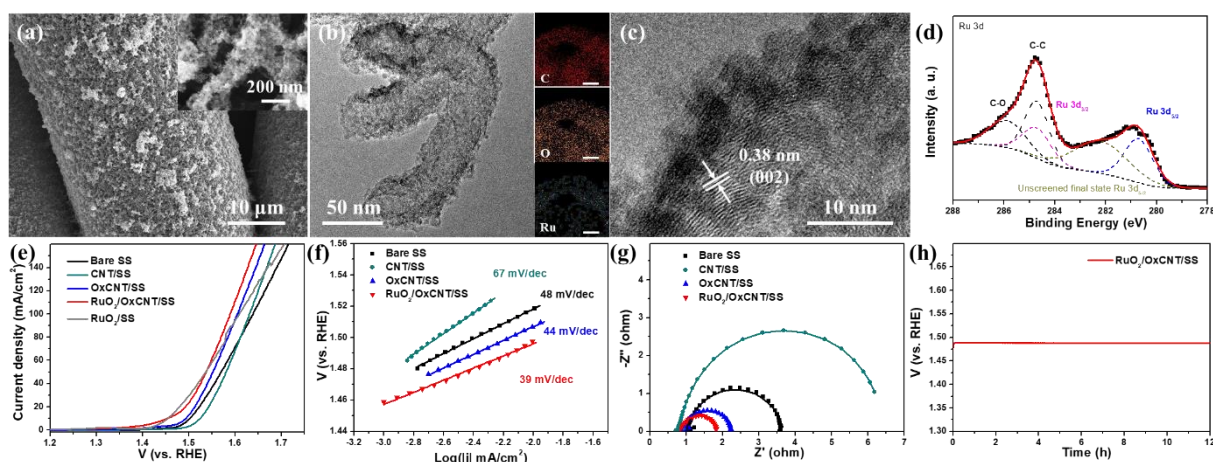


**Figure 5-3.** (a) SEM image of the  $\text{RuO}_2/\text{OxCNT}/\text{SS}$  and HRSEM shown in the inset. (b, c) TEM and HRTEM images of the  $\text{RuO}_2/\text{OxCNT}$ . The element mapping of the C, O and Ru is shown in the inset of (b) with the scale bars of 50 nm. (d) XPS spectrum of the Ru 3d for  $\text{RuO}_2/\text{OxCNT}/\text{SS}$  (e) Polarization curves of bare SS, CNT/SS, OxCNT/SS,  $\text{RuO}_2/\text{OxCNT}/\text{SS}$  and  $\text{RuO}_2/\text{SS}$  recorded without iR correction for the OER in 1 M KOH. (f, g) Tafel and EIS measurements for the corresponding prepared electrodes. (h) Long-term assessment of the  $\text{RuO}_2/\text{OxCNT}/\text{SS}$  acquired at a constant current density of  $10 \text{ mA}/\text{cm}^2$ .

The increase in oxygen concentration observed in the RuO<sub>2</sub>/OxCNT/SS sample when compared to OxCNT/SS, supports the successful deposition of ruthenium oxide. The TEM image of the RuO<sub>2</sub>/OxCNT (Figure 5-3(b)) shows a change of the morphology of the surface of the OxCNT, and TEM mapping (Figure 5-3(b), bottom right) shows a uniform distribution of O and Ru on the RuO<sub>2</sub>/OxCNT. The HRTEM image of RuO<sub>2</sub>/OxCNT (Figure 5-3(c)) shows the lattice fringes of 0.35 nm, which can be correspond well to the (002) planes of CNT. The XPS spectrum of the Ru 3d (Figure 5-3(d)) has a peak of Ru 3d<sub>5/2</sub> located at 280.7 eV, in agreement with Ru with a valence of +4.<sup>[39]</sup> The defect on the surface of RuO<sub>2</sub>/OxCNT/SS didn't change significantly with similar  $L_a$  (Table S 5-2).

The RuO<sub>2</sub>/OxCNT/SS sample was used as the anode for the OER measurement. The polarization curves (Figure 5-3(e)) indicate that RuO<sub>2</sub>/OxCNT/SS exhibits an overpotential of 217 mV to reach a current density of 10 mA/cm<sup>2</sup>, while OxCNT/SS, CNT/SS and bare SS, exhibit overpotentials equal to 267 mV, 297 mV, and 277 mV, respectively, without iR compensation. The overpotential result of our RuO<sub>2</sub>/OxCNT/SS is better or comparable to the values recently reported in the literatures (**Table S 5-5**).<sup>[17, 19, 20-22, 24-26, 36, 40]</sup> Noteworthy, the overpotential required for obtaining a current density of 10 mA/cm<sup>2</sup> of the SS increased with approximately 20 mV after the growth of CNT but was reduced for higher current densities. The performance of the OxCNT/SS is better than that of the bare SS under both low and high current densities, possibly because of the oxygen species and/or defects created during the oxidation process.<sup>[41]</sup> The RuO<sub>2</sub>/OxCNT/SS presented the same overpotential at 10 mA/cm<sup>2</sup> as that of RuO<sub>2</sub>/SS (commercial RuO<sub>2</sub> deposited on SS without CNT) used as a reference, but a lower overpotential at higher current densities. The RuO<sub>2</sub>/OxCNT/SS has the smallest Tafel slope when compared to OxCNT/SS, CNT/SS and bare SS (Figure 5-3(f)). The ECSA of the RuO<sub>2</sub>/OxCNT/SS is almost 30 times higher than that of the bare SS, and more than 2 times higher than OxCNT/SS and CNT/SS (**Figure S 5-11**). The EIS results reveal that RuO<sub>2</sub>/OxCNT/SS exhibits the lowest  $R_{ct}$  of 1.03 Ω, while the  $R_{ct}$  values of OxCNT/SS, CNT/SS and bare SS are, 1.42 Ω, 5.77 Ω and 2.62 Ω respectively, (Figure 5-3(g), **Figure S 5-12** and Table S 5-6). This indicates a faster charge transfer for the OER on the RuO<sub>2</sub>/OxCNT/SS 3D electrode. Most importantly, the RuO<sub>2</sub>/OxCNT/SS has a good stability during a continuous measurement of 12 h at a constant current density of 10 mA/cm<sup>2</sup> (Figure 5-3(h)).



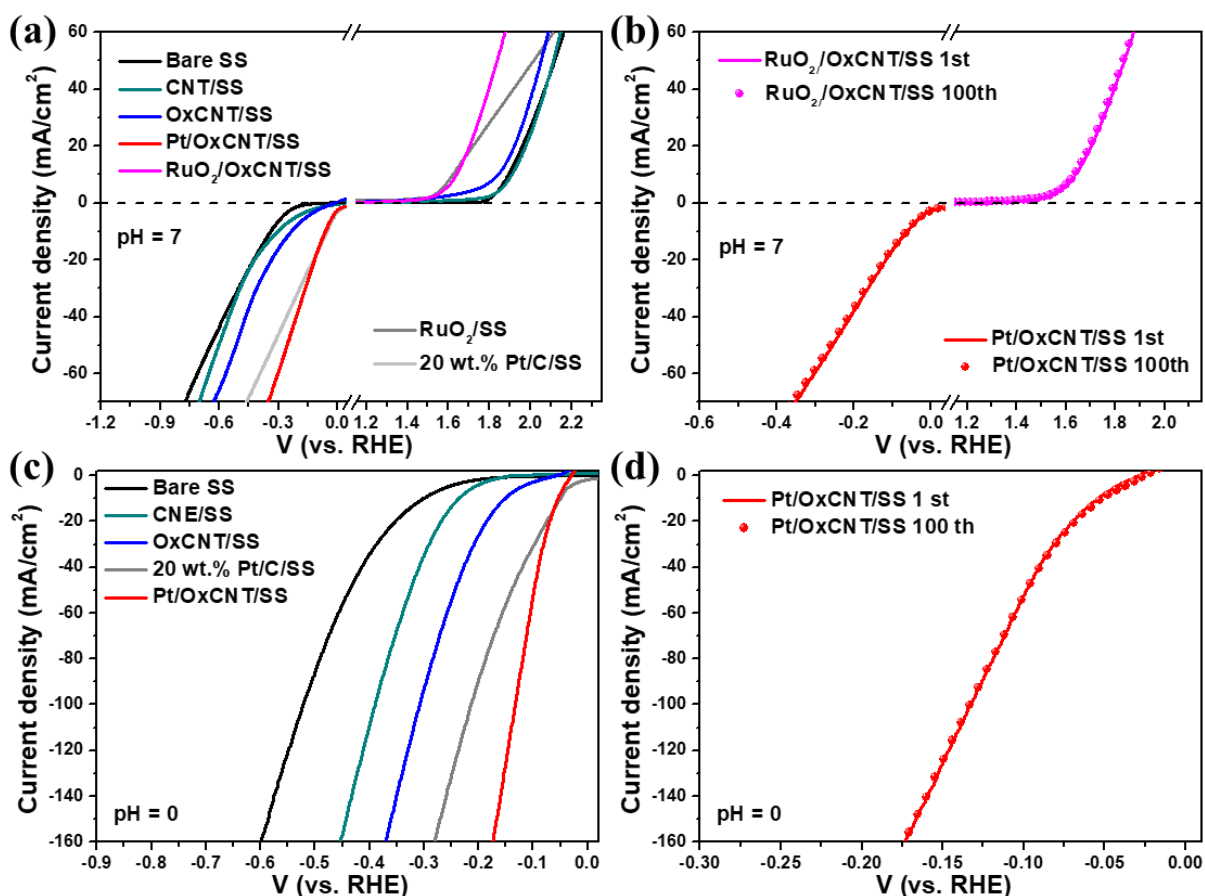


**Figure 5-4.** Polarization curves of the prepared 3D electrodes recorded in the (a) neutral electrolyte (1 M PBS) for OER and HER, and (c) acidic electrolyte (0.5 M H<sub>2</sub>SO<sub>4</sub>) for the HER. (b) The stability assessment of the RuO<sub>2</sub>/OxCNT/SS and Pt/OxCNT/SS for OER and HER in a neutral electrolyte. (c) The stability evaluation of the Pt/OxCNT/SS in an acidic electrolyte.

The water splitting performance of the prepared 3D electrodes were also evaluated in neutral and acid electrolytes. For water splitting in a neutral electrolyte (1 M PBS, pH = 7, **Figure 5-4(a)**), the Pt/OxCNT/SS and RuO<sub>2</sub>/OxCNT/SS exhibits overpotentials of 52 and 410 mV to reach a current density of 10 mA/cm<sup>2</sup> for the HER and OER, respectively, which are much better than that of the prepared OxCNT/SS, CNT/SS and Bare SS (Table S 5-3 and Table S 5-5). The Tafel plots (**Figure S 5-13(a-b)**) show that Pt/OxCNT/SS and RuO<sub>2</sub>/OxCNT/SS demonstrate the lowest Tafel slopes for HER and OER, respectively, compared to that of OxCNT/SS, CNT/SS and Bare SS, indicating the better kinetics during the corresponding reactions. The Pt/OxCNT/SS and RuO<sub>2</sub>/OxCNT/SS demonstrate comparable HER and OER performances with the reference of 20 wt. % Pt/C/SS and RuO<sub>2</sub>/SS at low current densities, but show much better activity at the high current densities (Figure 5-4(a)), possibly due to the better interface interaction between the CNTs and SS. The comparison of the prepared Pt/OxCNT/SS and RuO<sub>2</sub>/OxCNT/SS and recently reports on SS-based electrodes is shown in Table S 5-3 and Table S 5-5. The stability measurement (Figure 5-4(b)) shows that the polarization curves of Pt/OxCNT/SS and RuO<sub>2</sub>/OxCNT/SS are constant after repeating 100 times, indicating the good

stability of the prepared electrodes for HER and OER, respectively, in the neutral electrolyte. For water splitting in an acidic electrolyte (0.5 M H<sub>2</sub>SO<sub>4</sub>, pH = 0), the Pt/OxCNT/SS shows a HER performance with an overpotential of 54 mV to reach a current density of 10 mA/cm<sup>2</sup> (Figure 5-4(c), Table S 5-3). The HER activity of Pt/OxCNT/SS is much better than that of OxCNT/SS, CNT/SS and bare SS and other recently reported SS-based electrodes (Table S 5-3). Compared to the 20 wt. % Pt/C/SS, the HER performance of Pt/OxCNT/SS show a similar trend as in the neutral electrolyte. Tafel plots show that the Pt/OxCNT/SS has the lowest Tafel slope (Figure S 5-13(c)), indicating better kinetics for the HER in the acid electrolyte. The stability assessment reveals the good stability property of Pt/OxCNT/SS for the HER in the acidic electrolyte (Figure 5-4(d)). Graphite electrode was used as the counter electrode to assess the performance and stability of the prepared electrodes (**Figure S 5-14(a)** inset).<sup>[42]</sup> The Pt/CNT/SS demonstrated similar performance with different counter electrodes and good stability for 14 h using a graphite counter electrode (**Figure S 5-14(a, b)**). However, the RuO<sub>2</sub>/OxCNT/SS did not show high stability in the acidic electrolyte during the OER measurement (Figure S 5-13(d)). As shown in the inset of Figure S 5-13(d), the color of the electrolyte became yellow after repeating the polarization curves measurement for 100 times, due to the corrosion of SS in the acidic environment under anodic bias.<sup>[20]</sup> The prepared electrodes were also checked after the long-term measurement under critical operating conditions. The Pt/OxCNT/SS after long-time measurement under the acidic electrolyte and RuO<sub>2</sub>/OxCNT/SS under the alkaline electrolyte were characterized by Raman spectroscopy (**Figure S 5-15**) and XPS (**Figure S 5-16**). After the long-term measurement, the *I<sub>D</sub>/I<sub>G</sub>* and *L<sub>a</sub>* did not change drastically (Table S 5-2). From the O1s of Pt/CNT/SS, the content of -OH increased significantly, suggesting the surface of electrode was covered with a thin hydroxide layer (Figure S 5-16(b)). There are no obvious changes that appear in other spectra.

Subsequently, the Pt/OxCNT/SS and RuO<sub>2</sub>/OxCNT/SS 3D electrodes which show excellent HER and OER activities, were used, respectively, as the cathode and anode for the overall water splitting. First, we used a two-electrode cell configuration with a water-cooling system to keep a constant temperature of 25 °C (**Figure 5-5(a)**). The polarization curve (Figure 5-5(b)) indicates that the cell configuration of Pt/OxCNT/SS || RuO<sub>2</sub>/OxCNT/SS exhibits a 1.50 V to reach 10 mA/cm<sup>2</sup>. Comparatively, the configurations of OxCNT/SS || OxCNT/SS, CNT/SS || CNT/SS and SS || SS need voltages of 1.60 V, 1.70 V and 1.87 V, respectively, to reach the current density of 10 mA/cm<sup>2</sup>. Next, the overall water splitting performance of the prepared electrodes was also evaluated in the neutral electrolyte (Figure 5-5(c)). The configuration of Pt/OxCNT/SS || RuO<sub>2</sub>/OxCNT/SS needs 1.7 V to reach a current density of 10 mA/cm<sup>2</sup>, which

is much better than that of the OxCNT/SS || OxCNT/SS, CNT/SS || CNT/SS and SS || SS configurations. Also for overall water splitting, the configuration using the 3D electrodes of Pt/OxCNT/SS || RuO<sub>2</sub>/OxCNT/SS has a notable performance when compared to recent reports in the literature on SS-based electrodes for overall water splitting in both alkaline and neutral electrolytes (Table S 5-7).<sup>[23, 24, 36]</sup> The 20 wt.% Pt/C/SS || RuO<sub>2</sub>/SS configuration presented almost the same cell voltage at 10 mA/cm<sup>2</sup> when compared to the Pt/OxCNT/SS || RuO<sub>2</sub>/OxCNT/SS novel configuration, in both alkaline and neutral electrolytes. However, the later has a better performance with a much lower cell voltage at higher current densities.

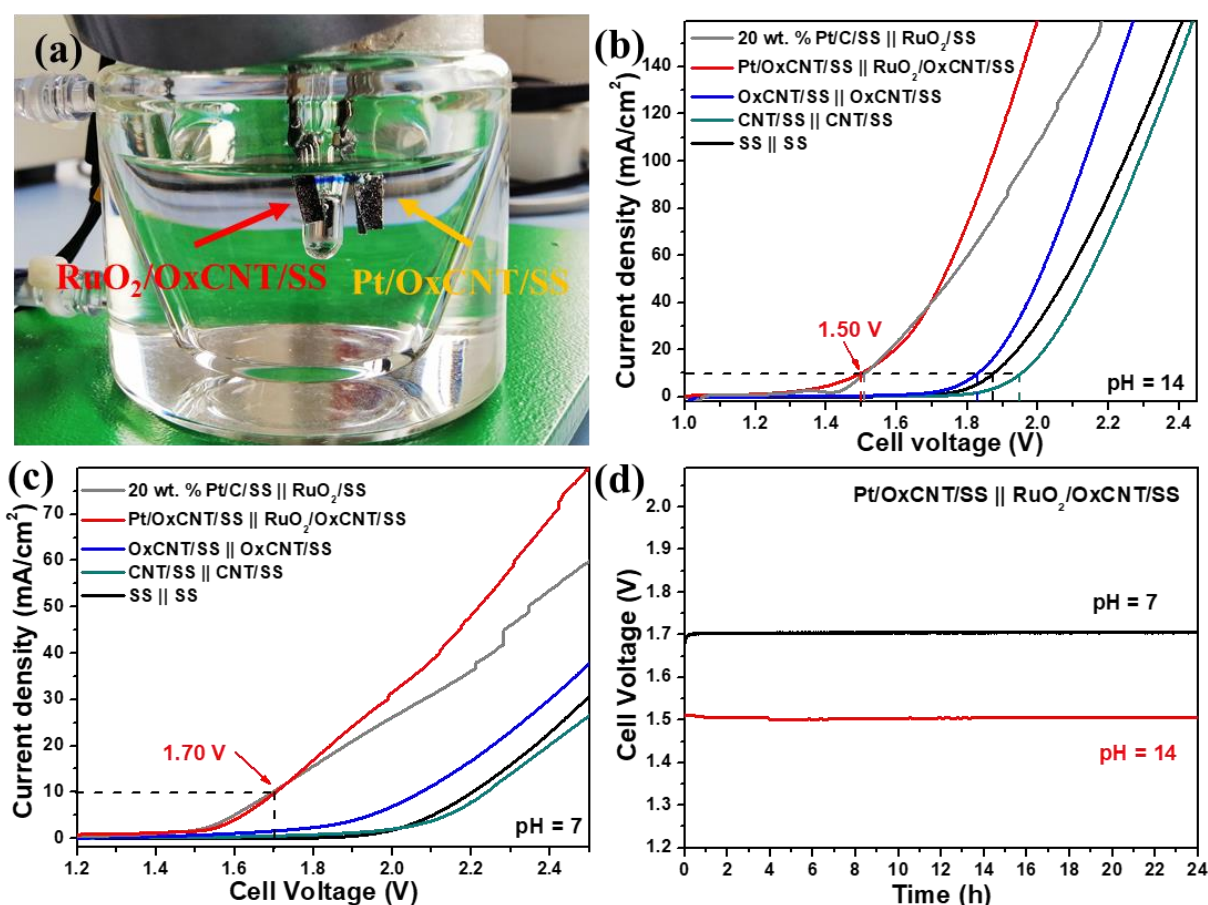


**Figure 5-5.** (a) Picture of the electrolysis setup for the overall water splitting with the two-electrode configuration, including a thermometer for temperature monitoring. (b, c) Polarization curves of the SS || SS, CNT/SS || CNT/SS, OxCNT/SS || OxCNT/SS, Pt/OxCNT/SS || RuO<sub>2</sub>/OxCNT/SS and 20 wt.% Pt/C/SS || RuO<sub>2</sub>/SS configurations investigated for overall water splitting in alkaline and neutral electrolytes, respectively. (d) Long-time measurement for the Pt/OxCNT/SS || RuO<sub>2</sub>/OxCNT/SS recorded at 10 mA/cm<sup>2</sup> in both alkaline and neutral electrolytes.

This effect can be due to the 3D hierarchical structure of the electrodes and the better interfacial interaction between the SS and the deposited catalysts, in a process that was improved by the growth of CNTs on the SS surface. Moreover, the Pt/OxCNT/SS || RuO<sub>2</sub>/OxCNT/SS configuration demonstrated well stability for the overall water splitting for at least 24 h (Figure 5-5(d)) in both alkaline and neutral electrolytes. As shown in Figure S 5-17(a),

the performance of the Pt/C/SS || RuO<sub>2</sub>/SS configuration decreased drastically at the beginning of the measurement. The as-prepared electrodes were investigated after the long-term measurement (Figure S 5-17(b)), which showed that the deposited electrocatalysts had exfoliated from the substrate owing to the unfavorable interface between the deposited electrocatalysts and the SS substrate. The instability of the Pt/C/SS and RuO<sub>2</sub>/SS further prove that our strategy using CNTs as the interfacial material is an effective way to increase the interface effect for the preparation of highly-active and stable electrodes.

## 5.5 Conclusions

We report an efficient and universal process to couple highly-active electrocatalysts with a flexible and corrosion-resistant SS mesh to obtain 3D electrodes with excellent activity for water splitting. Our strategy involves creating a CNT interfacial network, with excellent conductivity, between the SS and electrocatalysts deposited on it. The CNT offers a large surface area for the modification of the SS with high-active electrocatalysts, therefore promoting an intense interconnection between SS and electrocatalysts and resulting in a successful enhance of the stability of the overall system. Moreover, the prepared Pt/OxCNT/SS and RuO<sub>2</sub>/OxCNT/SS electrodes exhibit the best HER activity and the comparable OER performance, respectively, in a wide pH range, when compared to recently report SS-based electrodes in the literature. The ECSA, Tafel and EIS measurements show that the prepared Pt/OxCNT/SS and RuO<sub>2</sub>/OxCNT/SS 3D electrodes exhibit larger ECSA, better kinetics and faster charge transfer for the corresponding reactions than other prepared electrodes. Moreover, the Pt/OxCNT/SS || RuO<sub>2</sub>/OxCNT/SS cell configuration just need 1.50 and 1.70 V to obtain a current density of 10 mA/cm<sup>2</sup> for the overall water splitting in the alkaline and neutral electrolytes and is stable for at least 24 h. Our novel strategy has the potential to be applied in numerous other areas of research and industry that require coupling of stainless steel with other highly active and functional catalysts to construct 3D electrodes, such as in new supercapacitors development and in metal-air battery and fuel cell research.

## 5.6 Acknowledgment

This research was financially supported by the BMBF - project Struktursolar. X. Li acknowledges the financial support from Youth Innovation Promotion Association, Chinese Academy of Sciences (CAS). JMSS and R. Wehrspohn acknowledge the Deutsche Forschungsgemeinschaft (DFG) for the granted project WE 4051/21-1. The authors greatly acknowledge Dr. Frank Heyroth for the help with scanning electron microscopy energy

dispersive X - ray spectroscopy (SEM - EDS) and transmission electron microscopy (TEM) measurements performed at the Interdisciplinary Center of Materials Science-Martin Luther University Halle-Wittenberg (CMAT-MLU).

## 5.7 References

- [1] T. J. Meyer, *Nature* 2008, 451, 778; I. Roger, M. A. Shipman, M. D. Symes, *Nat. Rev. Chem.* 2017, 1, 0003; F. Song, L. Bai, A. Moysiadou, S. Lee, C. Hu, L. Liardet, X. Hu, *J. Am. Chem. Soc.* 2018, 140, 7748.
- [2] B. You, M. T. Tang, C. Tsai, F. Abild-Pedersen, X. Zheng, H. Li, *Adv. Mater.* 2019, e1807001.
- [3] V. Petrykin, K. Macounova, O. A. Shlyakhtin, P. Krtil, *Angew. Chem. Int. Ed. Engl.* 2010, 49, 4813; B. Lim, M. Jiang, P. H. Camargo, E. C. Cho, J. Tao, X. Lu, Y. Zhu, Y. Xia, *Science* 2009, 324, 1302.
- [4] L. Han, S. Dong, E. Wang, *Adv Mater* 2016, 28, 9266.
- [5] W. Chen, K. Sasaki, C. Ma, A. I. Frenkel, N. Marinkovic, J. T. Muckerman, Y. Zhu, R. R. Adzic, *Angew. Chem. Int. Ed. Engl.* 2012, 51, 6131.
- [6] C. Tan, Z. Lai, H. Zhang, *Adv. Mater.* 2017, 29, 1701392; Y. Guo, T. Park, J. W. Yi, J. Henzie, J. Kim, Z. Wang, B. Jiang, Y. Bando, Y. Sugahara, J. Tang, Y. Yamauchi, *Adv. Mater.* 2019, e1807134.
- [7] M. Gao, J. Liang, Y. Zheng, Y. Xu, J. Jiang, Q. Gao, J. Li, S. Yu, *Nat. Commun.* 2015, 6, 5982.
- [8] R. Zhang, X. Wang, S. Yu, T. Wen, X. Zhu, F. Yang, X. Sun, X. Wang, W. Hu, *Adv Mater* 2017, 29, 1605502; J. Joo, T. Kim, J. Lee, S. I. Choi, K. Lee, *Adv. Mater.* 2019, e1806682.
- [9] H. Sun, J. Zhu, D. Baumann, L. Peng, Y. Xu, I. Shakir, Y. Huang, X. Duan, *Nature Reviews Materials* 2018, 4, 45.
- [10] N. K. Chaudhari, H. Jin, B. Kim, K. Lee, *Nanoscale* 2017, 9, 12231.
- [11] J. Zhang, Q. Zhang, X. Feng, *Adv. Mater.* 2019, e1808167.
- [12] B. Liu, Y. F. Zhao, H. Q. Peng, Z. Y. Zhang, C. K. Sit, M. F. Yuen, T. R. Zhang, C. S. Lee, W. J. Zhang, *Adv Mater* 2017, 29.
- [13] P. Chen, K. Xu, T. Zhou, Y. Tong, J. Wu, H. Cheng, X. Lu, H. Ding, C. Wu, Y. Xie, *Angew. Chem. Int. Ed. Engl.* 2016, 55, 2488; Y. Hou, M. Qiu, T. Zhang, J. Ma, S. Liu, X. Zhuang, C. Yuan, X. Feng, *Adv. Mater.* 2017, 29.
- [14] T. Sharifi, E. Gracia-Espino, X. Jia, R. Sandstrom, T. Wagberg, *ACS Appl. Mater. Interfaces* 2015, 7, 28148.
- [15] J. P. Lai, S. P. Li, F. X. Wu, M. Saqib, R. Luque, G. B. Xu, *Energy Environ. Sci.* 2016, 9, 1210; X. Wang, H. Chen, Y. F. Xu, J. Liao, B. Chen, H. Rao, D. Kuang, C. Y. Su, *J. Mater. Chem. A* 2017, 5, 7191.
- [16] H. Schäfer, M. Chatenet, *ACS Energy Letters* 2018, 3, 574.
- [17] F. Yu, F. Li, L. Sun, *Int. J. Hydrogen Energ.* 2016, 41, 5230.
- [18] H. Schafer, S. M. Beladi-Mousavi, L. Walder, J. Wollschlager, O. Kuschel, S. Ichilmann, S. Sadaf, M. Steinhart, K. Kupper, L. Schneider, *ACS Catal.* 2015, 5, 2671.
- [19] H. Schäfer, D. M. Chevrier, K. Kuepper, P. Zhang, J. Wollschlaeger, D. Daum, M. Steinhart, C. Heß, U. Krupp, K. Müller-Buschbaum, J. Stangl, M. Schmidt, *Energy Environ. Sci.* 2016, 9, 2609; H. Schäfer, K. Kupper, J. Wollschlager, N. Kashaev, J. Hardege, L. Walder, S. Mohsen Beladi-Mousavi, B. Hartmann-Azanza, M. Steinhart, S. Sadaf, F. Dorn, *ChemSusChem* 2015, 8, 3099; H. Schäfer, S. Sadaf, L. Walder, K.

- Kuepper, S. Dinklage, J. Wollschläger, L. Schneider, M. Steinhart, J. Hardege, D. Daum, *Energy Environ. Sci.* 2015, 8, 2685.
- [20] H. Schäfer, D. M. Chevrier, P. Zhang, J. Stangl, K. Müller-Buschbaum, J. D. Hardege, K. Kuepper, J. Wollschläger, U. Krupp, S. Dühren, M. Steinhart, L. Walder, S. Sadaf, M. Schmidt, *Adv. Funct. Mater.* 2016, 26, 6402.
- [21] D. Tang, O. Mabayoje, Y. Lai, Y. Liu, C. B. Mullins, *ChemistrySelect* 2017, 2, 2230.
- [22] H. Zhong, J. Wang, F. Meng, X. Zhang, *Angew. Chem. Int. Ed. Engl.* 2016, 55, 9937.
- [23] M. S. Balogun, W. Qiu, Y. Huang, H. Yang, R. Xu, W. Zhao, G. R. Li, H. Ji, Y. Tong, *Adv. Mater.* 2017, 29, 1702095.
- [24] X. Liu, B. You, Y. Sun, *ACS Sustain. Chem. Eng.* 2017, 5, 4778.
- [25] X. Huang, S. Chang, W. S. V. Lee, J. Ding, J. M. Xue, *J. Mater. Chem. A* 2017, 5, 18176.
- [26] J. Chen, J. Ren, M. Shalom, T. Fellinger, M. Antonietti, *ACS Appl. Mater. Interfaces* 2016, 8, 5509.
- [27] N. Sano, K. Nojima, T. Kodama, H. Tamon, *Carbon* 2016, 103, 151.
- [28] C. T. Wirth, B. C. Bayer, A. D. Gamalski, S. Esconjauregui, R. S. Weatherup, C. Ducati, C. Baetz, J. Robertson, S. Hofmann, *Chem. Mat.* 2012, 24, 4633.
- [29] Z. Zhuang, S. A. Giles, J. Zheng, G. R. Jenness, S. Caratzoulas, D. G. Vlachos, Y. Yan, *Nat. Commun.* 2016, 7, 10141.
- [30] M. Gong, W. Zhou, M. C. Tsai, J. Zhou, M. Guan, M. C. Lin, B. Zhang, Y. Hu, D. Y. Wang, J. Yang, S. J. Pennycook, B. J. Hwang, H. Dai, *Nat. Commun.* 2014, 5, 4695.
- [31] A. M. El-Sawy, I. M. Mosa, D. Su, C. J. Guild, S. Khalid, R. Joesten, J. F. Rusling, S. L. Suib, *Adv. Energy Mater.* 2016, 6, 1501966.
- [32] Y. Li, W. Zhou, H. Wang, L. Xie, Y. Liang, F. Wei, J. C. Idrobo, S. J. Pennycook, H. Dai, *Nat Nanotechnol* 2012, 7, 394.
- [33] L. G. Cançado, K. Takai, T. Enoki, M. Endo, Y. A. Kim, H. Mizusaki, A. Jorio, L. N. Coelho, R. Magalhães-Paniago, M. A. Pimenta, *Applied Physics Letters* 2006, 88, 163106.
- [34] V. Datsyuk, M. Kalyva, K. Papagelis, J. Parthenios, D. Tasis, A. Siokou, I. Kallitsis, C. Galiotis, *Carbon* 2008, 46, 833.
- [35] W. Yuan, Y. Cheng, P. K. Shen, C. M. Li, S. P. Jiang, *J. Mater. Chem. A* 2015, 3, 1961.
- [36] G. He, W. Zhang, Y. Deng, C. Zhong, W. Hu, X. Han, *Catalysts* 2017, 7, 366; L. Wang, X. Huang, S. Jiang, M. Li, K. Zhang, Y. Yan, H. Zhang, J. M. Xue, *ACS Appl. Mater. Interfaces* 2017, 9, 40281.
- [37] H. Liang, A. N. Gandi, D. H. Anjum, X. Wang, U. Schwingenschlogl, H. N. Alshareef, *Nano Lett.* 2016, 16, 7718.
- [38] W. Cui, Q. Liu, N. Cheng, A. M. Asiri, X. Sun, *Chem. Commun.* 2014, 50, 9340.
- [39] R. Bi, X. Wu, F. Cao, L. Jiang, Y. Guo, L. Wan, *J. Phys. Chem. C* 2010, 114, 2448.
- [40] M. S. Balogun, W. Qiu, Y. Huang, H. Yang, R. Xu, W. Zhao, G. R. Li, H. Ji, Y. Tong, *Adv Mater* 2017, 29; A. Balram, H. Zhang, S. Santhanagopalan, *Mater. Chem. Front.* 2017, 1, 2376; F. Moureaux, P. Stevens, G. Toussaint, M. Chatenet, *J. Power Sources* 2013, 229, 123; S. K. Tiwari, A. K. L. Singh, R. N. Singh, *J. Electroanal. Chem.* 1991, 319, 263; S. Anantharaj, M. Venkatesh, A. S. Salunke, T. V. S. V. Simha, V. Prabu, S. Kundu, *ACS Sustain. Chem. Eng.* 2017, 5, 10072; Q. Zhang, H. Zhong, F. Meng, D. Bao, X. Zhang, X. Wei, *Nano Res.* 2018, 11, 1294; H. Schafer, K. Kupper, K. Muller-Buschbaum, D. Daum, M. Steinhart, J. Wollschläger, U. Krupp, M. Schmidt, W. Han, J. Stangl, *Nanoscale* 2017, 9, 17829; J. S. Chen, J. Ren, M. Shalom, T. Fellinger, M. Antonietti, *ACS Appl Mater Interfaces* 2016, 8, 5509; F. J. Pérez-Alonso, C. Adán, S. Rojas, M. A. Peña, J. L. G. Fierro, *Int. J. Hydrogen Energ.* 2014, 39, 5204.
- [41] X. Lu, W. L. Yim, B. H. Suryanto, C. Zhao, *J. Am. Chem. Soc.* 2015, 137, 2901.
- [42] H. Zhang, X. Li, A. Hähnel, V. Naumann, C. Lin, S. Azimi, S. L. Schweizer, A. W. Maijenburg, R. B. Wehrspohn, *Adv. Funct. Mater.* 2018, 1706847.

- [43] A. Tkachuk, F. Duewer, H. T. Cui, M. Feser, S. Wang, W. B. Yun, Z. Kristallogr 2007, 222, 650; A. T. L. Tan, J. Beroz, M. Kolle, A. J. Hart, Adv. Mater. 2018, 30, e1803620.



## 5.8 Supporting Information

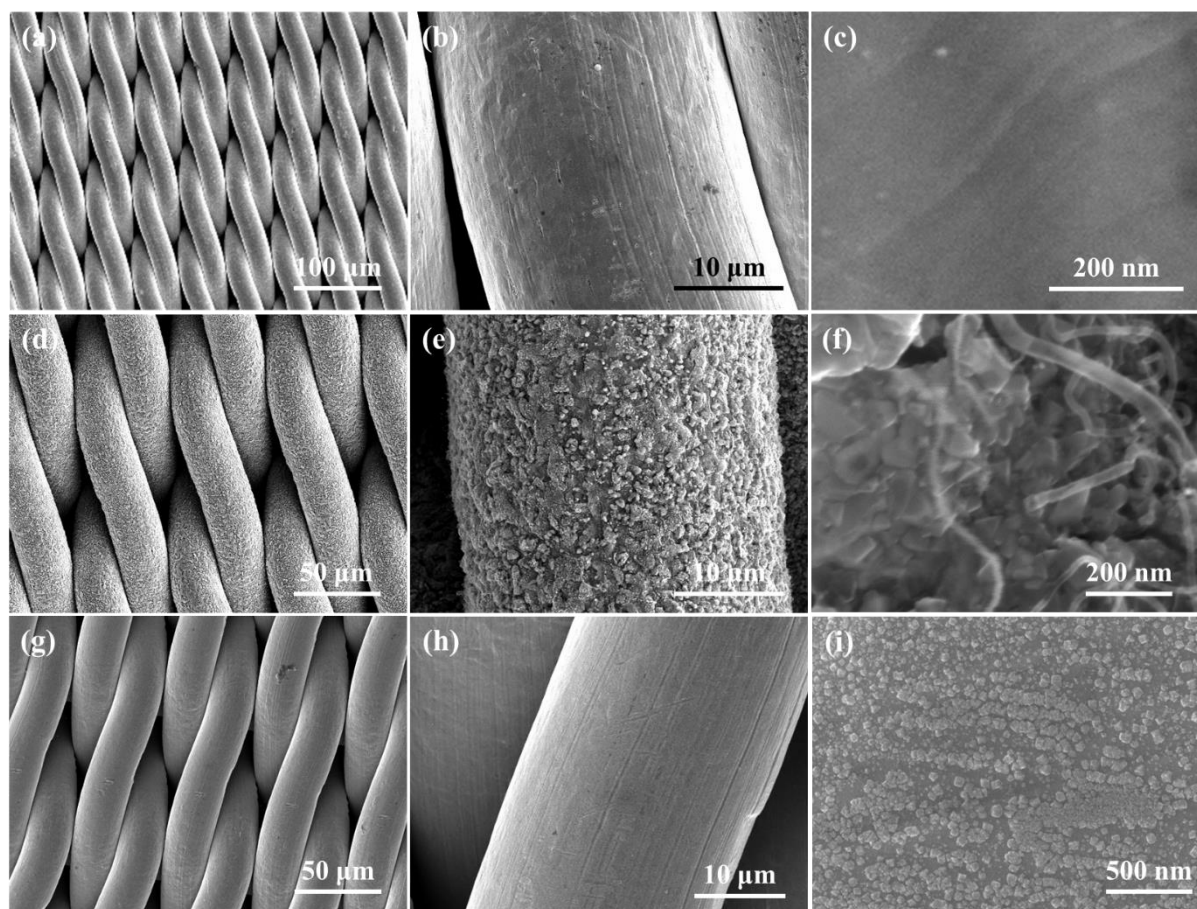


**Figure S 5-1.** Scanning electron microscopy (SEM) images of the surface modification of the stainless-steel (SS) mesh. Images (a-c) show the bare SS mesh with increasing magnifications. Images (d-f) show the CNT/SS prepared without the deposition of Fe nanoparticles with different magnifications, and (g-i) show the SEM images of the deposited Fe nanoparticles on the bare SS mesh by a double pulse deposition (DPD) process, resulting in FeNPs/SS.

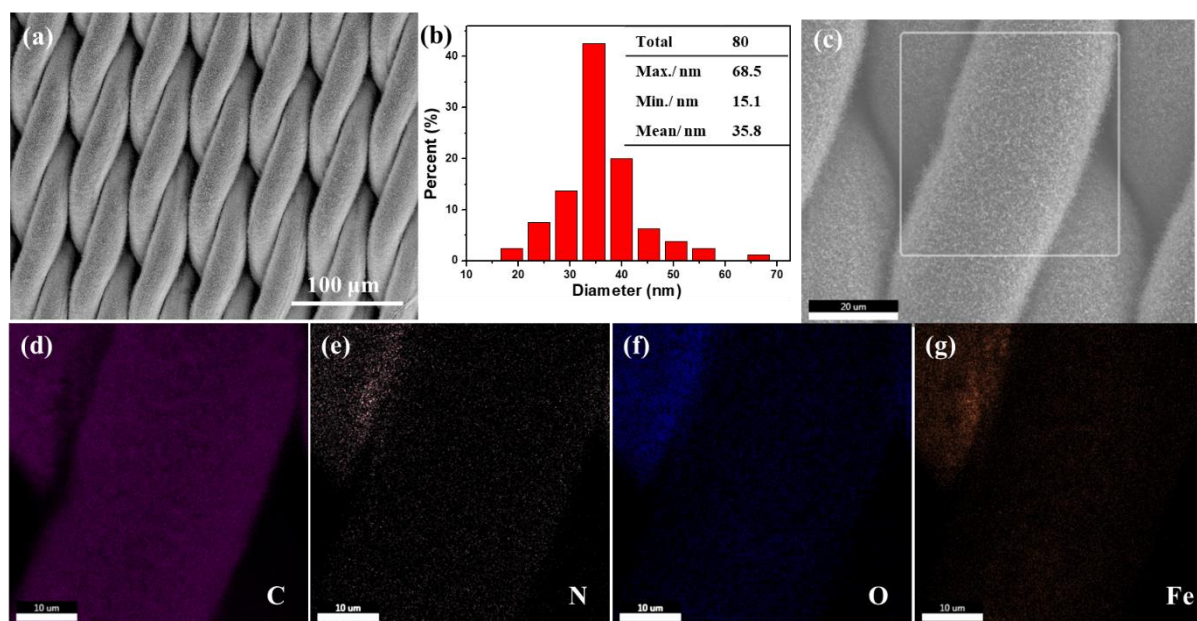


**Figure S 5-2.** (a) The SEM image of the as-prepared CNT/SS. (b) the distribution of the diameter of the grow carbon nanotubes (CNTs) on the SS. (c-f) The selected area mapping of the CNT/SS of overlay, C, N, O and Fe, respectively. The area acquired for the EDS mapping was marked in (c).



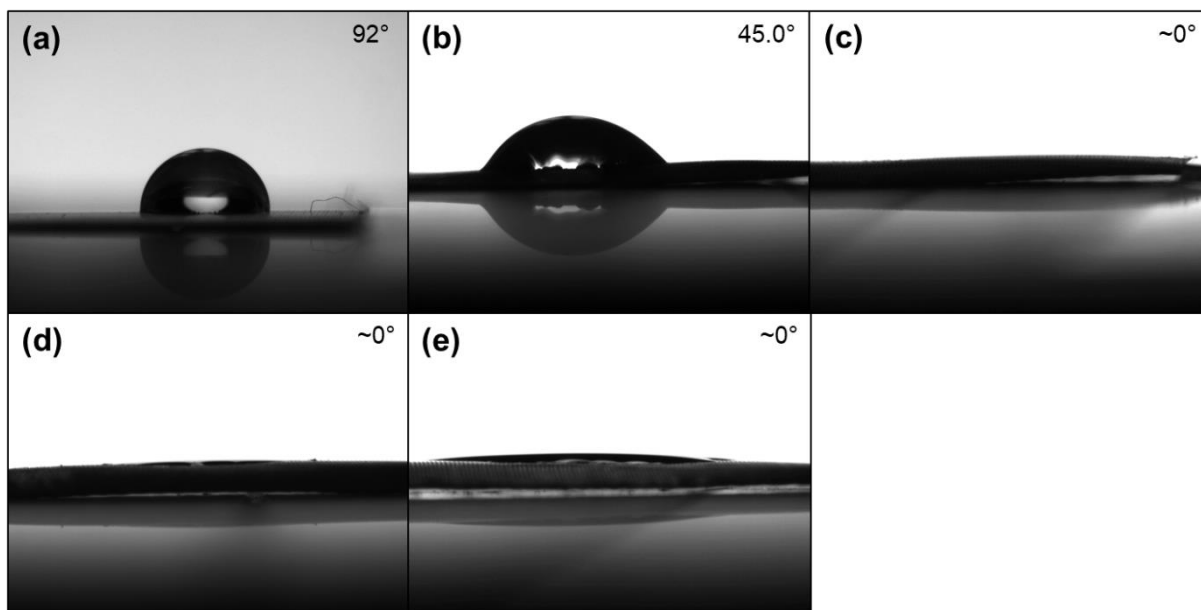


**Figure S 5-3.** Contact angle measurement for the (a) bare SS and prepared (b) CNT/SS, (c) OxCNT/SS, (d) Pt/CNT/SS and (e) RuO<sub>2</sub>/CNT/SS.

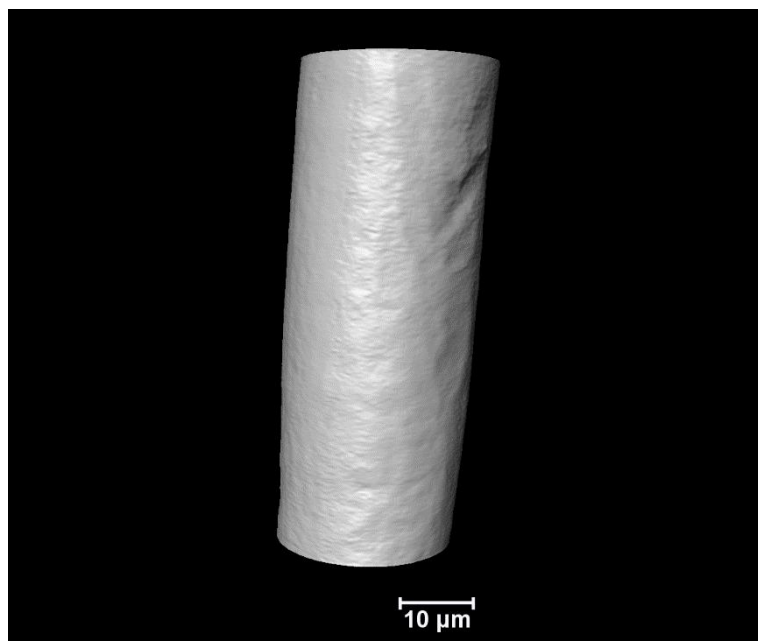


**Figure S 5-4.** 3D representation of a single bare SS wire obtained from X-ray computed tomography with nanometric resolution (nano-CT).

**Table S 5-1.** Summary of the SEM-EDS results of the as-prepared electrodes.

Sample	(wt%)	C	O	N	Fe	Ni	Cr	Mo	Si	Pt	Ru
Bare SS		1.77	--	1.17	64.02	12.18	18.25	1.95	0.66	--	--
CNT/SS		81.18	1.09	1.71	6.61	1.15	6.52	0.94	0.80	--	--
OxCNT/SS		59.61	13.60	2.03	9.41	1.71	9.40	3.32	0.93	--	--
Pt/OxCNT/SS		54.80	14.74	1.21	8.64	2.09	8.15	0.22	0.62	9.71	--
RuO <sub>2</sub> /OxCNT/SS		47.37	20.32	1.13	7.95	2.29	8.70	1.26	0.37	--	9.79
OxSS		2.08	2.74	1.20	60.83	14.00	14.41	3.92	0.82	--	--

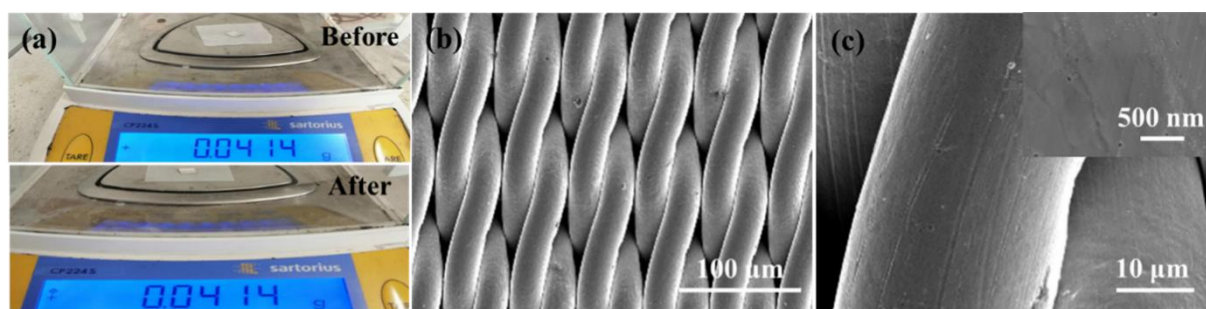


**Figure S 5-5.** (a) Photographs of the weight change of the bare SS after the oxidation treatment. (b, c) SEM images of the SS after the oxidation treatment denoted as OxSS. High-resolution SEM image of the OxSS is shown in the inset of (c).

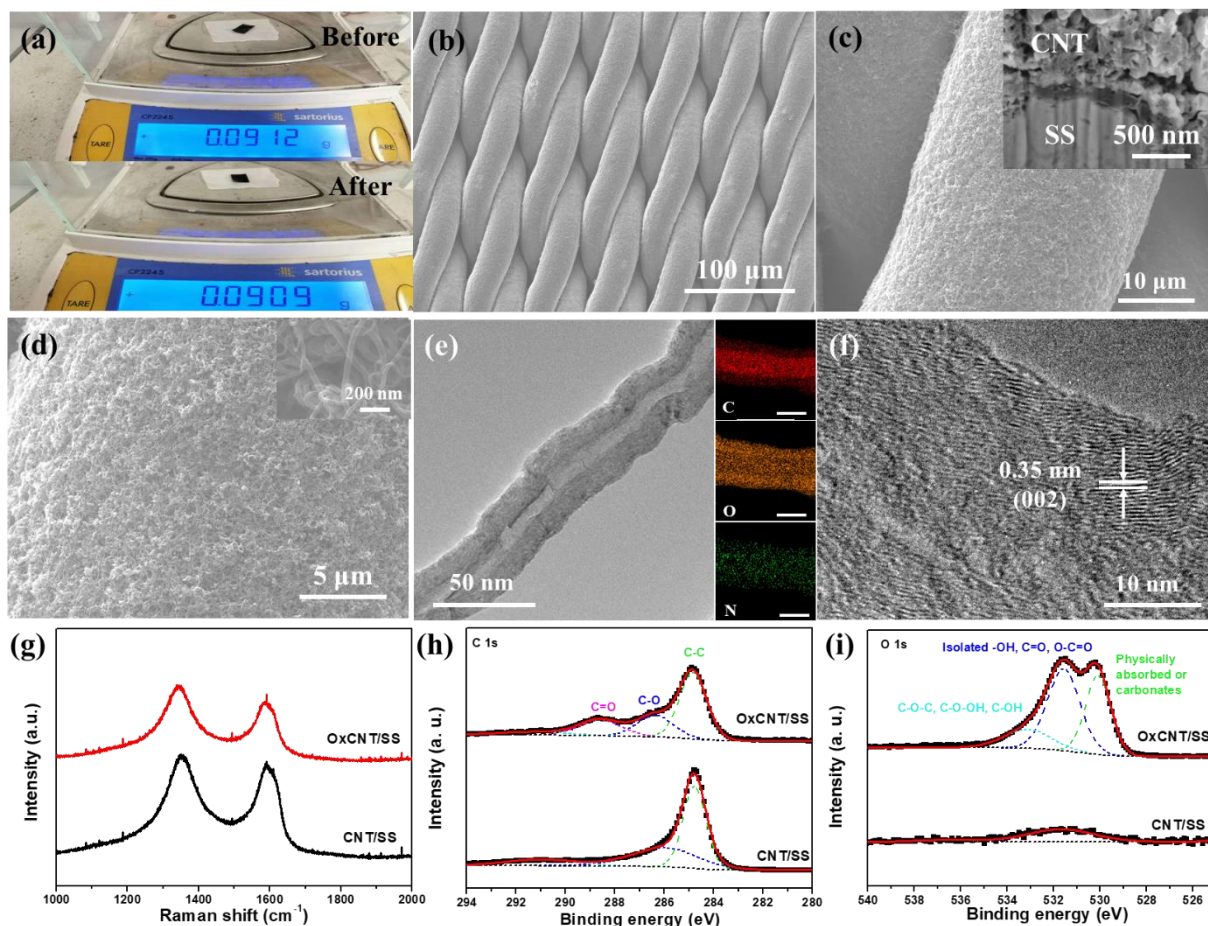


**Figure S 5-6.** (a) Photograph of the weight change of the OxCNT/SS after the oxidation treatment, (b-d) SEM images of the CNT/SS after the oxidation treatment, denoted as OxCNT/SS. The cross section prepared by FIB and HRSEM image of OxCNT are shown in the inset of (c) and (d), respectively. (e) TEM image of the OxCNT and element mapping of C, O and N as shown in the insets on the right. (f) HRTEM image of the OxCNT. (g) Raman spectra of the synthesized CNT/SS and OxCNT/SS. (h, i) XPS spectra of C 1s and O 1s for CNT/SS and OxCNT/SS.

**Table S 5-2.** Summary of the fitted Raman spectra of the as-prepared electrodes.

Sample	$I_D$	$I_G$	$I_D/I_G$	$L_a$ (nm)
CNT/SS	1341.8	1586.7	1.06	18.1
OxCNT/SS	1353.2	1591.7	1.12	17.2
Pt/OxCNT/SS	1350.2	1586.8	1.11	17.3
RuO <sub>2</sub> /OxCNT/SS	1351.5	1589.3	1.13	17.0
Pt/OxCNT/SS after test <sup>a</sup>	1351.5	1586.7	1.11	17.3
RuO <sub>2</sub> /OxCNT/SS after test <sup>b</sup>	1351.7	1586.4	1.11	17.3

<sup>a</sup>: After the long-term measurement in 0.5 M H<sub>2</sub>SO<sub>4</sub>. <sup>b</sup>: After the long-term measurement with 1 M KOH.

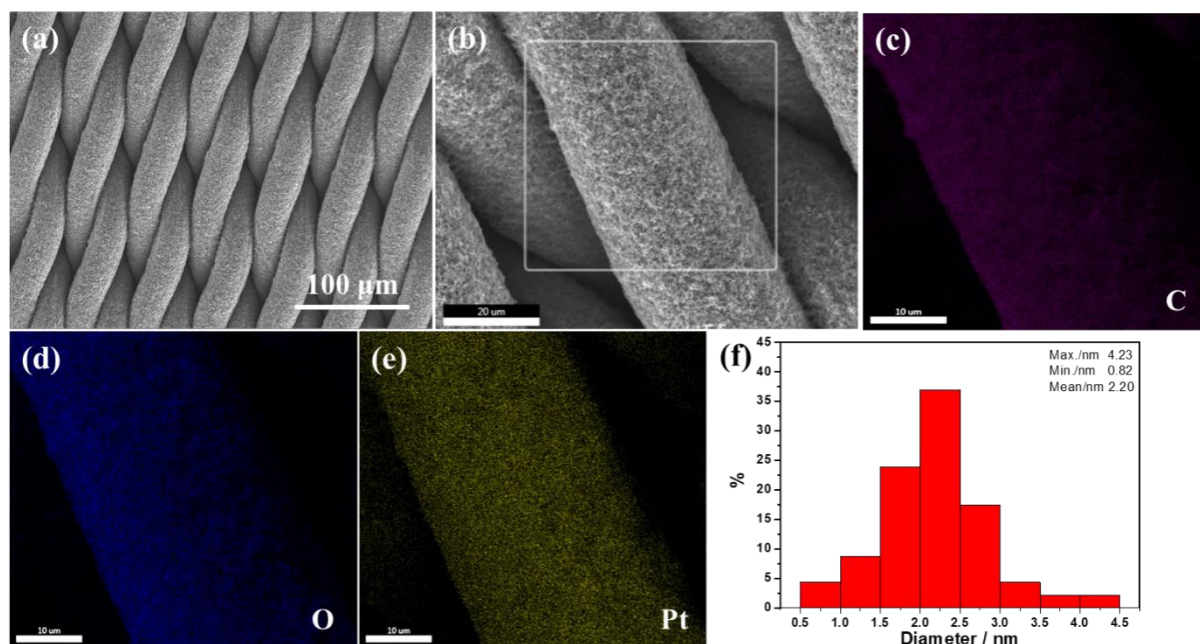


**Figure S 5-7.** (a-b) SEM images of the Pt/OxCNT/SS. (c-e) SEM-EDS mapping, respectively, for C, O and Pt of the Pt/OxCNT/SS collected in the area marked in the square in (b). (f) Particle size distribution of the Pt NPs deposited on the OxCNT.

**Table S 5-3.** HER activity comparison of the SS based electrode reported recently.

Sample	Over potential ( $\eta$ ) at 10 mA/cm <sup>2</sup>	Tafel slope (mV/dec)	Electrolyte	Ref.
Pt/OxCNT/SS	56	39.2	1 M KOH	This work
	52	51.5	1 M PBS	
	54	60.0	0.5 M H <sub>2</sub> SO <sub>4</sub>	
OxCNT/SS	257	105.6	1 M KOH	This work
	234	82.6	1 M PBS	
	151	96.0	0.5 M H <sub>2</sub> SO <sub>4</sub>	
CNT/SS	334	119.6	1 M KOH	This work
	301	111.9	1 M PBS	
	235	99.2	0.5 M H <sub>2</sub> SO <sub>4</sub>	
Bare SS	359	126.1	1 M KOH	This work
	337	154.0	1 M PBS	
	300	127.7	0.5 M H <sub>2</sub> SO <sub>4</sub>	
20 wt% Pt/C/SS	82	--	1 M KOH	This work
	55	--	1 M PBS	
	50	--	0.5 M H <sub>2</sub> SO <sub>4</sub>	
Modified Ni42 steel	299	117.5	1 M KOH	[S1]
Sulfurized stainless steel foil (AISI 316)	136	147	1 M KOH	[S2]
N, P doped etching SS (NESSP, AISI 304)	230	36	1 M KOH	[S3]
Ni <sub>0.33</sub> Co <sub>0.67</sub> S <sub>2</sub> NN/SS	350 (30 mA/cm <sup>2</sup> )	76	1 M KOH	[S4]
FeNi LDH@NWSSF	110	113	1 M KOH	[S5]

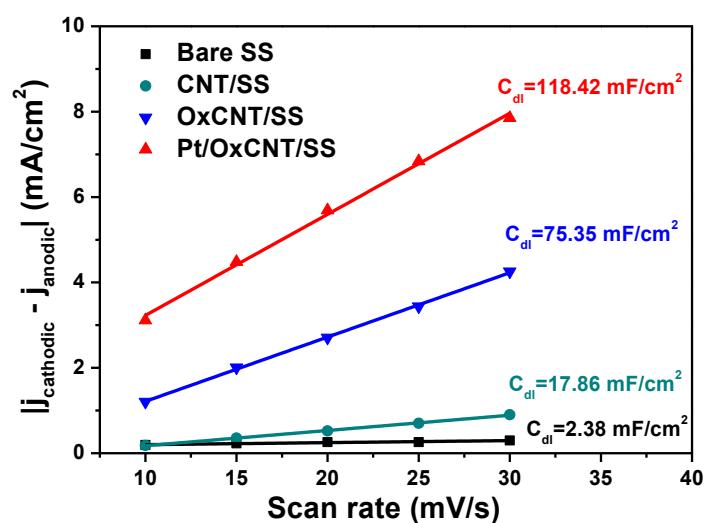


**Figure S 5-8.** Comparison of the electrochemical surface area (ECSA) for the as-prepared electrodes.

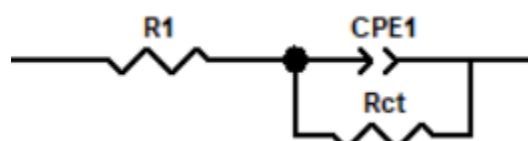


**Figure S 5-9.** Equivalent circuit diagram for the fitting of the electrochemical impedance spectra (EIS) for the HER.



**Table S 5-4.** Summary of the fitted EIS for the HER.

Sample	R1	CPE		Ret
		CPE-T	CPE-P	
SS	1.04	0.0012	0.8186	197.50
CNT/SS	0.77	0.0228	0.9263	65.92
OxCNT/SS	0.86	0.0692	0.8504	37.70
Pt/OxCNT/SS	0.76	0.0943	0.8221	0.47

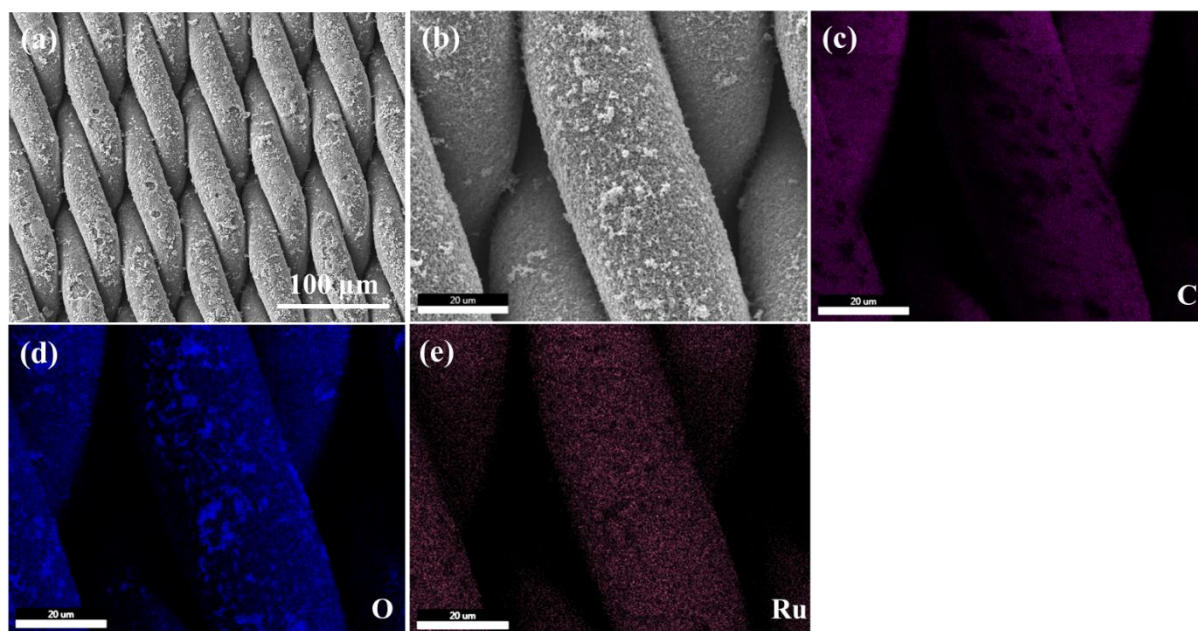


**Figure S 5-10.** (a-b) SEM images of RuO<sub>2</sub>/OxCNT/SS with different magnifications. (c-e) SEM-EDS mapping spectrum of C, O and Pt, respectively, for Pt/OxCNT/SS acquired in the area shown in (b).

**Table S 5-5.** Summary of the OER activity of recently published SS-based electrodes for the OER.

Sample	Over potential ( $\eta$ ) at 10 mA/cm <sup>2</sup>	Tafel slope (mV/dec)	Electrolyte	Ref.
RuO <sub>2</sub> /OxCNT/SS	217	38.8	1 M KOH	This work
	410	66.8	1 M PBS	
OxCNT/SS	267	44.0	1 M KOH	This work
	613	129.7	1 M PBS	
CNT/SS	297	66.7	1 M KOH	This work
	680	124.6	1 M PBS	
Bare SS	277	47.6	1 M KOH	This work
	663	115.9	1 M PBS	
RuO <sub>2</sub> /SS	217	--	1 M KOH	This work
	400	--	1 M PBS	
Modified Ni42 steel	254	71.6	0.1 M KOH	[S1]
	215	--	1 M KOH	
	491	150.88	0.1 M PBS	
AISI 316L steel	300	42	1 M KOH	[S6]
Unmodified AISI 316L steel	262	42	1 M KOH	[S7]
Sulfurized stainless steel foil (AISI 316)	262	42	1 M KOH	[S2]
Modified AISI 316 steel	280	34	1 M KOH	[S8]
FeNi LDH@NWSSF	210	56	1 M KOH	[S5]
N doped etching SS (NESS, AISI 304)	278	83	1 M KOH	[S3]
Modified AISI 304	260	41	1 M KOH	[S9]
Modified AISI 304	269.2	49	0.1 M KOH	[S10]
	212 (12 mA/cm <sup>2</sup> )	--	1 M KOH	
Ni <sub>0.33</sub> Co <sub>0.67</sub> S <sub>2</sub> NN/SS	286 (50 mA/cm <sup>2</sup> )	55	1 M KOH	[S4]
NiS@SLS	297 (11 mA/cm <sup>2</sup> )	47	0.1 M KOH	[S11]
Fe(Ni)OOH modified SS	300	34	1 M KOH	[S12]
Ni75Fe25-Sm	317(100 mA/cm <sup>2</sup> )	40	30 wt.% KOH	[S13]
Cellular stainless steel (CESS)	302	43	1 M KOH	[S14]
	270 (After activation)			
Ni(Fe)O <sub>x</sub> H <sub>y</sub> /SS	230 (20 mA/cm <sup>2</sup> )	36	1 M KOH	[S15]
X20CoCrWMo10-9	574	--	0.05 M H <sub>2</sub> SO <sub>4</sub>	[S16]
Surface-oxidized AISI 304	260 (1.5 mA/cm <sup>2</sup> )	--	0.1 M KOH	[S17]
	500 (0.65 mA/cm <sup>2</sup> )	--	0.1 M PBS	
Oxidized S235	347 (2 mA/cm <sup>2</sup> )	--	0.1 M KOH	[S18]
	462 (1 mA/cm <sup>2</sup> )	--	0.1 M PBS	
X20CoCrWMo10-9//Co <sub>3</sub> O <sub>4</sub>	230	47.1	0.1 M KOH	[S19]
	298	140.8	0.1 M PBS	
AISI 302	400 (6.3 mA/cm <sup>2</sup> )	33	1 M KOH	[S20]
Ni(OH) <sub>2</sub> /316L stainless steel nanoparticles on Ni foam	220	42	1 M KOH	[S21]

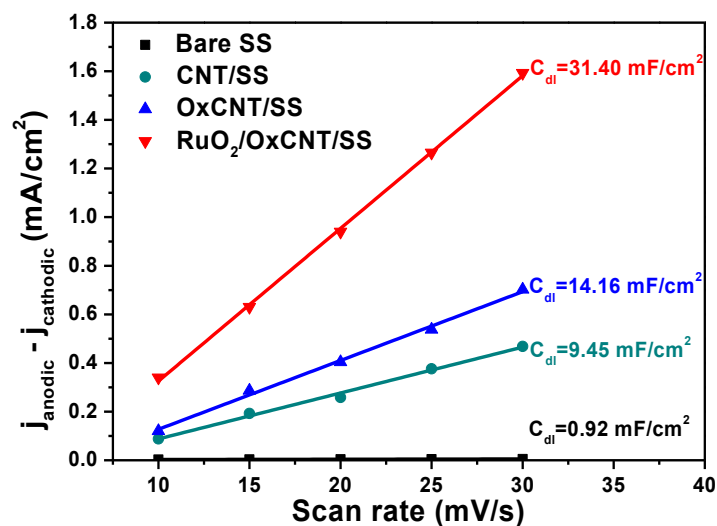


Figure S 5-11. ECSA measurement of the bare SS, CNT/SS, OxCNT/SS and RuO<sub>2</sub>/OxCNT/SS for the OER.

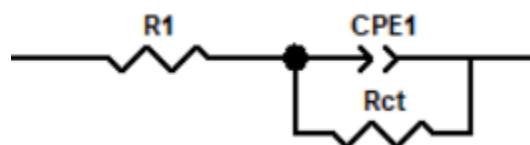
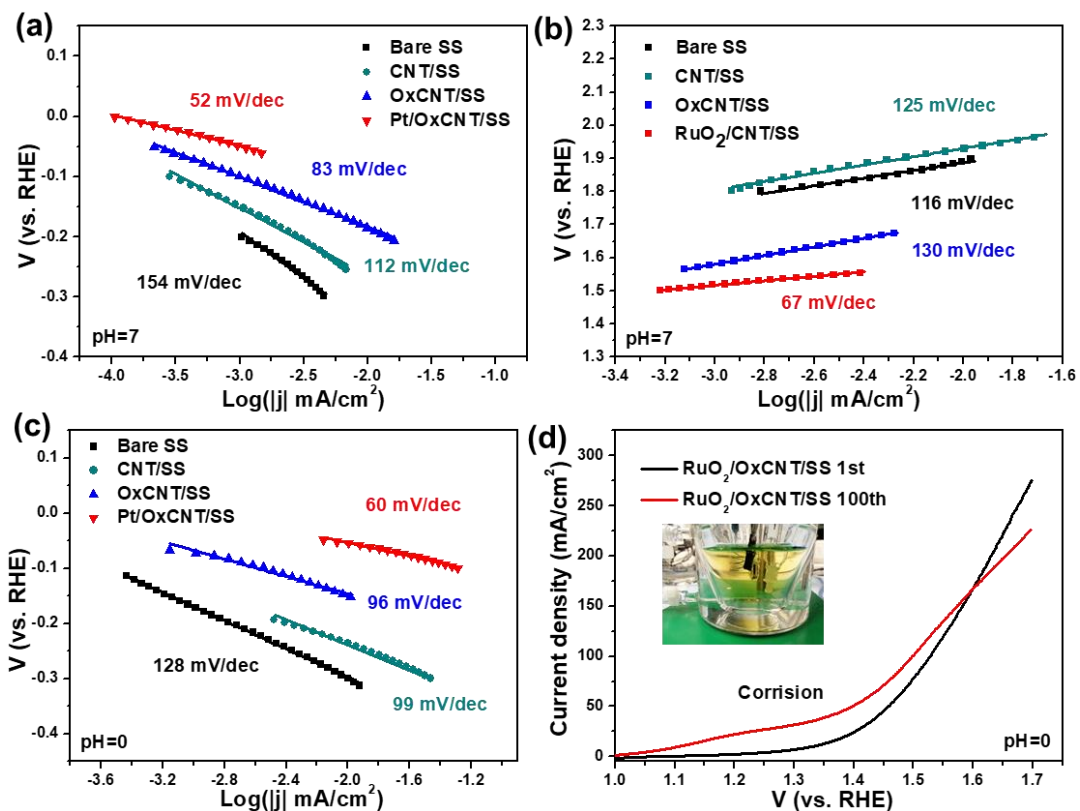


Figure S 5-12. Equivalent circuit diagram used for the fitting of the EIS results for the OER.

Table S 5-6. Summary of the fitted EIS results for the OER.

Sample	R1	CPE		Rct
		CPE-T	CPE-P	
SS	1.03	0.0150	0.8999	2.62
CNT/SS	0.77	0.0206	0.9250	5.77
OxCNT/SS	0.86	0.0569	0.8312	1.42
RuO <sub>2</sub> /OxCNT/SS	0.84	0.1122	0.8559	1.03





**Figure S 5-13.** Tafel plots of the prepared electrodes in the neutral electrolyte for (a) HER and (b) OER, and in the acidic electrolyte for (c) HER. (d) Stability assessment of the  $\text{RuO}_2/\text{OxCNT}/\text{SS}$  for the OER in the acidic electrolyte.

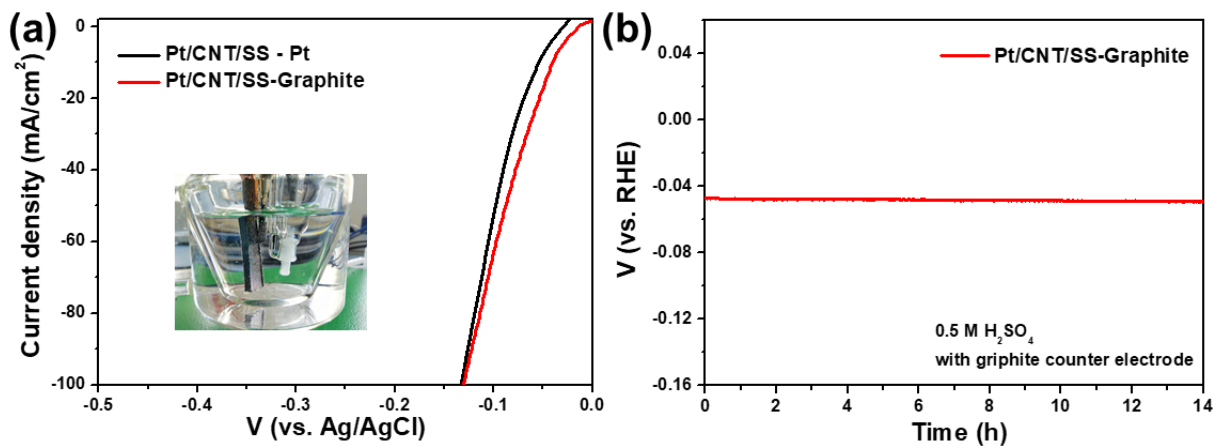


**Figure S 5-14.** (a) Comparison of polarization curves of  $\text{Pt}/\text{CNT}/\text{SS}$  with Pt and Graphite as the counter electrode for the HER in acidic electrolyte. The setup of the cell for water splitting measurement with Graphite as the counter electrode is shown inset. (b) Stability measurement of the  $\text{Pt}/\text{CNT}/\text{SS}$  with Graphite as counter electrode recorded at a constant current density of  $-10 \text{ mA}/\text{cm}^2$ .

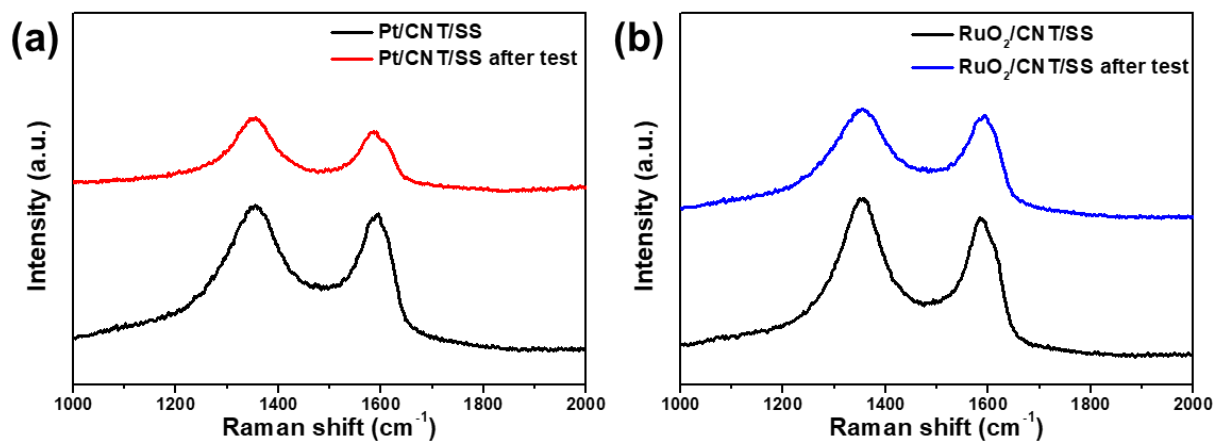


**Figure S 5-15.** Raman spectra of the as prepared electrodes before and after long term measurement, (a) Pt/CNT/SS in 0.5 M H<sub>2</sub>SO<sub>4</sub> and (b) RuO<sub>2</sub>/CNT/SS in 1 M KOH.

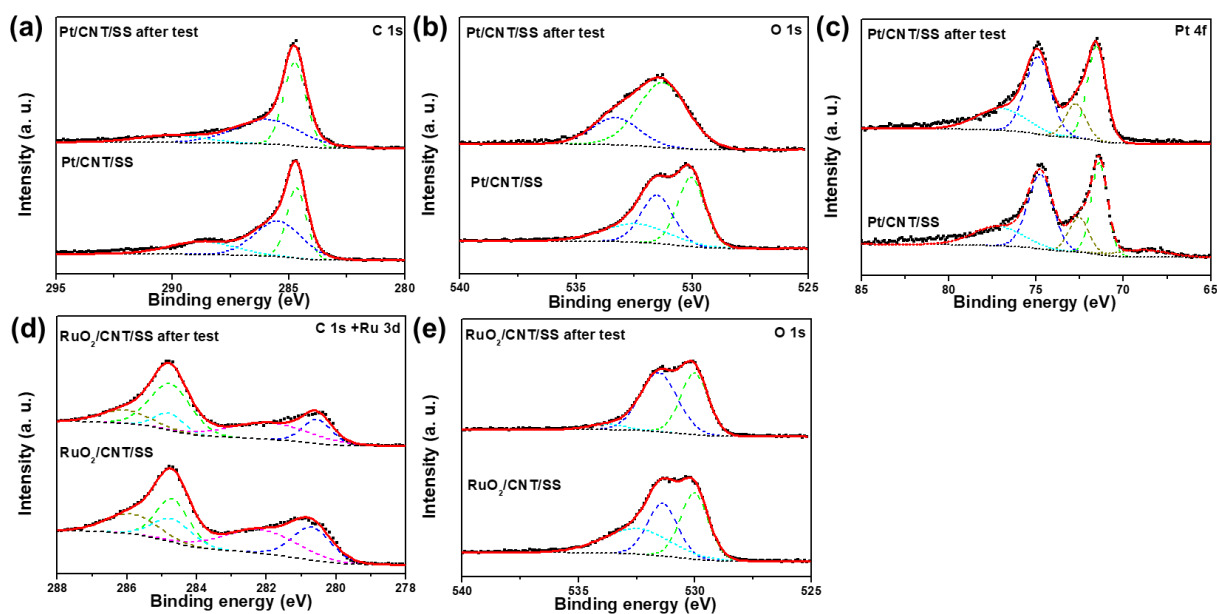


**Figure S 5-16.** (a-c) XPS spectra of the C 1s, O 1s and Pt 4f for Pt/CNT/SS before and after long-term measurement in 0.5 M H<sub>2</sub>SO<sub>4</sub>, respectively. (d, e) XPS spectra of the C 1s + Ru 3d and O 1s for RuO<sub>2</sub>/CNT/SS before and after long-time measurement in 1 M KOH.

**Table S 5-7.** Summary of the overall water splitting performance.

Sample	Potential (V) @ 10 mA/cm <sup>2</sup>	Electrolyte	Ref.
Pt/OxCNT/SS    RuO <sub>2</sub> /OxCNT/SS <sup>a</sup>	1.50 1.70	1 M KOH 1 M PBS	This work
20 wt% Pt/C/CNT    RuO <sub>2</sub> /SS	1.51 1.69	1 M KOH 1 M PBS	This work
OxCNT/SS	1.83 2.07	1 M KOH 1 M PBS	This work
CNT/SS	1.95 2.24	1 M KOH 1 M PBS	This work
Bare SS	1.88 2.21	1 M KOH 1 M PBS	This work
Sulfurized stainless steel foil (AISI 316)	1.64	1 M KOH	[S2]
NESSP    NESS (AISI 304) <sup>a</sup>	1.74	1 M KOH	[S3]
Ni <sub>0.33</sub> Co <sub>0.67</sub> S <sub>2</sub> NN/SS	1.67	1 M KOH	[S4]
FeNi LDH@NWSSF	1.56	1 M KOH	[S5]

<sup>a</sup> The meaning of the || is the separation of the cathode and anode used in the overall water splitting experiments with two different electrodes.

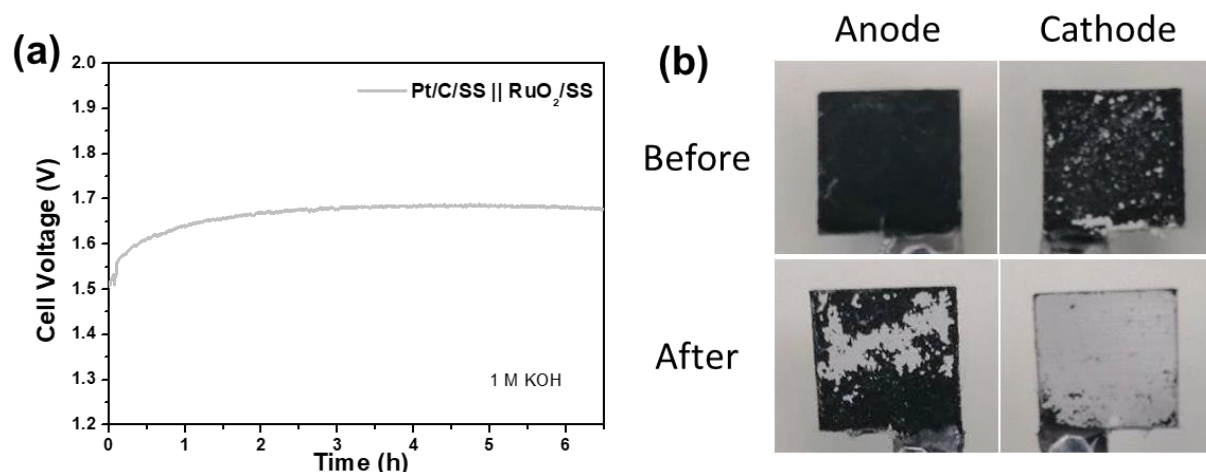


**Figure S 5-17.** (a) Long-term measurement of Pt/C/SS || RuO<sub>2</sub>/SS configuration recorded at 10 mA/cm<sup>2</sup> for the overall water splitting in 1 M KOH. (b) Images of Pt/CNT/SS (cathode) and RuO<sub>2</sub>/CNT/SS (anode) before and after the long-term measurement.

## Reference

- [S1] H. Schäfer, D. M. Chevrier, P. Zhang, J. Stangl, K. Müller-Buschbaum, J. D. Hardege, K. Kuepper, J. Wollschläger, U. Krupp, S. Dühnen, M. Steinhart, L. Walder, S. Sadaf, M. Schmidt, *Adv. Funct. Mater.* **2016**, 26, 6402.
- [S2] X. Liu, B. You, Y. Sun, *ACS Sustain. Chem. Eng.* **2017**, 5, 4778.
- [S3] M. S. Balogun, W. Qiu, Y. Huang, H. Yang, R. Xu, W. Zhao, G. R. Li, H. Ji, Y. Tong, *Adv Mater* **2017**, 29.
- [S4] G. He, W. Zhang, Y. Deng, C. Zhong, W. Hu, X. Han, *Catalysts* **2017**, 7, 366.
- [S5] L. Wang, X. Huang, S. Jiang, M. Li, K. Zhang, Y. Yan, H. Zhang, J. M. Xue, *ACS Appl. Mater. Interfaces* **2017**, 9, 40281.
- [S6] F. Moureaux, P. Stevens, G. Toussaint, M. Chatenet, *J. Power Sources* **2013**, 229, 123.
- [S7] F. Yu, F. Li, L. Sun, *Int. J. Hydrogen Energ.* **2016**, 41, 5230.

- [S8] H. Zhong, J. Wang, F. Meng, X. Zhang, *Angew. Chem. Int. Ed. Engl.* **2016**, *55*, 9937.
- [S9] S. Anantharaj, M. Venkatesh, A. S. Salunke, T. V. S. V. Simha, V. Prabu, S. Kundu, *ACS Sustain. Chem. Eng.* **2017**, *5*, 10072.
- [S10] H. Schäfer, S. Sadaf, L. Walder, K. Kuepper, S. Dinklage, J. Wollschläger, L. Schneider, M. Steinhart, J. Hardege, D. Daum, *Energy Environ. Sci.* **2015**, *8*, 2685.
- [S11] J. S. Chen, J. Ren, M. Shalom, T. Fellingner, M. Antonietti, *ACS Appl Mater Interfaces* **2016**, *8*, 5509.
- [S12] D. Tang, O. Mabayoje, Y. Lai, Y. Liu, C. B. Mullins, *ChemistrySelect* **2017**, *2*, 2230.
- [S13] F. J. Pérez-Alonso, C. Adán, S. Rojas, M. A. Peña, J. L. G. Fierro, *Int. J. Hydrogen Energ.* **2014**, *39*, 5204.
- [S14] X. Huang, S. Chang, W. S. V. Lee, J. Ding, J. M. Xue, *J. Mater. Chem. A* **2017**, *5*, 18176.
- [S15] Q. Zhang, H. Zhong, F. Meng, D. Bao, X. Zhang, X. Wei, *Nano Res.* **2018**, *11*, 1294.
- [S16] H. Schafer, K. Kupper, K. Muller-Buschbaum, D. Daum, M. Steinhart, J. Wollschlager, U. Krupp, M. Schmidt, W. Han, J. Stangl, *Nanoscale* **2017**, *9*, 17829.
- [S17] H. Schafer, S. M. Beladi-Mousavi, L. Walder, J. Wollschlager, O. Kuschel, S. Ichilmann, S. Sadaf, M. Steinhart, K. Kupper, L. Schneider, *ACS Catal.* **2015**, *5*, 2671.
- [S18] H. Schäfer, K. Kupper, J. Wollschlager, N. Kashaev, J. Hardege, L. Walder, S. Mohsen Beladi-Mousavi, B. Hartmann-Azanza, M. Steinhart, S. Sadaf, F. Dorn, *ChemSusChem* **2015**, *8*, 3099.
- [S19] H. Schäfer, D. M. Chevrier, K. Kuepper, P. Zhang, J. Wollschlaeger, D. Daum, M. Steinhart, C. Heß, U. Krupp, K. Müller-Buschbaum, J. Stangl, M. Schmidt, *Energy Environ. Sci.* **2016**, *9*, 2609.
- [S20] S. K. Tiwari, A. K. L. Singh, R. N. Singh, *J. Electroanal. Chem.* **1991**, *319*, 263.
- [S21] A. Balram, H. Zhang, S. Santhanagopalan, *Mater. Chem. Front.* **2017**, *1*, 2376.

## **6 Atomic Layer Deposition of Cobalt Phosphide for Highly Efficient Hydrogen Evolution Reaction.**

Cobalt phosphide prepared by atomic layer deposition is reported for the first time. The optimized recipe employs an extra H<sub>2</sub> plasma etching step to remove excess phosphorus. The as-deposited well-crystallized Co-P films demonstrate significantly higher activities towards electrochemical and photoelectrochemical hydrogen evolution reaction than that prepared by a traditional post-phosphorization method, and can be deposited on various complex three-dimensional substrates.

This chapter can be referred to:

Haojie Zhang, Dirk J. Hagen, Andreas Graff, Frank Heyroth, Bodo Fuhrmann, Ilya Kostanovskiy, Stefan L. Schweizer, Francesco Caddeo, A. Wouter Maijenburg, Stuart Parkin and Ralf B. Wehrspohn\*, 2020, 10.1002/anie.202002280.

## 6.1 Abstract

Transition-metal phosphides (TMP) prepared by atomic layer deposition (ALD) is reported for the first time. Ultrathin Co-P films were deposited by using  $\text{PH}_3$  plasma as the phosphorus source and an extra  $\text{H}_2$  plasma step to remove excess P in the growing films. The optimized ALD process followed the self-limited layer-by-layer growth behavior, and the deposited Co-P films were highly pure and smooth. The Co-P films deposited via ALD exhibited better electrochemical and photoelectrochemical hydrogen evolution reaction activities than similar Co-P films prepared by the traditional post-phosphorization method. Moreover, the deposition of ultrathin Co-P films on periodic trenches was demonstrated, which highlights the broad and promising potential application of this ALD process for a conformal coating of TMP films on complex three-dimensional (3D) architectures.

## 6.2 Introduction

H<sub>2</sub>, owing to its greatest gravimetric energy density (142 MJ kg<sup>-1</sup>) and zero-carbon emission property, has been regarded as an ideal energy carrier for clean and sustainable energy storage and supply in order to meet the serious global energy crisis and environmental pollution.<sup>[1]</sup> Pt-based components as the state-of-the-art electrocatalysts for the hydrogen evolution reaction (HER) exhibit excellent catalytic activity in electrolytes with a wide pH-range.<sup>[2]</sup> However, the scarcity and high costs of Pt seriously restrict their large-scale commercialization. Therefore, enormous research efforts are focused on developing alternatives for Pt-based electrocatalysts, such as carbon-based materials, sulfides, selenides, nitrides and phosphides, to reduce the costs for efficient water splitting.<sup>[3]</sup> Among these candidates, transition-metal phosphides (TMP) have attracted increasing research interest due to their excellent performance, various crystalline phases, and tunable electronic structure.<sup>[4]</sup> Inspired by this, various strategies have been employed to prepare TMP-based electrocatalysts, including the solvent-phase method, the solid-state method, the gas-solid method, and the electrodeposition method.<sup>[5]</sup> For example, Jiang et al. prepared cobalt-phosphorous-derived Co-P films on Cu foil by electrodeposition, exhibiting remarkable bifunctional activities for both the HER and the oxygen evolution reaction (OER).<sup>[6]</sup> Jaramillo and coauthors combined CoP thin films with Si photo-absorbers to prepare highly efficient precious metal-free crystalline silicon photocathodes by an evaporation-phosphorization process.<sup>[7]</sup> Recently, Li et al. synthesized P-rich CoP<sub>2</sub> *via* a hot injection method, exhibiting excellent electrochemical activities for the HER.<sup>[8]</sup> However, the controllable and homogeneous deposition of an ultrathin TMP film on complex three-dimensional (3D) structures is still a great challenge.

Atomic layer deposition (ALD) has become a powerful technology for the preparation of high-quality thin-film materials on various complex substrates.<sup>[9]</sup> ALD is a surface self-limited and saturated deposition process enabling the layer-by-layer and large-scale deposition of uniform and reproducible films. Due to this specific advantage, ALD is suitable for depositing homogeneous coatings on various complex 3D structures, thus exhibiting a huge potential in various applications (e.g. microelectronics and catalysis). Up to now, no ALD-process for the direct deposition of TMP was reported and only a few publications reported the preparation of TMP films by post-treatment of ALD-grown films. For example, Rongé et al. used ALD for the deposition of metal phosphates (M = Co and Fe), which were subsequently reduced by thermal annealing in a reducing environment (H<sub>2</sub>) or electrochemical treatment for the preparation of metal phosphides.<sup>[10]</sup> However, the high-temperature annealing (950 °C)

resulted in the formation of particulate films, while the ability of the electrochemical treatment to reduce the complete film remains doubtful. Looking for suitable chemistry for TMP-ALD processes, it is worth noticing recent advances in the ALD of transition metal sulfides. Guo et al. reported a universal ALD process to deposit pyrite-type metal disulfides ( $\text{FeS}_2$ ,  $\text{CoS}_2$ , and  $\text{NiS}_2$ ).<sup>[11]</sup> The well-crystallized films prepared with optimized ALD recipes could be uniformly deposited even into deep, narrow trenches with high aspect ratios.

Probably, the main reason for the unsuccessful development of an ALD recipe for the deposition of TMP so far is the serious decomposition of  $\text{PH}_3$  during the  $\text{PH}_3$  plasma treatment step in the standard ALD process, which leads to an excess content of phosphorus (P) residing in the deposited layer.<sup>[12]</sup> The excess P, which cannot be eliminated in the subsequent Ar purge step, would continue to react with the precursor, thus leading to an uncontrollable deposition.<sup>[13]</sup> Gudovskikh and colleagues studied the deposition process of GaP in a chemical vapor deposition (CVD) system by in-situ optical emission spectroscopy (OES).<sup>[13]</sup> They found that the presence of traces of  $\text{PH}_3$ , which comes from the reaction of  $\text{H}_2$  and P species on the chamber wall, can significantly affect the deposition process and that an additional  $\text{H}_2$  plasma step effectively removed the P species on the chamber wall, resulting in a reduced growth rate and a more homogeneous deposition. A “third”  $\text{H}_2$  or  $\text{H}_2$  plasma step was also successfully applied in various ALD processes to obtain the desired stoichiometry. For example, Mackus et.al. used  $\text{H}_2$  or  $\text{H}_2$  plasma to reduce  $\text{PtO}_x$  to Pt in room temperature ALD processes employing  $(\text{Me})_3\text{Pt}(\text{MeCp})$  and  $\text{O}_2$  plasma as precursor-reactant pair.<sup>[14]</sup> Similar combinations of oxidizing and reducing reagents have also been employed for the deposition of Ir,<sup>[15]</sup> Co,<sup>[16]</sup> and Cu<sup>[17]</sup>. Therefore, an additional step to remove the excess P is the key to obtain a self-limited and layer-by-layer deposition of TMP-based catalysts via ALD.

Herein, we report a plasma-assisted ALD process for depositing ultrathin Co-P films using  $\text{PH}_3$  plasma and bis(N-t-butyl-N'-ethylpropanimidamido) cobalt (II) ( $\text{Co}(\text{AMD})_2$ ) as the phosphorus source and metal precursor, respectively. In addition, an  $\text{H}_2$  plasma step was employed during the deposition to remove excessive phosphorus. The optimized recipe followed the ideal layer-by-layer ALD growth behavior over a wide temperature range, resulting in pure and stable polycrystalline Co-P films. The electrodes prepared by depositing such Co-P films on fluorine-doped tin oxide (FTO) glass and p-type Si wafer, exhibited improved electrochemical and photoelectrochemical HER activities in alkaline electrolyte when compared to that of Co-P films prepared by a conventional post-phosphorization method. Furthermore, we demonstrate that the ALD Co-P can be conformally deposited into deep Si



trenches, highlighting the promising potential application of depositing TMP on complex 3D architectures.

### 6.3 Experiment Sections

**Chemicals.** The metal precursors bis(N-t-butyl-N'-ethylpropanimidamido) cobalt (II) ( $\text{Co(AMD)}_2$ ,  $\text{C}_{18}\text{H}_{38}\text{CoN}_4$ , min. 98%) and Trimethyl(methylcyclopentadienyl)platinum(IV) ( $\text{C}_9\text{H}_{16}\text{Pt}$ , 99%) were purchased from Strem Chemicals Inc. (France). Fluorine doped tin oxide (FTO) glass (2.2 mm,  $\sim 7$  ohms/sq) and potassium hydroxide (KOH, ACS reagent  $\geq 85\%$ ) were purchased from Sigma Aldrich Inc. (Germany). p-B Si wafers with (100) orientation and 525  $\mu\text{m}$  thickness were bought from Siegert wafer GmbH (Germany). All chemicals were directly used without further purification.

**Atomic layer deposition (ALD) of Cobalt phosphide (Co-P).** The Co-P layers were deposited by an Oxford FlexAL ALD system equipped with an inductively-coupled-plasma source, using  $\text{Co(AMD)}_2$  and  $\text{PH}_3$  as the metal precursor and phosphorus source, respectively. The metal precursor was kept in a stainless-steel cylinder container and heated to 70 °C during the deposition to offer enough vapor pressure. The  $\text{Co(AMD)}_2$  was delivered into the chamber with the assistance of 50 sccm Ar carrier gas for a period of  $t_1$  followed by 100 sccm Ar for purging ( $t_{1p}$ ). The  $\text{PH}_3$  plasma was generated by supplying radio frequency (RF) power on a diluted  $\text{PH}_3$  (100 sccm, 3% in Ar). The RF power was set at 80 W for all recipes and the  $\text{PH}_3$  plasma was generated inside a quartz tube located at the top of the reactor. The  $\text{PH}_3$  plasma was applied for  $t_2$  and purged with 100 sccm Ar for  $t_{2p}$  ( $t_{2p} = 2 * t_2$ ). Subsequently, an additional  $\text{H}_2$  plasma step was applied (100 sccm, RF = 100 W,  $t_3 = 2 * t_2$ ) to remove the excess phosphorus in the deposited layer, followed by an Ar purge for  $t_{3p}$  (100 sccm,  $t_{3p} = t_3$ ). The deposition temperature was varied from 120 to 300 °C, and the chamber pressure for reactant pulse and purge were 100 and 30 mtorr, respectively. The ALD film growth behavior was studied on Si by changing the precursor dose time ( $t_1$ ) and  $\text{PH}_3$  plasma treatment time ( $t_2$ ) in each cycle. Co-P films were deposited on FTO glass and p-B Si wafers for electrochemical and photoelectrochemical water splitting measurements, respectively.

**Preparation of Co-P films by a traditional post-phosphorization method.** Firstly, cobalt oxide was deposited on FTO ( $\text{CoO}_x/\text{FTO}$ ) or Si wafers ( $\text{CoO}_x/\text{Si}$ ) by an  $\text{O}_2$  plasma-enhanced ALD process by using  $\text{Co(AMD)}_2$  (80 °C) and  $\text{O}_2$  plasma (300 W) as the metal precursor and oxidant at 220 °C by using Oxford FlexAL ALD with the chamber pressure of 100 mtorr. Every cycle consisted of 2s precursor exposure and 10 s  $\text{O}_2$  plasma exposure

followed by 10 s purge after every exposure (growth rate: 0.022 nm/cycles). Subsequently, as-prepared  $\text{CoO}_x$  was converted to Co-P (Co-P/FTO-thermal or Co-P/Si-thermal) by a post-phosphorization method as described in the literature.<sup>[19]</sup> Briefly, the as-prepared  $\text{CoO}_x/\text{FTO}$  or  $\text{CoO}_x/\text{Si}$  were placed at the downstream of the phosphorus source ( $\text{NaH}_2\text{PO}_2 \cdot \text{H}_2\text{O}$ ) and heated to 300 °C in  $\text{N}_2$  gas environment for 2 h in a furnace equipped with a quartz tube.

**Deposition of Pt on FTO by ALD (Pt/FTO).** The Pt/FTO reference sample was prepared by depositing 10 nm Pt on FTO with 225 cycles by using trimethyl(methylcyclopentadienyl)platinum(IV) (40 °C) and  $\text{O}_2$  plasma (300 W) as the metal precursor and reactant, respectively, at 220 °C in our Oxford FlexAL ALD. The chamber pressure was kept at 100 mtorr throughout the ALD process. Every ALD cycle consisted of 3 s precursor dose followed by 5 s purge and 8 s  $\text{O}_2$  plasma treatment followed by 7 s purge.

**Characterization.** The thickness and composition of the deposited Co-P films were measured by Rutherford backscattering spectrometry (RBS). The transmission electron microscopy (TEM) and energy-dispersive X-ray spectroscopy (EDS) measurements were performed with an aberration-corrected transmission electron microscopy (FEI Titan3 G2 60-300) equipped with an X-ray detector (Super-X). The cross-section lamella of the Co-P film on a Si wafer was prepared by a focus ion beam (FIB) integrated into an FEI Quanta 650 FEG scanning electron microscope (SEM). X-ray photoelectron spectroscopy (XPS) data were obtained by a Thermo Scientific K-alpha X-ray photoelectron spectrometer system equipped with a monochromatic Al  $\text{K}\alpha$  X-ray source. The C 1s peak (248.8 eV) was used as the reference for the calibration of all XPS data. The XPS depth profile was measured by etching via Ar sputtering at 500 eV and recording the spectra every 10 s. The atomic force microscopy (AFM) measurement was conducted by a Bruker Dimension Icon® Atomic Force Microscope. The method used for the determination of the electrochemical surface area (ECSA) and the calculation of the TOF are explained in detail in the Supporting Information.

**Electrochemical measurement.** The electrochemical water splitting measurements were recorded by an Autolab PGSTAT302N Potentiostat with a three-electrode electrolysis cell in 1 M KOH. A graphite rod and an Ag/AgCl (saturated KCl) electrode were used as the counter and the reference electrode, respectively. The linear sweep voltammetry (LSV) measurements were recorded at a scan rate of 50 mV  $\text{s}^{-1}$ . The electrochemical impedance spectroscopy (EIS) data were collected at -0.2 V (vs. RHE) with a frequency range from 100 kHz to 0.1 Hz. The stability of the Co-P/FTO electrode was evaluated by a chronopotentiometric measurement at

a constant current density of  $-10 \text{ mA cm}^{-2}$ . All potentials were corrected with iR compensation and converted to the potential of the reversible hydrogen electrode (RHE).

**Electrochemical surface area (ECSA) determination and turnover frequency (TOF) calculation:** The ECSA determination and TOF calculation were done according to previous reports.<sup>[1]</sup> Specifically, the ECSA was determined by an electrochemical capacitance measurement in which the currents were recorded by scanning the potential in a non-faradaic range (0.1 V – 0.2 V vs. RHE) at different scan rates (10, 15, 20, 25 and 30  $\text{mV s}^{-1}$ ). Subsequently, the capacitance ( $C_{dl}$ ) was estimated by the half of the slope, which is obtained by linearly fitting the curve of the capacitive current ( $\Delta j = j_{anodic} - j_{cathodic}$ ) versus the scan rate. Then, the  $C_{dl}$  can be further converted into the ECSA by using the specific capacitance value for a standard with  $1 \text{ cm}^2$  of real surface area. In our case, the FTO glass was considered as the standard and the ECSA of the deposited films can be calculated according to:

$$A_{ECSA} = \frac{C_{dl} (\text{catalyst}, \text{mF cm}^{-2})}{C_{dl} (\text{FTO}, \text{mF cm}^{-2}) \text{ per ECSA cm}^2}$$

The TOF values were calculated according to the equation:

$$\text{TOF} = \frac{\text{number of total hydrogen turnovers/geomeric area (cm}^2\text{)}}{\text{number of surface active sites/geomeric area (cm}^2\text{)}}$$

The number of total hydrogen turnovers were calculated based on the current density ( $j$ , iR-corrected) as following:

$$\begin{aligned} \# \text{ H}_2 &= |j| \frac{\text{mA}}{\text{cm}^2} \cdot \frac{1 \text{ C s}^{-1}}{1000 \text{ mA}} \cdot \frac{1 \text{ mol e}^-}{96495.3 \text{ C}} \cdot \frac{1 \text{ mol H}_2}{2 \text{ mol e}^-} \cdot \frac{6.022 \times 10^{23} \text{ H}_2 \text{ molecules}}{1 \text{ mol H}_2} \\ &= 3.12 \times 10^{15} \frac{\text{H}_2 \text{ s}^{-1}}{\text{cm}^2} \text{ per } \frac{\text{mA}}{\text{cm}^2} \end{aligned}$$

Because the deposited Co-P films are mix with high crystallinity regions and amorphous regions, it is difficult to determine the surface active sites from the crystal structure. Therefore, we take both P and Co atoms as the active sites and CoP unit cell volume as the unit cell volume for our deposited films. So, the number of atoms per unit cell will be 9.2 (30 % more P than Co than that of CoP) with a unit volume of  $93 \text{ \AA}^3$ .<sup>[2]</sup> Thus, the number of surface active sites can be calculated according to:

$$\begin{aligned} \# \text{ surface active sites} &= \left( \frac{\text{the number of atoms per unit cell}}{\text{the volume of the unit cell}} \right)^{\frac{2}{3}} \\ &= \left( \frac{9.2 \text{ atoms per unit cell}}{93 \text{ \AA per unit cell}} \right)^{\frac{2}{3}} = 2.139 \times 10^{15} \text{ atoms per real cm}^2 \end{aligned}$$

Therefore:

$$\text{TOF} = \frac{3.12 \times 10^{15} \frac{\text{H}_2 \text{ s}^{-1}}{\text{cm}^2} \times |j|}{\# \text{ surface active sites} \times A_{\text{ECSA}}}$$

**Photoelectrochemical Measurements.** The PEC measurements were performed with a similar three-electrode configuration to the electrochemical measurement. As-prepared Co-P/Si and Co-P/Si-thermal photoelectrodes (6.7 nm of catalysts layers) were used as the working electrodes. For all samples, the photocurrents were recorded by an Autolab PGSTAT302N Potentiostat with a scan rate of 50 mV s<sup>-1</sup> under the illumination of an LED solar simulator (WAVELABS SINUS 70, Germany) in 1 M KOH. The spectrum of the LED solar simulator was calibrated to the standard AM 1.5 G spectrum with the wavelength range from 350 to 1100 nm and the intensity of 780 W m<sup>-2</sup>. The transient photocurrent response was obtained by recording the photocurrent under chopped light irradiation (1s/1s-on/off cycle).

## 6.4 Results and Discussion

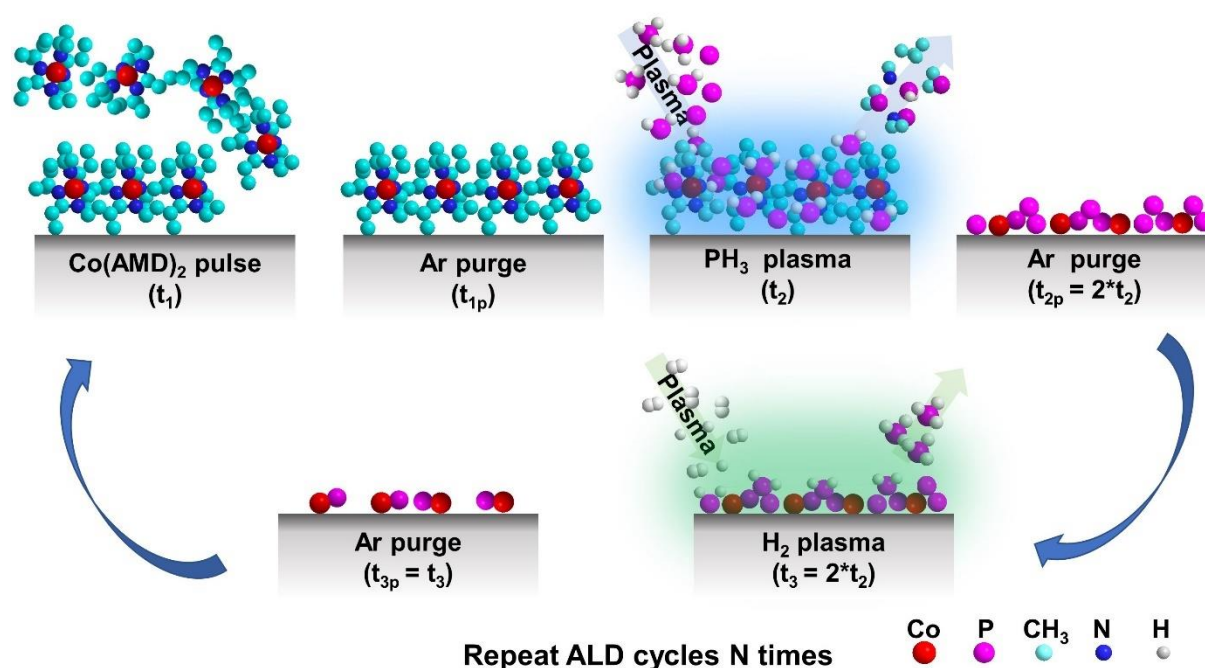
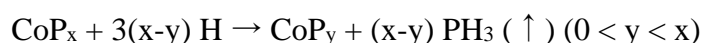
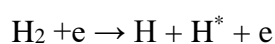


**Figure 6-1.** Illustration of the improved ALD process for the deposition of CoP.

The controllable deposition of stable Co-P ultrathin films by ALD was conducted at a pressure of 100 mtorr with the assistance of PH<sub>3</sub> (3% in Ar) plasma and H<sub>2</sub> plasma as illustrated in **Figure 6-1**. Planar Si wafers with a native oxide layer (SiO<sub>x</sub>) were used as substrates to study and optimize the deposition behavior of Co-P. This procedure induced a saturated growth process which was demonstrated by varying the exposure time of the metal precursor (t<sub>1</sub>) and the PH<sub>3</sub> plasma (t<sub>2</sub>) at a substrate temperature of 265 °C (Figure 6-2(a, b)). Figure 6-2(a) reveals that the growth rate increases initially with the increase of t<sub>1</sub> until saturation is achieved as t<sub>1</sub> exceeding approximately 3 s at fixed t<sub>2</sub> (5 s) and H<sub>2</sub> etching time (t<sub>3</sub> = 10 s). Similarly, while fixing t<sub>1</sub> at 3 s, the growth rate increased firstly with increasing t<sub>2</sub> and then reached saturation as t<sub>2</sub> exceeding approximately 5 s (Figure 6-2(b)). The impact of the H<sub>2</sub> plasma step was also investigated by changing its length from 0 to 3\*t<sub>2</sub>. As shown in Figure S6-1, the saturation of the growth rate and P/Co ratio was achieved when t<sub>3</sub> ≥ 2\*t<sub>2</sub>. Additionally, it can be concluded that the H<sub>2</sub> plasma step did not etch the formed Co-P layer. The Rutherford backscattering spectrometry (RBS) revealed that the ratio of P/Co is approximately 1.3 under the saturated growth rate condition. These results indicate that the self-limited layer-by-layer deposition behavior was achieved with sufficient exposure of Co(AMD)<sub>2</sub> and PH<sub>3</sub> plasma. Therefore, the saturated condition of t<sub>1</sub> = 3 s, t<sub>2</sub> = 5 s and t<sub>3</sub> = 10 s were used as a standard recipe for the deposition of Co-P films if not mentioned otherwise. Figure 6-2(c) shows that the thickness of the deposited Co-P films has a linear relationship with the number of ALD cycles with a slope of 0.022 (nm/cycle) under the standard recipe conditions, indicating a controllable deposition behavior. For the comparison, Co-P films deposited without the assistance of H<sub>2</sub> plasma, demonstrated an uncontrollable deposition behavior with a high growth rate of 0.16 nm/cycle. RBS revealed that the as-deposited Co-P film deposited without H<sub>2</sub> plasma etching exhibited a high P content (P/Co = 3.5). Moreover, the as-deposited Co-P film was not stable and was easily oxidized to phosphates in air (Figure S6-2). Therefore, the following reactions may happen during the H<sub>2</sub> plasma step:<sup>[13]</sup>



Next, the influence of the temperature on the deposition of Co-P films was investigated. As shown in Figure 6-2(d), the deposition process exhibited a wide temperature window from 120 to 300 °C with an almost constant growth rate. Moreover, RBS revealed that the deposited films exhibited an almost constant P/Co ratio (Figure 6-2(d)). The precursor decomposition was

also investigated by only pulsing  $\text{Co(AMD)}_2$  at 265 °C without  $\text{PH}_3$  and  $\text{H}_2$  plasma steps (denoted as  $\text{Co(AMD)}_2\text{-decom./Si}$ ). XPS measurements indicate that only a small amount of Co (5.59 atomic %) is present on the substrate surface (Figure S6-3(a-c)) after 200 cycles, which is consistent with a molecular monolayer that probably decomposed after exposure to the air. The XPS profile (Figure S6-3(d)) further reveals that there is no obvious layer on the substrate, indicating that there is negligible precursor decomposition at 265 °C, which has little impact on the ALD process. Nevertheless, we focus on the characterization of Co-P films deposited at 265 °C in the following.

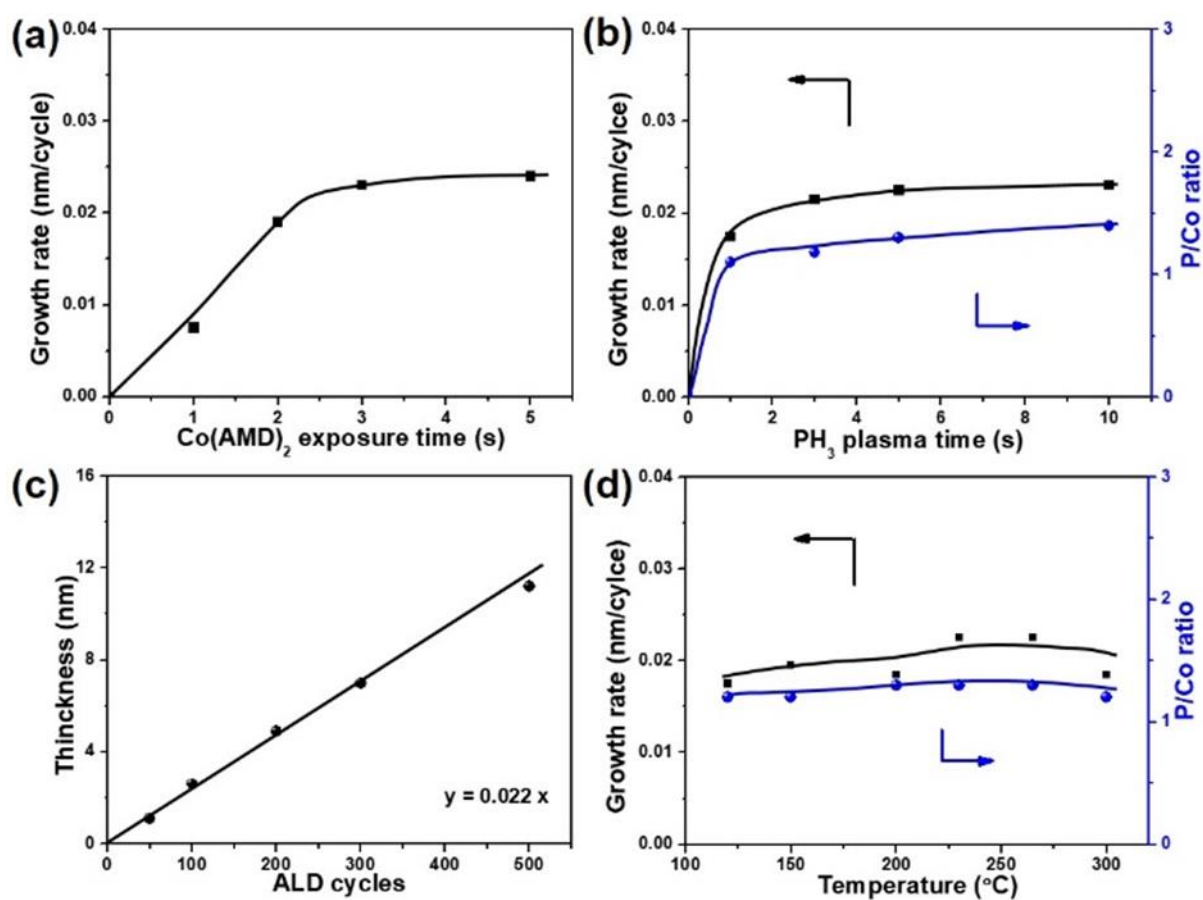


**Figure 6-2.** Exploration of Co-P ALD process (a) Growth rates versus the metal precursor exposure time at fixed  $t_2$  (5s) and  $\text{H}_2$  plasma etching time  $t_3$  (10 s). (b) Growth rates and their corresponding P/Co atomic ratios of prepared Co-P films versus  $\text{PH}_3$  plasma treatment time at constant  $t_1$  (3s). (c) Thickness of deposited Co-P films as a function of total number of ALD cycles. (d) Temperature dependency of the growth rates and the P/Co ratios.

The morphology of the deposited Co-P films was characterized by transmission electron microscopy (TEM). As shown in Figure 6-3(a), the top view TEM image of the Co-P film deposited on an amorphous  $\text{SiN}_x$  membrane with 300 cycles (6.7 nm) revealed that the as-deposited film exhibits regions of high crystallinity and regions of amorphous material. The region with high crystallinity demonstrates a lattice spacing of 0.25 nm, which can be associated to the (200) facet of CoP (PDF#29-0497).<sup>[18]</sup> However, it should be noted that amorphous Co-P can also be observed from this top view TEM image. The cross-section view of Co-P films

deposited on Si (Figure 6-3(b)) also indicates the polycrystalline property with crystal lattices of 0.28, 0.20 and 0.19 nm which can be associated to the (011), (210) and (211) facets of CoP, respectively. The electron diffraction pattern (Figure 6-3(a) inset) indicates that the main crystal structure of the Co-P film is associated with the crystal structure of CoP, which is consistent with the HRTEM results. Furthermore, similar morphology and crystalline phase are obtained for Co-P films deposited at 125 °C (Figure S6-4(a,b)) highlighting the wide temperature window for our process. The energy-dispersive X-ray spectroscopy (EDS) mapping of the Co-P films further revealed the high quality of the deposited layer (Figure 6-3(b), inset). Strong O signals are only observed at the surface of the Co-P films and its interface with the Si substrate, which can be assigned to the formation of a surface oxide due exposure to air (or adsorbed O<sub>2</sub>/H<sub>2</sub>O species) and the native oxide layer of the Si wafer. An optical photograph of one piece of Co-P/Si (6.7 nm Co-P) and the corresponding atomic force microscopy (AFM) measurement (Figure 6-3(c)) indicate that the deposited films are fairly smooth with a roughness of 0.37 nm.

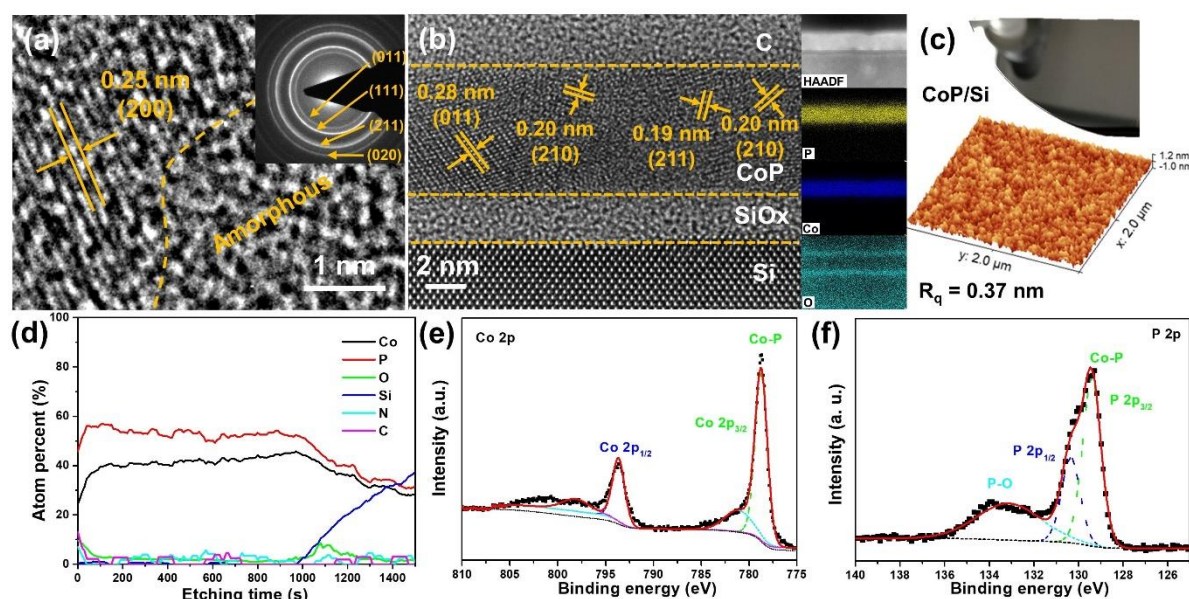


**Figure 6-3.** Structural and compositional analysis of Co-P films deposited at 265 °C. TEM images of (a) top view of Co-P film deposited on amorphous SiN<sub>x</sub> membrane and the corresponding electron diffraction as shown inset. (b) cross-section view of Co-P film deposited on Si at 265 °C with the corresponding EDS mapping (inset). (c) Optical photograph of one piece of Co-P/Si and the corresponding AFM measurement. (d) XPS profile of a Co-P film with a thickness of 25 nm. (e, f) XPS spectra of Co-P/Si for (e) Co 2p and (f) P 2p, respectively.

The purity of the deposited Co-P films was also characterized by X-ray photoelectron spectroscopy (XPS). The depth profile of the deposited Co-P films (Figure 6-3(d)) indicates that they are pure with negligible N, C and O contaminations. The surface O species were also detected, which is consistent with the EDS mapping. The Co 2p spectrum (Figure 6-3(e)) acquired from the surface of the Co-P films shows a pair of spin-orbit split peaks at 778.8 eV (Co 2p<sub>3/2</sub>) and 793.8 eV (Co 2p<sub>1/2</sub>), which are characteristic peaks of CoP.<sup>[19]</sup> In addition, the P



2p spectrum Figure 6-3(f) shows doublet peaks at 129.4 eV (P 2p<sub>3/2</sub>) and 130.3 eV (P 2p<sub>1/2</sub>) and an extra peak at 133.1 eV, which correspond to Co-P and P-O bonds, respectively. Furthermore, similar spectra were obtained for Co 2p and P 2p after storage for ~3 months in the ambient environment, indicating good stability and resistance to oxidation in air (Figure S6-5). It should be mentioned that a stronger O signal is observed on the surface of Co-P films, but the inner layer of Co-P is still no O (Figure S6-6), which indicates that the O species on the surface of Co-P films increase slowly with the storage time and provide protection against oxidation of the film bulk which is in sharp contrast to the Co-P films deposited without the H plasma step.

The HER activity of the Co-P films prepared with our ALD process was assessed by depositing Co-P films on an FTO glass substrate, and the corresponding optical photograph is shown in Figure S6-7. As shown in Figure 6-4(a), the sample labelled as Co-P/FTO, which was fabricated by depositing 6.7 nm Co-P on FTO at 265 °C using our optimized ALD recipe, demonstrates a significantly enhanced HER performance compared to bare FTO and Co-P/FTO-thermal which was prepared by the traditional thermal post-phosphorization of CoO<sub>x</sub> (10 nm) deposited by ALD on FTO.<sup>[19]</sup> The as-prepared Co-P/FTO electrode requires an overpotential of 254 mV to deliver a current density of 10 mA cm<sup>-2</sup> ( $\eta_{10}$ ), which is much lower than that of bare FTO ( $\eta_{10}$  = 663 mV) and Co-P/FTO-thermal ( $\eta_{10}$  = 320 mV) but still higher than that of Pt/FTO ( $\eta_{10}$  = 105 mV). Figure 6-4(b) shows that Co-P/FTO exhibits better reaction kinetics with a smaller Tafel slope of 59 mV dec<sup>-1</sup> than that of bare FTO (253 mV dec<sup>-1</sup>) and Co-P/FTO-thermal (95 mV dec<sup>-1</sup>). Electrochemical impedance spectroscopy (EIS) measurements were also employed to investigate the reaction mechanisms (Figure 6-4(c) and Table S 6-1), and the related results were fitted with the equivalent circuit as shown in the inset of Figure 6-4 (c). The EIS results reveal that Co-P/FTO exhibits a smaller charge transfer resistance ( $R_{ct}$  = 22.8  $\Omega$ ) than Co-P/FTO-thermal ( $R_{ct}$  = 69.5  $\Omega$ ), suggesting facilitated electron transfer for HER.<sup>[20]</sup> The thickness-dependent HER activities of Co-P/FTO are also investigated. As shown in Figure S6-8, an optimized performance is achieved with a ~6.7 nm Co-P film. The electrochemical surface area (ECSA) measurement indicates that Co-P/FTO with a higher capacitance ( $C_{dl}$ ) has more accessible active sites than CoP/FTO-thermal (Figure S6-9). The turnover frequency (TOF) for Co-P/FTO is estimated to be 0.08 s<sup>-1</sup> ( $\eta$  = 100 mV), which is higher than that of other cathodes reported in the literature (Table S6-2).<sup>[8,21]</sup> Furthermore, the as-prepared Co-P/FTO electrode exhibited good stability over an examination time of 36 h (Figure 6-4 (d)) at a current density of 10 mA cm<sup>-2</sup>. Next, Co-P films deposited on p-B Si wafer



(Co-P/Si) were evaluated for photoelectrochemical water splitting, which shows that the Co-P/Si demonstrates a better photoelectrochemical HER performance than that of the Co-P/Si-thermal (Figure 6-4(e)). It can be observed that the Co-P/Si demonstrates a more positive onset potential (0.27 V) than the Co-P/Si-thermal (-0.18 V), which is defined as the required potential for achieving a current density of  $-0.1 \text{ mA cm}^{-2}$ . A saturated photocurrent of  $\sim 32 \text{ mA cm}^{-2}$  is achieved by Co-P/Si, which is higher than other reports (Table S6-3).<sup>[8,22]</sup> The virtually instantaneous photoresponse for Co-P/Si under chopped light irradiation (Figure 6-4(f)) reveals that our deposited Co-P films have the potential to be used as the cocatalyst to improve the photoelectrochemical activity of semiconductors.

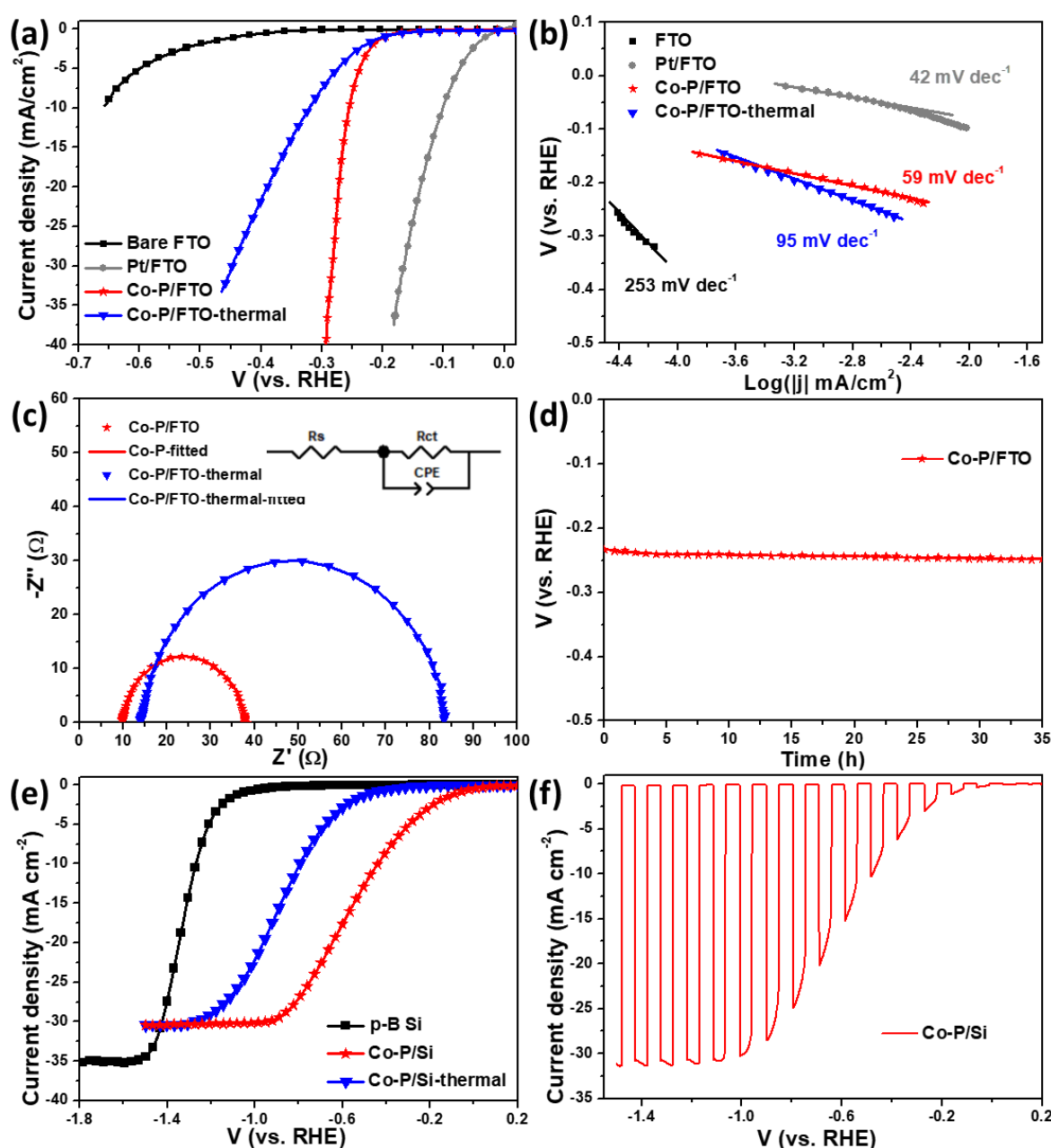


**Figure 6-4.** (a) LSV curves of the prepared Co-P/FTO, Co-P/FTO-thermal, Pt/FTO and bare FTO electrodes for HER in 1 M KOH. (b, c) The corresponding Tafel and EIS measurements of the prepared electrodes. The

corresponding equivalent circuit for the EIS fitting is shown in the inset of (c), where  $R_s$  is the ohmic resistance,  $R_{ct}$  is the charge transfer resistance, and CPE is the constant phase element. (d) Long-time measurement of the prepared Co-P/FTO for HER acquired at  $10 \text{ mA cm}^{-2}$ . (e) LSV curves of the prepared Co-P/Si, Co-P/Si-thermal and p-B Si for photoelectrochemical HER in 1 M KOH with the illumination of a solar simulator. (f) Transient photocurrent responses to chopped light irradiation of Co-P/Si.

We also evaluated the coverage ability of the ALD process by depositing Co-P films into deep-narrow Si trenches (**Figure 6-5(a)**). By Comparing with the bare Si trenches (Figure S6-10(a, b)), it can be seen that the Co-P films conformably cover the trenches (Figure 6-5(b, c)). These results clearly reveal the homogenous coating ability of our ALD process, and further indicates the promising potential application of a conformal coating of ultrathin Co-P films on complex 3D structures.

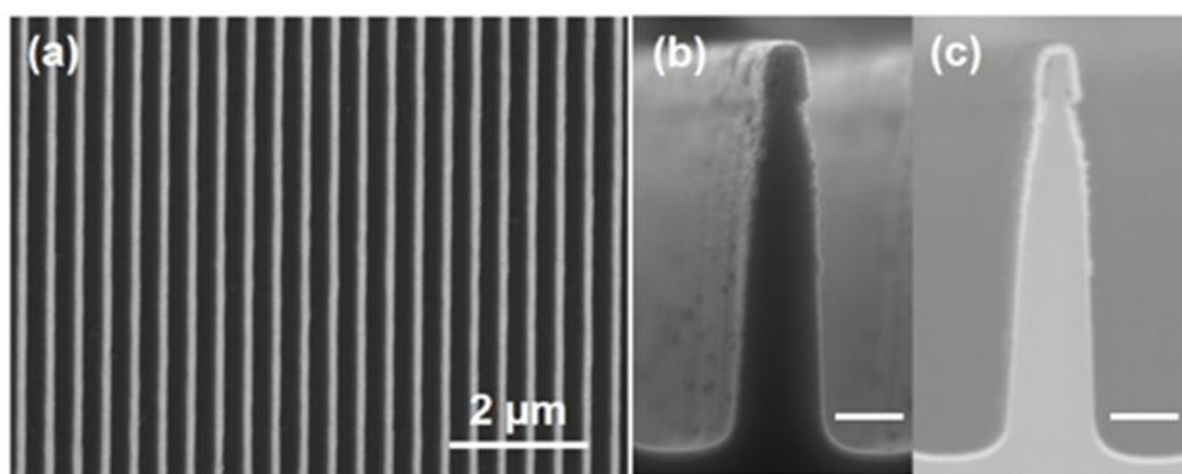


**Figure 6-5.** (a) Top view of Co-P coated Si trenches. (b) Cross-section view secondary-electron (SE) SEM image and (c) the corresponding backscattered- electron (BSE) image of conformally coated Si trenches with Co-P films. The scale bars in (b) and (c) are 200nm.

## 6.5 Conclusions

In summary, we reported a new ALD process for the preparation of ultrathin Co-P films with the assistance of  $\text{H}_2$  plasma to remove the excess phosphorus during each ALD cycle. The optimized ALD process follows the self-limited layer-by-layer deposition behavior to produce high quality and smooth Co-P films. The as-prepared Co-P films on FTO glass and Si demonstrate enhanced electrochemical and photoelectrochemical HER activities than that of Co-P/FTO-thermal prepared by a post-phosphorization method. Furthermore, Co-P films can be conformably deposited into periodic Si trenches, highlighting the capacity for controllable and conformal coating of Co-P films on complex 3D structures.

## 6.6 Acknowledgment

The authors thank Dr. Bodo Kalkofen, Dr. Dirk Sander and Dr. Fang Gao for their helps with the maintenance of the ALD system and Dr. Sara Azimi for her help to improve the ALD

system at the Max Planck Institute of Microstructure Physics. The financial support by the BMBF-project Struktursolar is highly acknowledged.

## 6.7 References

- [1] a) S. Chu, A. Majumdar, *Nature* 2012, 488, 294; b) S. E. Hosseini, M. A. Wahid, *Renewable Sustainable Energy Rev.* 2016, 57, 850; c) L. Schlapbach, A. Züttel, *Nature* 2001, 414, 353.
- [2] a) R. Subbaraman, D. Tripkovic, D. Strmcnik, K.-C. Chang, M. Uchimura, A. P. Paulikas, V. Stamenkovic, N. M. Markovic, *Science* 2011, 334, 1256; b) N. Cheng, S. Stambula, D. Wang, M. N. Banis, J. Liu, A. Riese, B. Xiao, R. Li, T.-K. Sham, L.-M. Liu et al., *Nat. Commun.* 2016, 7, 13638.
- [3] a) S. Sultan, J. N. Tiwari, A. N. Singh, S. Zhumagali, M. Ha, C. W. Myung, P. Thangavel, K. S. Kim, *Adv. Energy Mater.* 2019, 9, 48; b) H. Sun, Z. Yan, F. Liu, W. Xu, F. Cheng, J. Chen, *Adv. Mater.* 2019, e1806326; c) X. Du, J. Huang, J. Zhang, Y. Yan, C. Wu, Y. Hu, C. Yan, T. Lei, W. Chen, C. Fan et al., *Angew. Chem. Int. Edit.* 2019, 58, 4484; d) J. Li, R. Güttinger, R. Moré, F. Song, W. Wan, G. R. Patzke, *Chem. Soc. Rev.* 2017, 46, 6124.
- [4] J. Joo, T. Kim, J. Lee, S.-I. Choi, K. Lee, *Adv. Mater.* 2019, 31, e1806682.
- [5] a) J. F. Callejas, C. G. Read, C. W. Roske, N. S. Lewis, R. E. Schaak, *Chem. Mat.* 2016, 28, 6017; b) Y. Wang, B. Kong, D. Y. Zhao, H. T. Wang, C. Selomulya, *Nano Today* 2017, 15, 26; c) G. Zhao, K. Rui, S. X. Dou, W. Sun, *Adv. Funct. Mater.* 2018, 28, 1803291; d) M. Sun, H. Liu, J. Qu, J. Li, *Adv. Energy Mater.* 2016, 6, 1600087; e) H. Zhang, A. W. Maijenburg, X. Li, S. L. Schweizer, R. B. Wehrspohn, *Adv. Funct. Mater.* 2020, 10.1002/adfm.202003261.
- [6] N. Jiang, B. You, M. L. Sheng, Y. J. Sun, *Angew. Chem. Int. Edit.* 2015, 54, 6251.
- [7] T. R. Hellstern, J. D. Benck, J. Kibsgaard, C. Hahn, T. F. Jaramillo, *Adv. Energy Mater.* 2016, 6, 1501758.
- [8] H. Li, P. Wen, D. S. Itanze, M. W. Kim, S. Adhikari, C. Lu, L. Jiang, Y. Qiu, S. M. Geyer, *Adv. Mater.* 2019, 31, e1900813.
- [9] a) S. Sharma, J. Waldman, S. Afshari, B. Fekete, *Renewable Sustainable Energy Rev.* 2019, 101, 112; b) B. C. Mallick, C.-T. Hsieh, K.-M. Yin, Y. A. Gandomi, K.-T. Huang, *ECS J. Solid State Sci. Technol.* 2019, 8, N55-N78.
- [10] J. Rongé, T. Dobbelaere, L. Henderick, M. M. Minjauw, S. P. Sree, J. Dendooven, J. A. Martens, C. Detavernier, *Nanoscale Adv.* 2019, 1, 4166.
- [11] Z. Guo, X. Wang, *Angew. Chem. Int. Edit.* 2018, 57, 5898.
- [12] G. Bruno, P. Capezzuto, M. Losurdo, *J. Phys. IV France* 1995, 05, C5-481-C5-488.
- [13] A. V. Uvarov, A. S. Gudovskikh, *J. Phys.: Conf. Ser.* 2018, 1038, 12108.
- [14] A. J. M. Mackus, D. Garcia-Alonso, H. C. M. Knoop, A. A. Bol, W. M. M. Kessels, *Chem. Mater.* 2013, 25, 1769.
- [15] J. Hämäläinen, E. Puukilainen, M. Kemell, L. Costelle, M. Ritala, M. Leskelä, *Chem. Mater.* 2009, 21, 4868.
- [16] M. Daub, M. Knez, U. Goesele, K. Nielsch, *Journal of Applied Physics* 2007, 101, 09J111.
- [17] T. S. Tripathi, M. Karppinen, *Chem. Mater.* 2017, 29, 1230.
- [18] L. Su, X. Cui, T. He, L. Zeng, H. Tian, Y. Song, K. Qi, B. Y. Xia, *Chem. Sci.* 2019, 10, 2019.
- [19] H. J. Zhang, X. P. Li, A. Hahnel, V. Naumann, C. Lin, S. Azimi, S. L. Schweizer, A. W. Maijenburg, R. B. Wehrspohn, *Adv. Funct. Mater.* 2018, 28, 1706847.
- [20] S. Song, M. Guo, S. Zhang, K. Zhan, Y. Yan, J. Yang, B. Zhao, M. Xu, *Electrochim. Acta* 2020, 331, 135431.

- [21] a) R. Zhang, X. Wang, S. Yu, T. Wen, X. Zhu, F. Yang, X. Sun, W. Hu, *Adv. Mater.* 2017, 29, 1605502; b) E. J. Popczun, J. R. McKone, C. G. Read, A. J. Biacchi, A. M. Wiltrout, N. S. Lewis, R. E. Schaak, *J. Am. Chem. Soc.* 2013, 135, 9267; c) E. J. Popczun, C. G. Read, C. W. Roske, N. S. Lewis, R. E. Schaak, *Angew. Chem. Int. Edit.* 2014, 53, 5427.
- [22] a) T. R. Hellstern, J. D. Benck, J. Kibsgaard, C. Hahn, T. F. Jaramillo, *Adv. Energy Mater.* 2016, 6, 1501758; b) J. Zhao, L. Cai, H. Li, X. Shi, X. Zheng, *ACS Energy Lett.* 2017, 2, 1939; c) S. M. Thalluri, J. Borme, K. Yu, J. Y. Xu, I. Amorim, J. Gaspar, L. Qiao, P. Ferreira, P. Alpuim, L. F. Liu, *Nano Res.* 2018, 11, 4823.

## 6.8 Supporting Information

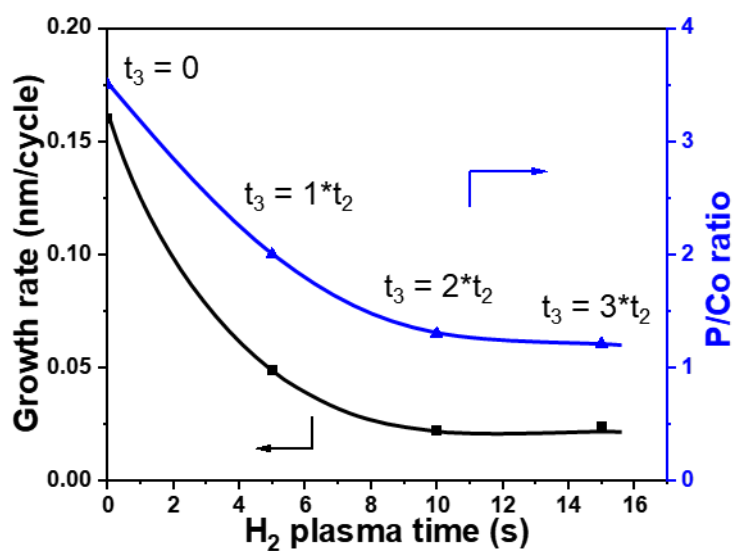


Figure S6-1. Growth rate and P/Co ratio versus the H<sub>2</sub> plasma time.

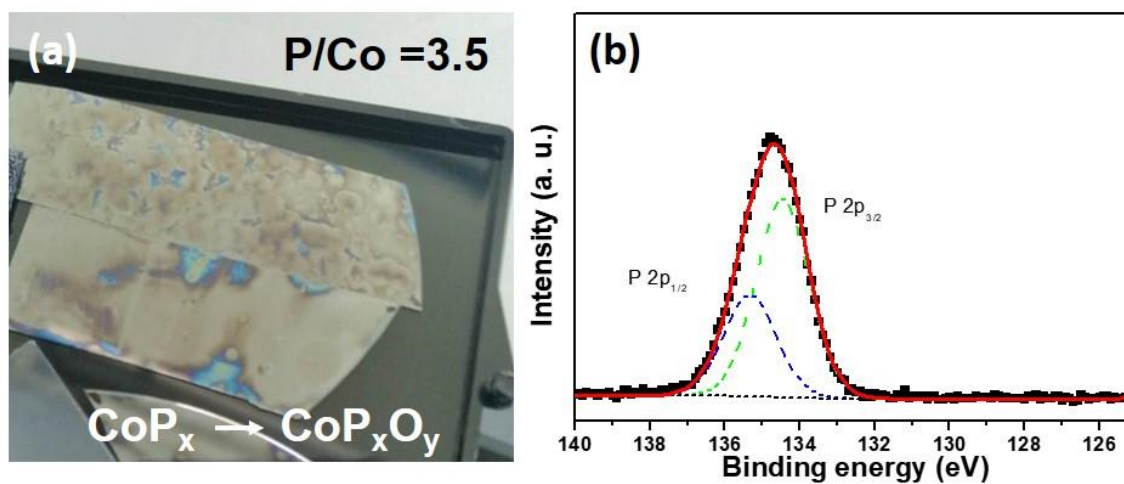


Figure S6-2. (a) Photograph of CoP<sub>x</sub> films deposited with a regular ALD process (without H<sub>2</sub> plasma) after storage in air for 1 day. (b) The corresponding XPS P 2p spectrum of the sample as shown in (a).

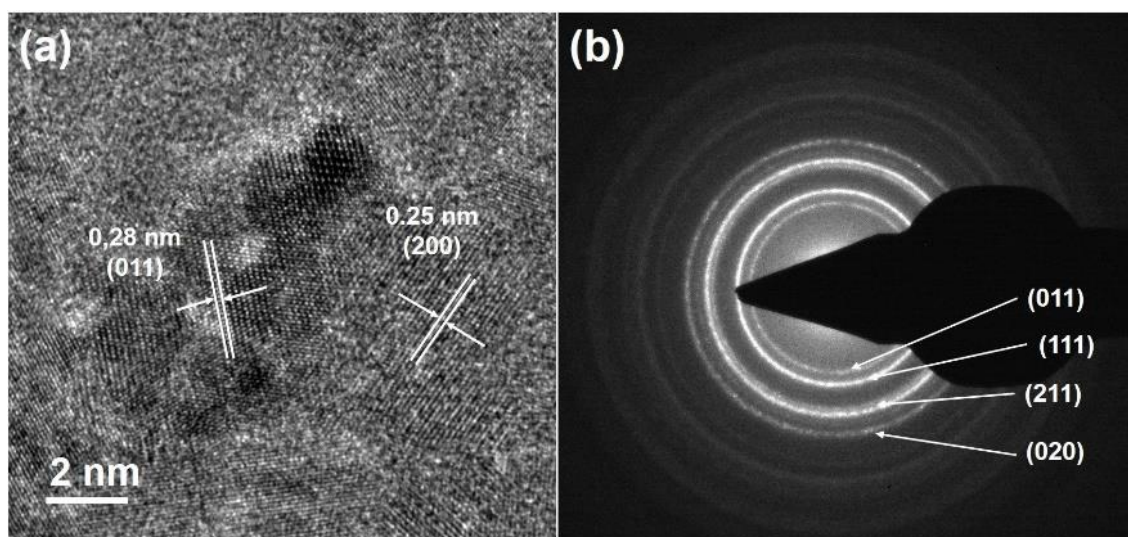
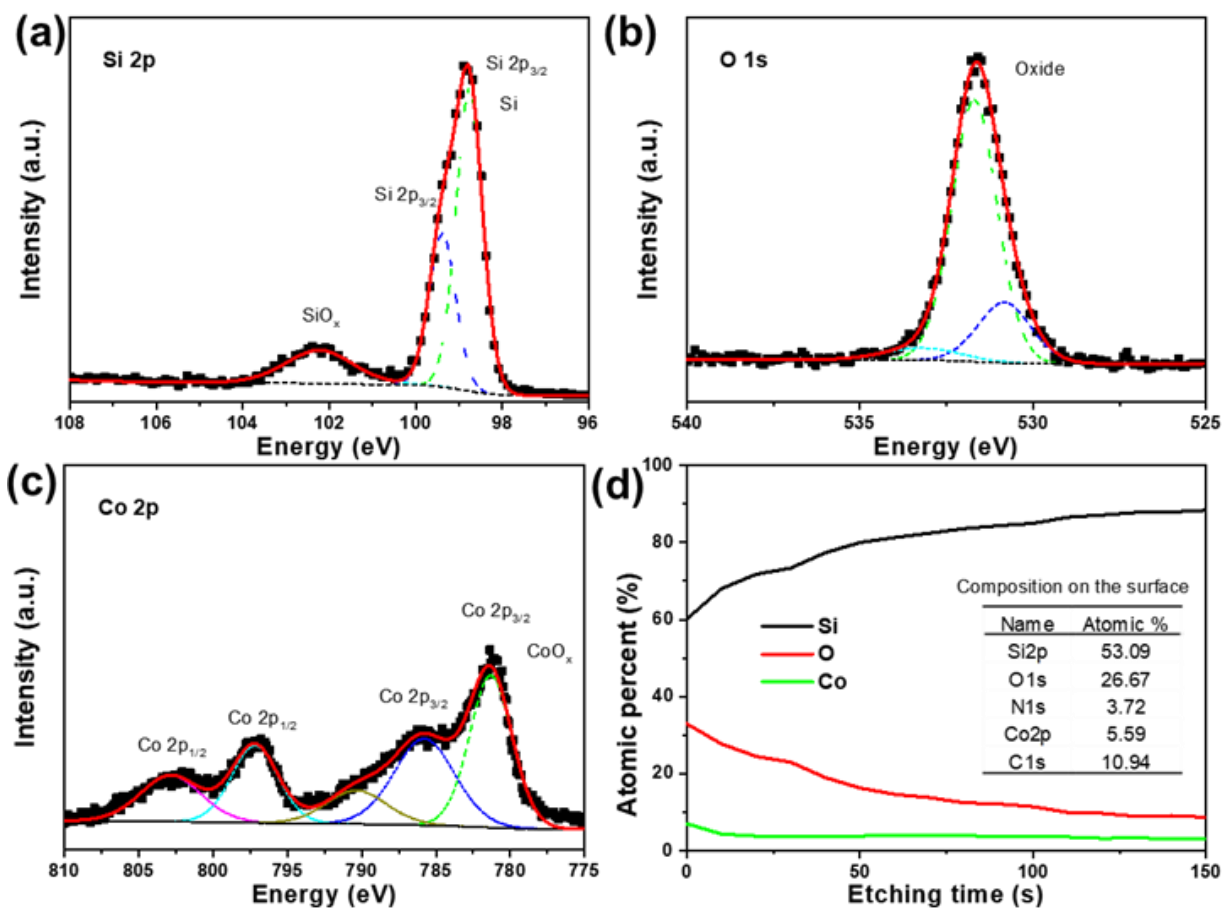


Figure S6-4. (a) Top-view HRTEM image of Co-P film deposited at 125 °C (Co-P/Si@125 °C) and (b) the corresponding electron diffraction.

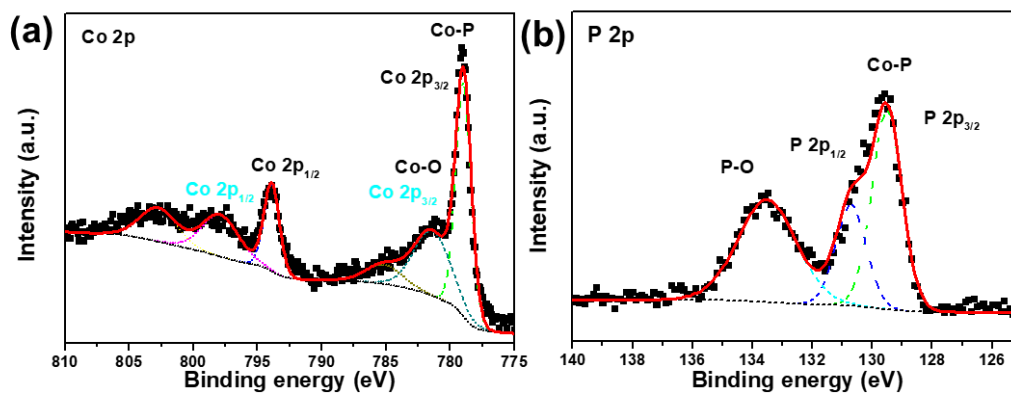


Figure S6-5. XPS spectra of Co-P films after storage in air for ~3 months. (a) Co 2p and (b) P 2p were acquired from the surface.

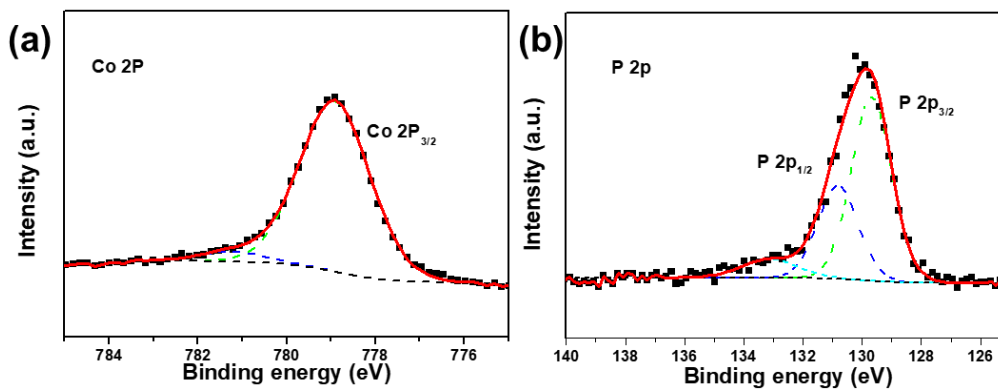


Figure S6-6. XPS spectra of Co-P/Si films after storage for ~3 months in air. (a) Co 2p and (b) P 2p were acquired after 10 s etching with 1000 eV.

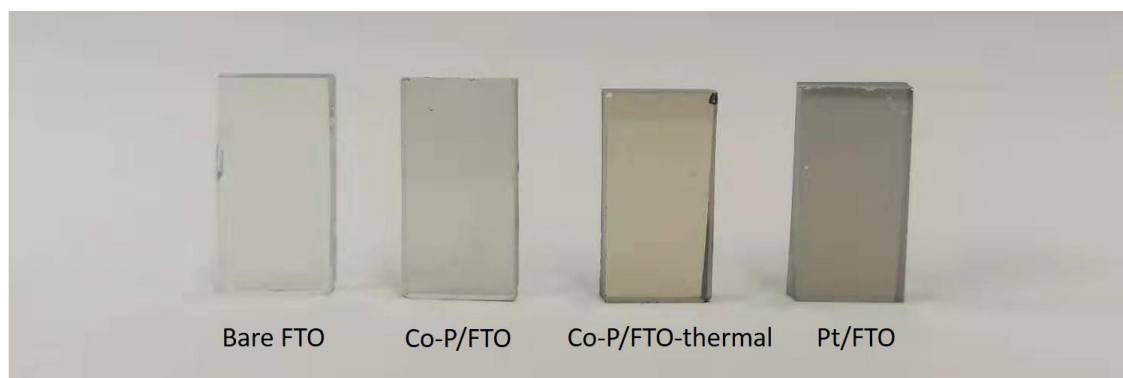


Figure S6-7. Photographs of the prepared electrodes: Bare FTO, Co-P/FTO, Co-P/FTO-thermal and Pt/FTO.

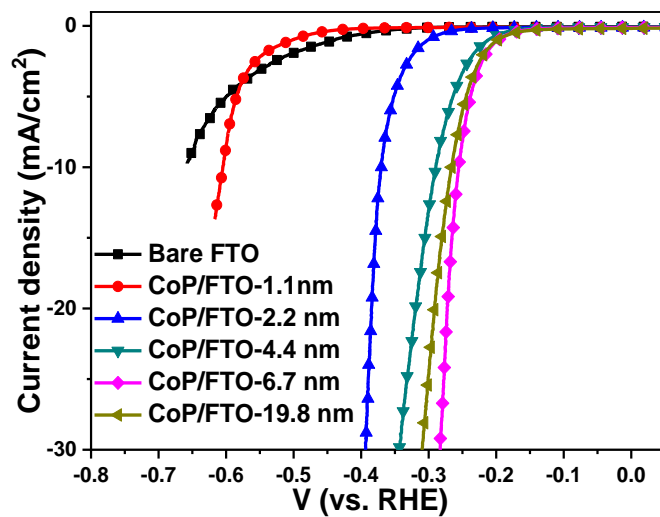


Figure S6-8. HER activities of cathodes prepared by depositing Co-P films on FTO with different thicknesses.

Table S6-1. Fitted results of the EIS measurement for the prepared Co-P/FTO and Co-P/FTO-thermal.

Samples	$R_s$ ( $\Omega$ )	$R_{ct}$ ( $\Omega$ )	CPE	
			$Y_0$ ( $\mu\text{Mho}$ )	N
Co-P/FTO	9.7	28.2	0.196	0.91
Co-P/FTO-thermal	14.1	69.5	0.378	0.91

Where  $R_s$  is the ohmic resistance,  $R_{ct}$  is the charge transfer resistance, and CPE is the constant phase element.



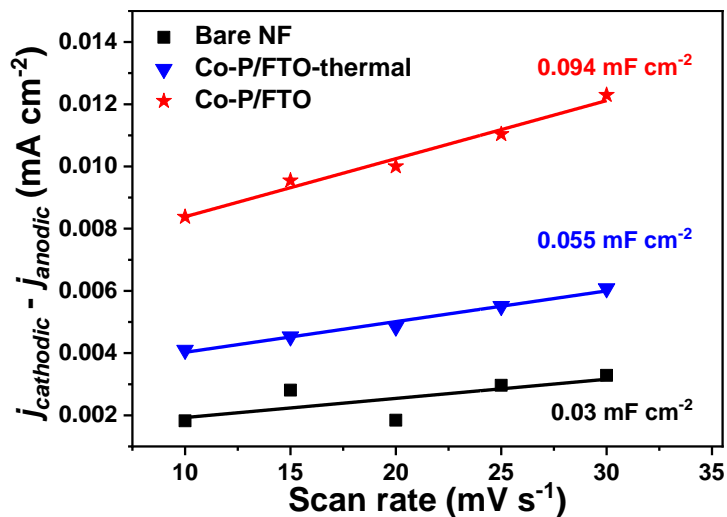


Figure S6-9. The double-layer capacitances calculated by linear fitting the curve of capacitive current versus scan rate at a voltage of 0.15 V vs. RHE.

Table S6-2. Comparison of electrochemical HER activities of TMP-based cathodes.

Samples	Substrate	$\eta$ (10 mA cm <sup>-2</sup> )	TOF (s <sup>-1</sup> )	Electrolyte	Ref.
Co-P/FTO	FTO	254	0.08	1 M KOH	This work
NiCo <sub>2</sub> P <sub>x</sub>	NF	58	0.056	1 M KOH	[3]
CoP <sub>x</sub>	NF	94	0.015	1 M KOH	[3]
Ni <sub>2</sub> P NCs	Ti	130( $\eta_{20}$ )	0.015	0.5 M H <sub>2</sub> SO <sub>4</sub>	[4]
CoP NCs	Ti	85( $\eta_{20}$ )	0.046	0.5 M H <sub>2</sub> SO <sub>4</sub>	[5]
CoP <sub>2</sub> NCs	GC	39	0.561	0.5 M H <sub>2</sub> SO <sub>4</sub>	[2]

Note: GC, glassy carbon; NF, nickel foam; TOF was calculated at  $\eta = 100$  mV.

Table S6-3. Comparison of PEC HER activities of Si-based photocathodes.

Samples	$E_{\text{onset}}$ (mV)	$J_{sc}$ (mA cm <sup>-2</sup> )	Electrolyte	Ref.
Co-P/Si	270	~32	1 M KOH	This work
NiFe LDH/p-Si	300	~27.5	1 M KOH	[6]
SiNW@Co <sub>2</sub> P	250	~26	0.5 M H <sub>2</sub> SO <sub>4</sub>	[7]
p-Si/AZO/TiO <sub>2</sub> /CoP <sub>2</sub>	480	~19	0.5 M H <sub>2</sub> SO <sub>4</sub>	[2]
CoP-n <sup>+</sup> Si	400	19.8	0.5 M H <sub>2</sub> SO <sub>4</sub>	[8]

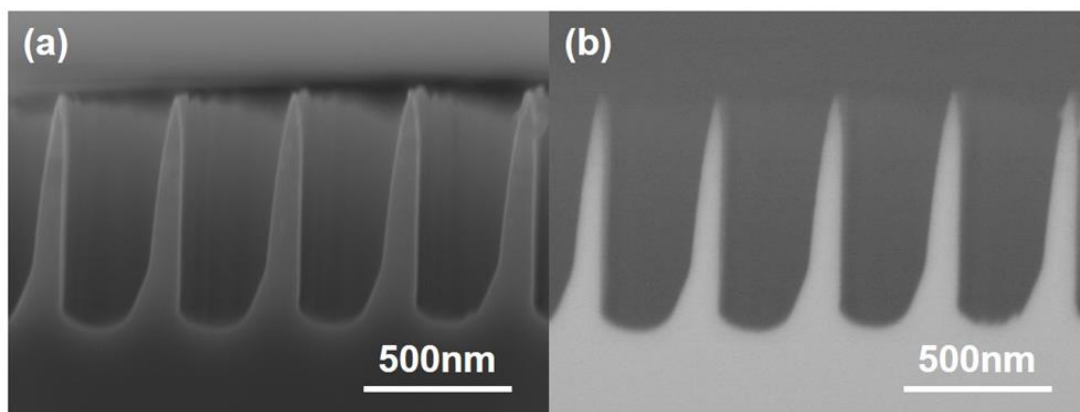


Figure S6-10. (a) Secondary-electron (SE) SEM image and (b) corresponding backscattered-electron (BSE) image of the cross-section of bare Si trenches.

#### References:

- [1] a) H. Liang, A. N. Gandhi, D. H. Anjum, X. Wang, U. Schwingenschlöggl, H. N. Alshareef, *Nano Lett.* **2016**, *16*, 7718; b) H. J. Zhang, X. P. Li, A. Hahnel, V. Naumann, C. Lin, S. Azimi, S. L. Schweizer, A. W. Maijenburg, R. B. Wehrspohn, *Adv. Funct. Mater.* **2018**, *28*, 1706847.
- [2] H. Li, P. Wen, D. S. Itanze, M. W. Kim, S. Adhikari, C. Lu, L. Jiang, Y. Qiu, S. M. Geyer, *Adv. Mater.* **2019**, *31*, e1900813.
- [3] R. Zhang, X. Wang, S. Yu, T. Wen, X. Zhu, F. Yang, X. Sun, W. Hu, *Adv. Mater.* **2017**, *29*, 1605502.
- [4] E. J. Popczun, J. R. McKone, C. G. Read, A. J. Biacchi, A. M. Wiltrout, N. S. Lewis, R. E. Schaak, *J. Am. Chem. Soc.* **2013**, *135*, 9267.
- [5] E. J. Popczun, C. G. Read, C. W. Roske, N. S. Lewis, R. E. Schaak, *Angew. Chem. Int. Edit.* **2014**, *53*, 5427.
- [6] J. Zhao, L. Cai, H. Li, X. Shi, X. Zheng, *ACS Energy Lett.* **2017**, *2*, 1939.
- [7] S. M. Thalluri, J. Borme, K. Yu, J. Y. Xu, I. Amorim, J. Gaspar, L. Qiao, P. Ferreira, P. Alpuim, L. F. Liu, *Nano Res.* **2018**, *11*, 4823.
- [8] T. R. Hellstern, J. D. Benck, J. Kibsgaard, C. Hahn, T. F. Jaramillo, *Adv. Energy Mater.* **2016**, *6*, 1501758.

## 7 Conclusions and Outlook

In this thesis, I provided a comprehensive summary of the basic knowledge of the OER and the HER, and the recent process of the global research on TMP-based heterostructures for efficient water splitting. The general reaction mechanism for the OER and the HER, as well as the related reaction mechanisms that take place on the surface of TMP-based heterostructures are also discussed. In order to reduce the cost of electrochemical water splitting, I employed two strategies to prepare robust and abundant 3D electrodes: a) the design and preparation of highly active catalysts, and b) the use of a cheaper substrate (SS) for the preparation of 3D electrodes. For the first strategy, we prepared a heterostructure by combining two different catalysts, namely NiFe LDH nanosheets and NiCoP nanowires, and the resulting 3D NiFe LDH/NiCoP@NF electrodes demonstrated a better bifunctional activity for both the HER and the OER when compared to its counterparts. A new recipe for preparing TMP by the ALD process was also explored and optimized for the first time. The CoP ultrathin films prepared with our ALD recipe show a higher HER activity than CoP films prepared by the traditional post-phosphorization method. For the second strategy, we used CNTs as the interface material to combine SS with highly active catalysts to improve the activity of SS-based 3D electrodes for efficient water splitting. The CVD process for growing CNTs on the surface of SS was optimized, and the as-prepared CNT/SS electrodes were successfully modified with the state-of-the-art catalysts Pt and RuO<sub>2</sub>. The resulting 3D Pt/OxCNT/SS and RuO<sub>2</sub>/OxCNT/SS exhibited a better HER and OER activity, respectively, than the reference of 20 wt% Pt/C/SS and RuO<sub>2</sub>/SS. Both strategies have promising potential for the further design and preparation of abundant and robust 3D electrodes for efficient electrochemical water splitting as well as for other electrochemical areas.

Based on those results discussed above, I would like to give some outlooks for further designing and preparing robust and abundant 3D electrodes for highly efficient electrochemical water splitting.

The heterostructure with a strong synergistic effect is an effective approach to improve the catalytic activity of prepared catalysts and a novel strategy to design and prepare bifunctional electrocatalysts for efficient water splitting. However, the related reaction mechanisms happening on the surface of the heterostructure are still not understood. Therefore, more efforts are needed in order to understand the reaction mechanisms on the surface of the heterostructure.

Employing CNT as an interface material can make extremely stable SS become more suitable to the decoration with highly active electrocatalysts for the preparation of SS-based 3D electrodes towards efficient water splitting. The possibility of modifying CNT/SS with abundant and efficient catalysts to further enhance the performance of 3D SS-based electrodes is still needed to be investigated further.

ALD is an innovative method for the conformal and controllable deposition of ultrathin TMP-based catalyst films. The TMP-based catalysts deposited by ALD show a promising application potential for designing and preparing 3D electrodes for (photo)electrochemical water splitting as well as other electrochemical areas by depositing TMP on various 3D structures. Our work explored and improved the ALD process to obtain the controllable deposition of highly pure and stable CoP, but other TMP, such as Ni-based, Fe-based and Mo-based phosphides as well as their bi-/trimestral phosphides should also be prepared by the ALD approach.

## 8 Acknowledgements

I hereby would like to give my best wish and thank to whom support or help me in the past three years. Without them, I cannot finish even start my Ph.D.

Firstly, I would like to express my sincere gratitude to my supervisor Prof. Dr. Ralf B. Wehrspohn. He offered me the chance to study and work in Halle and taken me into this interesting and promising research area. His inspirational guidance and suggestion encouraged me a lot to continue and explore the right way to do meaningful research.

Secondly, I want to thank my second supervisor Jun. Prof. Dr. A. Wouter Maijenburg who gave me access to his laboratory, discussed the experiment results with me and helped me to improve my writing. All the electrochemical measurements were carried out in his laboratory. Without his precious support, it would not be possible to conduct this research and publish the results in time.

Simultaneously, I want to thank Prof. Dr. Michael Bron at the Institute of Chemistry MLU. Without his support, I cannot manage to optimal the CVD process of growth of CNTs as discussed in chapter 4 and 5. I really appreciate his significant guidance and discussion during the experiment and publishing process.

I am also grateful for the support of Prof. Dr. Stuart Parkin at the Max Planck Institute of Microstructure Physics. With his support, we managed to move ALD to MPI successfully and upgraded the system to meet the requirement of deposition of metal phosphide as discussed in chapter 6. He strongly supported my research during pursuing my doctoral degree.

I want to thank my master supervisor Prof. Xiaopeng Li at the Donghua University. He brought me into the research field of electrochemical water splitting and gave me comprehensive training in scientific research and taught me how to write my first paper. If I didn't meet him, I may not enter the field of academic research.

Furthermore, I want to thank my colleagues, Dr. Stefan L. Schweizer, Dr. Juliana Martins de Souza e Silva, Dr. Alexander Sprafke, Dr. Chao Lin, Dr. Maria Gaudig, Dr. Cristine Santos de Oliveira, Peter Piechulla, Richard Schalinski, Junna Wang, Yingzhen Chen, Dr. Bodo Fuhrmann, Dr. Frank Heyroth, Frank Syrowatka, Sven Schlenker, Dr. Pei Wang, Xubin Lu, Dr. Bin Cui, Dr. Angelika Hähnel, Dr. Volker Naumann, Dr. Sara Azimi, Dr. Andreas Graff, Dr. Dirk Hagen, Dr. Ilya Kostanovskiy, Dr. Francesco Caddeo, Dr. Bodo Kalkofen, Dr. Dirk Sander, Dr. Yanzhang Yang, Dr. Songkai Xiao, Dr. Fang Gao, Dr. Guowei Li, Weikai Xiang, Behzad

Mahmoudi Alibeiglou, Titus Lindenberg, Ole Reichel, Dr. Kasper Wenderich, Dr. Robert Naumann, Prof. Dr. Norbert Bernhard, Prof. Dr. Robert Naumann, Dr. Paul-Tiberiu Miclea, Prof. Dr. Jörg Schilling, Dr. Akash Bhatnagar, Marian Lisca, Lutz Mühlenbein, Marcel Below, Xinye Li, Niranjan Ramakrishnegowda, Yeseul Yun, Simone Stahn, Claudia Stehr, Doreen Rawald, Sandra Gesemann, Romy Oleynik-Weber, Heike Gehritz, and Antje Paetzold for the material characterization, scientific discussion, nice collaboration and help in daily working time.

I also wish to thank my wife Yuan Wang, my parents, mother-in-law, father-in-law and my brothers and sisters for their support throughout my daily life. I cannot have a happy life and finish my degree without their support. I am also happy to have my newborn baby (Yelin Zhang) and thank him for bringing me so much happiness.

Last but not the least, I wish to thank my friends for their help and all the fun we had in daily life. The financial support from the BMBF is also acknowledged.

在此特别感谢我的妻子，王媛，在过去三年里为我和我的家庭的无私奉献与牺牲。没有她的付出和鼓励，我无法完成这篇论文。同时也对我的父母，岳父岳母，恩师，兄弟姐妹，亲朋好友，同学，同事，以及帮助过我的人表达我最诚挚的感谢和美好的祝福。

特此献给我新出生的宝宝(张烨霖)，祝福他能够健康快乐的成长，未来能够为自己的理想努力奋斗。

# Acronyms

ALD	Atomic layer deposition
AFM	Atomic force microscope
APCVD	Atmospheric pressure chemical vapor deposition
CC	Carbon cloth
CFP	Carbon fiber paper
CV	Cyclic voltammetry
CNT	Carbon nanotube
CVD	Chemical vapor deposition
ECSA	Electrochemical active surface area
EDS	Energy-dispersive X-ray spectroscopy
EIS	Electrochemical impedance spectroscopy
HER	Hydrogen evolution reaction
LSV	Linear sweep voltammetry
OER	Oxygen evolution reaction
NF	Nickel foam
RBS	Rutherford backscattering spectrometry
SEM	Scanning electron microscope
SS	Stainless steel
TEM	Transmission electron microscope
TM	Transition metals
TMO	Transition metal oxides
TMH	transition metal hydroxides
TMP	Transition metal phosphides
TMS	Transition metal sulfides
XPS	X-ray photoelectron spectroscopy

# Publications

## Papers

1. **H. Zhang**, D. Hagen, A. Graff, F. Heyroth, B. Fuhrmann, I. Kostanovskiy, S. L. Schweizer, F. Caddeo, A. W. Maijenburg, S. Parkin, and R. B. Wehrspohn, Atomic Layer Deposition of Cobalt Phosphide for Efficient Water Splitting. *Angew. Chem. Int. Ed.* 2020, 10.1002/anie.202002280.
2. **H. Zhang**, Y. Zhao, Y. Sun, Q. Xu, R. Yang, H. Zhang, C. Lin, K. Kato, X. Li, M. Yamauchi and Z. Jiang, A novel self-assembly approach for synthesizing nanofiber aerogel supported platinum single atoms, *J. Mater. Chem. A*, 2020, 8, 15094-15102.
3. **H. Zhang**, J. M. de Souza e Silva, C. S. de Oliveira, X. Lu, S. L. Schweizer, A. W. Maijenburg, M. Bron, R. B. Wehrspohn, Optimization of Chemical Vapor Deposition Process for Carbon Nanotubes Growth on Stainless Steel: Towards Efficient Hydrogen Evolution Reaction. *MRS Advances* 2020.
4. **H. Zhang**, A. W. Maijenburg, X. Li, S. L. Schweizer, R. B. Wehrspohn, Bifunctional Heterostructure Transition Metal Phosphides for Efficient Electrochemical Water Splitting, *Adv. Funct. Mater.* 2020, 30, 2003261.
5. **H. Zhang**, J. M. de Souza e Silva, X. Lu, C. S. de Oliveira, B. Cui, X. Li, C. Lin, S. L. Schweizer, A. W. Maijenburg, M. Bron, R. B. Wehrspohn, Novel Stable 3D Stainless Steel-Based Electrodes for Efficient Water Splitting. *Adv. Mater. Interfaces* 2019, 6(18), 1900774.
6. S. Ni,<sup>1</sup> **H. Zhang**,<sup>1</sup> Y. Zhao, X. Li, Y. Sun, J. Qian, Q. Xu, P. Gao, D. Wu, K. Kato, M. Yamauchi, Y. Sun, Single atomic Ag enhances the bifunctional activity and cycling stability of MnO<sub>2</sub>. *Chem. Eng. J.* 2019, 366, 631-638.
7. **H. Zhang**, X. Li, A. Hähnel, V. Naumann, C. Lin, S. Azimi, S. L. Schweizer, A. W. Maijenburg, R. B. Wehrspohn, Bifunctional Heterostructure Assembly of NiFe LDH Nanosheets on NiCoP Nanowires for Highly Efficient and Stable Overall Water Splitting. *Adv. Funct. Mater.* 2018, 28(14), 1706847.
8. C. Lin, X. Li, S. S. Shinde, D.-H. Kim, X. Song, **H. Zhang**, J.-H. Lee, Long-Life Rechargeable Zn Air Battery Based on Binary Metal Carbide Armored by Nitrogen-Doped Carbon. *ACS Appl. Energy Mater.* 2019, 2(3), 1747-1755.
9. C. Lin, S. S. Shinde, X. Li, D. H. Kim, N. Li, Y. Sun, X. Song, **H. Zhang**, C. H. Lee, S. U. Lee, J. H. Lee, Solid-State Rechargeable Zinc-Air Battery with Long Shelf Life Based on Nanoengineered Polymer Electrolyte. *ChemSusChem* 2018, 11 (18), 3215-3224.



10. C. Lin, Y. Zhao, **H. Zhang**, S. Xie, Y. F. Li, X. Li, Z. Jiang, Z. P. Liu, Accelerated active phase transformation of NiO powered by Pt single atoms for enhanced oxygen evolution reaction. *Chem. Sci.* 2018, 9 (33), 6803-6812.
11. C. Lin, S. S. Shinde, Y. Wang, Y. Sun, S. Chen, **H. Zhang**, X. Li, J.-H. Lee, Flexible and rechargeable Zn–air batteries based on green feedstocks with 75% round-trip efficiency. *Sustain. Energy Fuels* 2017, 1 (9), 1909-1914.

# International conferences

## Oral

1. **H. Zhang**, J. M. de Souza e Silva, X. Li, A. W. Maijenburg, S. Schweizer, R. Wehrspohn, Novel Stable Three-Dimensional (3D) Stainless Steel-Based Electrodes for Efficient Water Splitting, Materials research society (MRS) Fall 2019, Boston, USA, December 2019.

## Poster

1. **H. Zhang**, S. Schweizer, W. Maijenburg and R. Wehrspohn, Interface Engineering of the Photoelectrochemical Oxygen Evolution Performance of Cobalt Oxide Coated n-Si, SP7 International Conference on Semiconductor Photochemistry, Milan, Italy, September 2019.
2. **H. Zhang**, X. Li, A. Hähnel, V. Naumann, C. Lin, S. Azimi, S.L. Schweizer, A.W. Maijenburg und R.B. Wehrspohn, Bifunctional heterostructure assembly of NiFe LDH nanosheets on NiCoP nanowires for highly efficient and stable overall water splitting, GDCh Electrochemistry 2018, Ulm, Germany, September 2018.
3. **H. Zhang**, B. Fuhrmann, A.W. Maijenburg, S.L. Schweizer, A. Sprafke and R.B. Wehrspohn, Deposition of transition met oxide thin films on silicon wafer by atomic later deposition (ALD) for high-efficient photoelectrochemical water splitting, DPG Spring Meeting 2018, Berlin, Deutschland, March 2018.
4. **H. Zhang**, J. Wang, S. Schweizer, A. Sprafke, A.W. Maijenburg and R.B. Wehrspohn, Different surface texture p-silicon photocathodes prepared by metal assisted chemical etching for photoelectrochemical water splitting, MANS 2017, Leipzig, Deutschland, August 2017.
5. **H. Zhang**, J. Wang, S. Schweizer, A. Sprafke, and R.B. Wehrspohn, Different surface texture p-silicon photocathodes prepared by metal assisted chemical etching for photoelectrochemical water splitting, DPG Spring Meeting 2017, Dresden, Deutschland, March 2017.

# Curriculum Vitae

Haojie ZHANG (张豪杰)

Institute of Physics, Martin Luther University Halle-Wittenberg

Heinrich-Damerow-Str. 4, 06120 Halle (Saale), Germany

Email: haojie.zhang@student.uni-halle.de

haojiezhang1@outlook.com

Date of birth: 13<sup>th</sup> December 1990

## Education

- 11.2016 - now      Ph.D. Candidate
- Martin Luther University Halle-Wittenberg
- Supervisors: Prof. Ralf B. Wehrspohn, Jun.-Prof. A. Wouter Maijenburg
- 09.2013 - 06.2016      Master degree
- Shanghai Advanced Research Institute, Chinese Academy of Science
  - Shanghai University
- Shanghai, China
- Major: Applied chemistry
- Supervisors: Prof. Zheng Jiao, Prof. Yuhan Sun, Prof. Xiaopeng Li
- 09.2009 - 06.2013      Bachelor degree
- Zhengzhou University
- Zhengzhou, China
- Major: Chemical engineering and technology

# Declaration

Herein, I declare that this thesis is finished based on my own work in the past three years and it neither contains the materials published previously or written by other people, nor the substantial extent used to apply any other degree or diploma at any educational institutions, except the declaration made in the acknowledgment part in this thesis. Any contribution made to this work by others is expressly acknowledged in this thesis.

Halle, 20.01.2021  
Place and date

  
Signature: